Photo-luminescence Guided Metal Ion Sensing and Environmental Remediation Applications of Green Synthesized Iron and Iron-based Nanomaterials

Piyal Mondal

Photo-luminescence Guided Metal Ion Sensing and Environmental Remediation Applications of Green Synthesized Iron and Iron-based Nanomaterials

Thesis submitted in partial fulfillment of the requirement for the degree of

Doctor of Philosophy

By

Piyal Mondal

Roll No.: 156107029

Department of Chemical Engineering

Indian Institute of Technology Guwahati, Assam 781039

June, 2021

Dedicated to my Family members and the Almighty. Their Uncountable Blessings and Support has Helped Me to be the Better Person that I am Today.

Department of Chemical Engineering

Indian Institute of Technology Guwahati

Guwahati 781039, India

CERTIFICATE

It is certified that the work contained in the thesis entitled "**Photo-luminescence Guided Metal Ion Sensing and Environmental Remediation Applications of Green Synthesized Iron and Iron-based Nanomaterials**", by **Mr. Piyal Mondal** has been carried out under my supervision. The work documented in this thesis has not been submitted to any other University or Institute for the award of any degree or diploma.

Dr. Mihir Kumar Purkait

Professor

Department of Chemical Engineering

Indian Institute of Technology Guwahati

Guwahati 781039, India

Date 12/02/2021

Acknowledgements

I owe a debt of gratitude to many people who have helped me in completing this research work directly or indirectly throughout my stay in IITG. To begin with, I wish to express my sincere acknowledgement and respect to my supervisor, **Prof. Mihir Kumar Purkait** for being a source of my inspiration and guidance all throughout my research work. I am thankful to him for his useful suggestions and constant encouragement throughout my entire work period and feel fortunate enough to have worked under him all these years. The calm demeanour, dedication towards work and ease of handling the toughest of situations are the traits that I hope to inculcate from my supervisor. He has been a moral support throughout my bad times and has always provided me with the freedom to carry out my work without any pressure in the most amicable manner. For this I shall forever be indebted to him.

I would like to thank my doctoral committee members, **Prof. Subrata K. Majumder**, **Prof. Pallab Ghosh** (Department of Chemical Engineering), and **Prof. Siddhartha S. Ghosh** (Department of Biotecgnology) for their valuable suggestions and constructive criticism during the project evaluations, which helped me to make necessary improvements in various stages of my research work. I would specially like to thank **Prof. Subrata K. Majumder, Prof. Siddhartha S. Ghosh** and **Prof. Pallab Ghosh** for the rigorous and remarkable questions that they raised during the seminar presentations which had helped me a lot in understanding many facts related to my work as well as in improving my presentation and writing skills. I am also thankful to all the faculty members of the Chemical Engineering Department for their encouragement and help at various stages during my stay in this Department.

I would also like to extend my sincere gratitude to the technical officers of my Department specially, **Mr**. **Harsaraj Biswanath,** senior technical superintendents **Dr. Lukumoni Borah** and **Mr. Dipak K. Barman,** technical superintendent **Mr. Jayanta K.**

Mout, junior technical superintendents **Mr. Balen C. Mahanta, Mr. Debajit Borah** and **Mr. Pankaj S. Baruah** and the office staff, **Mr. Sailen Das, Mr. Deep J. Sinha** and **Mr. Bhagya Boro**. The experimental works presented in this thesis as well as all the official paper work would never have been possible without the help of these proficient technicians. I am also very thankful to **Mr. Bijoy Kumar Choudhury** (Senior Technician, Department of Mechanical Engineering), who helped me in installing my experimental setup. I would also like to express my gratitude to the **Central Instruments Facility, IITG** for analysing all my samples with the utmost precision and timely disposition.

I extend my sincere thanks to the lab seniors **Dr. Nilay Sharma**, **Dr V. Shyam K. Yadav**, **Dr. Randeep Singh**, **Dr. Murchana Changmai**, **Mr. Abhik Bhattacharjee**, and **Mr. Somnath Chanda,** for helping me out innumerable times with my work. My labmates **Pranjal, Ankush, Deepti, Naveen, Anweshan, Niladri, Simons** and **Dr. Dibyajyoti Haldar** were constant supports in all my work and helped me in having a pleasant work environment in the lab with their untimely help, support and valuable cooperation. My labmate **Mr. Anweshan** has been of immense help and I could not thank him enough for his contributions towards my work. I would like to take the opportunity to thank my friends **Ms. Sushma Chakraborty**, **Mr. Sunil Prakash, Mr. Pyarimohan Dehury, Mr. Siddharth Thakur, Mrs. Sutapa Das**, **Mr. Jinesh Machale**, **Ms. Kajal Ingtipi**, **Ms. Surabhi Patel** the research scholars of Chemical Engineering Department for their immense support, help, and well wishes throughout my Ph.D. tenure. I would also like to extend my heartfelt thanks to all of my juniors **Mukesh**, **Lhingcy**, **Prangan**, Ph.D. batch mates and the other research scholars at Chemical engineering department, my IITG friends and my childhood friends who have shared their thoughts and views with me.

I have no words to thank **Lord Ganesha**, and **Lord Shiva** who are my strength and wisdom.

Acknowledgements

Last but not the least; I would like to thank my father **Mr. Dhrubajyoti Mondal**, my mother, **Mrs. Bharati Mondal** my elder sister **Mrs. Meghashree Paikara**, my brother-in-law **Mr. Samaresh Paikara**, my smart and lovely niece **Samadrita Paikara**, and my younger brothers **Souvik Mondal** and **Argha Chakraborty.** I would take this opportunity to thank my wife **Mrs. Nilanjana Chakraborty** for her limitless love and support which made me a better person today, and for being always by my side during hard times. The Ph.D. journey wouldn't have been complete without her, I will be always grateful to her. I could not thank God enough for bestowing me with such a supportive family. Their love, affection, blessings and sacrifices made me stronger to overcome my huddles and achieve my target.

Piyal Mondal

Abstract

A rapid growth in the field of industries and academia has resulted in the immense development and amplification of nanomaterials and nanocomposites for environmental remediation application purposes. Over the past few decades, green synthesis has played a major role in nurturing nanoparticle synthesis. The advantages of such nanoparticles are due to their eco-friendly nature, low cost, and higher stability. Green synthesized nanoparticles have been utilized extensively for various environmental-related applications like wastewater treatment, and antimicrobial activities. The need for such nanomaterials in today's world is very crucial since environmental pollution has grasped the world. Greener, safer and effective methods are tomorrow's need for attaining a sustainable environment.

Recent researches have pointed out various sources of green material utilizing which metallic nanoparticles can be synthesized and could be applied towards environmental remediation applications due to their better stability, higher surface area, and antioxidant properties. The present study utilizes a green source to be an effective tool to generate Iron (Fe) nanoparticles with a multipurpose role. Green synthesized Fe NPs towards dye degradation, pollutant removal from wastewater are common applications, but utilizing the photoluminescent activity of green synthesized nanoparticles towards heavy metal sensing ability is a new approach. Moreover synthesizing bimetallic nanocomposites through green synthesis and apart from its fluoride removal efficiency, the heavy metal sensing ability was also investigated in this study and is believed to be a new horizon for future research.

This work addresses the state of the art, research motivation towards the green synthesis approach. It provides a complete description of the methods and experiments involved in green extract preparation, analyzing its total phenolic, flavonoid, tannin content, and

investigating its antioxidant properties. The study involves a vivid analysis of selecting suitable green sources among different spices (clove, cardamom, bay-leaf; common name) based on its total phenolic content (TPC), flavonoid content (TFC), tannin content (TTC), and antioxidant property. The selected green source (clove) mediated iron nanoparticles were then utilized for degradation of crystal violet dye, and its efficiency was compared with the other green source mediated iron nanoparticles. Moreover, the work analyzes better solvents for extraction of polyphenols, flavonoids, tannins, and their antioxidant property from clove as a green source. Moreover, optimization of maximum phenolic and flavonoid content of the clove extract was carried out by controlling parameters such as time of extraction, extraction temperature, and volume of extraction solvent. The study presents the morphological and chemical property dependency of synthesized Fe NPs with pH. This work also investigates the photoluminescence behavior of synthesized Fe NPs towards the heavy metal ion sensing ability. The Fe NPs were found to act as a better Fe^{3+} ion detector within a linear range of micromolar concentration, in presence of other heavy metal ions. Its efficiency was studied in presence of real-life water samples collected from the Indian Institute of Technology, Guwahati campus, India. Further, it describes the preparation of the clove extract mediated ZVI NPs embedded pH-responsive polymeric membrane for reducing nitrobenzene to aniline present in wastewater. The nitrobenzene reduction process was maximized by optimizing the controlling parameters such as time, medium pH, iron NPs content. Furthermore, the membrane was also utilized for studying the fluoride rejection behavior. The work focuses on the effectivity of clove extract in preparing iron-aluminum bimetallic nanocomposite and its application towards removing fluoride and enhancing the overall quality of real-life water collected from Northeast regions of India. Finally, it describes the dual activity of such green synthesized iron-aluminum nanocomposite by investigating its heavy metal sensing ability in the real-life

water sample. In presence of various heavy metals, the nanocomposite was found to be effective in detecting Fe^{3+} ion and showed a linear range of applicability for real-life water collected from college campus IIT Guwahati, India. In conclusion, the work contains the inferences drawn from various chapters presented in this thesis and some suggestions towards scope for future work.

Research Publications (from thesis)

Patent Filed

Inventor: **Piyal Mondal**, Mihir Kumar Purkait. Title: AROMATIC CARBON COATED IRON ALUMINIUM NANOCOMPOSITE AND ITS GREEN SYNTHETIC PROCESS. Indian Patent Application No: 202031047652 Submitted on: 1st November, 2020.

Books Published

1. Mihir Kumar Purkait, Manish Kumar Sinha, **Piyal Mondal**, Randeep Singh (Released date: 1st September 2018): **Stimuli-Responsive Polymeric Membranes,** Volume 25, 1st Edition ISBN: 9780128139615. Imprint: Academic Press (Elsevier).
2. Mihir Kumar Purkait, **Piyal Mondal**, Chang Tang Chang (Released Date: 6th September 2019): **Treatment of Industrial Effluents** authored by 1st Edition ISBN: 9780429401763. Imprint: CRC Press (Taylor & Francis).
3. Randeep Singh, **Piyal Mondal**, Mihir Kumar Purkait (Submission Date 31st March 2021): **pH responsive membranes: Biomedical applications** authored by. Imprint: CRC Press (Taylor & Francis).
4. **Green Synthesized Iron-based Nanomaterial: Application and Potential Risk** authored by **Piyal Mondal** and Mihir Kumar Purkait. Publisher: CRC Press (Taylor & Francis) (To be submitted on 26th November, 2021)

Book Chapters

1. **Piyal Mondal,** Mihir Kumar Purkait. Bio-based polymeric nanocomposites for stimuli responsive membranes. **Handbook of Polymer and Ceramic Nanotechnology**. Publisher: **Springer**, ISBN: 9783030405120. doi: 10.1007/978-3-030-10614-0_79-1.
2. **Piyal Mondal,** Mihir Kumar Purkait. Polymer-Based Bioinspired, Biomimetic and Stimuli-Responsive Reverse Osmosis Membranes. **Advancement in Polymer-Based Membranes for Water Remediation**. Publisher: **Elsevier** (Submitted).
3. **Piyal Mondal**, Anweshan, Mihir Kumar Purkait* Bio-based Iron-Nanoparticles (NPs) Incorporated Polymeric Nano-filtration Membranes (PNCMs) for Wastewater Treatment. **Bio-Nano Filtration in Industrial Effluent Treatment: Advanced and Innovative Approaches. Publisher:** CRC Press (Submitted).
4. Pranjal P. Das, **Piyal Mondal**, Mihir K. Purkait. Recent Advances in Synthesis of Iron Nanoparticles via Green Route and its Application in Biofuel Production**. Green Route Synthesis of Nanomaterial for Bioenergy Applications**. Publisher: **Springer Nature** (To be Submitted)

Journal articles

1. **Piyal Mondal,** A. Anweshan, Mihir Kumar Purkait (2020). Green synthesis and environmental application of Iron-based nanomaterials and nanocomposite: A review Chemosphere (259) 127509. Published 28/06/2020.
2. **Piyal Mondal** & Mihir Kumar Purkait (2019): Preparation and characterization of novel green synthesized iron–aluminum nanocomposite and studying its efficiency in fluoride removal. Chemosphere (235) 391-402. Published 25/06/2019.
3. **Piyal Mondal** & Mihir Kumar Purkait (2018): Green synthesized Iron nanoparticles supported on pH-responsive polymeric membrane for Nitrobenzene reduction and

fluoride rejection study: Optimization approach. Journal of Cleaner Production (170) 1111-1123. Published 25/09/2018.

4. **Piyal Mondal** & Mihir Kumar Purkait (2017): Effect of Polyethylene glycol methyl ether blend Humic acid on poly (vinylidene fluoride-co-hexafluropropylene) PVDF-HFP membranes: pH responsiveness and antifouling behavior with optimization approach. Polymer Testing (61) 162-176. Published 15/05/2017.
5. **Piyal Mondal** & Mihir Kumar Purkait (2017): Green synthesized Iron nanoparticle embedded pH-responsive PVDF-co-HFP membranes: Optimization study for NPs preparation and Nitrobenzene reduction, Separation Science and Technology, 52 (14), 2338-2355. Published 17/02/2017.
6. **Piyal Mondal,** Mihir Kumar Purkait. Preparation and characterization of green synthesized zero-valent Fe NPs from *Syzygium aromaticum* (clove), *Elettaria cardamomum* (cardamom), *Laurus nobilis* (bay leaf) and investigating its dye degradation efficiency (submitted to Chemosphere Journal)
7. **Piyal Mondal,** Mihir Kumar Purkait. Facile one-step green synthesis of Novel Photo-luminescent Fe-Al Nanocomposite and studying its Fe^{3+} ion sensing ability *(submitted to Journal of Cleaner Production)*
8. **Piyal Mondal,** Mihir Kumar Purkait. Synthesis of Iron dots through green route and studying its efficiency towards Fe^{3+} ion sensing property in real life water sample *(submitted to Sensors and Actuators B: Chemical)*

Awards and Recognitions

1. **Best Poster Award (2018):** Research paper entitled "Green synthesized iron NPs acting as an efficient catalyst, fluoride removal agent, metal sensor and pH-responsive agent" at Advanced Materials, Energy and Environmental Sustainability (ICAMEES 2018)

organized by Department of Chemistry and Physics UPES Dehradun, India (14^{th}-15^{th} December 2018)

2. **Best Poster Award (2017):** Research paper entitled "Green Synthesis of Iron Nanoparticles: Nitrobenzene Reduction and pH-Responsive color change" at International Conference on Chemical Engineering and advanced polymeric material, organized by BIT Mesra, Ranchi, India (18-20^{th} August 2016).

Conferences/Seminars and workshops

1. **Piyal Mondal** and Mihir Kumar Purkait**, "**Green synthesized iron NPs acting as efficient catalyst, fluoride removal agent, metal sensor and pH responsive agent" at Advanced Materials, Energy and Environmental Sustainability (ICAMEES 2018) organised by Department of Chemistry and Physics UPES Dehradun, India during 14^{th}-15^{th} December 2018.
2. **Piyal Mondal** and Mihir Kumar Purkait, "Green Synthesis of Iron Nanoparticles: Nitrobenzene Reduction and pH Responsive color change" at TEQIP II sponsored International conference on Chemical Engineering and Advanced Polymeric Material (ICEAPM 2016), Organised by BIT Mesra, Ranchi, India during 18-20^{th} August 2016.
3. **Piyal Mondal** and Mihir Kumar Purkait, "Green synthesized Iron nanoparticle embedded pH-responsive PVDF-co-HFP membranes: Optimization study for NPs preparation and Nitrobenzene reduction" at 7^{th} DAE-BRNS Biennial Symposium, SESTEC 2016, organised by IIT Guwahati during 17-20 May 2016.
4. **Piyal Mondal** and Mihir Kumar Purkait, "Green Synthesis of Iron Nanoparticles from different plant extract" at Workshop on Indian Innovations in Materials Research: New Materials and Processes (IIMR-2015), Organised CSIR-CGCRI & IAPQR Kolkata, India during 25-27 June 2015.

5. **Piyal Mondal** and Mihir Kumar Purkait, "Preparation and Characterization of pH responsive PVDF-co-HFP membranes for protein separation" at Reflux 2015- Annual Symposium organized by Department of Chemical Engineering, IIT Guwahati, 27-29th March 2015.
6. Participated in National Workshop on **Advances in Separation Techniques** conducted under **TEQIP** sponsored by MHRD organised by Center for Educational Technology, IIT Guwahati, 15th March 2019.
7. Participated in Poster Presentation at **Research Coclave 2017** organized by SAB, IIT Guwahati during 16-19th March.

Research Publications (from other works)

Books

1. Mihir Kumar Purkait, Randeep Singh, **Piyal Mondal** and Dibyajyoti Haldar (Released Date: 7th April 2020): Thermal Induced Membrane Separation Processes authored by 1st Edition ISBN: 9780128188019. Imprint: Elsevier.
2. Mihir Kumar Purkait, **Piyal Mondal**, Murchana Changmai, Vikranth Volli, Chi Min Shu (Release date 23rd March, 2021) Hazards and Safety in Process Industries: Case Studies authored by. ISBN: 9780367516512. Imprint: CRC Press.

Book Chapters

1. Pranjal P. Das, **Piyal Mondal**, Prangan Duarah, Mihir Kumar Purkait (2021): **Advanced surfactant based technologies for environmental remediation applications.** Series Ed.: Ikhmayies, Shadia Jamil. (Volume 19: Advances in Surfactant Technologies) Advances in Material Research and Technology. Publisher: Springer Nature. ISSN: 2662-4761 (Under review)
2. Deepti, **Piyal Mondal**, Mihir Kumar Purkait (2021): **Utilization of advanced ceramics towards treatment of wastewater**. Series Ed.: Ikhmayies, Shadia Jamil. (Volume 13: Advance Ceramics) Advances in Material Research and Technology. Publisher: Springer Nature. ISSN: 2662-4761 (Under review)
3. Niladri S. Samanta, **Piyal Mondal**, Mihir Kumar Purkait (2021): **Zeolite based Advanced Composites for treating Wastewater and Environmental Remediation Applications.** Series Ed.: Ikhmayies, Shadia Jamil. (Volume 3: Advanced Composites)

Advances in Material Research and Technology. Publisher: Springer Nature. ISSN: 2662-4761 (Under review)

4. Ankush D. Sontakke, **Piyal Mondal**, Mihir Kumar Purkait (2021): **Graphene Oxide based Advanced Nanomaterials for Environmental Remediation Applications.** Series Ed.: Ikhmayies, Shadia Jamil. (Volume 8: Advanced Nanomaterials) Advances in Material Research and Technology. Publisher: Springer Nature. ISSN: 2662-4761 (Under review)
5. Pranjal P. Das; **Piyal Mondal**; Mihir K. Purkait. Treatment of industrial wastewater utilizing conventional and integrated advanced oxidation processes. **Advanced Oxidation Processes for Wastewater Treatment: An Innovative Approach.** Publisher: **CRC Press** (Under Review)
6. Deepti, **Piyal Mondal**, Mihir Kumar Purkait. Emerging technologies and its advancements towards wastewater treatment from various industries. **Emerging Technologies in Wastewater Treatment.** Publisher: **CRC Press** (Under Review)
7. Prangan Duarah, Piyal Mondal, Pranjal P. Das, Mihir Kumar Purkait. Potential of NF membrane for the removal of aquatic pollutants from the industrial wastewater: Review. **Membrane and Membrane-Based Processes for Wastewater Treatment.** Publisher: **CRC Press** (Under Review).
8. Ankush D. Sontakke, **Piyal Mondal**, Mihir K. Purkait. Utilization of Green Synthesized Metallic Nanoparticles for Biofuel Production. **Green Route Synthesis of Nanomaterial for Bioenergy Applications**. Publisher: **Springer Nature** (To be Submitted)
9. Prangan Duarah, Abhik Bhattacharya, **Piyal Mondal**, Mihir K. Purkait. Green synthesized carbon and metallic nanomaterials for biofuel production: Effect of

operating parameters. **Green Route Synthesis of Nanomaterial for Bioenergy Applications**. Publisher: **Springer Nature** (To be Submitted)

Journal Articles

1. **Piyal Mondal**, N. Samanta, A. Kumar, Mihir Kumar Purkait (2020). Recovery of H_2SO_4 from wastewater in presence of NaCl and KHCO3 through pH Responsive Polysulfone Membrane: Optimization Approach. **Polymer Testing (86) 106463**.
2. **Piyal Mondal,** Niladri Shekhar Samanta, Varnika Meghnani, Mihir Kumar Purkait (2019): Selective glucose permeability in presence of various salts through tunable pore size of pH-responsive PVDF-co-HFP membrane. **Separation and Purification Technology (221) 249-260.**
3. Pranjal P. Das, **Piyal Mondal,** A. Anweshan, A. Sinha, P. Biswas, S. Sarkar, Mihir Kumar Purkait (2020). Treatment of steel plant generated biological oxidation treated (BOT) wastewater by hybrid process. **Separation and Purification Technology (258) 1: 118013**.
4. Pranjal P. Das, A. Anweshan, **Piyal Mondal,** A. Sinha, P. Biswas, S. Sarkar, Mihir Kumar Purkait (2020). Integrated ozonation assisted electrocoagulation process for the removal of cyanide from steel industry wastewater. **Chemosphere (263) 128370.**
5. M. Changmai, P. P. Das, **Piyal Mondal,** M. Paswan, Mihir Kumar Purkait (2020): Hybrid Electrocoagulation-Microfiltration Technique for Treatment of Nanofiltration Rejected Steel Industry Effluent. **International Journal of Environmental Analytical Chemistry** https://doi.org/10.1080/03067319.2020.1715381.
6. M. Changmai**, Piyal Mondal**, Mihir Kumar Purkait (2020). Metal Removal Efficiency of Novel LD Slag Incorporated Ceramic Membran e from Steel Plant Wastewater

International Journal of Environmental Analytical Chemistry (Taylor & Francis), https://doi.org/10.1080/03067319.2020.1734198.

7. Adebola Abosede Adeyi[1], Toluwalope Gbemileke Abayomi[1,2*], Mihir Kumar Purkait[3], **Piyal Mondal[3] (2019):** Adsorptive Removal of Phosphate from Aqueous Solution by Magnetic-Supported Kaolinite: Characteristics, Isotherm and Kinetic Studies. **Open Journal of Applied Sciences (9) 544-563.**
8. Mukesh Sharma[a], **Piyal Mondal[b]**, Arun Chakraborty[c], Mihir Purkait[d] and Jayanarayanan Kuttippurath[e] (2018): Effect of different molecular weight polyethylene glycol (PEG) on flat sheet cellulose (CA) membranes for evaluating power density performance in pressure retarded osmosis study. **Journal of Water Process Engineering (30) 100632 (Elsevier).**
9. M. Sharma, **Piyal Mondal,** A. Chakraborty, M.K. Purkait**.** Hydrophilic Graphene-oxide Impregnated Cellulose Acetate Ion Exchange Membrane for Environmental Remediation Applications**. Journal of Applied Polymer Science (Wiley & Sons)** (Under Review)
10. N. Samanta, S. Banerjee, Piyal Mondal, Anweshan, M.K. Purkait. Preparation and Characterization of Zeolite from Waste Linz-Donawitz (LD) process slag of Steel Industry for Removal of Fe^{3+} from Drinking Water**. Advance Powder Technology (Elsevier)** (Under Review)
11. **Piyal Mondal,** N. Das, Mihir Kumar Purkait. Preparation and Characterization of PSF-co-(PVDF-co-HFP) membrane with better ion selectivity for proton exchange and separation of anionic dye applications *(To be submitted)*

CONTENTS

LIST OF FIGURES

LIST OF FIGURES

LIST OF TABLES

LIST OF TABLES

Nomenclature

Notations

C_e	Equilibrium concentration
J_W	Pure water flux
k_1	Rate constant pseudo first order reaction
k_2	Rate constant pseudo second order reaction
K_F	Freundlich adsorption constant
K_L	Langmuir adsorption constant
q_e	Equilibrium adsorption capacity
q_m	Monolayer adsorption capacity
β	Redlich-Peterson constant
R_L	Dimensionless separation factor
q_t	Time dependent adsorption capacity
h_0	Initial adsorption rate
k_{id}	Intraparticle diffusion rate constant
k_r	Boyd rate constant
K_{sv}	Quenching consant
ΔG^0	Free energy change
ΔH^0	Enthalpy change
ΔS^0	Entropy change
E_a	Activation energy of adsorption

Abbreviations

AAS	Atomic absorption spectroscopy
ANOVA	Analysis of variance
CCD	Central Composite design
DPPH	2, 2-diphenyl-1-picrylhydrazil
DSC	Differential scanning calorimetry
EDX	Energy-dispersive X-ray spectroscopy
FESEM	Field emission scanning electron microscope
FRAP	Ferric reducing antioxidant potential
FRET	Fluorescence resonance energy transfer
FTIR	Fourier transform infrared Spectroscopy
HPLC	High pressure liquid chromatography
NMP	N-methyl pyrrolidone
PCS	Photon correlation spectroscopy
PEGME	Polyethylene glycol methyl ether
PET	Photoinduced electron transfer
PL	Photoluminescence
PVDF-co-HFP	Polyvinylidene fluoride-co-hexafluoropropylene
RSM	Response surface methodology
SPIONS	Super-paramagnetic iron nanoparticles
TFC	Total flavonoid content

TGA	Thermo-gravimetric analysis
TISAB	Total ionic strength adjustment buffer
TPC	Total polyphenolic content
TPTZ	2,4,6-tripyridyl-s-triazine
TTC	Total tannin content
UV-Vis	Ultraviolet-visible spectrophotometry
XRD	X-ray diffraction analysis
ZVI NPs	Zero-valent iron nanoparticles

Chapter 1

Introduction

Piyal Mondal, A. Anweshan, Mihir Kumar Purkait (2020). Green synthesis and environmental application of Iron-based nanomaterials and nanocomposite: A review Chemosphere (259) 127509. Published 28/06/2020

Chapter 1

Introduction

This chapter enlists all the possible greener routes for synthesizing iron nanoparticles (NPs) along with iron-based nanocomposites (NCs), and bimetallic nanocomposites. Synthesis involving biocompatible reagents, microorganisms, various plant parts, and plant waste materials, have been discussed elaborately to provide a vivid idea and literature survey regarding the green synthesis of Iron and iron-based nanomaterials. Moreover, the focus has been made on various iron-related bimetallic nanocomposites, which was found to have better catalytic and adsorptive properties in comparison to only iron NPs. Various environmental applications of such iron NPs and iron-based NCs have been discussed related to dye degradation, heavy metal removal, fluoride removal along with wastewater treatment, and other waterborne pollutant removals. Moreover, the chapter details out all possible green synthesis plant sources and the morphology of prepared iron NPs with specific application and efficiency. It also provides a future scope for further research work which can focus towards better and advance applications of such green synthesized materials.

1.1. Background

Nanotechnology is defined as the transformation of matter using physical, chemical, and biological techniques and processes with or without incorporating other ingredients to produce substances with specialized functionalities, enhanced characteristics and specific attributes, which can be used in diverse field of applications [1]. A nanoparticle (NP) can

be defined as a minuscule particle which has at least one of its size/dimension, not more than 100 nm [2]. The NPs thus produced are distinct from the bulk materials, as they exhibit unique electrochemical, optical, and thermal properties, along with a substantially larger surface area to volume ratio [1]. These unique properties of the NPs are responsible for their popularity and widespread use in the field of agriculture, biotechnology, chemistry, communications, consumer goods, defence, electronics, energy, environmental remediation, heavy industries, material science, medicine, microbiology, optics, and various engineering fields [3].

Metals and their corresponding oxides are extensively converted into NPs using both physical and chemical processes [4]. The chemical synthesis methods, like element lowering and sol serum approach, intensively use toxic and hazardous substances such as sodium borohydride, hypophosphite, and hydrazine hydrate, which harm the environment [5]. So, the development of a competent, cost-efficient and sustainable green process for the synthesis of NPs is an on-going effort. Stable and well-functionalized NPs have been produced from organisms like bacteria, actinomycetes, fungi, yeast, viruses, and other microbes [6]. These microorganisms serve as environment-friendly and sustainable precursors. However, factors like local availability of resources, social adaptability, and economic feasibility heavily influence the overall sustainability of the process [7]. Apart from metal NPs, metal-based NCs have also been extensively utilized for various environmental hazard purposes [7,8].

The nanoparticle synthesis employing green chemistry techniques has several advantages concerning the conventional methods, namely being safe to handle, does not contaminate the environment, and relatively inexpensive. Gonzalez-Moragas et al. (2015) prepared super papramagnetic iron-oxide NPs (SPIONs) of size 5.9 ± 1.4 nm through microwave assisted commercial chemical process using iron (III) acetylacetonate as a precursor with

a production cost of €130 per 10 g of SPION [9]. Whereas for preparing green synthesized iron NPs from plant extract it costed around USD 0.5-10 per gram depending upon species and purity [10]. The advantage of such green synthesized NPs is that it doesn't require synthetic reducing agents which are environmentally hazardous. Moreover, such process doesn't require external capping and stabilizing agents. Commercially available Fe NPs have a diverse price spectrum depending on factors like oxidation state, particle size, functionalization, and a dispersion medium which can range from USD 50-500 per gram (Sigma Aldrich, St. Loius, MO, USA). Various chemical conventional techniques have shown such disadvantages of high cost [11]. Other advantages and salient features of green synthesis processes are: firstly, the dual utility of the active natural component, like the extract, both as reducing and capping agent. This ability enables the production of small size NPs in large scale units [12]. Secondly, the time taken for reducing the metal ions is short, and the product formed after that is immensely stable due to the presence of stabilizing agents in the extract. Last but not least, a plethora of both microscopic and macroscopic organisms are available that could be utilized for the desired nanoparticle functionality [13].

Iron NPs (Fe NPs) exhibit superb dimensional stability, non-toxicity and have an affinity to form oxides. Apart from having a high surface area, electrical and thermal conductivity, Fe NPs also possess magnetic properties and are known as magnetic NPs [14]. Super-paramagnetism is a unique consequence of magnetic NPs. It is observed in ferromagnetic or ferrimagnetic nanomaterials, only when the size and number of domains, are both adequately small, broadly between 10-150 nm in diameter depending on the material [15]. At these extreme sizes, they become a single domain magnetic material that has no hysteresis loop; also, their magnetization can randomly flip direction under the influence of temperature [16]. Iron NPs that exhibit super-paramagnetism are termed as

superparamagnetic iron oxide NPs (SPIONs), and it finds wide application in biomedical field.

Iron is abundant in nature, less expensive and its magnetic behavior has engrossed synthesis of NPs having an enormous scope in environmental separation application. However, it is envisaged that NPs of various metal and metal oxides such as silver, gold, copper, and zinc have been studied thoroughly than that of iron NP. Few review papers concentrated on specific green methods using sources from plant parts [10].

1.2. Green route synthesis of Iron NPs and NCs

An efficient and eco-friendly methodology to synthesize NPs ideally should use renewable energy, minimize waste discharge, and optimize energy consumption, according to the principles of green chemistry [17]. Thus, it may be conceptualized that the green synthesis process must utilize plants, microbes, bio-polymers, and waste materials for the active bio-component along with low heating requirements and benign solvents [10]. Water is considered as the universal solvent, has been reported in many studies as a solvent with biomolecules, mostly polyphenols, extracted from plants as reducing, capping, and stabilizing agents. These bioactive polyphenols have been extracted from leaves, stems, roots, flowers, fruits, fruit peels, seeds, gums, and even wastes of various vegetations [18]. Agglomeration being the main problem in chemical synthesis of NPs, green route techniques has quite significantly limited that aspect. Especially for plant extract and microorganism mediated synthesis, the polyphenolic content and natural proteins acts as stabilizer and coating agent over the prepared NPs, which restrict the agglomeration. Most of the prepared NPs through green route techniques are generally stored in aquoues form at definite pH to provide stability and uniform particle size [9]. Better stabilization can also be obtained by utilizing biocompatible reagents and other chemical surface coatings,

which provide less reactivity when comes in contact with environmental fluids. NPs stored in powder form should be kept in vacuum otherwise agglomeration occurs in presence of moisture from the environment.

1.2.1. Biocompatible reagents utilized for green synthesis

1.2.1.1. Biopolymers and ascorbic acid

The use of innocuous synthetic biocompatible substances for the preparation and stabilization of magnetic nanoparticle polymer composites is well documented in the literature. He et al. (2005) investigated starch stabilized bimetallic Fe/Pd NPs in an aqueous medium. Starch is a hydrophilic polymer with around 20% amylose content, is reported to significantly improve the stability and dispersion of the iron NPs [19]. Moreover, Gao et al. (2008) prepared a magnetic Fe_3O_4 nanoparticle using sodium alginate biopolymer via a redox-based hydrothermal method from ferric chloride hexahydrate and urea as precursors. The resultant NPs were of uniform spherical morphology with a mean diameter of 27.2 nm [20]. Jegan et al. (2011) pioneered the synthesis of a magnetite (Fe_3O_4) agar nanocomposite via co-precipitation of ferric and ferrous ions. The nanomaterial was well dispersed in the solution with size 50-200 nm [21]. In Table 1.1 various iron NPs synthesis utilizing numerous biocompatible green reagents acting as reducing and capping agents are mentioned.

Nadagouda et al. (2007) studied the synthesis of Fe and Cu NP using Vitamin C (ascorbic acid). The salts of the transition metals were readily reduced to their respective nanostructure in aqueous ascorbic acid solution [22]. Similarly, Savasari et al. (2015) synthesized zero-valent iron (ZVI) nanoparticle in ascorbic acid medium. The individual particles also exhibited spherical morphology, having an average particle size of 20-75 nm assembled in a chain formation. Furthermore, ascorbic acid has stabilizing property and

has been reported as a functionalizing agent. Ascorbic acid was utilized by Sreeja et al. (2015) to prepare, coat, and functionalize superparamagnetic iron oxide NPs (SPION) with 5 nm diameter in a stable dispersion for medical application. The size and shape of the SPION were determined using a transmission electron microscope (TEM) [23].

1.2.1.2. Amino Acid, haemoglobin and myoglobin

Krishna et al. (2012) employed the wet chemical co-precipitation method to synthesize amine-functionalized γ-Fe_2O_3 NPs using L-Lysine (lys). The magnetization of γ-Fe_2O_3/lys magnetic NPs was 40.6 emu g^{-1}, with an average particle size of 14.5 nm [24]. Likewise, a study by Siskova et al. (2013) reported the production of ZVI using various amino acids, namely L-glutamic acid, L-glutamine, L arginine, and L-cysteine along with the effect of pH on ZVI yields [25].

Haemoglobin and myoglobin are naturally occurring biomolecules that contain iron. An investigation by Sayyad et al. (2012) reported the synthesis of Fe NPs stabilized at room temperature in a single-phase reduction reaction. The NPs, thus produced, were crystalline with a narrow size band of 2-5 nm. This protocol is vital for the production of bio-compatible NP required for medical applications [26].

1.2.1.3. Sugar and Glucose

Utilizing D-glucose as a reducing agent, polycrystalline Fe_3O_4 NPs were prepared by Lu et al. (2010) with gluconic acid as a stabilizer and dispersing agent. The prepared NPs were spherical in nature with an average diameter of 12.5 nm [27]. Furthermore, glucose and gluconic acid were utilized as capping agents by Sun et al. (2009) for fabricating magnetite NPs by the hydrothermal reduction process [28].

Table 1.1: Iron based nanoparticle synthesis utilizing biocompatible green reagents

Green reagents	Nanoparticle	NPs Size	Morphology	Reference
α-D-glucose	Fe_3O_4 NPs	~12.5 nm	Spherical	[27]
Starch	Fe/Pd bimetallic nanoparticle	14.1 nm	Discrete (well dispersed)	[19]
Maltose	Fe_3O_4 NPs	12.1 ± 2.1 nm	Spherical	[30]
Sucrose	Fe_3O_4 NPs	4-16 nm	Spherical	[28]
α-D-maltose	Fe_3O_4 NPs	9.7 ± 1.0 nm	Mostly spherical	[30]
α-D-mannose	Fe_3O_4 NPs	13.1 ± 0.3 nm	Rod like	[30]
α-D-galactose	Fe_3O_4 NPs	12.4 ± 0.3 nm	Spherical	[30]
α-D-lactose	Fe_3O_4 NPs	3.8 ± 0.21 nm	Dendritic nanostructure	[30]
D-glucose	Fe_3O_4 NPs	10-20 nm	Coral like	[25]
Agar	Fe_3O_4-polymer composite	50-200 nm	Spherical	[21]
Sodium alginate	Fe_3O_4 NPs	27.2 nm	Spherical, and hexagonal	[20]
Ascorbic acid (Vitamin C)	Fe metal nanoshell	<100 nm	Cubical	[22]
Ascorbic acid	nZVI	20-75 nm	Spherical chain	[23]

Ascorbic acid	Fe_3O_4 NPs	15 ± 4 nm	Irregular	[26]
Urease	Fe_3O_4 NPs	19±5 nm	Nanosphere at 60 ºC	[32]
		Thickness <2-3nm	Nanosheet at 40 ºC	
		L>100nm, C.S~10±4 nm	Nanorods at 40 ºC	
Yeast	Fe_3O_4 NPs	16 nm	Wormhole like	[33]
Chitosan	Fe_3O_4 NPs	22 ± 7.8 nm	Roughly spherical	[34]
Agar	Fe_3O_4 NPs	20-30 nm	Non spherical	[36]
Ascorbic acid	Superparamagnetic iron oxide	5 nm	Spherical	[35]
L-lysine amino acid	Fe_3O_4 NPs	17.5 nm	Spherical	[24]
Haemoglobin and myoglobin	Fe NPs	2-5 nm	Aggregates	[26]
D-glucose gluconic acid	Fe_3O_4 NPs	12.5 nm	Roughly spherical	[27]

Moreover, Yan et al. (2015) utilized wood derived sugars and synthesized carbon encapsulated iron NPs through the hydrothermal carbonization process. Nano-spheres having a diameter of 100-150 nm were formed with an iron core of size 10-25 nm capable of catalytically converting syngas into liquid hydrocarbons [29].

Demir et al. (2014) studied the effect of lactose, mannose, galactose, maltose, and fructose (different saccharides) on the synthesis of magnetite NPs. All saccharides, except fructose, exhibited dual-purpose applicability both as a reducing agent as well as a capping agent. Since due to it's non-reducing nature fructose acts as only a capping agent. The particle size distribution of synthesized Fe_3O_4 NPs was in the range of 3.8-13.1 nm, and the morphology of the NPs was a combination of a slightly agglomerated sphere, rod, and dendritic nanostructure. Superparamagnetic characteristics were exhibited by Fe_3O_4 NPs prepared with galactose, mannose, and maltose. Consequently, the saccharides capped magnetite (Fe_3O_4) NPs can be used in biomedical imaging applications [30].

1.2.1.4. Synthetic tannic and gallic acid

Both Tannic and Gallic acids are polyphenols and are considered as weak acids. They can be obtained from both natural and synthetic sources. Herrera-Becerra et al. (2010) obtained a well-dispersed spherical iron oxide (Fe_2O_3) NPs of less than 10 nm diameter with high crystallinity, using the synthetic tannic acid solution at pH 10 combined with ultra-sonication [31]. Similarly, Dorniani et al. (2012) prepared magnetic Fe NPs via the sonochemical process and applied a coat of Chitosan and Gallic acid on the NPs to form a core-shell arrangement. XRD analysis confirmed that pure Fe_3O_4 NPs were synthesized having a cubic inverse spinel structure. The average particle size obtained was 11 nm with a spherical structure. The synthesized magnetic NPs were found to be smaller than iron oxide-chitosan-gallic acid (FCG) nanostructure, having an average diameter of 13nm. The

prepared NPs showed a magnetic saturation of 26.07 emu g^{-1}. The FCG NPs were demonstrated to be capable of targeted drug delivery [32].

1.2.1.5. Polysaccharides and cellulose

Polysaccharides are polymeric carbohydrates with glycosidic linkages. Chang et al. (2011) synthesized superparamagnetic Fe_3O_4 NPs using different polysaccharides, like soluble starch, carboxymethyl cellulose sodium (CMC), and agar. The polysaccharides enhanced the biocompatibility and biodegradability of Fe_3O_4 NPs apart from acting as a capping and stabilizing agent. Starch stabilized NPs were found to be 10 nm smaller than CMC and agar. The saturation magnetization of agar-based NPs was found to be 20.43 emu g^{-1}, whereas that of starch and CMC based NPS were found to be 36.16 emu g^{-1}, and 35.75 emu g^{-1} respectively. Extremely small hysteresis loop and coercivity characteristics were exhibited by the polysaccharide-Fe_3O_4 NPs [33].

Cellulose is the most abundant naturally occurring polymer in the world as it is an essential structural component of the primary cell wall of all plants, various types of algae, and the oomycetes [34]. Materials with high cellulosic content can be used to prepare and stabilize Fe NPs. López-Téllez et al. (2013) extracted cellulosic components from ethanol cured powdered Orange peel to prepare iron oxide nano-rods. The study demonstrated the interaction between reduced metal ions and functional groups of cellulosic components through electrostatic and weak van der Waals forces. Such interactions helped to stabilize the NPs after formation. The resultant nano-rods acted like an adsorbent with an adsorption capacity of 7.44 mg g^{-1} for the removal of hexavalent chromium [35].

1.2.2. Synthesis by Microorganisms

The synthesis of NPs based on microorganisms has gained substantial popularity due to its benefits over traditional chemical protocols. The advantages are enlisted as synthesis at

ambient conditions, highly energy-efficient, production of limited toxic by-products, naturally abundant and renewable precursors, robust and scaling-up is easy [36]. Through extracellular or intracellular processes, microorganisms like fungi, bacteria, and yeast can synthesize NPs. These mechanisms involve the reduction of metal ions by enzymes along with producing well-dispersed NPs with lower average particle size distribution. The nanoparticle surface gets incorporated with natural proteins, tannins, and peptides as capping agents. Such surface coating provides better stability and dispersion of NPs by reducing agglomeration [37]. The intracellular mechanism involves diffusion of metal ions into the cell, and the enzymes resent reduce the ions to form NPs. Whereas, the extracellular mechanism involves the electrostatic attraction of metal ions to the cell wall and carrying out the enzymatic reduction of metal ions. Table 1.2 represents various microorganisms utilized by various research groups for synthesizing iron and iron-based nanomaterials as reducing and capping agents.

1.2.2.1. Bacteria

In a study by Bharde et al. (2008) reported the use of *Actinobacteria* sp. under aerobic conditions to prepare spherical iron oxide NPs [38]. In another study, the same bacterium species was used to synthesize maghemite (γ-Fe_2O_3) and greigite (Fe_3S_4) by changing the metal ion precursor (Bharde et al., 2005). Furthermore, it was established that *Actinobacter* sp. employed extracellular mechanism, involving iron reductase enzyme, to synthesize the magnetic NPs [39].

Moon et al. (2010) in a similar study synthesized mono-dispersed, sphere-shaped 13.1 nm magnetite Fe_3O_4 NPs under anaerobic conditions from FeOOH using *Thermoanaerobacter* sp., an extremophile. The results suggest that, around $500/kg is the estimated cost for commercial production of nano-magnetite (25–50 nm) [40]. In comparison to chemical

synthesis, a fraction of cost is required to produce 5-90 nm pure or substituted magnetites through the microbial process. Sundaram et al. (2012) used *Bacillus subtilis* strains isolated from rhizosphere soil to prepare Fe_3O_4 NPs with spherical morphology and 60-80 nm diameter [41]. Elcey et al. (2014) isolated *Thiobacillus thioparus* from iron ore mining zones to produce iron oxide NPs termed as magnetosomes, having magnetic properties [42].

Likewise, Mukherjee (2017) isolated and incubated *Microbacterium marinilacus* from sediments of Damodar River in India to synthesize magnetosomes having a size distribution from 32 to 48nm. Further the synthesized NPs were tested against gram-positive *Bacillus cereus*, and gram-negative *Escherichia coli* for antimicrobial studies, through agar-plate-well-diffusion [43]. In another study, Das et al. (2018) reported the synthesis of maghemite NPs, with an average diameter of 18 nm, in an anaerobic process, using native hypersaline sulfate-reducing bacterial strain LS4, isolated and cultured from sediment of saltpan, Goa, India [44].

1.2.2.2. Fungi

Fungi like *Fusarium oxysporum* and *Verticillium* sp., are exploited to prepare magnetic NPs of different sizes at ambient temperature via extracellular hydrolysis of the anionic iron complexes. Bharde et al. (2006) reported the synthesis of magnetite NPs using fungi that showed the ferrimagnetic transition signature with negligible spontaneous magnetization at low temperatures [45]. Kaul et al. (2012) explored five different species of fungi, namely *P. chlamydosporium, A. fumigates, A. wentii, C. lunata,* and *C. globosum*, to prepare iron NPs [46].

Table 1.2: Microorganism mediated synthesis of Iron based nanoparticles

Microorganisms	Species name	Nanoparticle	Average size	Morphology	Reference
Bacteria	*Actinobacter sp.*	Fe_3O_4	10-40 nm	Cubical	[36]
	Actinobacter sp.	γ-Fe_2O_3	<50 nm	Spherical	[38]
	Thermoanaerobacter sp.	Fe_3O_4	~13 nm	Spherical	[37]
	Bacillus subtilis	Fe_3O_4	60-80 nm	Spherical	[40]
	Thiobacillus thioparus	Fe_3O_4	-	-	[41]
	Microbac- terium marinilacus	Magnetic Iron oxide nanoparticles	2-10 nm	Spherical	[39]
	Desul- fovibrio, strain LS4	Maghemite (Fe_2O_3) nanoparticles	19 nm	Round shaped	[42]
Fungi	*Fusarium oxysporum and Verticillium sp.*	Fe_3O_4	20-50 nm	Spherical	[45]
	P. chlamydosporium, A. fumigates, A. wentii, C. lunata and C. globosum	Maghemite (Fe_2O_3) nanoparticles	~12-50 nm	Spherical	[48]

	Aspergillus sp.	Fe_3O_4	50-200 nm	Spherical	[46]
	Alternaria alternate	Fe Nanoparticles	~9nm	Cubical	[47]
	Pleurotus sp.	Fe Nanoparticles			[49]
	Aspergillus niger YESM 1	Magnetic Fe and Fe_3O_4 (magnetite) nanoparticles	18 and 50 nm for Fe and Fe_3O_4 NPs respectively	Spherical	[50]
	Alternaria alternate	γ-Fe_2O_3 (iron oxide) nanoparticles	75-650 nm	Quasi-spherical as well as rectangular NPs	[48]
Algae	*Sargassum muticum*	Magnetic Fe_3O_4 nanoparticles	18 ± 4 nm	Cubical	[51]
	Chlorococcum sp.	Iron nanoparticles	20-50 nm	Spherical	[52]

A study by Mohamed et al. (2015) reported the formation of cubic Fe NPs of size 9 ± 3 nm, having antibacterial activity against *B. subtilis*, *E. coli*, *S. aureus,* and *P. aeruginosa*, employing *Alternaria* alternata fungus in lightless conditions [47]. Sarkar et al. (2017) used *Alternaria alternate*, a phytopathogenic fungus for the synthesis of iron oxide NPs via an extracellular mechanism to study its mechanical properties [48]. Abdeen et al. (2016) explored the green processes to synthesize magnetic Fe NPs and magnetite NPs using *Asperigillus niger* via the intracellular mechanism [48]. Mazumdar et al. (2011) employed a filamentous fungus *Pleurotus* sp. to prepare iron NPs and ferrous sulfate as a precursor [49]. Characterization study of the NPs was carried out using TEM, SEM, and FTIR spectroscopy. Another method for synthesizing spherical Fe NPs with particle size 10–24.6 nm, using *Aspergillus oryzae* TFR9 (fungus), was proposed by Tarafdar et al. (2013) which found large application in the field of engineering, agriculture, and biomedical [50].

1.2.2.3. Algae

Algae refer to a diverse group of photosynthetic eukaryotic organisms that are polyphyletic. They consist of both unicellular and multicellular organisms. Mahdavi et al. (2013) used the extract from the macroalgae, brown seaweed (*Sargassum muticum*) to synthesize iron oxide (Fe_3O_4) NPs with superparamagnetic characteristics and having an average particle size of 18 ± 4 nm. X-ray diffraction (XRD) revealed that the NPs were crystalline and had a cubic morphology. The antimicrobial activity of the green synthesized Fe_3O_4 NPs was comparably higher than the NPs synthesized by conventional chemical methods [51]. In a different study carried out by Subramaniyam et al. (2015) reported the formation of spherical-shaped Fe NPs ranging in size from 20–50 nm using soil microalgae, *Chlorococcum* sp., with an iron chloride precursor. The study suggested

that the amine and carbonyl functional groups on polysaccharides and glycoproteins present in the algal cell were involved in the nanoparticle formation and verified by FTIR analysis [52].

1.2.3. Plant mediated synthesis

The NPs prepared from microorganisms have low dispersion, and the rate of formation is slow as well when compared to plant-mediated synthesis. A study by Kalaiarasi et al. (2010) reported that plant-based synthesis of metallic nanoparticles is facile, most cost-efficient with high repeatability and reproducibility [53]. It has been well established that plant extracts are most suitable for producing highly stable metal NPs at rapid rates and large quantities. Plant-based nanomaterial synthesis is preferred as a plethora of different naturally occurring, and robust biomolecular reducing agents can be extracted from various plants. Various herbs and plants have a high concentration of antioxidants as active phytochemical constituents in fruits, leaves, seeds, and stems. The production of nanomaterials from processes utilizing botanical phytochemicals significantly reduces environmental pollution, thereby setting benchmarks in economically feasible and ultra-sustainable clean and green technologies. Table 1.3 represents various plant parts utilized as a source for reducing agent and capping agents in synthesizing iron and iron-based nanomaterials by several researchers.

Table 1.3: Green synthesized iron based nanoparticles from plant sources

Part of plant	Name of source	Average size	Morphology	Reference
Plant	Soya bean sprouts	~8 nm	Spherical	[53]
	Aloe vera	93-227 nm	Spherical	[55]
	Aloe vera	~6-30 nm	Agglomerated irregular	[54]
Marine plant	*Sargassum muticum*	18 ± 4 nm	Cubic	[58]
	Kappaphycus alvarezii	14.7 ± 1.8 nm	Spherical	[56]
	Padina pavonica	10-19.5 nm	Spherical	[59]
	Sargassum acinarium	21.6-27.4 nm	Spherical	[57]
Seed	Grape seed proanthocyanidin	~30 nm	Irregular shape	[62]
	Syzygium cumini	9-20 nm	Agglomerated spherical	[60]
	Carom and clove	0.088-3.95	Spherical, irregular	[61]
Leaf	Carob	4-8 nm	Well monodisperse	[59]
	Tridax procumbens	< 100 nm	Irregular shape	[56]
	Artemisia annua	3-10 nm	Spherical	[62]

	Caricaya Papaya	33 nm	Agglomerated plate and capsule like structures	[65]
	Perilla frutescens	~50 nm	Spherical	[63]
	Green tea	5.7 ± 4.1 nm	Spherical	[64]
Fruit peel	Plantain peel	30-50 nm	Spherical	[60]
	Punica Granatum	D: 40 nm, L: >200 nm	Rod shaped	[65]
	Rambutan	100-200 nm	Agglomerated spinel	[67]
	Ananas comosus	10-16 nm	Aggregated spherical	[69]
	Citrullus lanatus	< 17 nm	Aggregated spherical	[66]
Fruit	*Passiflora tripartita*	18.2-24.7 nm	Spherical	[68]
	Averrhoa carambola	1.9-3.1 nm	Spherical	[70]
	Lemon	14-17 nm	Spherical	[72]
	Couroupita guianensis	17 ± 10 nm	Spherical	[73]
	Pepper	50 nm	Dendrite like	[71]
	Terminalia chebula	<80 nm	Amorphous	[74]
	Zanthoxylum rhetsa	12.2 ± 0.8 nm	Cluster like	[70]

Root & Shoot	*Mimosa pudica* (root)	60-80 nm	Agglomerated rough spherical	[65]
	Vaccinium corymbosum (shoot)	52.4 nm	Irregular shape, non agglomerated	[66]
Waste	Tea waste	5-25 nm	Cuboid/pyramid	[73]
	Rice straw	9.9 ± 2.4 nm	Aggregated spherical	[75]
	Coffee waste hydrochar	10-40 nm	Spherical	[74]
	Acacia mearnsii (biochar)	18-35 nm	Uneven	[71]

1.2.3.1. Synthesis by leaf, fruit, and seed extract

Huang et al. (2015) investigated the factors that determine the efficiency of Fe NPs prepared using green tea leaf extracts for the removal of Malachite Green dye. The study explored the variation in the volume of tea extract, temperatures, and pH of the solution to understand the optimum conditions and reported that increasing the volume of extract and pH of the solution negatively impacted dye removal. However, increasing temperature improved nanoparticle reactivity. A maximum dye degradation of 90.56% was obtained by the prepared Fe NPs [54]. -Wang et al. (2014) prepared spheroid shaped 20-80 nm, Fe NPs employing extract from dried eucalyptus leaf for the treatment of eutrophic wastewater. Through investigation it was observed about 71.7% of total N and 84.5% of COD was removed from the wastewater [55]. In another study, Machado et al. (2013b) explored the application of the green-synthesized ZVI NPs to remove one of the prevalent anti-inflammatory drug, ibuprofen, from sandy soils. About 54-66% removal was obtained when nano zero-valent iron (nZVI) NPs were utilized in aqueous solution, whereas about 95% degradation was obtained when nZVI was utilized as a catalyst in the Fenton process to remove ibuprofen [56]. Fazlzadeh et al. (2017) prepared zero-valent iron nanoparticles (ZVI NPs) of irregular morphology with an average particle size of 100 nm from three plant extracts, inclusive of *Rosa damascene* (RD), *Thymus vulgaris* (TV), and *Urtica dioica* (UD) for the removal of hexavalent chromium in the aqueous phase [57]. Dried green tea was reported by Borja et al. (2015) for synthesizing nano zerovalent iron. Green tea leaves composed of abundant polyphenols, and bioactive compounds that were extracted through microwave assistance. The obtained nanoparticles were spherical in nature which ranged from 8-23 nm [58]. Singh et al. (2017) synthesized uniform shaped 10±3nm iron oxide nanoparticles from green tea leaves extract. The synthesized iron oxide nanoparticles were superparamagnetic in nature with a magnetic saturation of 61emu g^{-1}. Further the synthesized nanoparticle was applied for methylene blue dye removal. A

maximum adsorption capacity of 7.25 mg g^{-1} was obtained with reaction kinetic following pseudo-second-order along with the Langmuir isotherm model from the extract which consist of alkaloids, flavonoids, carbazole, and polyphenols [59].

Mohan Kumar et al. (2013) utilized *Terminalia chebula* fruit extract, a plant rich in polyphenolic content, and studied its redox potential through Cyclic voltammetry. Sufficient reduction potential of 0.63 V was obtained concerning *Camellia sinensis* (green tea), with a redox potential of 0.33 V. Morphology analysis showed that chain like iron NPs were formed in the agglomerate form with an average particle diameter of 80nm [60].

Saikia et al. (2017) reported the utilization of fruit extract and rice paddy husk for the synthesis of silica-supported iron oxide nanocomposite. In the first step, *Zanthoxylum rhetsa* fruit extract was employed for synthesizing iron-oxide nanoparticles through an iron (III) solution as a precursor. Second step comprised of utilizing rice straw for preparing silica by boiling the raw material with sodium hydroxide solution and sulphuric acid. Finally, iron oxide-silica composite was prepared by mixing the prepared raw materials and refluxed with methanol. An average spherical particle diameter of 5-21nm was obtained. Further the prepared Fe_2O_3@silica nanocomposite was utilized for ipso-hydroxylation of phenylboronic acid to phenols. A maximum yield of 98% was obtained at the end of 120 min in the presence of H_2O_2 as a catalyst [61].

Blueberries were utilized by Manquián-Cerda et al. (2017) as a source for green synthesis of nZVI NPs. An agglomerated form was obtained with an average particle diameter of 52.4 nm. Ferric reducing antioxidant power along with the total phenolic content of the prepared fruit extract showed the capability of forming better-stabilized iron NPs. The surface area of the synthesized nanoparticle was found to be 70.7 m^2/g. The synthesized NPs were utilized for removing As(V) and was found to have a sorption capacity of 52.23±6.06 mg/g [62].

Researchers found it suitable to utilize the seeds from the fruit as a source of green reducing solvent for preparing nanomaterials. Hence, Venkateswarlu et al. (2014) utilized *Syzygium cumini* seed extract to prepared magnetic Fe_3O_4-NPs. The huge content of carbohydrates and polyphenols helped in synthesizing Fe_3O_4 nanoparticles by simple reduction reaction acting both as reducing and capping agent. The synthesized nanomaterial showed excellent ferromagnetic behavior with a saturation magnetization value of 13.6 emu/g. However, Raman spectroscopy characterization confirmed the formation of pure Fe_3O_4 without any impurity. Morphological characteristics conveyed crystalline inverse spinel cubical structure with an average particle diameter ranging from 9-20 nm. An average surface area of 3.517 m^2/g was obtained. Such prepared magnetic nanoparticle was believed to have wide application in the field of biomedicine and separation aspects [63].

Moreover, Sajadi et al., 2016 utilized *Silybum marianum L.* seed extract to synthesize copper supported iron oxide nanoparticles. Cu/Fe_3O_4 nanoparticles were synthesized by mixing plant extract with a mixture containing iron (III) chloride and copper (II) chloride solutions as precursors. The morphological analysis confirmed the synthesis of crystalline spherical nanoparticles with an average particle diameter ranging from 8.5−60 nm. Further the prepared nanomaterial was utilized for catalytic reduction of nitroarenes in an ethyl alcohol solution in the presence of sodium borohydride as a catalyst. An experimental study reveals that a maximum of 95% yield was obtained in the first cycle, whereas the yield reduced to 92% at the end of the fifth recycle. This suggests the practical reusability of the synthesized nanomaterial in catalytic application purposes [64].

1.2.3.2. Synthesis by stolon and root

Buazar et al., (2016) utilized starch-rich potato extract for synthesizing Fe_3O_4-NPs. The starch content extract plays an effective role in reducing along with stabilizing the Fe_3O_4-NPs

with capping agents mainly consisting of carbohydrate groups. The oxidation of starch extract was started with the addition of NaOH, which further produced electrons for producing Fe^0 nanoparticles. The crystalline structure of magnetite NPs were formed with a face-centered cubic shape having an average particle diameter of 40±2.2 nm. The superparamagnetic nature of the nanoparticle produced a saturation magnetization of 28.78 emu/g. Furthermore, the synthesized magnetite NPs were utilized for catalytic degradation of organic methylene blue contaminants at room temperature [65].

Niraimathee et al. (2016) by using *Mimosa pudica* root extract reported the production of Fe_3O_4-NPs. The synthesized iron oxide NPs showed a sharp absorbance peak of 294 nm through UV analysis. The superparamagnetic behavior of the Fe_3O_4-NPs was indicated by the saturation magnetization value which was found to be ~55.40 emu/g, considerably higher than reported values. Morphological analysis showed that the synthesized NPs were spherical in shape with an average particle diameter of 67 nm. The single-crystal domain of the magnetic NPs was observed which signifies a single orientation of magnetic moment. The magnetization value was found to decrease to zero from the plateau value on the removal of the magnetic field [66].

1.2.3.2. Fruit peel and plant wastes

Fruit peel/skin protects the fruit's flesh from the environment and insects. Fruit and vegetable peels have been used as a natural fertilizer which is otherwise considered as waste in the society. However, such agro-waste was utilized as a natural source and utilized for nanoparticle synthesis. Intensive research work has been performed utilizing fruit peel extract as a source for NPs synthesis. Venkateswarlu et al. (2014) utilized *Ananas comosus* (pineapple) and *Citrullus lanatus* (watermelon) fruit peel extract for synthesizing Fe_3O_4-NPs. Such fruit peel extracts both generated spherical shaped Fe_3O_4-NPs with an average size of

~17 nm. The pineapple peel extract mediated magnetic Fe_3O_4-NPs possessed a saturation magnetization of 21.7emu/g. Batch adsorption studies revealed that for 60 mg/L Cd(II) solution about 0.1mg/L adsorbent dosage resulted in 96.1% removal at pH=6. The maximum adsorption capacity of 49.1 mg/g was obtained. Similarly, for watermelon peel extract mediated Fe_3O_4-NPs was found to possess magnetic property with 28.4emu/g of saturation magnetization. The prepared magnetic iron oxide nanoparticle was utilized for Mercury (II) removal. The experimental batch study confirmed about 97.8% removal of Hg (II) for 60 mg/L stock solution, when treated with 0.1 mg/L dosage at pH=7. Maximum adsorption capacity of 52.1 mg/g was obtained for watermelon peel extract mediated Fe_3O_4-NPs [63].

Wei et al. (2016b) utilized *Citrus maxima* peels as a reducing agent for synthesizing iron oxide nanoparticles, which were further utilized for removing Cr(VI) from aqueous solution. Such usage of fruit peel served for resource utilization along with waste minimization, which otherwise would have been discarded as waste for landfills. The extract was prepared by putting the peels with ultrapure water at a high temperature for 80 min. The obtained extract was then centrifuged and membrane filtered. The obtained iron oxide NPs were spherical in shape with an average diameter of 93.8nm. Batch experiments were conducted using 100 mg/L of Cr(VI) solution using 2mL of the nanoparticle. Results conveyed that 99.29% Cr(VI) removal was obtained at the end of 90 min [67].

Similarly Ehrampoush et al., 2015 synthesized magnetic iron oxide nanoparticles utilizing tangerine peel extract. The synthesized nanoparticles were employed for Cd(II) removal from aqueous solution. Morphological investigated revealed spherical-shaped nanoparticles with an average diameter of 50nm. The highest removal of 89.6% was observed at pH 4 for 20mg/L Cd(II) concentration with 0.4 g/L adsorbent dosage, at the end of 90 min. Beccera et al. (2007) utilized *Medicago sativa* (alfalfa) biomass as raw material for obtaining biosynthesized iron oxide nanoparticles. Such utilization of waste biomass acted as a source

of recycling waste products. The obtained iron oxide nanoparticles had an average diameter of <5 nm. Alfalfa biomass was first milled down to powder form and was then introduced to the ferrous ammonium sulfate salt solution. In this study, the effect of pH condition was determined, since it played a vital role as a size-limiting parameter during the synthesis of the iron nanoparticle. Through experimental results it was found that at optimum pH=10 average nanoparticle diameter was 3.6 nm [68].

In another study sorghum bran was utilized by Njagi et al. (2011) to explore the effect of abundant phenolic compounds present for synthesizing iron oxide nanoparticles. The process started off utilizing 0.1 M $FeCl_3$ solution and sorghum bran extract in a volume ratio of 2:1 for 1h. The amorphous nature of the synthesized iron oxide nanoparticles was noticed with an average spherical particle diameter of 40–50 nm. The synthesized iron oxide nanoparticles were utilized for catalytic degradation of bromomethyl blue in the presence of H_2O_2. Maximum degradation of 90% was achieved for 500 mg/L bromomethyl blue solution with 0.66 mM iron nanoparticles dosage in the presence of 2% H_2O_2 within 30 min [69].

Lunge et al. (2014) utilized tea residues for synthesizing Fe_3O_4-NPs and further employed it for Arsenic removal studies. Experimental studies revealed that maximum adsorption capacity of 188.69 mg/g and 153.8 mg/g were obtained for arsenic (III) and arsenic (V) removal [70]. In another study Khataee et al. (2017) prepared coffee waste hydrochar loaded Fe_3O_4 nanoparticles and applied for Acid Red 17 (azo dye) removal study. An effective surface area 34.7 m^2/g was obtained, and it was found that with an increase in initial dye concentration removal efficiency decreases from 100 to 74%. Whereas, the presence of NaCl and Na_2SO_4 salts decreased the efficiency from 100 to 91%, and 100 to 85% respectively. Hence such studies prove that natural residuals provide excellent surface stabilizing properties and can be utilized towards various environmental applications [71].

Senthil and Ramesh (2012) reported the antibacterial effect of *Tridox procumbens* leaf extract mediated iron nanoparticles. Due to the higher carbohydrate content of the leaf it acted as an efficient reducing agent. Morphological analysis showed irregular spherical shaped iron oxide NPs with a rough surface. The crystalline structure of Fe_3O_4 was confirmed by XRD analysis which confirmed the crystalline size ranging from 80-100 nm. *Pseudomonas aeruginosa* was utilized for studying the antibacterial activity of green synthesized iron oxide NPs using agar well diffusion method, and results showed its efficient antibacterial activity [72]. Another synthesis method was employed by Kiruba-Daniel et al. (2013), where *Dodonaea viscosa* leaf extract was utilized to synthesis Fe NPs. During the experiment 5 mL of leaf extracted was added to 10 mL of 10mM $FeCl_3$ solution. The immediate color change indicated the formation of nZVI nanoparticles. The synthesized nanoparticles were found to be spherical in nature with an average diameter within 50-60 nm. The rich content of polyphenols such as tannins, santin, saponins, and Pendleton in *Dodonaea viscosa* leaf extract was found useful in synthesizing nanoparticles with stabilized capping [73].

1.3. Green synthesis of iron-based bimetallic nanoparticles

Mondal and Purkait (2019) synthesized iron-aluminum nanocomposite utilizing clove extract as the reducing agent. The synthesized nanocomposite was found to be coated with various groups such as –OH, -COOH and -C=O obtained from the bioactive components of clove extract, confirmed by FTIR analysis. Morphological analysis showed an irregular spindle-like structure formation. The structure confirmed the presence of carbon coating which was due to the presence of several polyphenolic and flavonoid components present in clove extract. The average particle size of the nanocomposite was found to vary with pH. With an increase in pH from 3 to 12, the average size decreased from 148.9 nm to 81.6 nm. Furthermore, the prepared Fe-Al nanocomposite was utilized for fluoride removal applications. Maximum

adsorption capacity of 42.95 mg g^{-1} with 82.1% fluoride removal was obtained at 25ºC for 1.25 gL^{-1} nanocomposite dosage. The reaction followed pseudo-second-order kinetics with a multistage diffusion control process. It showed a very good efficiency of 83% fluoride removal for fluoride contaminated water collected from various districts of Assam, India. Various coexisting ions such as Cl^-, HCO_3^-, SO_4^{-2} were found to decrease the fluoride adsorption, with chloride affecting the most ~31.8%. The fluoride removal mechanism was reported to be due to the ion exchange mechanism, where the surface phenolic –OH groups of the nanocomposite were replaced by the fluoride ions in the aqueous solution. The studies revealed that on such green synthesized Fe-Al nanocomposite proved to be a better adsorbent towards removing fluoride from water sample collected from various districts of India-Assam (82.6 % removal), and Manipur (83% removal) [74].

Similarly for synthesizing bimetallic Fe/Ni nanocomposite Weng et al. (2017) utilized methanol extract of a eucalyptus leaf as the reducing agent. GCMS analysis of extracts was carried out for identifying the various components present. Mostly alkanes, phenols, aldehydes, and amines were found in the majority, and suggest that those bioactive components acted as reducing and capping agent. The prepared bimetallic nanocomposite was utilized for the degradation of methyl orange (MO). Experiments were carried out for 10 mgL^{-1} MO with an adsorbent dosage of 0.5 gL^{-1} and were observed a maximum degradation of 29.2% using green synthesized Fe NPs, and about 99.6% degradation using Fe/Ni NPs following pseudo-first-order kinetics [75].

1.4. Environmental application of green synthesized iron-based NPs and NCs

1.4.1. Degradation of dyes

For synthesizing iron nanoparticles Hoag et al. (2009) employed green tea and utilized for catalyzing hydrogen peroxide for bromomethyl blue degradation in aqueous solution. It was concluded from the study that concerning Fe-EDTA and Fe-EDDS, enhanced catalytic activity was produced by such nanoscale zero-valent iron obtained by green synthesis (nZVI). With an increasing dosage of green synthesized nZVI, the degradation of bromomethyl blue was found to increase due to enhanced catalyzation of hydrogen peroxide [76]. Several studies related to dye removal application utilizing various green synthesized iron-based nanomaterials are reported in Table 1.4.

Similarly, Njagi et al. (2011) synthesized iron nanoparticles utilizing sorghum bran extracts and studied its catalytic activity towards degradation of dye bromothymol blue. Degradation of bromomethyl blue in the presence of iron nanoparticles and H_2O_2 dictates that the synthesized nanoparticles produced free radicals from H_2O_2 which catalyzed the degradation reaction for bromothymol blue. The rate of reaction depends on the catalysis of H_2O_2 which ultimately enhanced the degradation rate of bromothymol blue [69]. Oolong tea extract was utilized for the synthesis of iron nanoparticles by Huang et al. (2013). The nanoparticles were employed for malachite green (MG) degradation. The experimental results conveyed that the polyphenolic content in oolong tea extract served the purpose of both reducing and capping agents during the synthesis. The high polyphenolic content paved the way for lesser aggregation along with enhanced reactivity of the synthesized nanoparticles. On application towards 50 mgL-1 MG solution the nanoparticles resulted in 75.5% dye removal [77].

Table 1.4: Green synthesized iron based nanoparticles for dye degradation application

Source	Nanoparticle	Morphology	Dye removed	Efficiency	Reference
Pomegranate leaves	Fe_3O_4 NPs	45-60 nm, spherical	Congo red	93% removal at 60 min	[76]
Pisum sativum peels	Iron oxide magnetic NPs	20-30 nm, spherical	Methyl orange	96.2% removal at 60 min	[77]
Eucalyptus leaf extract	Fe/Ni bimetallic NPs	20-50 nm, spherical abd irregular	Methyl orange	99.6% removal at 180 min	[78]
Cupressus sempervirens leaf	nZVI	1.5nm, nanoclusters	Methyl orange	95.8% removal at 6h	[80]
Moringa oleifera leaves	Ni/Fe_3O_4 NPs	16-20nm, spherical	Malachite green	~91.6% removal at 25 min	[79]
Green tea leaves	Superparamagnetic Fe_3O_4 nanoparticles	10±3nm, spherical, narrow size distribution	Methylene blue	95% removal at 16 min	[65]
Pepper extract	Iron oxide/palladium nanocomposite	~50nm, spherical and dendrite nanostructures	Acid black acid brown	97% removal at 120 min	[80]
Tie Guanyin tea extract	nZVI	6.58±0.76nm, spherical	Bromothymol blue	>90% removal at 30 min	[63]

Cynometra ramiflora fruit extract	Fe_3O_4 NPs	58.5-78.1 nm, spherical	Methylene blue	100% removal at 110 min	[75]
Cynometra ramiflora	Fe_3O_4 NPs	>100nm, spherical aggregates	Rhodamine B	100% removal at 15 min	[81]
Camellia sinensis	nZVI	5-15 nm,spherical crystalline	Bromothymol blue	83.3% removal at 20 min	[76]
Green tea	Fe_3O_4 NPs	40-60 nm, amorphous	Aqueous cationic and anionic dyes	100% removal at 6h	[82]
Eucalyptus Tereticornis	Fe-Polyphenol NPs	40-60 nm, cubical	Azo dyes (adsorption)	Maximum adsorption capacity 1.6g dye/g NPs	[65]
Eucalyptus tereticornis, Melaleuca nesophila, and *Rosemarinus officinalis*	Fe-Polyphenol NPs	50-80 nm, spherical	Azo dyes (degradation)	100% removal at 200 min	[83]
Grape	Fe_3O_4 NPs	15-100 nm, quasi-spherical shaped	Acid orange (Azo dues)	80% removal at 180 min	[68]
Sorghum bran	Fe NPs	4-50 nm, spherical amorphous	Bromomethyl blue	90% removal at 30 min	[84]

A similar study was carried out by Kuang et al. (2013) where three different tea extracts were used such as oolong tea (OT), green tea (GT), and black tea (BT) separately for iron nanoparticles synthesis. Furthermore, the synthesized nanoparticles were utilized as a catalyst for the degradation of monochlorobenzene (MCB) for Fenton-like oxidation. The highest polyphenol content of the chosen extracts resulted in better synthesized Fe NPs for enhanced degradation purposes. GT based iron NPs resulted in 69% MCB degradation, whereas OT and BT based nanoparticles resulted in 53% and 39% MCB degradation in 180 min [78].

Wang (2013) for combating dye degradation synthesized nanoparticles involving iron-polyphenol complex. Eucalyptus leaves were utilized as reducing and capping agents, and the synthesized nanoparticles were employed against Acid black 194 dye for the adsorption-flocculation test. The adsorption capacity of the synthesized nanoparticles was found to be 1.6g Acid black 194 per gram of nanoparticles at 25ºC [79]. Moreover, Wang et al. (2014) utilized three different plant sources i.e., *E. tereticornis*, *M. nesophila,* and *R. officinalis* for synthesizing Fe NPs and were utilized towards decolorization of Acid black dye. The extract of *E. tereticornis* generated Fe NPs showed 100% removal of Acid black dyealong with 87% removal of total organic carbon (TOC). Such Fe NPs showed better catalytic properties as compared to the others. The as-synthesized nanoparticles showed a lower average diameter with better dispersion property in an aqueous medium [80].

In another work, Luo et al. (2014) studied the removal of acid orange II dye by utilizing iron nanoparticles synthesized by grape leaf extract. The study revealed the reactivity of plant-mediated Fe-NPs was better than the Fe-NPs synthesized from methanolic and aqueous extract of grape leaves. Hence, under various experimental conditions plant-mediated Fe nanoparticles proved to be more effective for catalytic degradation of dyes. Plant mediated Fe-NPs proved to be more suitable for Fenton-like reaction compared to the conventional Fenton reaction, where it acts as a Fenton catalyst with H_2O_2 [81].

Moreover, further research investigated iron oxide nanoparticle synthesis utilizing Pisum sativum peels. Results show that at the optimum condition of pH 6, removal of 96% of the dye was attained within one hour with an adsorbent dosage of 0.3 gL^{-1}. Similarly *Moringa oleifera* leaves were utilized by Prasad et al. (2017) for synthesizing iron oxide nanoparticles supported on nickel composite for degradation study of Malachite green dye. On analyzing the samples after 25 min of reaction through UV-Vis Spectrometer, it was noticed that 90 % of the organic dye was removed [82].

Ahmed et al. (2014) utilized microwave and microwave-hydrothermal techniques for synthesizing hematite quantum dots, and nanorods respectively. The prepared nanomaterials were utilized for the degradation of an organic dye and further the results were compared with commercially available hematite. The average particle size of ionic-liquid synthesized quantum dots, and nanorods were found to be ~10 nm, and 60 nm respectively. Microwave assisted quantum dots due to its higher surface area were found to have better catalytic efficiency as compared to synthesized nanorods, and commercially available hematite [83]. It was observed from literature that the chemically synthesized Au-Fe_3O_4-NPs supported on activated carbon (AC) showed better removal efficiency at nearly 4 min for R123 and DSB dyes with maximum adsorption capacity of 71.46 and 76.38 mg g^{-1} respectively under ultrasound assisted process. Moreover, prepared Ni doped Ferric Oxy-hydroxide FeO(OH) nanowires supported on AC for removing Indigo Carmine (IC) and Safranin-O (SO) dyes. The maximum adsorption capacities for IC and SO were found to be 37.85 mg g^{-1} and 29.09 mg $g^{-1}$for IC and SO, respectively at pH 5.0. Chemically prepared iron based nanocomposites also proved to be efficient adsorbent for dye removal applications under small reaction time [84].

1.4.2. Removal of heavy metals

Rao et al. (2013) reported the removal of Chromium (VI) utilizing bio Fe^0/Fe_3O_4 nanocomposite and yeast cells. Such prepared nanocomposite proved to be good bio-sorbents for Cr (VI) removal. The sorption capacity of the iron oxide modified yeast cells enhanced by three times when compared to the unmodified yeast cells. The better adsorption capacity of modified adsorbent ~186.32 mg g^{-1} was reported for 1000 mgL^{-1} of Cr (VI) solution under optimum conditions when compared to unmodified adsorbent with adsorption capacity 137.31 mg g^{-1}[85].

Stable and efficient green synthesized nZVI were reported by Savasari et al. (2015) obtained utilizing ascorbic acid. The prepared nZVI was employed for the reduction of Cd (II) by adsorption studies. It was reported that by utilizing green synthesized iron nanoparticles heavy metals get removed via redox reaction, and surface adsorption process. The main factor which influences the reactivity of iron nanoparticles depends on the variable oxidation states of iron [86].

Similarly, Sebastian et al. (2018) developed magnetite nanoparticle using coconut husk extract and applied for the adsorption of calcium and cadmium present in low levels. Results confirmed that cadmium and calcium removal was more than 40% and 50% respectively at the end of 120 min. Experiments suggest that maximum removal was achieved by 30min and reached equilibrium after that. The initial concentration of metal ions was fixed at 50 mgL^{-1}, and it was noticed that with increasing adsorbent dosage adsorption rate enhanced until attaining saturation [87].

Tangerine peel extract was utilized by Ehrampoush et al. (2015) for preparing iron oxide nanoparticles and utilized for removing trace amount cadmium present in water bodies. Experimental studies revealed maximum removal of 90% was achieved at pH 4 within 90 min [68]. Similarly, to remove Pb(II) from water, graphene oxide-based iron oxide

nanocomposite was synthesized by Prasad et al. (2017). Experimental results report removing Pb (II) about 96% at pH 5, where rapid adsorption occurred within 40min and equilibrium reached at 80min. The adsorption study was found to be pH-dependent, and the adsorbents were reusable by treating with definite concentration acid to desorb Pb(II) ions [82].

Studies have shown that by utilizing *Lantana camara* fruit extract superparamagnetic iron oxide nanoparticles were synthesized for the removal of Ni(II) ions from aqueous solution [88]. Experimental batch studies were performed to optimize the influencing parameters on adsorption processes such as stock solution concentration, adsorbent dosage, pH, temperature, and contact time. Due to the electrostatic attraction phenomenon between adsorbate and adsorbent at high pH, the adsorption process enhanced. An optimum pH 6 was chosen for the process since at high basicity nickel tends to form hydroxides. Higher pH involves the presence of negative ions such as hydroxides and carboxyl which indulges the better adsorption for nickel. Similarly, at lower pH desorption occurs distorting the electrostatic balance between adsorbate and adsorbent. Sorption capacity enhances with increasing nickel ion concentration in the solution, but on the other hand the adsorption efficiency decreases due to lack of active sites. Due to greater surface area possessed by smaller sized adsorbents, adsorption efficiency increases with a smaller particle size of nanoparticles [88].

Moreover, many research studies related to heavy metal removal applications through various green synthesized iron-based nanomaterials are reported in Table 1.5.

Table 1.5: Green synthesized iron based nanoparticles for heavy metal romoval application

Source	Nanoparticle	Morphology	Metal removed	Efficiency	Reference
Syzygium jambos L. Alston leaf extract	nZVI	Spherical, crystalline	Chromium (VI)	99.45% at 90 min	[85]
Coconut husk extract	Fe_3O_4 NPs	Amorphous	Calcium and Cadmium	Ca ~55%, Cd ~40% at 120 min	[87]
Citrus maxima	Fe NPs	Irregular	Chromium (VI)	99.29% at 90 min	[86]
Plant extracts: Rosa damascene, *Thymus vulgaris*,and *Urtica dioica*	Fe NPs	Irregular and non-uniform shapes	Chromium (VI)	100% efficiency for all extract mediated NPs at 25 min	[75]
Eucalyptus leaf extracts	nZVI and Fe-oxide NPs	Spherical	Chromium (VI)	98.9% at 35 min	[65]
Tangerine peel extract	Fe-oxide NPs	Spherical	Cadmium	90% at 90 min	[78]
Plant leaves	Graphene oxide/Fe-oxide NPs	Spherical NPs assembled over RGO sheets	Lead	96% at 80 min	[88]
Eichhornia crassipes leaves	nZVI	Mostly spherical	Chromium (VI)	89.9% at 90 min	[79]

Moringa oleifera leaves	Fe-oxide NPs	Nanosphere agglomerate	Fluoride	1.4 mg/g at 40 min	[71]
Lantana camara fruit extract	Fe-oxide NPs	Spherical	Nickel	99% at 100 min	[74]
Fatty acids in Olive oil	Fe-oxide NPs	Spherical	Nickel	72% at 20 min	[63]
Vaccinium corymbosum leaves and shoots extract	Fe (oxide, hydroxide), and nZVI	Spherical, agglomerated	Arsenate	76% at 120 min	[67]
Eucalyptus leaves extract	nZVI, Fe-oxide NPs	Spherical,	Chromium (VI) and Copper ions	58.9 % Cr (VI) and 33.0 % Cu (II) at 60 min	[68]
Moringa oleifera seed and leaf extract	Fe-NPs	Spherical, thick surface layer	Nitrate	For surface water: 70%(leaf extract) 74% (seed extract) at 1440 min	[81]
Commercially available tea	Fe/Clay supported	Crystalline	Arsenic (III)	99% at 30 min	[76]
Mentha spicata L.	Fe/Chitosan supported	Cubic, dispersed	Arsenic (III), (V)	100% at 30 min	[85]
Eucalyptus globulus	Fe/Chitosan supported	Nono-sized clusters	Arsenic (V)	147µg/g maximum adsorption capacity	[86]

1.4.3. Wastewater treatment

He et al. (2005) investigated the degradation of trichloroethylene (TCE) utilizing bimetallic Fe/Pd nanoparticles synthesized by starch. Less agglomerated starch coated nanoparticles were synthesized which proved to be effective in TCE degradation as compared to those synthesized without stabilizer. Maximum degradation of 98% was obtained within 1h when the reaction was carried out with nanoparticle dosage of 0.1 gL^{-1}[19].

Wang et al. (2014) investigated the treatment of eutrophic wastewater by employing iron nanoparticles biosynthesized using eucalyptus leaf extract. Such an investigation first reported the treatment of such wastewater using green synthesized nanoparticle. Fe NPs synthesized from eucalyptus leaf extract was found to have smaller average particle size as compared to those synthesized by chemical synthesis. Removal percentage of total nitrogen, total phosphorus, and COD was studied after 21 days and was found to 71.7%, 30.4%, and 84.5% respectively. The absence of precipitating agents such as calcium, or aluminum results in very low phosphorus removal [80].

Wang et al. (2014) have reported the removal of nitrate from wastewater by iron oxide nanoparticles synthesized utilizing green tea and eucalyptus leaves separately. Both the synthesis formed spheroidal particles. The study reports a comparison of nitrate removal from iron nanoparticles synthesized by plant materials and chemical synthesis. Results showed about 59.7% and 41.4% nitrate removal were obtained utilizing green tea and eucalyptus mediated NPs respectively, whereas nZVI and Fe_3O_4 nanoparticles provided 87.6% and 11.7% removal respectively [80]. There are numerous studies related to wastewater treatment and pollutant removal from wastewater by utilizing various green synthesized iron and iron-based nanomaterials shown in Table 1.6.

Table 1.6: Green synthesized iron based nanoparticles for wastewater treatment application

Source	Nanoparticle	Morphology	Pollutant removed	Efficiency	Reference
Silybum marianum L. (plant seeds)	Copper supports on Magnetite nanocatalyst	8.5-60 nm, spherical	Nitrobenzene	95% at 90 min	[80]
Euphorbia cochinchensis leaves Extracts	Iron oxide nanoparticles	100 nm, spherical	2,4-dichlorophenol	64% at 120 min	[90]
Euphorbia bungei boiss leaves	Cu/RGO/Fe_3O_4	RGO sheet dispersed with Fe_3O_4 and Cu NPs	Cyanation of aldehydes	93% at 120 min	[88]
Withania coagulans leaf extract	Pd/RGO/Fe_3O_4	<15 nm, spherical	Reduction of 4-nitrophenol	100% at 1 min	[91]
Zanthoxylum rhetsa fruit extract	Fe_2O_3@SiO_2	5-21 nm, cluster	Ipso-hydroxylation of boronic acid in water	98% at 120 min	[92]
Cynometra ramiflora leaf extract	Iron oxide nanoparticles	<100 nm, spherical aggregates	Degradation of Rhodamine B	100% at 15 min	[86]

Microwave-assisted synthesis	Silica-supported (MCM-41) iron oxide NPs	<50nm, spherical	Alkylation of toluene with benzyl chloride	99% at 3 min	[83]
Yeast	Protein capped nZVI	3-10nm, irregular	Pesticide (Dichlorvos)	100% at 60 min	[94]
Oak Leaves	nZVI	20-100 nm, irregular	Amoxicilin	100% at 95 min	[85]
Grape marc, black tea leaves, vine leaves	nZVI	15-45 nm,spherical agglomerates	Ibuprofen	50%, 50%, 55% at 193 h	[88]
Eucalyptus leaves	Fe-NPs	20-70 nm, spherical	Ametryn	100% at 135 min	[91]
Black tea extract and Ionic liquid (N-methyl-butylimidazolium-bromide)	Iron oxide NPs	5-50 nm, irregular	Propranolol	>90% at 40 min	[93]

Groiss et al. (2017) reported the synthesis of iron oxide nanoparticles utilizing *Cynometra ramiflora* leaf extract and employed it for degradation of Rhodamine B (a carcinogen) by Fenton-like catalytic process in the presence of hydrogen peroxide. The degradation was found to be optimum within 15 min when 1.11 mM nanoparticles were utilized with 2% H_2O_2. Such a process was found to produce minimum sludge and thus advantageous to other Fenton-catalyzed processes [89].

Wang et al., 2014 reported the removal study of total nitrogen, phosphorus, and COD from poultry breeding wastewater utilizing iron nanoparticles synthesized from eucalyptus leaves extract. The study shows that maximum removal of 71.7%, 30.4%, and 84.5% was obtained for total nitrogen, phosphorus, and COD respectively [80]. Similarly, iron nanoparticles were synthesized by Wei et al. (2016) utilizing *Citrus maxima* peel extracts for the removal of Cr (VI). Optimum citrus maxima peel extract: Iron (III) solution of 1:3 was maintained to synthesize better property iron nanoparticles which resulted in complete Cr(VI) removal within 90 min [67]. Similarly, removal of Cr(VI) was also reported by Fazlzadeh et al. (2017) using iron nanoparticles synthesized from three different plant extracts *Rosa damascene*, (RD), *Thymus vulgaris* (TV), and *Urtica dioica* (UD). Experimental studies show greater than 90% efficiency was obtained within 10 min [57]. Shanker et al., 2017 reported the degradation of eight selected priority polycyclic aromatic hydrocarbons (PAHs) in soil and water. Initial such high molecular weight PAHs vary from 50−250 mg L^{-1}. The optimum experimental condition at pH of 7.0 resulted in 80–90% degradation of anthracene and phenanthrene within 48 h [90].

Al-Ruqeishi et al. (2016) reported the treatment of high viscous oil utilizing iron oxide nanorods synthesized using mango tree leaves extract. Experimental study involved the blending of iron oxide nanoparticles with heavy crude oil and microwaved for the 80s. An appreciable reduction in viscosity up to 50% was obtained with 0.6 gL^{-1} nanorods at 30-50ºC

[91]. He et al. (2005) synthesized surfactant (CTAB) coated silica-stabilized iron oxide nanoparticles for microextraction of luteolin, quercetin, and kaempferol flavonoids. The process was performed utilizing the synthesized nanoparticles and ionic liquid (C_{16}mimBr) at room temperature. Results signified that CTAB-coated iron oxide nanoparticles showed an efficiency of 25–72% while ionic liquid coated iron oxide nanoparticles showed better performance with the efficiency of 85–93% [92].

1.4.4. Green synthesized iron NPs immobilized on polymer and other supports for pollutant degradation

Since, nanoparticles are prone to agglomeration which reduces its effectiveness towards the catalytic and adsorptive activity. Such limitation was overcome by immobilizing nanoparticles within polymeric, zeolitic, and silica-based supports. Smuleac et al. (2011) utilized polyvinylidene fluoride (PVDF) membrane as support to incorporate Fe and bimetallic Fe/Pd nanoparticles through the green synthesis technique. Through polymerization reaction PVDF membranes were modified with polyacrylic acid (PAA), whereas for synthesizing Fe and Fe/Pd nanoparticles, green tea extract served as a reducing agent. Nanoparticle embedded PVDF/PAA membrane was found to incorporate nanoparticles with average particle diameter 20–30 nm [93]. The synthesized nanoparticle impregnated membrane was utilized for studying the degradation of toxic organic pollutant, trichloroethylene (TCE). Catalytic reactivity of the membrane dechlorinated TCE compound, and was found to increase with more nanoparticle incorporation within the membrane. Moreover, it was reported that bimetallic Fe/Pd incorporation enhanced the catalytic process, rather than only Fe nanoparticles. Chang et al. (2011) studied with different extracts like the chestnut tree (*Castanea sativa*), eucalyptus (*Eucalyptus globulus*), gorse (*Ulex europaeus*), and Pine (*Pinus pinaster*), for synthesizing iron nanoparticles. The study reported the effect

of plant extract ratio on the formation of iron nanoparticles, and high antioxidant property present in eucalyptus was found to be most suitable for nanoparticle synthesis. Prepared nanoparticles were mixed with chitosan, and further the chitosan beads were characterized. Iron nanoparticle encapsulated with chitosan was utilized for As (V) removal. Moreover, the maximum adsorption capacity of 147µg g^{-1} was achieved with 25 gL^{-1} adsorbent dosage at pH 6-7 [94].

Saikia et al. (2017) reported the synthesis of iron oxide nanoparticles supported on silica through a cheap green method, and utilized it further as a catalyst for preparing phenol from boronic acids through ipso-hydroxylation reaction, instead of using hydrogen peroxide (H_2O_2). Experimental studies show, about 98% yield in aqueous solution when about 4 mg of nanocatalyst was utilized within 2h at 50ºC. Zheng et al., 2014 to extract organophosphorus pesticides from a solution prepared nano sorbent of iron oxide and ionic liquid upon polymeric support. Methanol proved to be the better dispersion medium for the prepared nano-adsorbents, as well as effective elution solvent. At an optimum condition of 2.4 gL^{-1} adsorbent dosage maximum yield of 81.4–112.6% was obtained at the end of 80 min [61].

Mondal and Purkait (2017) synthesized iron nanoparticles by employing cardamom extract with an average diameter of 32nm. Furthermore the nanoparticles were incorporated within pH-responsive poly(vinylidene fluoride-co-hexafluro propylene) (PVDF-co-HFP) by mixing method. The prepared nanoparticle embedded membrane was studied for nitrobenzene (NB) reduction purpose by varying iron NP content (wt%), pH, and time (min). At an optimum pH 11.9, iron content 0.01 wt%, NB degradation of 57% was obtained at the end of 50 min. Aniline conversion of 9.65ppm was obtained from 100ppm nitrobenzene [95].

In another work Mondal and Purkait (2018), utilized iron oxide incorporated pH-responsive polymeric membrane for degradation of nitrobenzene and fluoride rejection purpose simultaneously. In this work, clove extract was employed for synthesizing iron NPs with an

average diameter of 13.5nm having a core-shell structure with Fe^0 at the core. At the optimized condition of pH=3, iron content 0.01 wt%, and time 39 min, NB reduction of 86.7% was obtained with an aniline formation of 12.7ppm. Fluoride rejection was highest for a 20ppm stock solution of 72% at optimized conditions [96].

1.5. Future scope of work

Past reports show various plant sources such as leaf, stem, fruits, vegetables, fruit and vegetable peels, roots, and barks including plant wastes for preparing iron NPs and studied its application in various fields. Not much focus was made towards medicinal herbs and spices. More research and advancements are required to explore the uniqueness of green synthesized nanomaterials, and various other available resources for such synthesis should be practiced. Understanding the underlying mechanism of such synthesis plays an important role in discovering out new modifications and advancements. The future works should be concentrated on the chemical properties of polyphenolic components of the green extracts and its involvement in nanoparticle generation. Moreover, developments should lead toward an economically competitive process, can be scaled up, and eco-friendly in nature compared to conventional methods. Future studies should involve the use of more local resources to make things economically viable, and research should focus more on stability issues of synthesized nanomaterials for better biocompatible applications. Research should emphasis on synthesizing such green nanomaterials towards better efficiency in tackling contaminants with minimum eco-toxicological effects.

1.6. State of the art

With a brief overview of the contemporary research, this section outlines the research outcome of various literatures so as to identify few promising areas of research that needs to be addressed in this thesis. The state of the art has been presented for preparation of iron nanoparticles and nanocomposites through green synthesis route and its various application in real life.

1.6.1. Preparation of green synthesized Iron nanoparticles (FeNPs) utilizing extracts of *Syzygium aromaticum* (clove), *Elettaria cardamomum* (cardamom), *Laurus nobilis* (bay leaf) for dye degradation study

Over many years for treating dye contaminated solutions, various conventional treatment technologies were utilized such as chemical coagulation and flocculation, adsorption, membrane treatment, chemical oxidation, and photodegradation [97]. Techniques such as adsorption and flocculation produces effluent with better efficiencies in treating dye solutions with high flowrate handling capacity. Moreover, when compared to chemical oxidation it does not results in harmful substances formation, which posses a threat for environmental pollution. Various materials such as fly ash [98], clay [99], activated carbon [100] wheat straw [101], and others have also been utilized for dye adsorption. However, inorganic salts were often used as coagulants for treating dye solution such as $Al_2(SO_4)_3.18H_2O$, $FeSO_4.7H_2O$, and $FeCl_3.6H_2O$ [102]. Polyferric sulphate, an inorganic polymer flocculant [103], along with other flocculants of synthetic organic polymer and natural polymer like polyacrylamide [104], and chitosan [105] respectively were investigated for dye removal purpose. The drawbacks of such technique include residual dye containing sludge, selective poor efficiency towards some dyes, and high cost of raw material. Moreover, threat such as

organism DNA damage is also possessed while using synthetic organic polymer flocculants [106].

Literature review

Nowadays, membrane technology has emerged as an efficient technique for treating industrial and textile wastewater for maintaining its suitability as drinking water, usage in agricultural irrigation and industrial applications [107]. The advantages of such process include its operation at room temperature, high separation efficiency, by-product generation minimum, along with the scope of preparing membranes from waste which makes it low cost [108]. However, improvements are still needed and researches are being directed towards synthesizing membranes with enhanced performance by focussing on specific properties such as antifouling, selectivity, permeability, and scaling [109]. Various works have been reported in order to synthesize membranes with better performance with cheaper investment cost.

In the field of dye adsorption, nanotechnology has played a vital role in water purification. The noticeable advantages of such process include drastic costs reduction. The reduction in cost was attributed due to the higher surface area of nanomaterials which minimized the usage of adsorbents for such dye removal applications [110]. Due to non-complex synthesis process and their phenomenal ability to remove numerous contaminants, iron nanoparticles are nowadays being widely utilized as adsorbents [111]. Green synthesized iron nanoparticles have attracted researchers for dye removal application due to its effective methodology, less toxic nature and cost of production [112]. Plant extracts have been used intensively for such green synthesis purpose among bacteria, fungi, and others. Plant extract acts as a source of phytochemicals, which includes mainly polyphenols, solely responsible as reducing agents and capping material, favouring the growth of metal nanoparticle [113]. Vegetable raw materials have been used in several studies for preparing aqueous vegetal extracts such as

leaves, fruits, stems, etc., whereas in many studies discarded vegetal parts were reported for green synthesis of iron nanoparticle [114]. Several iron nanoparticle related dye removal applications show that either the removal process involves adsorption, or reduction of dyes resulting in decolorization [115]. The process involving adsorption depends on the oxide formation of iron nanoparticles, whereas the decolourization process involves the formation of zero-valent iron nanoparticles.

Possible scope for future research and work done

From the above literature review it may be envisaged that several authors have reported removal of dye by utilizing nanoparticles either through adsorption or degradation mechanism. Hence, the utilization of green synthesized iron NPs with the formation of zerovalent iron and its oxides which could act towards dye removal through adsorption along with degradation process needs to be explored. In this study, three different green sources rich in polyphenolic compounds were taken and utilized for the preparation of zero-valent iron nanoparticles (ZVI NPs). A comparative analysis of better phenolic and flavonoid content was done among the three green sources and also a better solvent for extraction was chosen for preparing the ZVI NPs. Morphological analysis and characterization of the ZVI NPs were performed utilizing Field emission scanning electron microscopy (FESEM), Transmission Electron Microscopy (TEM), Energy dispersive X-ray (EDX), X-ray Diffraction (XRD), UV-Visible Spectroscopy, Thermo-gravimetric analysis (TGA), and Fourier transform Infrared spectroscopy (FTIR). The clove extract mediated zero-valent iron nanoparticle due to its better phenolic, flavonoid content along with better antioxidant property was further utilized for studying the degradation and removal of cationic dye i.e. crystal violet. The better chemical property obtained zero-valent iron NPs among the

different extracts were then utilized for studying the adsorption kinetics and removal mechanism of methylene blue.

1.6.2. Role of extraction solvents and optimization of process parameters for maximizing total phenolic and flavonoid content of the *Syzygium aromaticum* (clove) extract

Spices and herbs besides being used as flavoring agents have also found wide applications due to its medical and antiseptic properties. Many spices and herbs have excellent preservative effects which are attributed due to the presence of antioxidant and antimicrobial constituents. From studies, it was observed that excellent antioxidant properties were exhibited by rosemary and sage, whereas other spices like turmeric, oregano, thyme, and nutmeg also showed better antioxidant activity [116,117]. Such plant extracts were investigated to consist of several phenolic compounds with strong antioxidant activity [118]. Utilization of spices and herbs extracts as reducing and stabilizing agents for synthesizing iron nanoparticles were not explored much needs to be investigated and optimized for studying its effect on synthesized nanoparticle morphology.

Literature review

In both edible and nonedible plants and herbs, commonly phenolic compounds are usually found in abundant amounts, which have been reported to have several biological effects, including antioxidant activity. In the food industry, there is a growing interest in phenolic rich extracts of fruits, herbs, vegetables, and other plant materials which results in retard oxidative degradation of lipids and thus enhances the food's quality and nutritional value. Among the scientists, the plant's antioxidant constituents have raised growing interest since it plays an important role in health maintenance and protection from coronary heart disease and cancer.

Keeping in mind the future trend which aims toward nutritional foods having specific health effects, such plant extracts have attracted the food manufacturers, and consumers also [119]. The preventive role of flavonoids and other phenolic compounds toward the development of cancer and heart disease has rendered it an important biomedical compound [120]. It was found that the consumption of fruits and vegetables in a controlled diet significantly increased the antioxidant capacity of plasma [121]. Plant materials such as vegetables, fruits, leaves, and roots, spices, and herbs are found to be potential sources of antioxidant compounds [122]. Commonly in leaves and flowering tissues, flavonoids along with phenolics components like, phenolic acids, stilbenes, tannins, are found in abundance, which is important for growth and defense mechanism [123]. The redox property of the phenolic compounds contributes to the antioxidant activity and render them to act hydrogen donators, reducing agents, and singlet oxygen quenchers. Moreover, they possess metal chelation potential which allows them suitable for the synthesis of metallic NPs [124-125].

Possible scope for future research and work done

From the above literature, it was obtained that plant parts along with different spice herbs possess abundant phenolic content and show antioxidant property which could be utilized as a green source for the preparation of NPs synthesis. Such prepared NPs can be utilized for various biomedical purposes due to its antioxidant and biocompatible nature. Previous research works have not focussed on the maximum yield of phenolic and flavonoid content within extracts by optimizing process parameters such as pH, amount of extraction solvent, and extraction temperature. In this study, clove spice was utilized to study its total phenolic, flavonoid and antioxidant content in order to utilize it as a green reducing source to prepare zero-valent iron NPs. The clove extract was first optimized according to time, water amount as extraction solvent, and temperature to maximize its phenolic and flavonoid content, since

phenolic and flavonoid content are directly related to the antioxidant property. Moreover, the pH of the extract was controlled to study its phenolic and flavonoid content behaviour. The optimization of the various processes was carried out using Design expert software 9.0 through ANOVA (analysis of variance) using the combination of response surface methodology (RSM) and central composite design (CCD).

1.6.3. Investigation of morphological variation of Fe NPs with pH change and studying the photoluminescence behavior of green synthesized Fe NPs towards heavy metal ion sensing application

Iron, being heavy metal over years has been one of the main contaminants involved in water pollution. It has severe impact on human health. An overdose of Fe^{3+} in human body can lead to various biological disorders. Iron plays a major role in enzyme catalysis, cellular metabolism, DNA and RNA synthesis and repair and as oxygen carrier in haemoglobin. Serious diseases like cancers, Parkinson's and Alzheimer's diseases can occur due to iron accumulation leads, whereas its deficiency causes diabetes, anaemia, breathing problems, liver, heart and kidney damages. In present days, various industries like iron manufacturing, electroplating and steel discharges very high doses of iron related wastewater (Fe^{2+} and Fe^{3+}) causing water pollution. Consumption of this water poses hazardous health issues in living organisms. Thus, the qualitative and quantitative determination of trace amounts of Fe^{3+} ions is currently of great interest to ensure the proper functioning of biological systems. Therefore, determination of Fe^{3+} in human body or water is very important. Several techniques such as atomic absorption spectrometry, inductively coupled plasma mass spectroscopy, electrochemical methods, and fluorescence spectrometry have been utilized detect Fe^{3+} [126, 127].

Literature review

Over years carbon dots (CDs) has given hope in many potential applications because of their good biocompatibility, chemical inertness, high stability, aqueous solubility and easy functionalization and their excellent optical properties such as tunable emission, stable photoluminescence for the last ten years [128, 129]. These potential applications have widely studied in various fields ranging from bio-imaging [130], sensors [131]. Metal oxide nanoparticles (NPs) in the past two decades have gained huge attraction which was attributed due to their unique and unusual physical and chemical properties [132]. Zerovalent iron (ZVI) and iron oxide (FeO) NPs has been extensively used since 1990s for various applications in the field of medicine [133], biotechnology [134], environmental remediation [135], and photocatalysis of pollutants [136]. Various methods both physical and chemical have been adopted for iron nanoparticles synthesis (ZVI, FeO-NPs). Though such processes are very effective, but they possess several limitations such as high cost, and high consumption of energy [137], moreover due to the use of toxic, corrosive, and flammable chemicals along with organic solvents, and reducing agents, such processes has negative impacts on the environment and human [138].

Recent literature showed the toxicological limitations of iron NPs can be eliminated through the green synthesis of FeO-NPs which utilizes biological sources like plant parts [139], bacteria [140], seeds [141], and algae [142]. Plant sources have been widely explored due to its phytochemicals content, which plays an important role in synthesis reaction [143]. Flavonoids [144], amines, terpenoids [145], carbohydrates [146], and phenols [147] controls the growth of the NPs and provides functional groups required for stabilization, oxidation, and reduction of metal oxide precursors [148].

Currently, the application of iron and its oxide NPs have been explored toward biotechnological, biomedical, and environmental fields. Several authors have reported its

antimicrobial properties which could be utilized to improve the freshwater quality and reduce pathogenic diseases [149]. Moreover, such iron based NPs have been implemented for environmental remediation through adsorption of heavy metals [150,151], as well as photo-degradation of organic compounds, such as dyes [152], and drugs [153].

Possible scope for future research and work done

From past literatures it was envisaged that fluorescence study of green synthesized iron NPs have not been explored. Carbon dots along with other noble metal such as gold and silver NPs have been extensively used for such purposes. In this chapter of the thesis investigation was carried out to find the better ratio of precursor iron salt solution and clove extract, which efficiently produced better zero-valent iron (ZVI) NPs. The effect of clove extract pH on the morphology of synthesized ZVI NPs and its various oxide forms was investigated deeply. In this study the photoluminescence property of the synthesized ZVI Nps was utilized towards detection and quantification of Fe^{3+} ion. The present study focussed on clove extract mediated zero-valent iron NPs synthesis and its utilization towards specific sensing of Fe^{3+} ion in presence of other heavy metals such as cadmium, lead, mercury, manganese, copper. Previously green synthesized iron NPs were only utilized for biomedical applications such as antimicrobial and drug delivery purposes along with other environmental remediation purpose. The synthesized iron NPs were characterized through various techniques and through morphological analysis it was found to form iron dot in the range of 1-5 nm. Through fluorescence spectroscopy presence of Fe^{3+} ion was detected and further quantified in real water samples collected from IIT Guwahati, Assam campus. The detection range and limit of detection were analyzed and were found to be in line with other studies previously reported.

1.6.4. Preparation of green synthesized zerovalent iron NPs embedded pH responsive PVDF-co-HFP polymeric membrane for nitrobenzene degradation and fluoride rejection

This chapter consists of two sections: Part (I) deals with the preparation and characterization of pH responsive PVDF-co-HFP membranes. Due to the blending of polyethylene glycol methyl ether (PEGME) and Humic acid (HA) as additive, the pH characteristic got incorporated within the polymeric membrane. This property was attributed due to the dibasic property of HA. The flux variation at different pH due to pore size alteration confirmed the pH responsiveness of the membrane. The variation of pore size according to pH was utilized for separating Bovine serum albumin (BSA)

1.6.4.1. Preparation of pH responsive polymeric PVDF-co-HFP membranes

Literature review

Nowadays membrane technology is being used in various fields of study like waste water treatment, desalination and food processing. In membrane preparation, hydrophilicity and hydrophobicity are the two terms which plays vital role. There are several researches that have focused on many membrane materials like; polyslfone (PSF), polyimide (PI), polyether imide (PEI) and poly(vinylidene fluoride) (PVDF) [154-158]. Recently poly (vinylidene fluoride-*co*-hexafluropropylene) (PVDF-HFP) in the field of membrane science has emerged to be superior to PVDF due to its excellent chemical and thermal resistances [159]. The ease of making membranes via phase inversion made it all the more acceptable [160,161]. Incorporation of hexafluropropylene (HFP) which is more amorphous, into the main constituent vinylidene fluoride (VDF) blocks PVDF-HFP possess more crystalline phase than PVDF. Many literatures highlight the fabrication of PVDF-HFP hollow fibers [162-165]. It

has been reported that pore size increases for membranes prepared from PVDF-HFP without any additives than for only PVDF membranes [166,167].

Hollow fiber PVDF-HFP membranes were prepared using PVP (Poly vinyl pyrrolidone) as additive with 5 wt% and 10 wt% in N-methyl pyrrolidone (NMP) casting solution. Macro-void formation was favored by the addition of PVP in the fabrication of PVDF-co-HFP membranes. The PWF increases from 42 to 107 L/m^2 h, and the contact angle falls from 78.2° to 72.6° [159]. Macropore suppression was also noticed due to the presence of relatively large amount of PVP [9]. Moreover hollow fiber PVDF-HFP membranes was prepared using PEG (Polyethylene glycol) 3 wt% and PEG/ LiCl (1:1) wt% in NMP casting solution. The PWF decreased from 167 to 117 L/m^2h, in response the contact angle increases to 95.2° from 93.4° [157]. Similarly, hollow fiber PVDF-HFP membranes was prepared using Lithium chloride (LiCl) 2 wt% and glycerol 10 wt% in NMP casting solution. The PWF increased from 49 to 51 L/m^2h, whereas the contact angle increases from 83° to 88° [158]. Flat asymmetric PVDF-HFP membranes was prepared using (NMP/ methanol) as the solvent to prepare casting solution with Polyethylene glycol (PEG) as additive. The highest PWF of 70.9 L/m^2h was achieved for (NMP/methanol) (80/5 wt%) and PEG (3 wt%) with contact angle 63.5°. Similarly, PWF of 25.75 L/m^2h and contact angle of 73° was achieved for (NMP/methanol) (70/15 wt%) with PEG (3 wt%) [160]. Polysulfone membranes were prepared by varying the molecular weight of PEGME from 550 Da to 5000 Da. PWF increases from 17.5 L/m^2 h to 227.8 L/m^2 h and the contact angle decreases from 71° to 47° [168]. PVP was reported to be an effective hydrophilic agent for fabrication of both PVDF homopolymer and PVDF-HFP copolymer where the thermodynamic effect also played a vital role [169].

Possible scope for future research and work done

In this work, a novel hydrophilic additive was prepared by blending PEGME and HA in 2:1 ratio. The hydrophilic additive was prepared on the fact that when number of oxygen containing functional groups such as (-OH) hydroxyl, (-COOH) carboxyl, (C=O) carbonyl increases, the probability of forming hydrogen bond with water molecules increases and hence hydrophilic property enhances in polymeric membranes. Humic acid contains numerous oxygen containing groups eg. COOH, OH, CO hence it serves the purpose for being used as a better hydrophilic agent when blended with PEGME (polyethylene glycol methyl ether) in this research article. Moreover, the humic acid being dibasic acid, had dissociation constant values pK_1 ~4 for de-protonation of carboxyl group and pK_2 ~8 for de-protonation of phenolic group. This property serves the purpose for the pH responsive character of the membranes prepared with HA and PEGME as additive. In most of previous works, PVDF-co-HFP polymer was utilized for fabricating hollow fiber membranes. Previous works didn't focus on both the hydrophilic and pH responsiveness property of the PVDF-co-HFP flat sheet asymmetric membranes.

1.6.4.2. Modifying pH responsive membrane by incorporating green synthesized zerovalent iron NPs for nitrobenzene reduction and fluoride rejection study

Literature review

Among the ground water contaminants, nitrobenzene (NB) and fluoride has been a well-known harmful component. NB has large application in pharmaceutical drugs, dyes, insecticides and herbicides [170]. Whereas high concentration of fluoride > 1.5 ppm (according to WHO) poses serious threats like neurological disorders, osteosclerosis, dental fluorosis, cancer as well as poor development of infant's brain [171]. It remains a challenge to detoxify water containing both NB and fluoride as contaminant. NB because of its high

resistance to chemical as well as biological degradation poses challenge for researchers [172]. Increasing awareness for both the compounds toxicity in the environment has made researchers to explore various effective techniques to minimize it. One of the most useful techniques for nitro-compounds is to reduce it to its amide form which is less harmful and easily biodegradable [173]. For fluoride various adsorbents, chemical precipitation, electrocoagulation has been used [174].

Nowadays, zero-valent iron (ZVI) has attracted much attention for the reduction of nitro compounds to its amide. Moreover, nano-sized iron particles (NPs) has proven to be the best than the granular form due to its large surface area to volume ratio which is useful for fluoride adsorption as well as high reactivity compared to its bulk form. It was used as one of the efficient catalyst for reducing hazardous organic compounds in wastewater [175]. Iron NPs via different routes mainly by chemical synthesis and biosynthesis (green synthesis) has been synthesized. Main problem associated with chemical synthesis is the generation of hazardous flammable hydrogen gas and other by-products. Synthesis via bioprocess yields no such hazardous by products, cheaper process as well as the agglomeration constraint for NPs gets somewhat resolved due to the presence of active bio molecules. The main constraint which lies with the preparation of iron NPs is the surface protection. Being highly reactive, the tendency of iron NPs to form oxide and hydroxide layer reduces its catalytic reactivity for reducing organic contaminants in wastewater. Hence, immobilization of iron NPs on solid supports like activated carbon, metal oxides and zeolites were performed [176-178]. The effective contact between reactive site of NPs and contaminants are reduced due to the dense structure of the support. This paved the way for immobilizing NPs in membranes via mixed matrix method or surface coating which provided better opportunity [179].

Polymeric membrane as cross-linker was investigated for obtaining smaller and well dispersed pattern of iron NPs [154,155]. Polymeric nanoparticles like Polyacrylic acid (PAA)

[160,180] and polyethylene glycol (PEG) [181,182] has also been used as cross linker. Swelling inhibition property and presence of OH groups in both ends makes them suitable for such purpose. Nowadays PVDF-co-HFP (poly vinylidene-co-hexafluropropylene) has emerged to be a better polymeric candidate due to its good thermal and chemical resistance. Moreover due to its hydrophobic nature it is easy to cast via phase inversion method

Possible scope for future research and work done

Immobilizing iron NPs within pH responsive polymeric (PVDF-co-HFP) membranes support and studying its reducing effect on nitrobenzene reduction and fluoride rejection by varying pH is a new approach. The pH responsiveness of polymeric membrane and the reducing activity of the dispersed iron NPs contributing towards the degradation of nitrobenzene as well as fluoride rejection is a new scope of study which has not been investigated, and covered in this part of thesis. In this chapter, the iron NPs impregnated pH responsive PVDF-co-HFP membranes were prepared and characterized by XRD, FESEM, EDX, TEM, TGA and Delsa-Nano particle size analyzer. The addition of iron NPs in different weight percentage as well as pH sensitivity of the membranes towards degradation of nitrobenzene along with reaction mechanism as well as fluoride rejection was investigated and analyzed in detail. Finally, various parameters on the formation aniline from nitrobenzene were optimized with the help of design expert software through analysis of variance (ANOVA) using the combination of response surface methodology (RSM) and central composite design (CCD).

1.6.5. Preparation and characterization of novel green synthesized iron-aluminium nanocomposite and studying its efficiency in fluoride removal

The intensive modern industrialization has turned out to be the main cause for degradation of natural environment in terms of sustainability. Contamination of the land and aquatic

genomes, due to heavy industrialization as well as haphazard ground water harvesting resulted in accumulation of toxic elements which produced disorders and diseases in living organisms [183,184]. Heavy metals have troubled the aquatic environment quite intensively and similarly fluoride has also been a chief contaminant in ground water. Up to a concentration of 1.0 mg/L, fluoride is especially beneficial for children, but above 1.5 mg/ L it possesses a serious threat such as dental problems and skeletal fluorosis [185]. Disintegration and leaching of the rocks and soil bearing fluoride and weathering of the volcanic particles has been the main source for fluoride. Beside this the rain water washing off the fluoride containing insecticides and pesticides from agricultural fields as well as untreated and uncontrolled discharges from the industrial belts also contributed for fluoride contamination. Particularly fluoride contamination has become a major challenge for the developing countries where India, Bangladesh and Sri Lanka also possess the threat [186].

Literature review

Several treatment techniques like reverse osmosis, ion exchange, surface adsorption, precipitation and membrane filtration were endorsed to lower the fluoride level of ground upto the permissible limit (<1.5 mg/ L). Surface adsorption has been widely accepted in rural sector for field implementation due to its simple operation, small space requirement and cost effectiveness. Numerous adsorbents like low cost materials [187], polymeric materials as well as mixed metal oxides and surface modified materials [188] have been investigated. Moreover, various adsorbents for defluoridation was also generated from waste residue of alum-manufacturing processes [189], untreated hydrated alumina (UHA) and thermally–treated hydrated alumina (THA) [190], aluminium oxide–manganese oxide composite material [9], nanoscale aluminium oxide hydroxide (AlOOH) and natural zeolite [191,192],

were among several attempts which have been made in Ethiopia for defluoridation of drinking water.

Bone char is the most suitable material for fluoride removal due to its particular chemical composition, which is rich in hydroxyapatite ($Ca_5(PO_4)_3(OH)$) [193],. Carbonaceous materials such as graphene and graphene oxide (GO) have attracted researchers for their unique properties. Excellent mechanical, thermal and electrical properties possessed by graphene oxide made it all the more attractive [194]. The methodology adapted through modified Hummers method garnished graphene oxide with numerous —COOH, —C=O and —OH groups on its surfaces which made it suitable for scavenging ionic s olutes from waste water [195]. Since GO is highly dispersible in water, it stands out to be the main limitation for using it in large scale, otherwise its separation process would become quite difficult. Extensive research regarding graphene based metal and metal oxide nanocomposite (NC) have been carried out previously by many groups [196]. Forming composites with organic as well as biological materials resulted in an enhancement of the adsorption capacity of the metal oxides. Adsorption capacity comparatively enhanced for the composite when compared with the individual materials [197].

Possible scope for future research and work done

From the literature survey it was observed that green synthesized iron based nanocomposites for fluoride removal purpose have not been explored as such. Hence in this study green synthesized iron-aluminium nanocomposite was prepared and utilized for fluoride removal studies. Previous works mainly utilized GO based metal-nanocomposite for treating fluoride contaminated water, which required the hectic preparation step for GO, whereas this study is a one step synthesis of metal-metal nanocomposite. This study also focuses on the characterization of surface functional groups of the prepared nanocomposite. It was found

that groups such as –C=O, –COOH, –OH are incorporated over the prepared nanocomposite due to green synthesis which facilitated the F^- ion adsorption. The adsorption capacity of the green synthesized iron-aluminium composite was found in good agreement with already prepared hydrous iron-aluminium mixed oxide as well as graphene oxide composite of iron-aluminium mixed oxide. Through this approach cost of using reducing agent as well as an alternative for forming organic composite (instead of GO) was achieved. In this study the clove extract acted as reducing agent as well as formed an organic coating (consisting of –COOH, C=O, -OH bonds) on the iron-aluminium nanocomposite which enhanced the adsorption capacity of the adsorbent.

1.6.6. Studying the specific metal ion sensing ability of clove extract mediated (*Syzgium aromaticum*) green synthesized iron-aluminium nanocomposite

Over years green synthesis has gained vast attention for synthesizing noble metal nanoparticles (NPs) like Au, Ag due to its wide application in biomedical field. Various plant extracts have been utilized as green synthesis source since the process is simple, inexpensive and provides stabilizing properties to the NPs [198-201]. Several research works were carried out to study the fluorescence and phosphorescence activity of quercetin and rutin [203,204]. Interaction of rutin and quercetin with bovine serum albumin and haemoglobin was studied in details to show the increase and quenching effect of fluorescence intensity [205]. Various research have reported the direct effect of fluorescence activity of such flavonols towards sensing various proteins and DNA related works [206-208]. Plant extract mediated green nanocomposites (NCs) which contains such fluorescence based flavonols coating on its surface has not been utilized previously for preparing NCs based metal sensor. Moreover, metal-metal nanocomposites till date have been prepared incorporating GO (graphene oxide)

and AC (activated carbon) for providing carbon containing groups along with other functional groups by surface modifications for better adsorbent purpose.

Literature review

Clove (*Syzgium aromaticum*) is known to be as medicinal aromatic flower bud originating from plant family named Myrtaceae. It has profound use, as spice in cuisine of Asian, African, and the Middle East countries. Clove has been known for its various medicinal uses due to high antioxidant content. High content of polyphenolic compounds, especially flavonoids impregnates the property of better antioxidant agent. In various medicinal plants, vegetables, fruits, vegetables as well as beverages, flavonoids are found in high content which are considered as a group of polyphenolic compounds [209,210].

Due to the presence of several hydroxyl groups at definite positions, such compounds results in higher antioxidant property along with anticancer activities, and moreover a C_2–C_3 double bond also adds up the phenomenon [211]. The positive effect of flavonoids includes anti-hepatotoxic, anti-osteoporotic, anti-allergic, and anti-inflammatory properties. Hence for cell cycle progression, such compounds are considered as potent regulators, which may further be investigated towards prevention of carcinogenesis [212]. In clove various flavonoid glycosides (like, rutin) are also found which denotes flavonoids bonded with sugars. Through hydrolysis of glycosidic bond, free flavonoid aglycones can be synthesized by enzymes or acidic conditions [206,207]. In this study for clove extract preparation, polyphenolic compounds such as gallic acid (phenolic acid), quercetin (flavonol), rutin (glycoside combined flavonol), and catechin (flavan-3-ol) which were found in high has been investigated.

Possible scope for future research and work done

From literature survey it was obtained that for detecting various heavy metal ions, photoluminescence activity of noble metal NPs and carbon dots have been extensively utilized. In order to explore the green synthesized materials towards photoluminescence activity, the prepared iron-aluminum (Fe-Al) nanocomposite was utilized for studying its photoluminescence behavior. In this part of the thesis a novel dual characteristic property of the green synthesized Fe-Al such as photoluminescence activity apart from its fluoride removal efficiency was explored. Due to the high polyphenolic and flavonoid content within the clove extract two photoluminescence band spectra emission was obtained and was found to be inherited within the green synthesized Fe-Al nanocomposite, which further on excitation exhibited single emission spectra. Effect of pH on the UV absorbance and photoluminescent (PL) behaviour of clove extract on the basis of electronic transition and tautomerism of de-protonated 3-OH flavonols were discussed in this section of the thesis. The PL peak of Fe-Al NCs solution shifted at varying pH, and was also observed to shift when treated with different Fe^{3+} concentration. In the presence of various heavy metal ions, ON-OFF PL intensity was observed for Fe^{3+} ion showing specific ion sensing ability. The nanocomposite was found effective to detect Fe^{3+} in the linear range of low concentration 0.078-0.125 μM. Moreover, for real water sample analysis the Fe-Al NCs based Fe^{3+} sensor proved to be efficient with negligible error% of detection.

1.7. Objectives and scope of work

This thesis is focused on the preparation of green synthesized Fe NPs from three different spices (green source) (common names: clove, cardamom, and bay-leaf). The green source and the solvent for extraction were selected based on better phenolic, flavonoid, tannin, and

antioxidant properties. The synthesized green Fe-NPs which comprises of zero-valent iron (ZVI) in the core and oxides at outer shell was then utilized as an adsorbent, reducing agent, and specific heavy metal ion sensor. Moreover, green synthesis of iron-aluminium nanocomposite was carried out, and further utilized as fluoride adsorbent, and specific heavy metal ion sensor. The main objectives are listed below:

- To analyze and select better source of aqueous green extract among clove (*Syzygium aromaticum*), cardamom (*E. Cardamomum*) and bay leaf (*Cinnamomum tamala*) on basis of flavonoid content, phenolic content, tannin content, and antioxidant properties.
- To study the better extraction of phenolic, flavonoid, tannin, and antioxidant property within selected green extract (from objective 1) by varying the extraction solvents such as water, methanol, and ethanol.
- To study the pH dependent morphological and chemical property variation of green synthesied zero-valent iron NPs and investigating its photoluminescence property towards sensing heavy metal ion in real life wastewater.
- To prepare zero-valent iron NPs impregnated pH responsive polymeric membrane and studying its effect on nitrobenzene reduction and fluoride rejection.
- To prepare green synthesized iron-aluminum (Fe-Al) nanocomposite and studying its effect in fluoride removal in real life contaminated water.
- To investigate the specific heavy metal ion sensing ability of green synthesized Fe-Al nanocomposite in presence of other heavy metals.

1.8 Organization of the thesis

In order to fulfil the above objectives the thesis is organized in eight chapters. The content of each chapter is given below.

Chapter 1 addresses the state of the art, research motivation of present work, possible scope of research, objectives and organization of the thesis. **Chapter 2** provides a complete description of the methods and experiments involved in green extract preparation, analyzing its total phenolic, flavonoid, tannin content and investigating its antioxidant properties. The chapter also discusses of synthesizing iron nanoparticles and all the various characterization techniques. **Chapter 3** provides a vivid analysis of selecting suitable green source among different spices (clove, cardamom, bay-leaf; common name) based on its total phenolic content (TPC), flavonoid content (TFC), tannin content (TTC) and antioxidant property. The selected green source (clove) mediated iron nanoparticles was then utilized for degradation of crystal violet dye, and its efficiency was compared with the other green source mediated iron nanoparticles. **Chapter 4** analyzes better solvent for extraction of polyphenols, flavonoids, tannins and its antioxidant property from clove as green source. Moreover, optimization of maximum phenolic and flavonoid content of the clove extract was carried out by controlling parameters such as time of extraction, extraction temperature, and volume of extraction solvent. **Chapter 5** presents the morphological and chemical property dependency of synthesized Fe NPs with pH. This chapter also investigates the photoluminescence behavior of synthesized Fe NPs towards the heavy meal ion sensing ability. The Fe NPs was found to act as a better Fe^{3+} ion detector within a linear range of micromolar, in presence of other heavy metal ions. Its efficiency was studied in presence of real life water samples collected from IIT Guwahati campus, India. **Chapter 6** describes the preparation of the clove extract mediated Fe NPs embedded pH responsive polymeric membrane for reducing nitobenzene to aniline present in wastewater. The nitrobenzene reduction process was maximized by optimizing the controlling parameters such as time, medium pH, iron NPs content. Furthermore the membrane was also utilized for studying the fluoride rejection behaviour. **Chapter 7** investigates the effectivity of clove extract in preparing iron-aluminium bimetallic

nanocomposite and its application towards removing fluoride and enhancing overall quality of real life water collected from North east regions of India. **Chapter 8** describes the dual activity of such green synthesized iron-aluminum nanocomposite by investigating it heavy metal sensing ability in real life water sample. In presence of various heavy metals the nanocomposite was found to be effective in detecting Fe^{3+} ion, and showed linear range of applicability for real life water collected from college campus IIT Guwahati, India. Finally, **Chapter 9** contains the inferences drawn from various chapters presented in this thesis and some suggestions towards scope for future work.

Chapter 2

Experimental methods and Characterization techniques

Chapter 2

Experimental methods and characterization techniques

This chapter gives a complete description of the experimentation involved in the preparation and characterization of green extracts. The chapter also provides information regarding the materials used for the preparation of green extracts and methods for analyzing and quantifying its total polyphenolic and flavonoid content. Optimization of process parameters utilizing central composite design (CCD) of experiments and response surface methodology (RSM) utilizing analysis of variance (ANOVA) for obtaining better polyphenolic and flavonoid content in the green extract has also been discussed. This chapter also provides analysis techniques for studying the total tannin content and antioxidant property of the green extracts. The chapter presents the detail of instruments used for the characterization of green extracts and green synthesized nanomaterials like FTIR, FESEM, TEM, TGA, HPLC, XRD, UV-VIS spectrophotometer, and Fluorescence spectrophotometer. This chapter provides a vivid idea about analyzing and quantifying various components in the green extract, and characterization techniques of green synthesized nanomaterials which were further utilized for applications in the next chapters.

2.1. Materials

The base green sources utilized for preparing extracts are clove (*Syzygium aromaticum*), cardamom (*Elettaria cardamomum*), and bay leaf (*Laurus nobilis*). Various solvents utilized for extraction are methanol and ethanol and millipore deionized water. Various analytical grade chemicals were utilized for analysis of polyphenolic, flavonoid, tannin,

and antioxidant potential properties of the green extract. The list of chemicals utilized is provided in Table 2.1. Millipore deionized water was utilized throughout all the experiments, and all the chemicals were utilized without anys further purification.

Table 2.1: Chemicals used in this thesis work

Sr. No	Chemical specification	Brand
1.	Clove, cardamom, bay leaf	The local market of Indian Institute of Technology Guwahati, Assam, India
2.	Magnesium powder ($\leq$ 99% purity)	Sigma-Aldrich Co., USA
3.	Absolute ethanol (99% purity)	Loba Chemie, India
4.	Iron (III) chloride ($FeCl_3$)	Otto Chemie, India
5.	Sodium hydroxide (NaOH)	Loba Chemie, India
6.	Concenrated hydrochloric acid (HCl, 99%)	Otto Chemie, India
7.	Methanol (synthesis grade, 98%)	Loba Chemie, India
8.	Folin-Ciocalteu's phenol reagent	Sigma-Aldrich Co., USA
9.	Gallic acid (analytical grade, 98%)	Sigma-Aldrich Co., USA
10.	Aluminum chloride ($AlCl_3$)	Sigma-Aldrich Co.,USA
11.	Sodium nitrite ($NaNO_2$)	Otto Chemie, India
12.	Quercetin (analytical grade, 98%)	Sigma-Aldrich Co., USA
13.	Rutin (analytical grade, 98%)	Sigma-Aldrich Co., USA
14.	Vanilin (analytical grade, 98%)	Sigma-Aldrich Co., USA
15.	Catechin (analytical grade, 98%)	Sigma-Aldrich Co., USA
16.	2, 2-diphenyl-1-picrylhydrazil (DPPH)	Sigma-Aldrich Co., USA
17.	Sodium acetate (purity, 98%)	Otto Chemie, India

18.	Sodium carbonate (Na_2CO_3) (analytical grade)	Sigma-Aldrich Co. USA
19.	Acetic acid (CH_3COOH)	LOBA Chemie, India
20.	Manganese chloride ($MnCl_2$)	Merk, Germany
21.	Mercury(II) chloride ($HgCl_2$)	Merk, Germany
22.	Cadmium chloride ($CdCl_2$)	Merk, Germany
23.	Lead(II) chloride ($PbCl_2$)	Merk, Germany
24.	Copper(II) chloride ($CuCl_2$)	Merk, Germany
25.	Sodium sulphate (Na_2SO_4)	Sigma-Aldrich Co. USA
26.	Sodium chloride (NaCl)	Sigma-Aldrich Co. USA
27.	Calcium chloride ($CaCl_2$)	
28.	Potassium bicarbonate ($KHCO_3$)	Sigma-Aldrich Co. USA
29.	Sodium fluoride (NaF)	Sigma-Aldrich Co. USA
30.	2,4,6-tripyridyl-s-triazine (TPTZ)	Sigma-Aldrich Co. USA
31.	Iron (II) sulfate ($FeSO_4$) (98% purity)	Loba Chemie, India
32.	Potassium bromide (FTIR grade, 99%)	Loba Chemie, India
33.	Polyethylene glycol methyl ether (PEGME) (M_w=5000 Dalton)	Sigma-Aldrich Co. USA
34.	Humic acid (analytical grade)	Sigma-Aldrich Co. USA
35.	Crystal violet dye (98% purity)	Loba Chemie, India

2.2. Preparation of powdered samples from *Syzygium aromaticum* (clove), *Elettaria cardamomum* (cardamom), and *Laurus nobilis* (bay-leaf)

The obtained clove, cardamom, and bay leaf were first washed several times with deionized millipore water to remove any particulate matter or contaminants and kept for

air-dry around 24 h. The three plant sources were then kept in a hot air oven for another 48h, and then ground to powder through grinder machine and further sieved and stored in hot air oven maintained at 60 ºC for further use.

2.3. Qualitative analysis of polyphenol and flavonoids

The three different green sources (common name- clove, cardamom, bay leaf) were first tested for the presence of polyphenols and flavonoids. After confirming their presence experiments were conducted for maximizing the extraction of polyphenols and flavonoids through quantification tests. The below three tests were carried out to detect the presence of polyphenols, and flavonoids in the three green sources.

2.3.1. Shinoda's test for flavonoids

In this test 5 mg, each of the raw materials in dried form was taken and dissolved in about 8-10 mL of ethanol. To the filtered solution, about 3 mg of magnesium powder was added followed by a few drops of concentrated HCl. An occurrence of orange color indicates the presence of flavonoids in the extracts.

2.3.2. Ferric chloride test for flavonoids

This test involves dissolving about 5 mg of dried raw materials each in ethanol (2 mL). After dissolving, it was filtered and, a few drops of 10% ferric chloride solution were added. After adding the ferric chloride solution occurrence of a green-blue coloration indicates the presence of phenolic hydroxyl group in the extracts.

2.3.3. Sodium hydroxide test for flavonoids

For conducting this test, dried powdered raw materials about 5 mg were dissolved in water, warmed, and filtered. 2 mL of 10% aqueous sodium hydroxide was added to the

filtered solution. After mixing the solutions, a yellowish-orange coloration is expected to occur, which on the addition of dilute hydrochloric acid turns the solution colorless. Such a color change indicates the presence of flavonoids.

2.4. Preparation of aqueous green extracts

During the preparation of the extract, 10g of each dried green source powder was taken and stirred slowly to about 40 ml of deionized water, methanol, and ethanol respectively. The solution was then kept on a magnetic hot plate stirrer at a moderate speed of 100 rpm with the temperature maintained at 60 ºC. It was taken care of that the heating temperature should not be very high since it might result in degradation of various useful polyphenolic components. At the end of 1h, it was noticed that all the powder materials settled at the bottom, for all the three extracts and the solution just starts to boil. The extraction process was stopped at this moment and the solution was kept to cool down at atmospheric conditions. The solution was then filtered out by normal grade filter paper, and the extracts were stored at 10ºC in a refrigerator for further quantitative analysis of their polyphenolic and flavonoid content.

2.5. Quantitative analysis of phenolic and flavonoid content of green extracts

2.5.1. Total polyphenolic content (TPC)

Total polyphenolic content of the green extracts was estimated by using Folin-Ciocalteu's phenol reagent (FCR) according to the method described by Singleton et al. [213] with slight modifications. Approximately 0.3 mL extracts were mixed with 1.8 mL of Folin-Ciocalteu's reagent and allowed to stand at room temperature for 5 minutes, and then 1.2 mL sodium carbonate (7.5%, w/v) solution was added to the mixture. The blank sample

was prepared by replacing 0.3 mL of the extract with 0.3 mL of distilled water. After standing for 60 min at room temperature, absorbance was measured at 765 nm using a spectrophotometer. Gallic acid was used as standard and results were expressed as mg gallic acid equivalents (GAE)/ g sample.

2.5.2. Total flavonoid content (TFC)

The flavonoid content of green extracts was determined using the aluminum chloride method described in literature with slight modifications [214]. 1 mL of extract followed by 0.3 mL of 5% (w/v) sodium nitrite solution and 4 mL of 80% (v/v) methanol were mixed for 5 minutes, and subsequently 0.3 mL of 10% (w/v) aluminium chloride solution was added and mixed. After 6 min, 3 mL of 1 (M) of sodium hydroxide solution was added. Immediately, the volume of the reaction mixture was made up to 10 mL with distilled water. The mixture was thoroughly vortexed and the absorbance was measured at 510 nm. Based on the standard curve prepared with rutin, the concentrations of TFC in the extracts were expressed as mg rutin equivalents (RU)/ g sample.

2.5.3. Total tannin content (TTC)

The tannin contents or Proanthocyanidin was determined by the method mentioned in literature with slight modification, using catechin as a reference compound [215]. A volume of 400µL of the extract is added to 3 mL of a solution of vanillin (4% in methanol) and 1.5 mL of concentrated hydrochloric acid. After 15 min of incubation, the absorbance was read at 500 nm. The condensed tannin was expressed as *g* catechin equivalents/100 *g* sample.

2.6. Determination of antioxidant capacity

2.6.1. DPPH Scavenging assay (%)

For studying the 2, 2-diphenyl-1-picrylhydrazil (DPPH) free radical scavenging activity of the green extracts a similar protocol as suggested in literature was followed with slight modifications [216]. The samples were prepared by mixing about 0.5 mL of green extract to 3 mL of absolute ethanol and 0.3 mL of DPPH solution (0.5 mM solution of DPPH prepared in ethanol). The mixture was shaken vigorously and kept in dark for 70 min to allow the scavenging process, where the purple color changes to yellow. Separately a control sample was prepared by mixing 3.5 mL of ethanol and 0.3 mL of 0.5 mM DPPH solution. The absorbance was then measured at 517 nm against a blank (a mixture of ethanol 3.3 mL and 0.5 mL of extract). Both the sample and the control were measured against the prepared blank solution. The capability of scavenging the free radical DPPH by the extracts in percentage was calculated by;

$$\% \text{ DPPH (scavenging)} = (A_0 - A_1)/A_0 \times 100 \quad (2.1)$$

Where A_0 denotes the absorbance of control; A_1 denotes the absorbance of the sample.

2.6.2. Ferric reducing antioxidant potential (FRAP) assay

The antioxidant activity of the green extracts was analyzed through ferric reducing antioxidant potential assay by following the modified Benzie and Strain method [217]. The FRAP reagent was prepared at pH 3.6 using 300 mM acetate buffer (3.1g sodium acetate, and 16 mL acetic acid), 10 mM TPTZ (2,4,6-tripyridyl-s-triazine) solution in 40 mM hydrochloric acid solution, and 20 mM $FeCl_3.6H_2O$ solution in distilled water. About 25 mL of acetate buffer and 2.5 mL of TPTZ were mixed with 2.5 mL $FeCl_3.6H_2O$ solution. About 40 µL of the green extract was allowed to react with 3 mL of FRAP

solution in dark conditions for 40 min. The absorbance intensity of the samples was measured at 593 nm. The standard reference of the calibration curve was obtained by using 200-1000 µM $FeSO_4$ solution. The analyzed results were expressed in terms of µM Fe(II)/ g dry sample.

2.7. Green synthesis of Iron nanoparticles (Fe NPs)

For the preparation of Fe NPs, 0.025 (M) $FeCl_3$ solution was prepared with millipore deionized water. The extracts of clove, cardamom, and bay leaf about 40 ml were taken in three different beakers of 100 ml capacity. About 10 ml of the prepared 0.025 (M) $FeCl_3$ solution was added to each extract of 40 mL and the mixture was kept on a magnetic hot plate stirrer with the temperature maintained at 80 ºC and stirring speed at 200 rpm. The color of the mixture with time changed to brownish-black indicating the formation of NPs, and at the same time, the pH of the three mixtures was maintained at 6.9±0.5. The process was stopped after 15 min of reaction and was kept under the atmospheric condition for another 20 min. The black precipitated solution formed which was further centrifuged at 3000 rpm and the residue was then dried by vacuum oven at 100 ºC for 24h.

2.8. Dye degradation study

The dye degradation study of the cationic dye (crystal violet) was carried out using the three Fe NPs prepared from clove, cardamom, and bay-leaf extract. In a 100 ml conical flask, about 40 mL of 100ppm crystal violet dye was taken and to it, 1.25 g/L dosage of three different Fe NPs was added. The mixture was then kept in a shaker at 200 rpm for 2h at 25 ºC. After every 10 min interval, the respective three samples were collected through a syringe filter to avoid any Fe NPs presence and analyzed through UV analysis for measuring respective sample dye concentration.

2.9. Response surface methodology (RSM) and Central composite design (CCD) for optimizing parameters

Response surface methodology (RSM) is an effective statistical tool for optimizing complex processes because it suggests easy as well as the efficient arrangement and interpretation of experiments compared to other methods [60, 61]. RSM is a collection of mathematical and statistical techniques for building an empirical model. Through the design of experiments, the response (output variable) was optimized which is influenced by several independent variables (input variables). The design of the experiment consists of a series of tests, called run where the input variables are changed to record the reasons for a change in output response. The application of RSM to design optimization is aimed at reducing the cost of expensive analysis methods (e.g. finite element method or CFD analysis) and their associated numerical noise. Such associated limitations can be overcome by using smooth functions that improve the convergence of the optimization process since they reduce the noise effect and allow the use of the derivative-based algorithm.

In statistics, a central composite design is an experimental design, useful in response surface methodology, for building a second-order (quadratic) model for the response variable, omitting the need to use a complete three-level factorial experiment. It is considered to be the most popular class of second-order designs. It has been extensively utilized by several researchers for optimization purposes [68]. The design consists of three distinct sets of experimental runs:

1. A factorial design in the factors studied, each having two levels.

2. A set of center points, experimental runs whose values of each factor are the medians of the values used in the factorial portion. This point is often replicated to improve the precision of the experiment.
3. A set of axial points, experimental runs identical to the center points except for one factor, which will take on values both below and above the median of the two factorial levels, and typically both outside their range. All factors are varied in this way.

In our study Design Expert Software, 9.0 was utilized for carrying out the optimization process utilizing RSM and CCD combination. The central composite design was selected for designing the experiments to maximize total phenolic and flavonoid content from green source extracts, by optimizing the variables such as time of extraction, temperature, and volume of the aqueous solution. The number of conducted experiments was calculated as following [218]:

$$N=2^k + 2k + n_c \quad (2.2)$$

Where k is the number of variables and n_c is the number of central points. The statistical models give a better insight into the complex, mutually influencing system of variables, the structure of the interactions, and the level of influence on the overall system [27, 28]. Moreover, statistical models also identify the most and least influential variables [29]. In our study, the selected quadratic model was used [30, 31].

$$y = \beta_0 + \sum_{i=1}^{2} \beta_i x_i + \sum_{i=1}^{2} \sum_{j=1}^{2} \beta_{ij} x_i x_j + \sum_{i=1}^{2} \beta_{ii} x_i^2 + \varepsilon \quad (2.3)$$

Where β_0 is a constant coefficient, ε represents the error, x_i and x_j are independent variables. β_i, β_{ii}, and β_{ij} represent coefficients of linear, quadratic, and interaction effects, respectively. The model was verified by statistical tests, e.g., analysis of variance (ANOVA), residuals analysis (RA), scaling residuals (SR), and prediction error sum of

squares (PRESS) [218]. The verified and validated model was applied to optimize the input variables and to maximize the output response.

2.10. Characterization techniques

2.10.1. Microscopic morphological analysis

Morphological analysis of green synthesized nanomaterials was performed by Field Emission Scanning Electron Microscope (FESEM, Make: Zeiss Model: Sigma, Germany) at 3 kV equipped with an energy dispersive X-ray (EDX) which was performed at 15 kV for analyzing the elemental composition. For both the FESEM and EDX analysis the powder nanomaterials were first dispersed in methanol solution (1:20 w/v ratio) through an ultrasonication process for 20 min. The dispersed solution of about 200 µL was then dropped cast on a 2×2 cm^2 glass plate covered with aluminum foil and then placed in a hot air oven at 60 ºC for removing methanol. The sample before analysis was coated with a thin gold layer.

Microscopic observation was also done by Transmission Electron Microscope (TEM, Make: Jeol, Model: JEM 2100, Japan) with an acceleration voltage of 20 kV. The powdered nanomaterial was first dispersed in methanol (99% purity) similar to as discussed in the previous paragraph. The dispersed sample was then drop cast about 100 µL on a TEM copper grid with carbon mesh and allowed to dry in an air oven at 60 ºC for removing methanol.

2.10.2. Optical analysis

To analyze the surface plasmon resonance of prepared green synthesized nanomaterials UV-Vis Spectrophotometer was utilized (Model No.: UV-2600, Make: Shimadzu,

Singapore). The as-synthesized nanomaterials in solution were scanned for an absorption peak within a range of 200-800 nm wavelength.

The photoluminescence property of green synthesized nanomaterials was analyzed using Perkin-Elmer fluorescence spectrophotometer (model: LS 55, USA). The prepared nanomaterials were dispersed in millipore deionized water and also in various pH solutions respectively for studying its photoluminescence property. The samples were then scanned over 320-420 nm with an increment of 10 nm.

2.10.3. Fourier-transform infrared (FTIR) spectroscopy

Fourier transform infrared (FTIR) spectroscopy analysis of the prepared nanomaterials was analyzed using FTIR Spectrometer (IRAffinity-1, Shimadzu, Japan). The synthesized nanomaterial powder was mixed with dried KBr powder (99% purity) in the ratio 1:10 w/w and formed a palette. The palette was then utilized for FTIR analysis with 30 numbers scans and apparatus resolution was set at 4.

2.10.4. Photon correlation spectroscopy (PCS)

The hydrodynamic size distribution and zeta potential of the synthesized green nanomaterials were performed by PCS (Delsa nano, Beckman Coulter, Switzerland). For analyzing hydrodynamic size distribution the powder samples were dispersed in methanol (1:20 w/v) utilizing an ultrasonication bath for 20 min at 30ºC. For studying the zeta potential analysis the powdered samples were mixed with Millipore deionized water in the ration (1: 10 w/v).

2.10.5. Thermo-gravimetric analysis (TGA)

Thermal stability analysis was performed by TGA instrument (Model No: TG 209 F1 Libra; Make: Netzsch, Germany), type of crucible: DSC/TG pan Al_2O_3. Argon was used

as both protective and purge gas at the flow rate of 20 ml/min and 60 ml/min, respectively. The temperature program was set from 23 °C to 1000 °C at an increment of 10 °C/min.

2.10.6. Powder X-Ray diffraction (XRD)

X-ray diffraction (XRD) patterns of the powder samples were analyzed using an XRD instrument (Make: Bruker, D8 Advance Model, Netherlands) equipped with monochromatic Cu Kα radiation (λ = 0.154 nm) operated at 40 mA and 40 kV. The 2θ value ranged from 10º to 80 º with a step time of 0.5 s.

2.10.7. High-Pressure liquid chromatography (HPLC)

High-Pressure Liquid Chromatography (Make: Shimadzu; UV-detector of deuterium lamp SPD- 20A, Singapore) was utilized for analyzing different components in plant extract and nitrobenzene reduction study. For analyzing the flavonoid components and quantifying their value, about 20µl of samples were injected into the C-18 column (10 × 4 mm) and analyzed at 280 nm. Methanol: water (70:30 v/v) was used as the mobile phase at the flow rate of 1 ml/min. A similar process was also followed for studying the nitrobenzene, and aniline quantification.

2.10.8. Fluoride analysis

The fluoride concentration of the collected samples from different regions of Assam was measured with a multi-parameter analyzer (CONSORT- C863, Made in Belgium) aided with a fluoride electrode. A known concentration fluoride sample ranging from 10 ppm to 100 ppm was first calibrated utilizing the multi-parameter analyzer. The unknown fluoride-containing samples were then analyzed. Samples preparation includes mixing of the fluoride solution with a total ionic strength adjustment buffer (TISAB) in the ratio 1:5 (v/v).

Chapter 3

Preparation of green synthesized Fe-NPs utilizing green extracts of *Syzygium aromaticum* (clove), *Elettaria cardamomum* (cardamom), *Laurus nobilis* (bay leaf) and investigating its dye degradation efficiency

Piyal Mondal, Mihir Kumar Purkait. Preparation and characterization of green synthesized zero-valent Fe NPs from *Syzygium aromaticum* (clove), *Elettaria cardamomum* (cardamom), *Laurus nobilis* (bay leaf) and investigating its dye degradation efficiency (submitted to Chemosphere Journal)

Preparation of green synthesized Fe-NPs utilizing aqueous extracts of *Syzygium aromaticum* (clove), *Elettaria cardamomum* (cardamom), and *Laurus nobilis* (bay-leaf) and investigating its dye degradation efficiency

This chapter provides a detailed investigation of choosing better aqueous extract from three different green sources such as clove, cardamom, and bay-leaf. The extracts were screened in terms of total polyphenolic content, flavonoid content, tannin content and antioxidant properties. The qualitative analysis of all the three extracts showed the presence of polyphenols, flavonoids. Among others, aqueous extract of clove was found to have higher content of polyphenols, flavoinoids and tannins. The antioxidant study of clove extract also proved to be better than other green sources. Iron (Fe) NPs were prepared utilizing the three green extracts and were characterized by UV-Vis Spectroscopy, FESEM, EDX, TEM, XRD, FTIR to provide insights about the morphological and surface functional groups coating of the prepared ZVI NPs. UV-Vis spectroscopy shows the surface plasmon resonance of the prepared Fe NPs and confirmed the π-π and n-π* electronic transition of sp^2 hybridized carbon of the polyphenolic groups. The total phenolic, flavonoid and tannin content of the clove extract was found to be the highest among other extracts and the values obtained were 130.75±4.57 mg rutin/g sample, 59.56±2.5 mg gallic acid/g sample, and 3.46±0.15 g gallic acid/100g sample respectively. Antioxidant activity of the clove extract measured by DPPH scavenging and FRAP assay test showed the antioxidant property of the extract was better than other*

extracts. The TEM and FESEM analysis confirmed the spherical nanosized shape of iron particles, whereas FTIR spectroscopy confirmed the impregnation of the polyphenolic and aromatic fumctional groups present in green extracts over the Fe NPs. XRD analysis showed the formation of zero-valent iron along with its various oxide form, and confirmed the core shell structure of the formed ZVI NPs with ZVI in the core and oxides on the outer shell. Crystal violet dye degradation was found to be highest for clove extract mediated ZVI NPs about 83.8% whereas it decreased for cardamom and bay-leaf mediated ZVI NPs to 79.8% and 68% respectively. Pseudo second order reaction kinetic model better fitted the degradation process and was found to enhance with decreasing pH.

3.1. Experimental

3.1.1. Materials

Clove, cardamom, and bay-leaf were selected as green sources. Millipore de-ionized water were utilized as extraction solvent. Folin-Ciocalteu's reagent, rutin, gallic acid, vanillin, catechin, quercetin, Na_2CO_3, NaOH, and conc. HCl were utilized for analyzing total phenolic, flavonoid, and tannin content. DPPH, CH_3COOH, CH_3COONa, TPTZ, and $FeCl_3.6H_2O$ were used for measuring antioxidant potential. Crystal violet dye, was utilized to study the dye degradation study. The details of all the chemicals used are mentioned in Table 2.1 of Chapter 2.

3.2. Results and discussion

3.2.1. Qualitative analysis of polyphenolic and flavonoid content of green extracts

The qualitative analysis of the three green sources (preparation already discussed in Chapter 2) when analyzed for the presence of polyphenols and flavonoids showed positive

results for all the three tests namely Ferric chloride test, Shinoda's test, and Sodium hydroxide test. From Figure 3.1(a) it was observed that during Ferric Chloride test (discussed in Chapter 2), all the three extracts color changed to bluish green which confirmed the presence of polyphenols in all the extracts.

Shinoda's test (discussed in Chapter 2) confirmed the presence of flavonoids as shown in Figure 3.1(b). It depicted that all the three extracts showed positive results during the test, where an orange coloration confirmed the presence of flavonoids.

Similarly, Figure 3.1 c(i) depicts that during Sodium hydroxide test for flavonoids presence (discussed in Chapter 2) the extract turned yellowish on addition of NaOH solution due to a chemical complex formation. Further Figure 3.1 c(ii) shows on addition of dilute hydrochloric acid the chemical complex bond breaks and the solution turns colorless [210]. The formation of yellowish coloration and its colorless transformation confirms the presence of flavonoids in all the three extracts.

Hence the performed tests confirmed that the three extracts from clove, cardamom, and bay-leaf showed the presence of polyphenolic compounds, and flavonoids which are very essential components to be used as reducing and stabilizing agents towards nanoparticle synthesis.

3.2.2. Quantitative analysis of total phenolic content (TPC), total flavonoid content (TFC), total tannin content (TTC), and antioxidant properties of green extracts

In order to choose a better green extract to be used as a reducing agent for synthesizing Iron (Fe) nanoparticles, flavonoids, phenolic and tannin content plays a vital role.

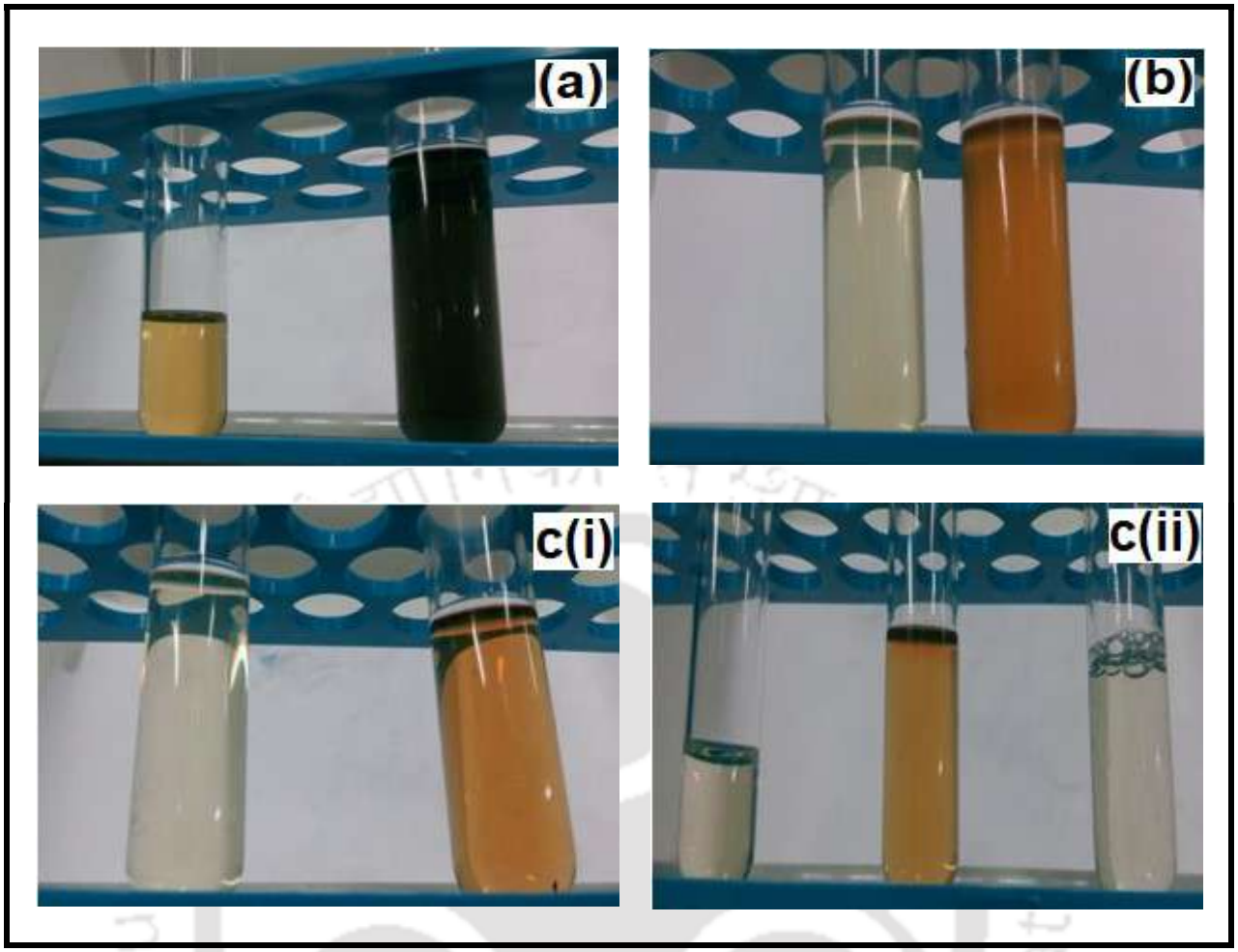

Figure 3.1: (a) Ferric chloride test for polyphenols (b) Shinoda's test for flavonoids (c) Sodium hydroxide test for flavonoids

From Table 3.1 it was observed that the TPC, TFC and TTC amount (experimental procedure discussed in Chapter 2) in clove extract was the highest about 130.75±4.57 mg rutin/g sample, 59.56±2.5 mg gallic acid/ g sample and 3.46±0.15 g gallic acid/100g sample respectively among the cardamom and bay-leaf extract. Since the phenolic, flavonoid, and tannin contents were higher in clove extract, hence it was evident that the antioxidant capacity of clove extract would be better than other extracts [205].

From Table 3.1 it was found that the DPPH scavenging property of clove extract was highest about 86.7±4.8 % along with highest FRAP assay of 48.45±2.7µM Fe(II)/g dry sample. Thus from the obtained results it could be concluded that among the three extracts, based on phenolic content, flavonoid content, tannin content, and antioxidant

potential, clove extract was more suitable reducing agent to be utilized as a green source for synthesizing Iron (Fe) nanoparticles [213].

Table 3.1: Comparative analysis of phenolic, flavonoid, tannin, and antioxidant potential for aqueous extract of clove, cardamom, and bay-leaf

Parameters	Clove extract	Cardamom extract	Bay-leaf extract
Total phenolic content (mg rutin/g sample)	130.75±4.57	96.67±3.7	75.32±2.9
Total flavonoid content (mg gallic acid/g sample)	59.56±2.5	41.3±2.2	32.5±1.8
Total tannin content (g gallic acid/100g sample)	3.46±0.15	2.97±0.18	2.74±0.12
DPPH scavenging (%)	86.7±4.8	70.5±3.7	65.5±2.9
FRAP assay	48.45±2.7	33.27±2.3	25.07±1.4

3.2.3. UV-Vis analysis of green synthesized iron NPs

As discussed in Chapter 2 about the preparation of Fe NPs utilizing green extracts of clove (Fe NPs_CL), cardamom (Fe NPs_CD), and bay-leaf (Fe NPs_BL), it was observed from Figure 3.2 (a) that the precursor salt $FeCl_3$ (0.025M) solution produced an absorption peak at 300 nm. Whereas 1:1 mixture of precursor salt and green extracts which produced green synthesized Fe NPs showed a modified absorption peak at 230nm, and 280nm respectively (Figure 3.2b). The shift in absorption peak confirmed that the Fe NPs got coated with the plant biomolecules as discussed in previous section due to the presence of phenolics and flavonoid compounds in the three extracts [211, 212]. Moreover, the absorption peak at 230 and 280 nm confirmed the π-π^* and n-π^* electronic transition of sp^2 hybridized

carbon of the polyphenolic groups present in the green extracts [219]. Among the other green extracts, clove extract mediated Fe NPs (Fe NPs_CL) showed strong absorption peak at 230, 280 nm which confirmed the efficient synthesis of Fe NPs due the presence of higher phenolic, flavonoid and antioxidant potential in clove extract [219].

The clove extract through UV analysis was found to have higher absorption peak at 280 nm when the pH was maintained at 4 which could be denoted due the better n-π* electronic transition of sp^2 hybridized carbon of the polyphenolic groups [211,219]. Optimization of precursor salt and clove extract mixture ratio through UV analysis showed that 1:4 ratio yielded better synthesized stabilized Fe NPs since higher absorption peak was obtained at 230, and 280 nm. The further characterizations of the clove extract mediated Fe NPs were prepared utilizing the mentioned procedure.

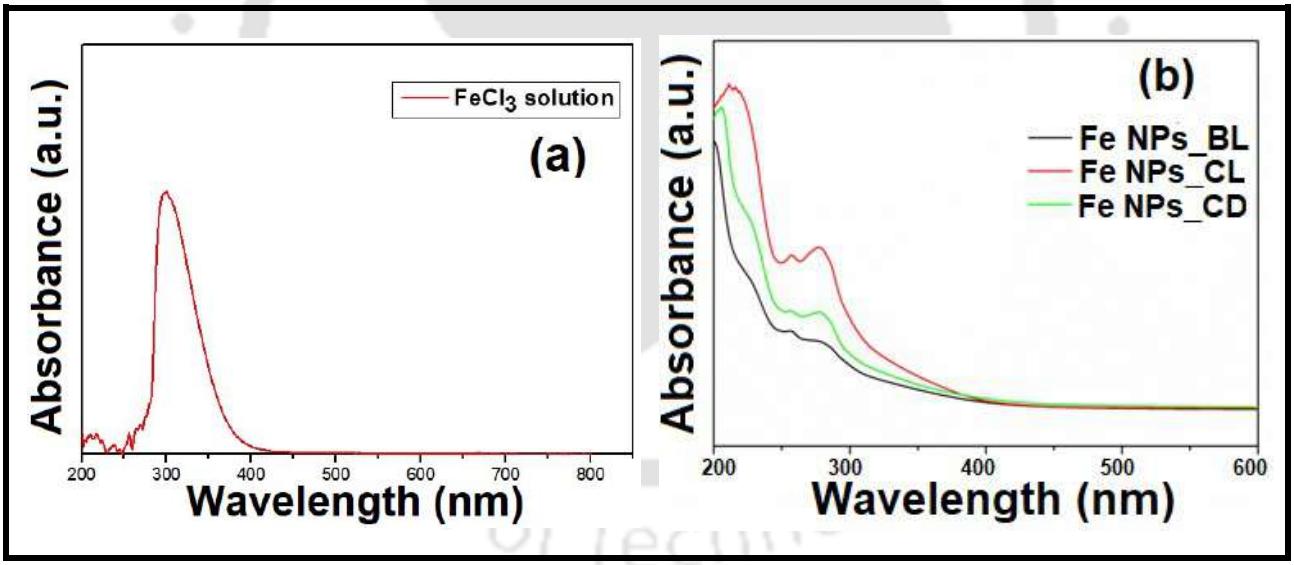

Figure 3.2: (a) UV absorbance of precursor $FeCl_3$ salt (b) UV absorbance of synthesized Fe-NPs from aqueous extract of clove, cardamom, and bay-leaf

3.2.4. FTIR analysis of green synthesized Fe NPs

The FTIR spectroscopy of Fe NPs synthesized utilizing clove, cardamom, and bay-leaf extract are shown in Figure 3.3 (a), (b), and (c) respectively. The spectroscopy analysis

confirmed presence of aromatic coatings over all the synthesized Fe NPs through observed peaks near 1320-1350 cm^{-1} (–C–OH stretching vibration), 1610-1630 cm^{-1} (–OH bending vibration), 2925-2980 cm^{-1} (aromatic –C-H stretch), and 3312-3630 cm^{-1} (–OH stretching vibration). Whereas, few peaks at 1720 and 2780 cm^{-1} denotes the presence of –C=O and carboxyl –OH groups only for clove extract Fe NPs. Moreover, common peaks were found near 679-921 cm^{-1} (denoted Fe-O bonds) and 1018-1446 cm^{-1} (Fe-OH bonds) for all the prepared Fe NPs.

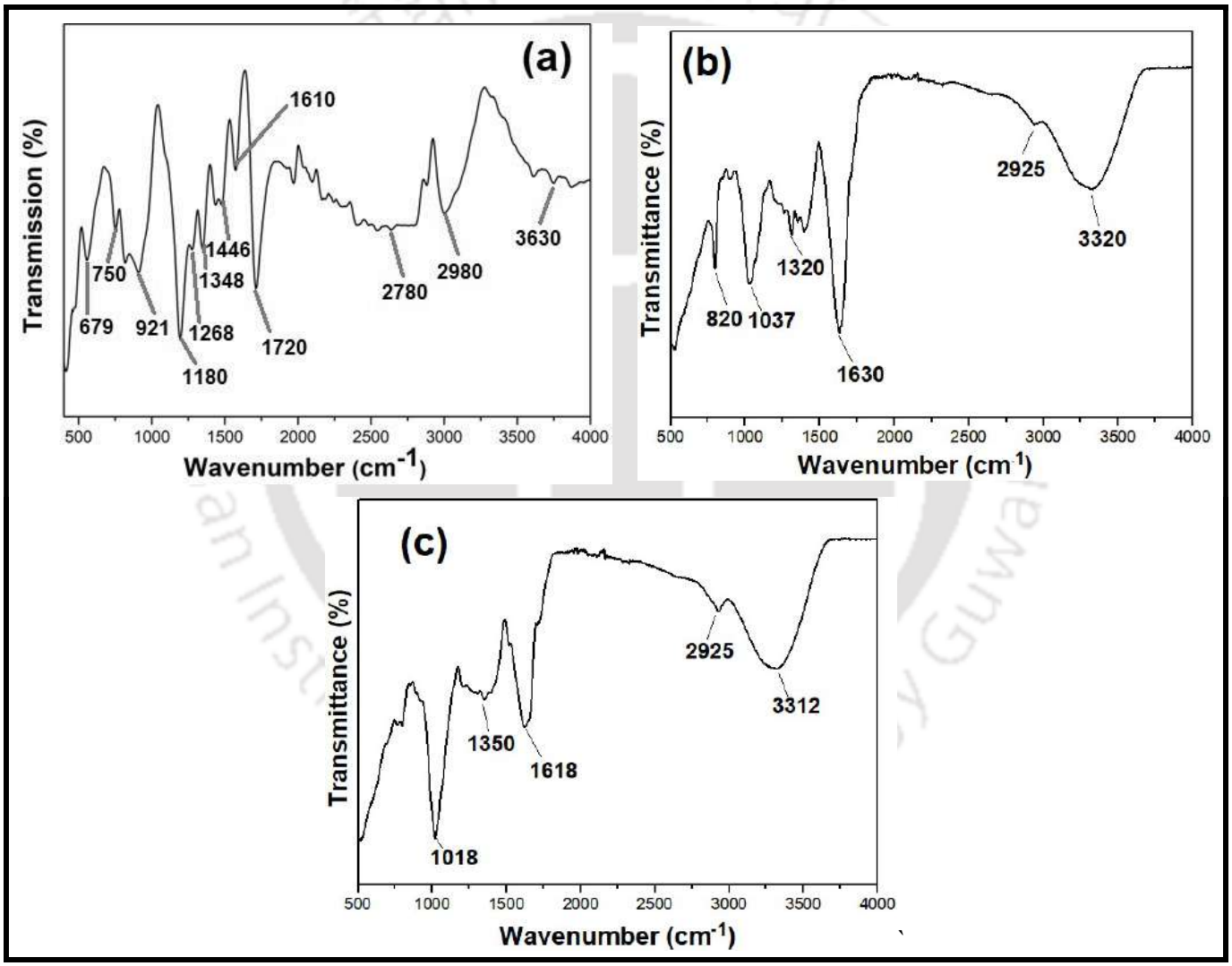

Figure 3.3: FTIR analysis of Fe-NPs prepared from (a) clove exract (b) cardamom extract and (c) bay-leaf extract

3.2.5. Morphological, elemental and stability analysis of green synthesized Fe-NPs

The TEM images of the green synthesized Fe NPs are shown in Figure 3.4 (a), (b), and (c) prepared from clove, cardamom, and bay-leaf extract respectively. Fe NPs synthesized from clove extract produced spherical nanosized particles with an average diameter of 8.46±0.6 nm, which was found to be the lowest among the Fe NPs synthesized utilizing cardamom and bay-leaf extracts, having average diameter of 15.46±0.4 nm, and 21.46±0.3 nm respectively. The aggregation of clove extract mediated Fe NPs were found to be the least, hence confirming better aromatic coating and stabilization producing lower average sized Fe nanoparticles.

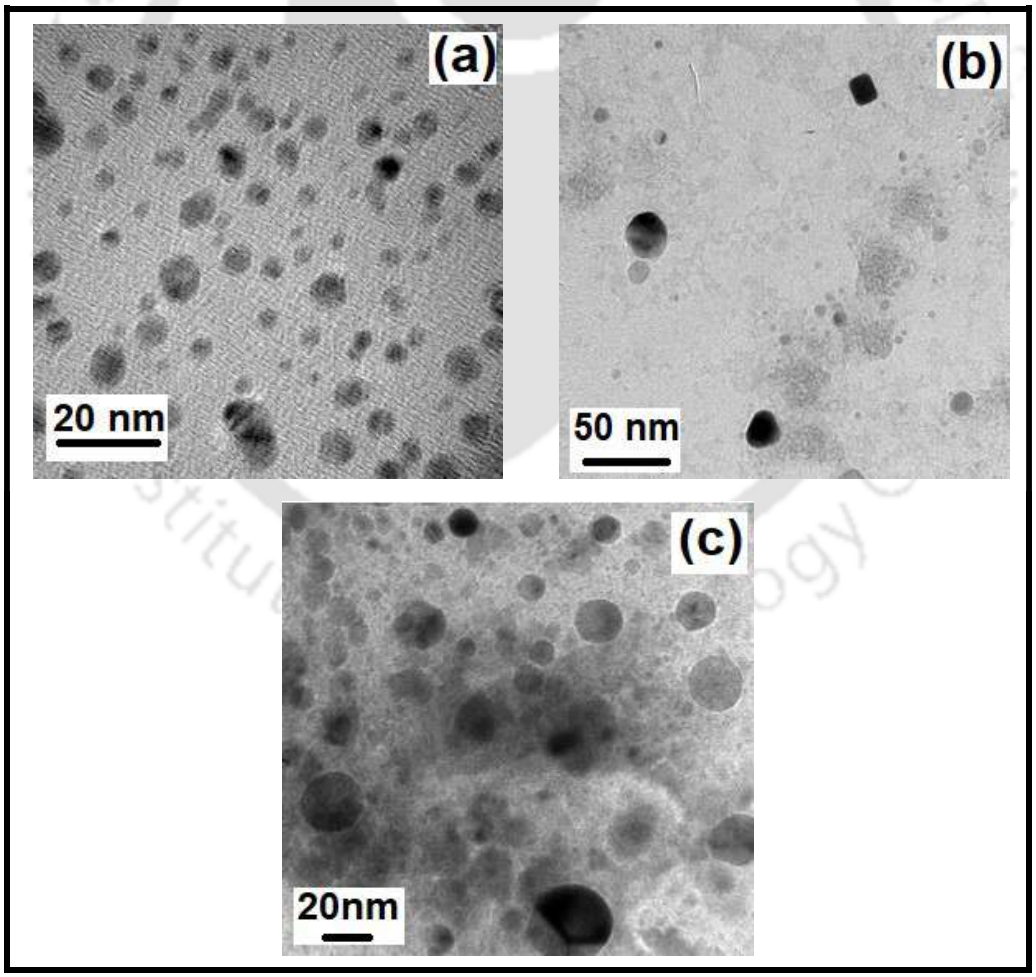

Figure 3.4: TEM analysis of Fe-NPs synthesized from (a) clove, (b) cardamom, and (c) bay-leaf extract

FESEM images of the synthesized Fe NPs from clove, cardamom, and bay-leaf extract as shown in Figure 3.5 (a), (b), and (c) respectively depicts that uniformly sized lower average diameter NPs were synthesized from clove extract, with less agglomeration. Moreover zeta potential analysis confirmed that clove extract mediated Fe NPs were more stabilized due to better aromatic coating having higher surface charge of -25.6 mV with respect to cardamom and bay-leaf extract having surface charge of -18.2 mV, and -15.4 mV respectively.

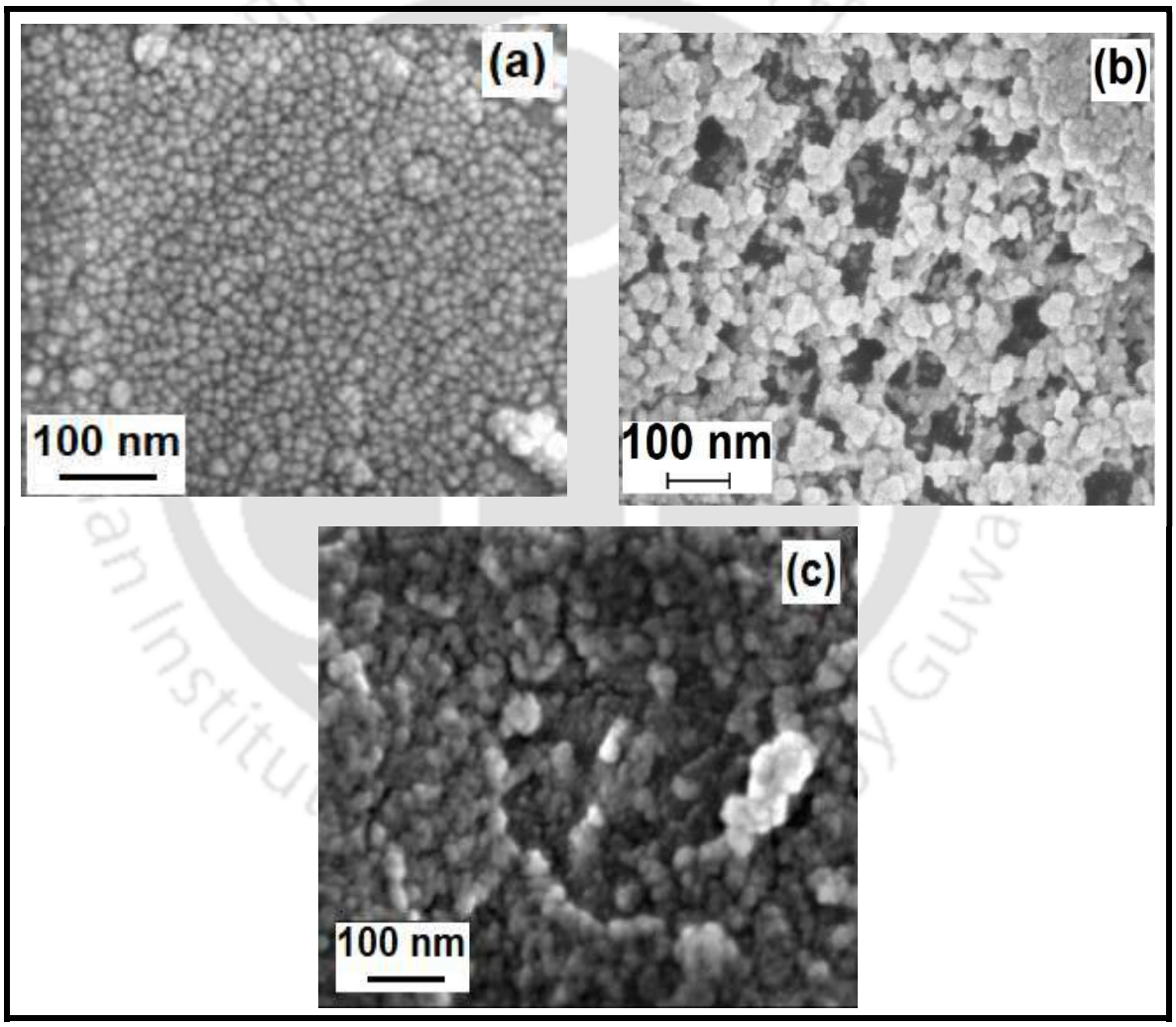

Figure 3.5: FESEM analysis of Fe-NPs synthesized from (a) clove, (b) cardamom, and (c) bay-leaf extract

The elemental analysis shown in Table 3.2 depicts that the Fe NPs synthesized from clove extract consisted least weight percentage of Oxygen (O), and highest weight percentage of Iron (Fe) with respect to other extracts. The obtained results confirmed that chance of formation of zero-valent iron was highest with less oxide formation due to higher Fe/O ratio obtained in clove extract mediated Fe NPs. Such results could be attributed due to the better aromatic coating provided by the clove extract since it possessed higher phenolic, flavonoid and antioxidant potential with respect to other extracts. Presence of Carbon (C) confirmed the aromatic coating of the extracts over the synthesized Fe NPs from all the three plant extracts. Chlorine (Cl) content was found in all the three Fe NPs synthesized from different extracts which was due to the precursor salt utilized for preparing Fe NPs. The results confirmed the formation of a core shell structure of synthesized Fe NPs with zero-valent iron in the core and oxide formation on the outer shell.

Table 3.2: Elemental analysis of Fe-NPs synthesized from clove, cardamom, and bay-leaf extract

Fe NPs	Elemental weight (%)			
	Carbon (C)	Iron (Fe)	Oxygen (O)	Chlorine (Cl)
Clove extract	45.8	29.1	13.5	11.6
Cardamom extract	42.8	19.4	27.2	10.6
Bay-leaf extract	39.6	11.2	40.8	8.4

3.2.6. XRD analysis of green synthesized iron NPs

XRD characterization of the green synthesized Fe NPs is shown in Figure 3.5 prepared from clove extract (FeNPs_CL), cardamom extract (FeNPs_CD), and bay-leaf extract (FeNPs_BL). The figure depicts that for FeNPs_CL zero-valent iron (Fe^0) existed corresponding to the 110, 200, and 211 planes accompanied with iron oxide states.

Whereas for FeNPs_CD and FeNPs_BL the Fe^0 content got reduced with increasing oxide state formation. The planes were confirmed from previous literature [220, JCPDS 65-4899]. It was observed that zero-valent iron and its oxide co-existed together for Fe NPs prepared from clove and cardamom extract, whereas for FeNPs_BL complete oxide formation took place. The existence of Fe^0 state was highest for FeNPs_CL, which confirmed clove extract being the better reducing and stabilizing agent among the cardamom, and bay-leaf extract which was evident from its higher phenolic, flavonoid, and antioxidant capacity. The results also confirmed the core shell structure of Fe NPs formed where Fe^0 state occupied the core position surrounded by oxide state on the outer shell, as discussed in elemental analysis Section 3.2.5.

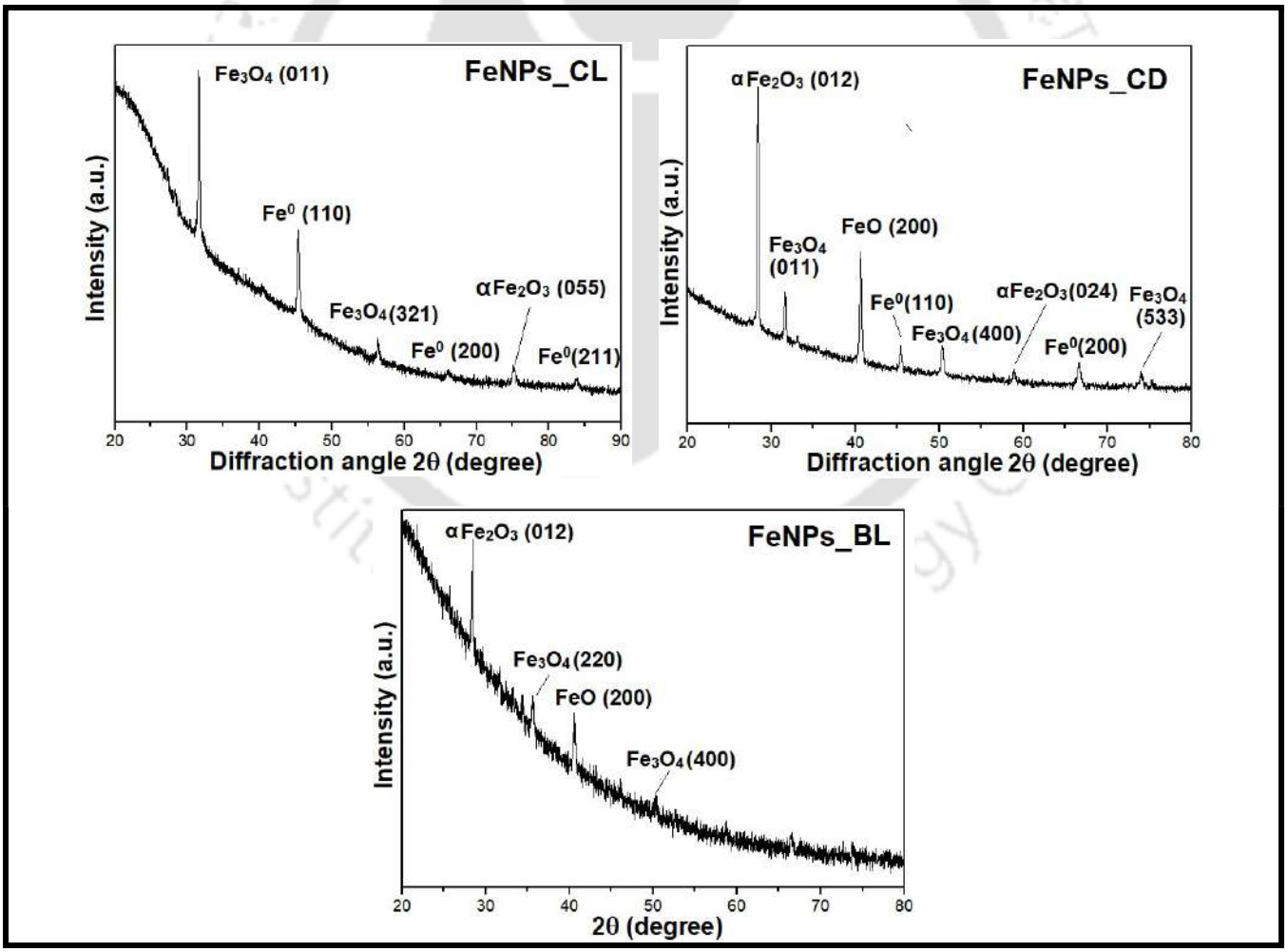

Figure 3.6: XRD analysis of Fe-NPs synthesized from (a) clove, (b) cardamom, and (c) bay-leaf extract

3.2.7. Dye degradation study

The green synthesized Fe NPs from different extracts were utilized to study the degradation of cationic dye (crystal violet). Figure 3.7(a) shows the dye concentration reduction (%) variation with time when 1.25 g/L dosage of Fe NPs were utilized. Clove extract mediated FeNPs_CL was found to reduce the dye concentration efficiently about 83.8% at pH 7 with respect to cardamom, and bay-leaf mediated Fe NPs which resulted into 79.88% and 63.75% dye degradation respectively. The absorption peaks at visible range 592 nm (denoted due to function group –C=N–), 247 nm and 300 nm (denoted due to the benzene like aromatic rings) were found to decrease with time indicating the cleaving of such bonds thus resulting in degradation of dye molecules [223]. Such result could be attributed to the fact that FeNPs_CL consisted of higher amount of aromatic coating (consisting of phenolic, flavonoid, and tannin content) along with zero-valent iron with respect to its oxide state with respect to FeNPs_CD, and FeNPs_BL. Since zero-valent iron along with aromatic coating plays a vital role due to its better reducing property hence FeNPs_CL was found to degrade the crystal violet dye more efficiently than the other green extract mediated Fe NPs [220]. Figure 3.7(b) shows the trend of dye degradation (%) in presence of FeNPs_CL with varying pH. The highest dye degradation of 91.1% was obtained at pH3, while with increasing pH at 7 and 12 the dye degradation value decreases to 83.8%, and 72.2% respectively. Such results depict that at lower pH, the zero-valent state of FeNPs_CL predominates over the oxide state, enhancing the reducing activity, while at higher pH the oxide state formation predominates reducing the dye degradation activity.

The fitting of reaction kinetics data of the dye degradation study at varying pH for FeNPs_CL were shown in Figure 3.8(a), and (b) for pseudo-first-order and pseudo-second-order kinetic models respectively. It was observed that pseudo-second-order

reaction kinetic model better fitted the dye degradation data for varying pH with better R^2 values.

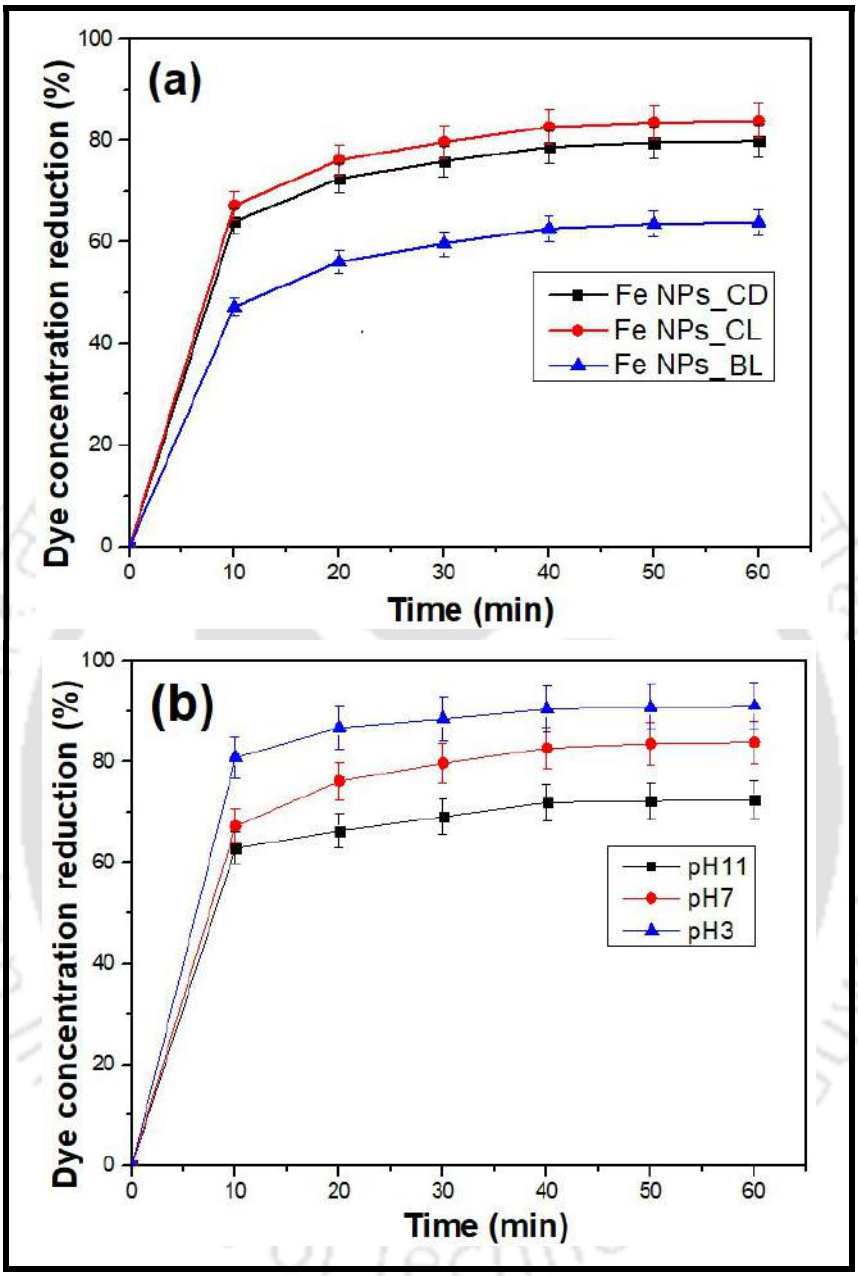

Figure 3.7: (a) Dye degradation study due to Fe-NPs synthesized from clove, cardamom, and bay-leaf extract (b) Dye degradation study by clove extract mediated Fe-NPs at different pH

3.2.8. Dye degradation mechanism

The possible dye degradation mechanism utilizing green synthesized FeNPs_CL was shown in Figure 3.9. The clove extract mediated Fe NPs due to its negative surface charge

(as discussed in section 3.2.5) adsorbs the crystal violet dye molecules (cationic dye) readily on its surface. The dye molecules got adsorbed on the reactive sites of the core shell FeNPs_CL which consisted of iron oxide, and clove aromatic components on outer shell side [221].

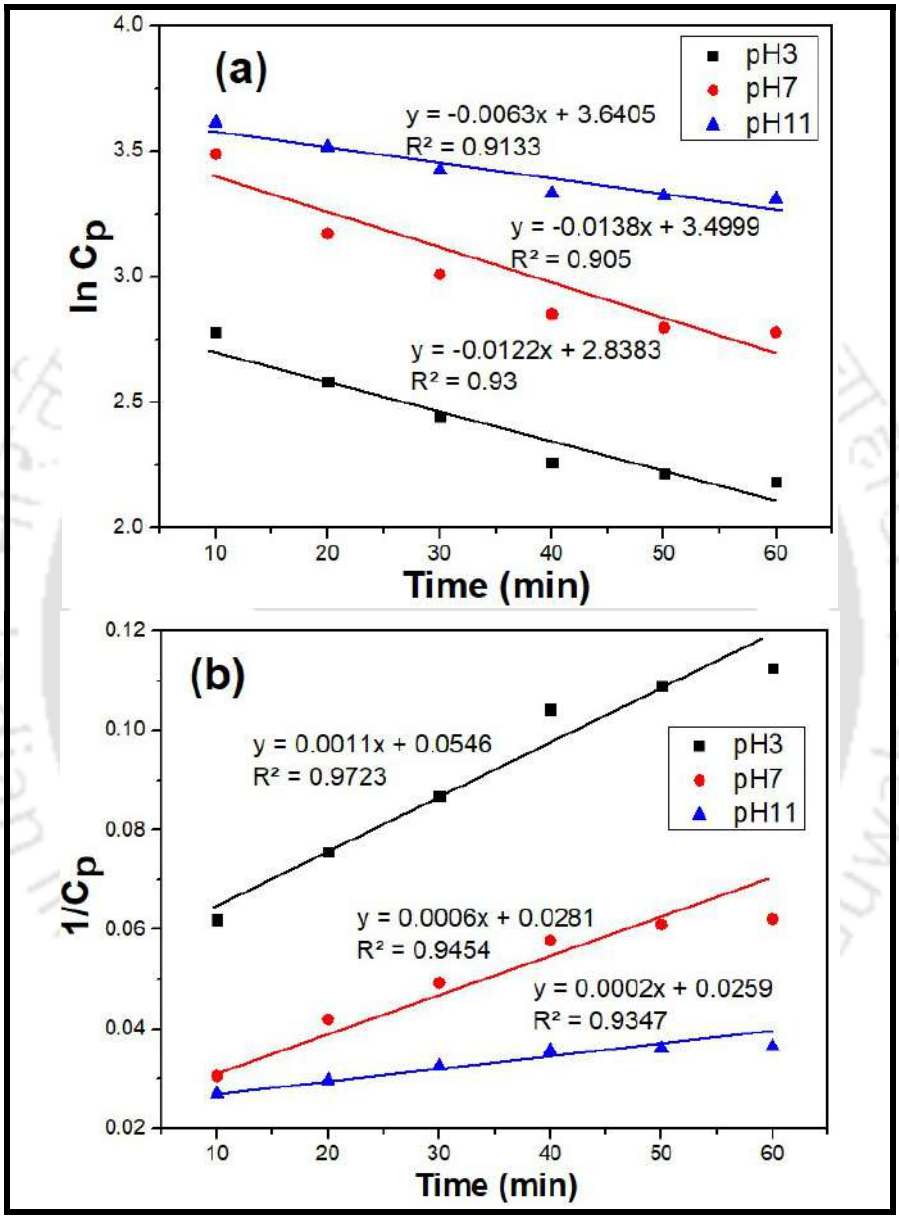

Figure 3.8: Experimental degradation data fitting on (a) pseudo-first order, and (b) pseudo-second order kinetic model

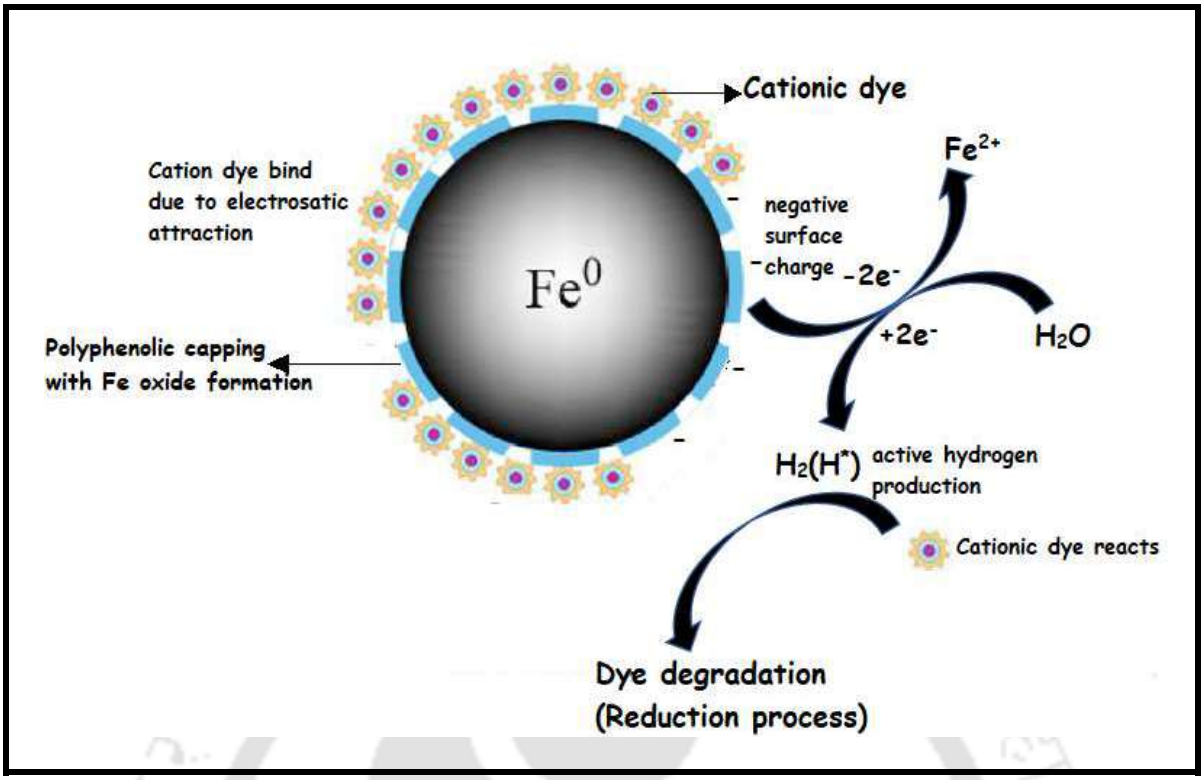

Figure 3.9: Dye degradation mechanism of crystal violet by clove extract mediated Fe-NPs

From past studies it was obtained that the organic aromatic coating over the FeNPs_CL has influence on the removal efficiency of dye molecules. Similarly, iron oxide coating capped over FeNPs_CL also affects the interaction with cationic dye molecules. The iron oxide coating itself in the presence of oxygen can achieve a good dye removal effect [222].

Moreover, Fe^0 plays a vital role in dye degradation process, where Fe^0 losses electron on reacting with H_2O molecules generating H* (active hydrogen) from the H^+ ions of water molecules [223]. The generated active hydrogen possess high reducing capability, and thus the cationic dye molecules by accepting the electrons from active hydrogen results in the cleaving of –C=N– and –C=C– bonds present in the benzene ring. Thus the possible crystal violet dye degradation mechanism by FeNPs_CL includes adsorption and reduction process simultaneously, where the dye molecules gets adsorbed on iron oxide and reduced by zero-valent iron [221,222].

Chapter 4

Selection of better extraction solvent and optimizing process parameters for maximizing total phenolic (TPC), and total flavonoid content (TFC) of *Syzygium aromaticum* (clove) extract

Chapter 4

Selection of better extraction solvent and optimizing process parameters for maximizing total phenolic (TPC), and total flavonoid content (TFC) of *Syzygium aromaticum* (clove) extract

Previous chapter provides a detail analysis of choosing clove extract over cardamom and bay-leaf extract based on its TPC, TFC, TTC and antioxidant properties. This chapter deals with choosing better extraction solvent among ethanol, methanol and de-ionized water for extracting polyphenols and flavonoids along with studying their antioxidant properties from clove. De-ionized water extracted the highest amount of polyphenols, flavonoid and tannins from clove with respect to ethanol and methanol extract. Moreover, the important flavonoid and phenolic contents such as rutin, quercetin, and catechin were found to be abundant in aqueous extract about 1459.37±65.7, 63745.15±350.2, and 177.64±8.8 mg/L when compared to methanol and ethanol extract. Furthermore, the process parameters such as time of extraction, temperature, and volume of extraction solvent were optimized utilizing response surface methodology (RSM) and central composite design (CCD) to maximize TFC and TPC to obtain better aqueous extract of clove, to act as an efficient green solvent for synthesizing ZVI NPs. The effect of different variables and their interaction towards yielding better TFC and TPC content were analyzed through analysis of variance (ANOVA) study.

4.1. Experimental

4.1.1. Materials

Methanol, ethanol, and millipore water were utilized as extraction solvent. Folin-Ciocalteu's reagent, rutin, gallic acid, vanillin, catechin, quercetin, Na_2CO_3, NaOH, and conc. HCl were utilized for analyzing total phenolic, flavonoid, and tannin content. DPPH, CH_3COOH, CH_3COONa, TPTZ, and $FeCl_3.6H_2O$ were used for measuring antioxidant potential. The details of all the chemicals used are mentioned in Table 2.1 of Chapter 2.

4.2. Results and discussion

4.2.1. Comparison of total phenolic content (TPC), total flavonoid content (TFC), total tannin content (TTC), and antioxidant potential of various solvent mediated clove extract

Table 4.1 depicts the comparative analysis of the above mentioned contents when clove extract was prepared from different solvents such as aqueous solution, methanol, and ethanol. From the previous chapter only aqueous extract of clove was found to have better TPC, TFC, TTC, and antioxidant potential over cardamom, and bay-leaf extract.

In order to further enhance the TPC, TFC, TTC, and antioxidant potential of clove extract various solvents were utilized. From Table 2.1 it was observed that the aqueous solution mediated clove extract yielded higher TPC, TFC, and TTC amount of 130.75±4.57 mg rutin/g sample, 59.56±2.5 mg gallic acid/g sample, and 3.46±0.15 g gallic acid/100g sample respectively with respect to other solvents. Moreover, the aqueous solution mediated clove extract resulted better DPPH scavenging (%) of 86.7±4.8%, and FRAP assay of 48.45±2.7 µM Fe(II)/g dry sample with respect to cardamom, and bay-leaf extract. Such results satisfy that this extract could be utilized for preparing better aromatic

coated stabilized and physico-chemical property oriented Fe NPs as discussed in Chapter 5 for environmental remediation purposes.

Table 4.1: Comparative analysis of TPC, TFC, TTC, and antioxidant potential of various solvent mediated clove extract

Parameters	Aqueous extract	Methanol extract	Ethanol extract
Total phenolic content (TPC) (mg rutin/g sample)	130.75±4.57	119.20±4.6	123±5.3
Total flavonoid content (TFC) (mg gallic acid/g sample)	59.56±2.5	48.67±2.1	52±2.8
Total tannin content (TTC) (g gallic acid/100g sample)	3.46±0.15	2.6±0.13	3.1±0.1
DPPH scavenging (%)	86.7±4.8	78.34±4.2	80.6±3.8
FRAP assay (μM Fe(II)/g dry sample)	48.45±2.7	41.47±1.6	44±2.3

4.2.2. Comparative analysis of specific flavonoids for different solvent mediated clove extracts

In this present study specific flavonoids which are generally found in plant extracts like rutin, quercetin, and catechin are quantified from various solvent mediated clove extracts. Since such flavonoids have higher antioxidant capacity, they play an important role in green extract acting as reducing and stabilizing agent during nanoparticle synthesis.

Figure 4.1(a), (b), and (c) shows the HPLC analysis of the pure rutin, quercetin, and catechin where at specific retention time sharp peaks were obtained for pure components.

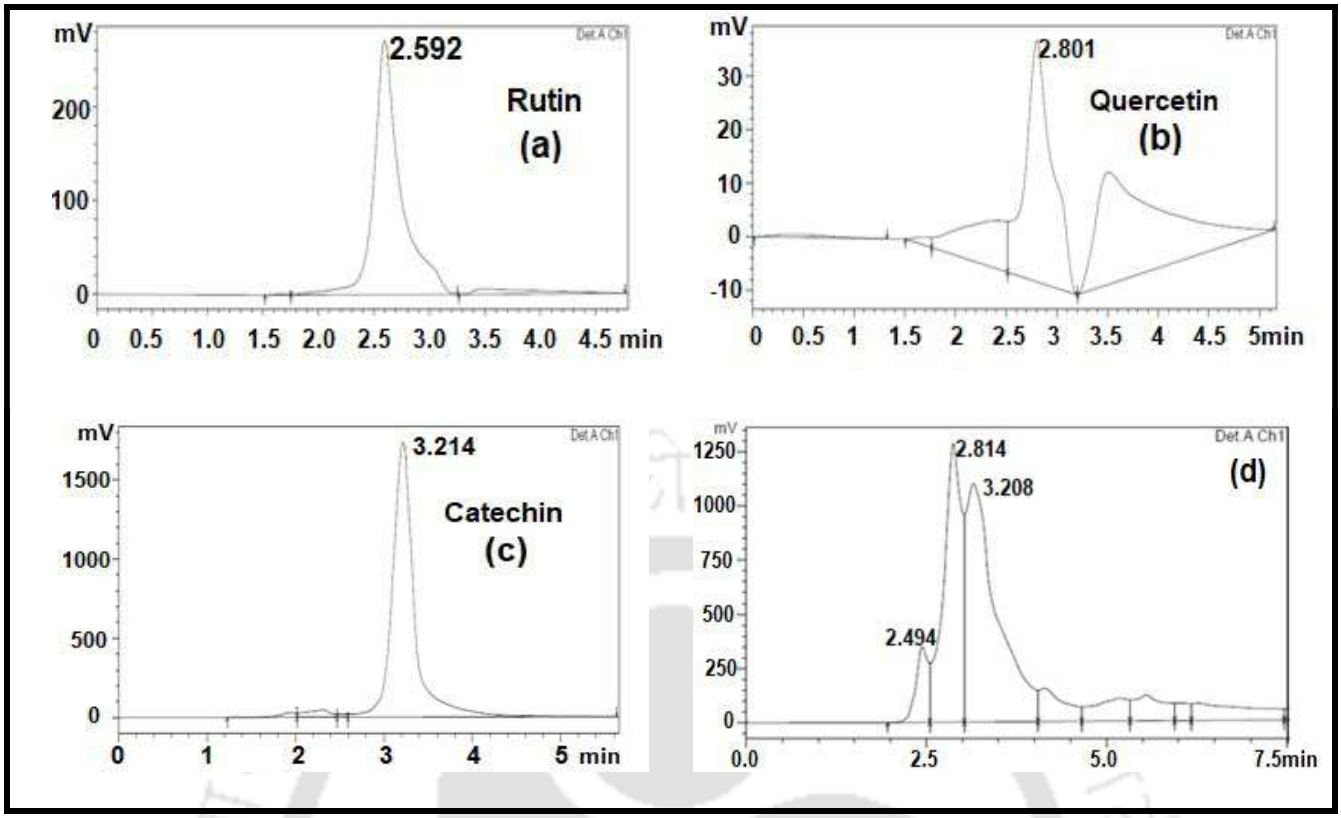

Figure 4.1: HPLC analysis of pure (a) rutin (b) quercetin (c) catechin, and (d) clove extract

Figure 4.1(d) shows that for aqueous soyhlution mediated clove extract similar peaks at such specific retention time were obtained. Such outcomes confirm the presence of rutin, quercetin, and catechin within the aqueous clove extract. Further quantification of such flavonoids in Table 4.2 shows that aqueous extract of clove possessed the higher amount of rutin (1459.37±65.7 mg/L), quercetin (63745.15±350.2 mg/L), and catechin (177.64±8.8 mg/L) in comparison to the other solvents mediated clove extract.

Table 4.2: Comparative analysis of specific flavonoids for different clove extract

Parameters	Aqueous extract	Methanol extract	Ethanol extract
Rutin (mg/L)	1459.37±65.7	-	-
Quercetin (mg/L)	63745.15±350.2	40222.72±203.2	16023.15±166.4
Catechin (mg/L)	177.64±8.8	1134.41±35.67	286.96±11.54

4.2.3. Central composite design and response surface methodology

From above results it was concluded that the clove extract prepared from aqueous solution was better among other solvents in terms of TPC, TFC, TTC and antioxidant potential capacity.

Table 4.3: Central composite design matrix for optimization of TFC and TPC of aqueous clove extract

Run no:	Coded Values			Point Type	Response			
					TFC		TPC	
	A Time	B Temp	C Water		Actual	Predicted	Actual	Predicted
1	1.681	0	0	Axial	56.25	55	130.8	128.37
2	0	0	0	Center	43.1	43.02	120.54	120.4
3	0	0	-1.681	Axial	70.8	69.73	179.45	181.43
4	-1	1	-1	Fact	46.3	47.53	173	171.12
5	0	0	0	Center	42.8	43.02	120	120.4
6	0	-1.681	0	Axial	41.25	42.63	65.6	63.04
7	1	-1	1	Fact	43.1	42.02	65.8	67.82
8	0	0	0	Center	43.1	43.02	120.54	120.4
9	0	0	0	Center	43	43.02	120.45	120.4
10	0	0	0	Center	43.2	43.02	120.6	120.4
11	0	1.681	0	Axial	34.69	33.13	132.7	135.15
12	1	1	-1	Fact	55.57	56.55	168.8	166.97
13	0	0	1.681	Axial	20.4	21.32	70	67.87
14	0	0	0	Center	42.9	43.02	120.2	120.4
15	-1	1	1	Fact	23.156	22.44	97.37	95.2
16	-1	-1	1	Fact	16.6	15.75	47.48	49.45
17	1	-1	-1	Fact	73.68	74.52	124.66	126.9
18	-1	-1	-1	Fact	44.44	43.31	132.12	130.32
19	1	1	1	Fact	25.26	26.52	110.89	112.79
20	-1.681	0	0	Axial	24.4	25.35	114.04	116.4

Hence, after selecting the better solvent for preparing clove extract, the next step is to optimize the parameters such as time (min), temperature (ºC), and millipore aqueous content (mL) to obtain maximized TPC, and TFC amount in clove extract since these two plays very important role in providing better antioxidant property to the extract. Design Expert Software 9.0 was utilized to optimize the parameters by choosing a quadratic model for obtaining maximized TPC, and TFC amount in the aqueous clove extract.

Table 4.4: Limits and constraints for optimization study of TFC and TPC of aqueous clove extract

Parameters	Goal	Lower Limit	Upper Limit	Lower Weight	Upper Weight	Importance
Time	in range	30	50	1	1	3
Temp.	in range	50	80	1	1	3
Water	in range	30	50	1	1	3
TFC	Maximize	16.6	73.68	1	1	3
TPC	Maximize	47.48	179.45	1	1	3

Table 4.3 shows the central composite design matrix for each experimental setup from the combination of varied parameters range provided in Table 4.4. Parameters such as time were varied within 30-50 min, whereas temperature and millipore water content was varied within 50-80 ºC, and 30-50 mL respectively. Table 4.3 represents the coded value for each parameter, where +1 represents highest value within range, -1 represents lowest value, and 0 denotes mid-values within range for each parameter. There is a term known as alpha calculated to be +1.681 and -1.681 (coded value) which was denoted to be a certain value above and below the range for each parameters.

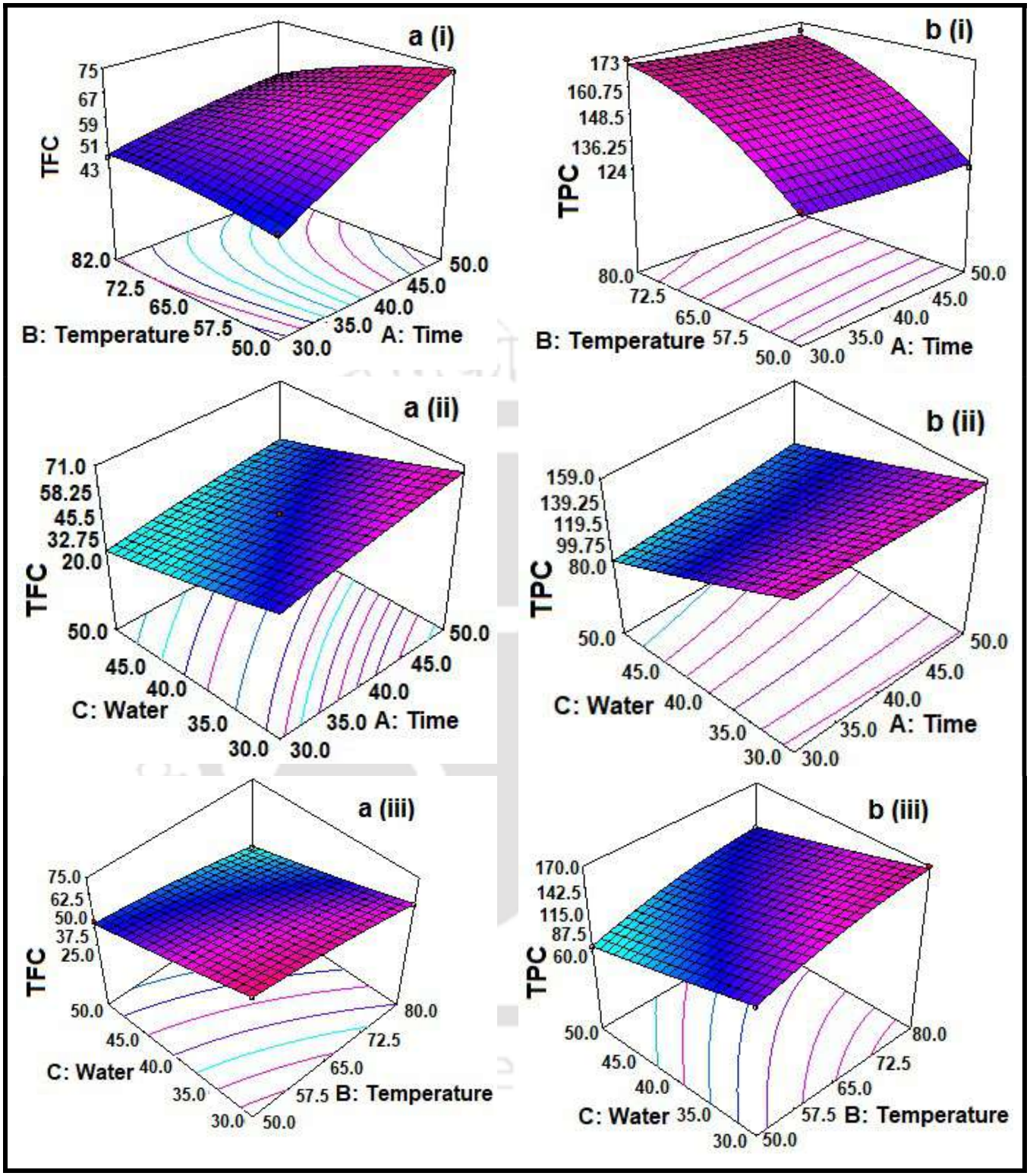

Figure 4.2: (a) Represents the RSM study of maximizing TFC in clove extract by optimizing parameters A: time, B: temperature, and C: de-ionized water volume. (b) RSM study of maximizing TPC through optimizing A: time, B: temperature, and C: de-ionized water volume.

Table 4.5: Analysis of variance for TFC and TPC content of clove extract

Source	Sum of square	Degree of freedom	Mean square	F- Value	P value Prob>F
Total flavonoid content (TFC)					
Model	4341.5	9	482.4	284.73	< 0.0001[s]
A-Time	1063.15	1	1063.15	627.53	< 0.0001
B- Temp	108.8	1	108.8	64.2	< 0.0001
C- Water	2831.72	1	2831.72	1671.4	< 0.0001
AB	246.2	1	246.22	145.3	< 0.0001
AC	12.23	1	12.23	7.2	0.02
BC	3.04	1	3.04	1.8	0.21
A^2	14.45	1	14.46	8.54	0.01
B^2	47.64	1	47.64	28.12	0.0003
C^2	11.15	1	11.15	6.58	0.028
Residual	16.94	10	1.7		
Lack of Fit	8.65	5	1.36	1.57	< 0.267[ns]
Pure Error	0.11	5	0.021		
$R^2 = 0.996$, $R^2_{adj} = 0.992$, $R^2_{pred} = 0.969$, adequate precision = 63.85					
Total phenolic content (TPC)					
Model	23181.6	9	2575.73	396.58	< 0.0001
A-Time	172.73	1	172.73	26.6	0.0004
B-Temp	6278.03	1	6278.03	966.6	< 0.0001
C- Water	15567.67	1	15567.67	2397	< 0.0001
AB	0.3	1	0.3	0.046	0.83
AC	236.63	1	236.63	36.43	0.0001
BC	12.2	1	12.2	1.88	0.2
A^2	7.18	1	7.18	1.11	0.32
B^2	817.13	1	817.13	125.8	< 0.0001
C^2	32.7	1	32.7	5.03	0.05
Residual	24.95	10	6.5		
Lack of Fit	7.67	5	1.43	1.96	< 0.205[ns]
Pure Error	0.28	5	0.056		
$R^2 = 0.997$, $R^2_{adj} = 0.994$, $R^2_{pred} = 0.978$, adequate precision = 73.24					

[s] significant at prob>F value less than 0.05, [ns] not significant at prob>F value greater than 0.1.

Table 4.3 shows that there are total of 20 runs, and the result of each experimental runs obtained denoted as actual values, whereas the values obtained from the quadratic model chosen for modeling the design of experiments is represented as the predicted values. The maximum and the minimum obtained experimental values of TPC and TFC are shown in Table 4.4.

Figure 4.2 shows the 3D response surface methodology diagrams obtained from experimental results, which depicts the effect of the variation of the parameters (time, temperature, water content) on the TFC, and TPC responses. The region with pink color shows highest response value, followed by bluish region indicating lowest response value. Figure 4.2 a(i) and a(ii) depicts that at lower temperature and water content, with higher time interval better yield of TFC was obtained, whereas 4.2 a(iii) conclude that at lower temperature and water content better TFC yield was obtained. Similarly from Figure 4.2 b(i) it was noticed that higher temperature and at lower time interval better TPC was obtained, whereas Figure 4.2 b(ii) and b(iii) depicts that for lower water content, with higher time and temperature, higher TPC yield was obtained.

The adequacy of the model was ensured and tested by Fischer variation (F-value), probability values (p-value) and the correlation coefficient (R^2). From Table 4.5, the F values for both the quadratic model of TPC, and TFC was quite high and p values <0.0001 for both the models indicates strong significance. It means that there is a probability of 0.01% to not follow the model. The predicted R^2 value of 0.97 and 0.98 was in reasonable agreement with the adjusted R^2 of 0.99 and 0.99 for TFC and TFPC formation, respectively. It shows that the chosen quadratic model fitted quite nicely.

From Table 4.5, the linear terms, time (A), temperature (B) and water content (C) with p-values (prob>F) <0.0001 indicated the significant role of the factors contributing for TFC extraction. Similarly for TPC extraction analysis it was observed that time (A) (p value

<0.0004) played a less significant role than temperature (B) and water content (C) with p value <0.0001. The interactive term AB (p-value <0.001) was found to be more significant in compare to AC (p-value <0.02) for TFC analysis, whereas for TPC analysis interactive term AC (p-value <0.0001) only played the significant role. The p value (Prob>F) for all the model terms (A, B, C, AB, AC, BC, A^2, B^2 and C^2) having less than 0.05 indicates that they all are significant. Moreover the lack of fit test for TFC, and TPC analysis showed that the p-values were 0.267, and 0.205 which concluded that it is non-significant. Thus, it is concluded that the quadratic model chosen for both TFC, and TPC analysis had a poor lack of fit and thus the models are significant. The quadratic models of TFC and TPC are given by Eq. 4.1 and 4.2 respectively, where A, B, and C are coded values.

$$\mathbf{TFC = 43.02 + 8.82\times A - 2.82\times B - 14.4\times C - 5.55\times A\times B - 1.24\times A\times C + 0.62\times B\times C - 1\times A^2 - 1.82\times B^2 + 0.88\times C^2} \quad (4.1)$$

$$\mathbf{TPC = 120.39 + 3.56\times A + 21.44\times B - 33.76\times C - 0.19\times A\times B + 5.44\times A\times C + 1.24\times B\times C + 0.71\times A^2 - 7.53\times B^2 + 1.51\times C^2} \quad (4.2)$$

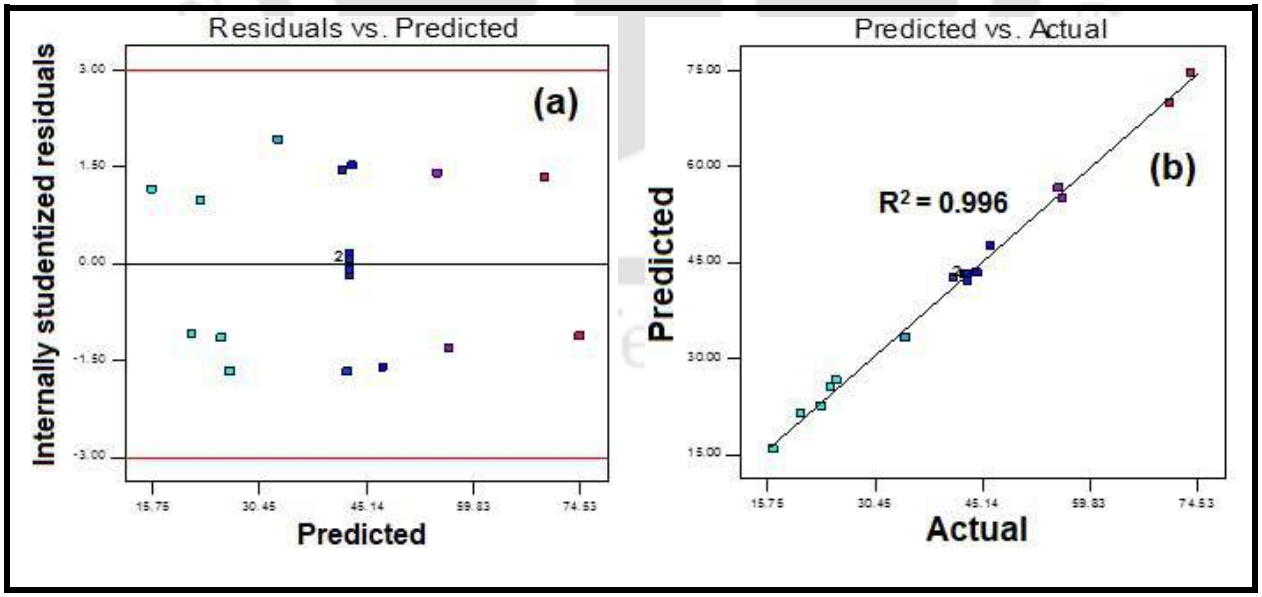

Figure 4.3: (a) Residuals vs. predicted graph for TFC analysis (b) Predicted vs. actual graph for TFC optimization

Figure 4.3(a) shows that the predicted TFC values obtained from the chosen quadratic model had residuals within the range of ±3%, which is quite good and acceptable, while Figure 4.3(b) shows that the actual (obtained from experiments) and predicted values (from quadratic model) of TFC showed good linearity with R^2 value 0.996. Similarly, from Figure 4.4(a) it was obtained that the predicted TPC values from the quadratic model showed residual within the range of ±3%, which is quite good. Moreover, the actual and predicted TPC values followed good linearity with R^2 value 0.997.

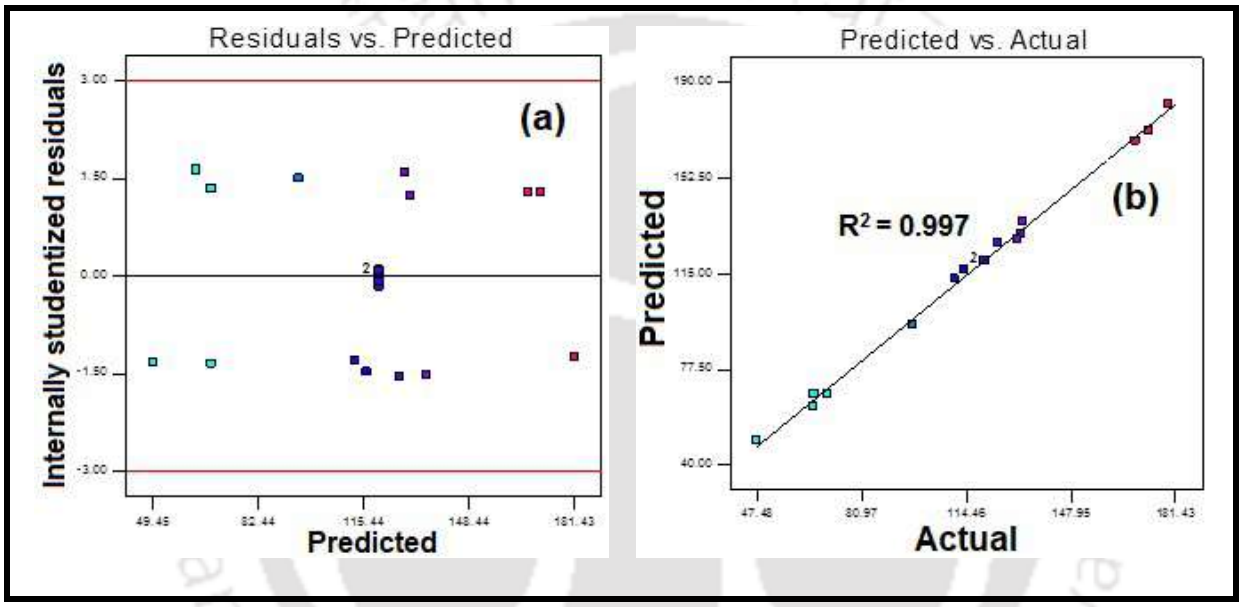

Figure 4.4: (a) Residuals vs. predicted graph for TPC analysis (b) Predicted vs. actual graph for TPC optimization

Table 4.6 shows that the optimized conditions obtained from the Design expert software, when TPC and TFC values were maximized keeping all the parameters within range (Table 4.4). The desirability value indicates that the probability of obtaining such values under experimental condition could achieve 85% accuracy. The maximum TFC and TPC values obtained after optimizing the parameters were 67.05 mg rutin/g sample, and 155.15 mg gallic acid/g sample respectively. When the experiment was conducted at the optimized conditions mentioned in Table 4.6 it was noticed that the experimental TFC, and TPC values were coinciding well with the predicted values and were within the acceptable error range of 4.4%

and 3.2% respectively (Table 4.7). Moreover UV-vis spectroscopy analysis of optimized clove extract at different pH is shown in Figure 4.5. The optimized clove extract obtained showed various peak intensity ~280 nm (highest for pH 4) due to pH variation, which was attributed due to the better n-π* electronic transition of sp^2 C of polyphenolic groups (C=O) and indicated better aromatic content in the extract.

Table 4.6: Optimized condition for maximized TFC and TPC of clove extract

For optimization of TFC and TPC					
Time (min)	**Temp (°C)**	**Water (mL)**	**TFC (mg RU/g)**	**TPC (mg GAE/g)**	**Desirability**
50	65	30	67.05	155.15	0.85

Table 4.7: Experimental and predicted results of TFC and TPC at optimized condition

Responses	Predicted value	Experimental value	Error (%)
TFC (mg RU/gm)	67.05	70.17	4.4
TPC (mg GAE/gm)	155.15	160.23	3.2

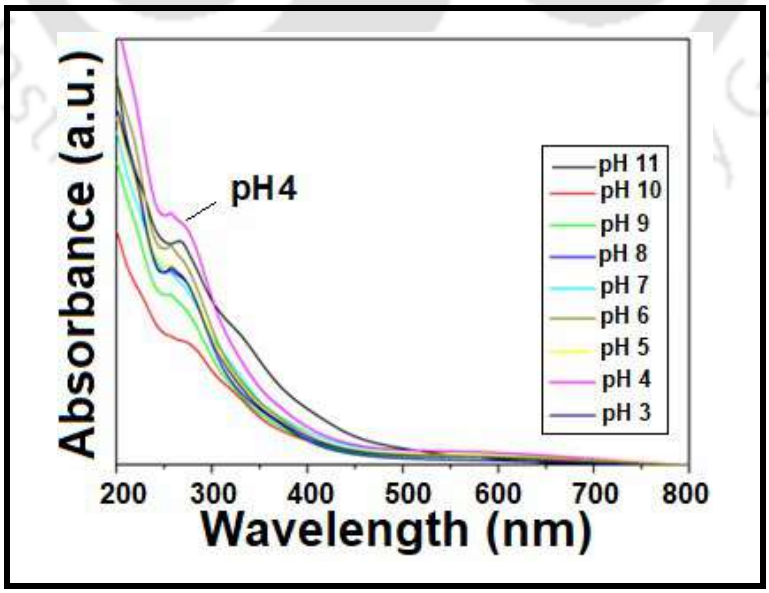

Figure 4.5: UV-vis spectroscopy analysis of optimized clove extract at different pH

Chapter 5

Studying the pH dependent morphological insights of *Syzygium aromaticum* (clove) extract mediated Fe NPs and its photoluminescence effect towards heavy metal ion detection

Piyal Mondal, Mihir Kumar Purkait. Synthesis of Iron dots through green route and studying its efficiency towards Fe^{3+} ion sensing property in real life water sample *(submitted to Sensors and Actuators B: Chemical)*

Chapter 5

Studying the pH dependent morphological insights of *Syzygium aromaticum* (clove) extract mediated Fe NPs and its photoluminescence effect towards heavy metal ion detection

This chapter deals with the preparation of Fe-NPs utilizing the clove extract optimized with maximum TPC and TFC amount as discussed in the previous chapter. It was observed that 1:4 ratio of 0.025 (M) $FeCl_3$ solution and optimized clove extract resulted in better Fe-NPs generation with better aromatic polyphenolic coating. Moreover, a detailed study of morphological variation of synthesized Fe-NPs by varying clove extract pH was carried out in this chapter. It was obtained through TEM analysis that the average spherical particle diameter increased from 1.63±0.06 nm to 15.27±0.23 nm with increase in pH of clove exract from 3 to 7 respectively. Whereas, on increasing the pH further from 7 to 1,2 the diameter decreases to 4.48±0.55 nm. The FESEM morphological analysis depicts the same trend with relative higher average diameter due to agglomeration effect. The XRD analysis shows that with variation in the pH of clove extract, variation in formation of zerovalent iron (ZVI) NPs along with various oxides were formed. Moreover, this chapter deals with the photoluminescent (PL) property study of the prepared ZVI NPs and was found that at pH 3, highest PL intensity (800 a.u.) was obtained, at an excitation wavelength of 380 nm. PL quenching effect of the ZVI NPs was found to be specific for Fe^{3+} ions in presence of other various heavy metal ions. A linear quenching range around 0.625 µM-10.00 µM for Fe^{3+} ions with 0.27 µM limit of detection (LOD) value was obtained. Moreover, the prepared ZVI NPs was utilized for detection and quantification of Fe^{3+} ion in real water sample collected from

IIT Guwahati campus, India, and was found to be an efficient sensor with negligible error (%) of analysis.

5.1. Experimental

5.1.1. Materials

In this chapter various heavy metal salts were utilized for carrying out specific heavy metal ion sensing applications such as $FeCl_3$, $MnCl_2$, $HgCl_2$, $CdCl_2$, $PbCl_2$, $CuCl_2$, $CaCl_2$, and $FeCl_2$ was utilized. The optimized clove extract maintained at pH 4 as discussed in previous chapter 4 was utilized for preparing the Fe NPs. The details of the chemicals utilized were already mentioned in Table 2.1 of chapter 2. The chemicals were used without any further purification.

5.1.2. Experimental methods

5.1.2.1. UV-vis spectroscopy analysis for polyphenolic content

UV-Vis Spectroscopy was utilized to optimize the ratio of metal salt (0.025 M) to clove extract ratio. In previous chapter 4, it was obtained that clove extract maintained at pH 4 produced highest peak at 280 nm, which was denoted due to the better electronic transistion of of sp^2 C of polyphenolic groups (C=O). It indicated better aromatic content in the extract. Since the total poly-phenolic content increases the antioxidant property of the extract hence such extract was utilized for preparing Fe NPs.

5.1.2.2. Photoluminescence activity of Fe-NPs at different pH

For studying the PL activity at different pH solutions, the prepared Fe NPs about 0.05 gm was dispersed in 20 mL millipore de-ionized water. The Fe-NPs solution was kept in an ultrasonication bath for 30 min. After sonication, the dispersed Fe-NPs solution was added about 1mL each in eight different beakers containing 20 mL of different pH solutions ranging from 3-12. After mixing them the final solution was again sonicated for 15 min, and then about

3 mL of each pH controlled Fe-NPs solution was transferred to cuvette and analyzed through a fluorescence spectrophotometer to check the PL intensity.

5.1.2.3. Photoluminescence activity of Fe-NPs in presence of heavy metals

20µM concentration standards of different metal ion solution were prepared for Mn^{2+}, Hg^{2+}, Cd^{2+}, Pb^{2+}, Cu^{2+}, Fe^{2+} Ca^{2+}, and Fe^{3+} respectively. For studying the quenching effect of different metal ions on the PL intensity of Fe-NPs at definite pH, about 200µL of each metal ion solution was added to 3mL of Fe-NPs dispersed solution, further sonicated and then transferred in cuvette for analysis in Fluorescence spectrophotometer.

5.1.2.4. Determination of specific heavy metal ion sensing property and analyzing linear range of applicability

Similarly in order to optimize the linear variation of PL quenching of Fe-NPs by Fe^{3+} ion, various concentration of Fe^{3+} solution was prepared ranging from 0.039-30µM. After preparing the stocks, 200µL of Fe^{3+} ion sample were added to 3mL of Fe-NPs solution in a cuvette and then analyzed in Fluorescence Spectrophotometer.The effect of PL quenching effect of Fe^{3+} ion due to interference of other heavy metals present in water were investigated so that false signal is not generated during sensing application of Fe^{3+} metal ion. First, 200µL of 20µM of each Mn^{2+}, Hg^{2+}, Cd^{2+}, Pb^{2+}, Cu^{2+}, Ca^{2+} and Fe^{2+} were added to 3mL of prepared Fe-NPs solution and their PL quenching were recorded. Further to the above prepared solution of different metals, 200µL of 20µM Fe^{3+} ion solution was added and again the PL intensity was recorded. The volume ratio of Fe^{3+} ion solution to other metal ion solution was fixed at 1:1 ratio. The PL quenching activity due to interference of other heavy metals was analyzed through Fluorescence Spectrophotometer.

5.2. Results and discussion

5.2.1. UV-vis spectroscopy analysis

The obtained optimized clove extract at pH 4 (discussed in Chapter 4) was utilized for preparing Fe-NPs. Figure 5.1 shows that for various volume ratio of 0.025 (M) Fe salt solution to clove extract, could affect on the aromatic coating of the synthesized Fe-NPs. The figure depicts that highest absorption peak at 260 nm and 280 nm was obtained for 1:4 ratio of Fe salt solution to clove extract ratio. The result confirms that at 1:4 ratio better aromatic coating over synthesized Fe-NPs were obtained since the peaks at 260 nm, and 280 nm denotes better π -π* (C=C, and C=O) and n-π* (C=O) electronic transitions of the sp^2 C present in carboxyl and carbonyl groups of clove extract [211,219].

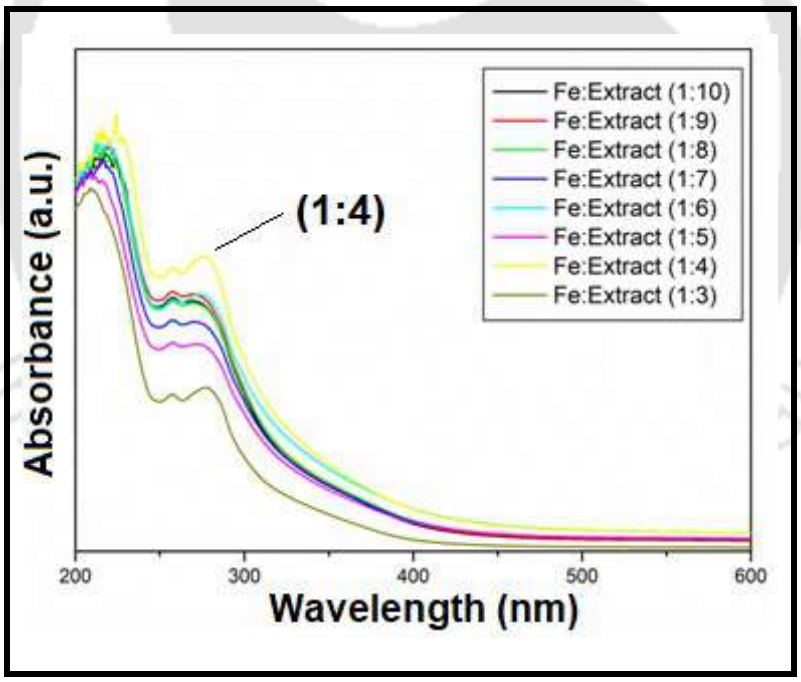

Figure 5.1: UV-vis spectroscopy for various volume ratio of Fe salt: clove extract

5.2.2. Morphological comparison of Fe-NPs with pH variation

Figure 5.2 and Figure 5.3 shows the TEM and FESEM-EDX analysis respectively of the synthesized Fe-NPs obtained from different pH varied clove extract in the range 4-12, when reacted with 0.025 (M) $FeCl_3$ solutions in the ratio 1:4.

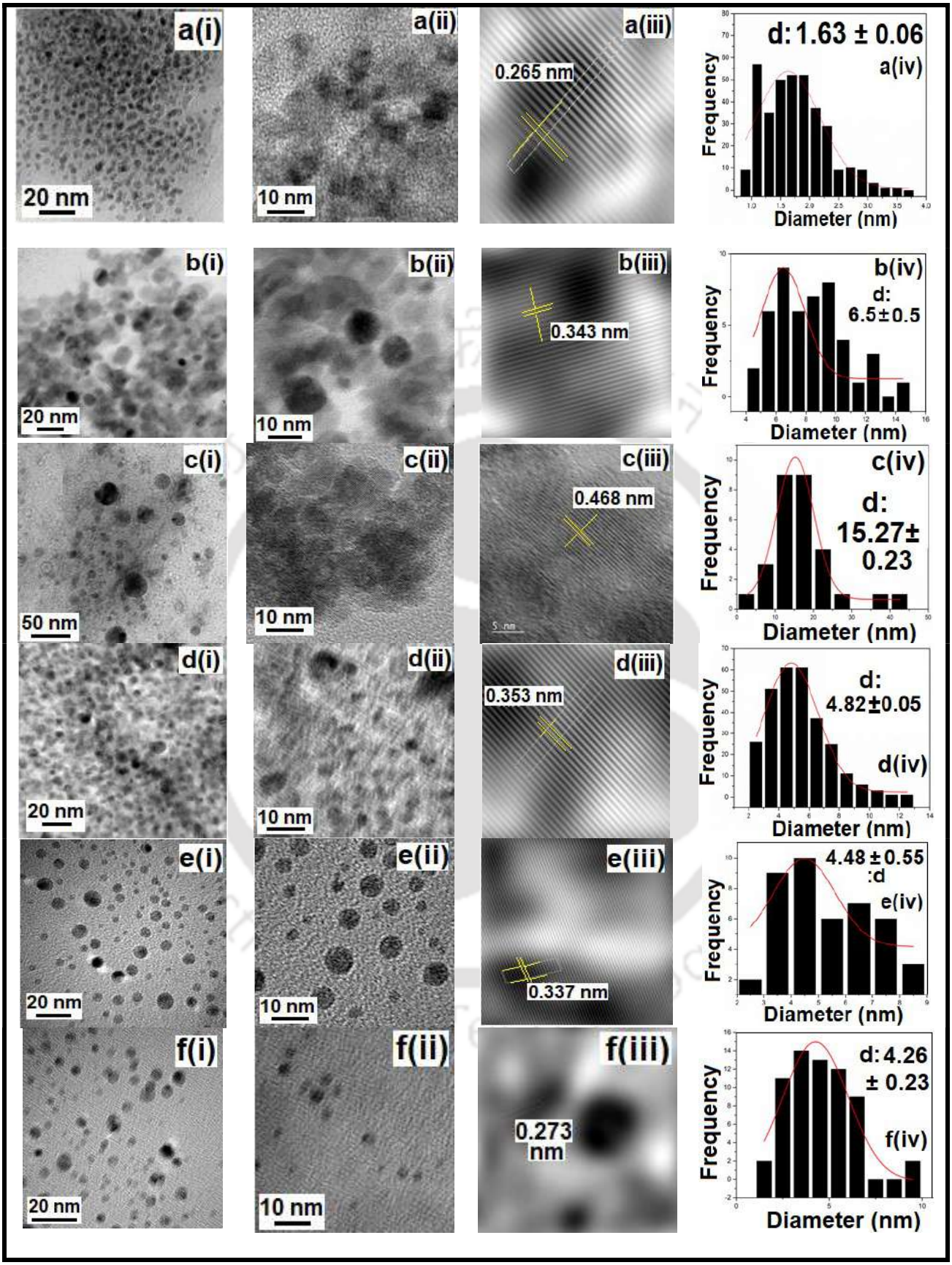

Figure 5.2: TEM images of prepared Fe-NPs at different pH of clove extract at (a) pH4 (b) pH5 (c) pH7 (d) pH9 (e) pH11 and (e) pH12

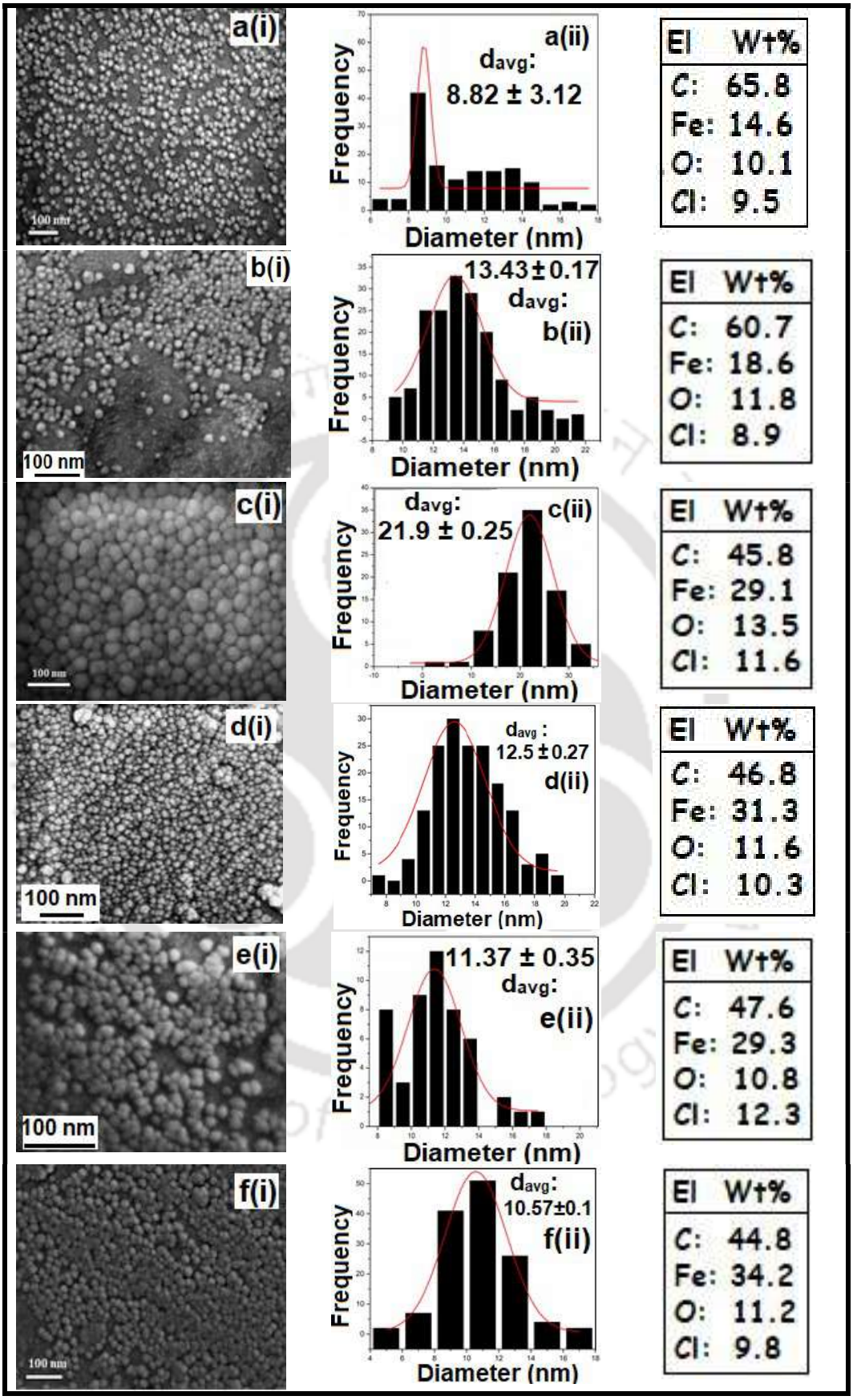

Figure 5.3: FESEM images of prepared Fe-NPs at different pH of clove extract at (a) pH4 (b) pH5 (c) pH7 (d) pH 9 (e) pH 11 and (f) pH12

From Figure 5.2 it was obtained that least average spherical particle diameter of 1.63±0.06 nm was obtained for pH4 clove extract mediated Fe-NPs, whereas with increasing the pH of clove at 7, the average particle diameter increases to 15.27±0.23 nm, which could be denoted due to the agglomeration and increasing oxide formation on the outer shell of Fe-NPs [175,176]. Moreover, on further increasing the clove extract pH at 12 the average particle diameter of synthesized Fe-NPs decreases to 4.26±0.23 nm. It was depicted from the TEM analysis that the pH of the clove extract played a vital role in synthesizing better coated Fe-NPs. Lower average spherical diamteter and well dispersed Fe-NPs was synthesized when clove extract was maintained at pH 4, and 12 confirming better reducing and stabilizing property of clove extract at such specific pH [178]. The d-spacing of the synthesized Fe-NPs shows that when the clove extract was maintained at pH 4 and pH 12, the d-spacing values obtained were least about 0.265 nm and 0.273 nm respectively.

Similarly, Figure 5.3 shows the average particle size of Fe-NPs synthesized utilizing different pH of clove extract by FESEM analysis along with its elemental analysis. The figure depicts the same trend of average Fe-NPs diameter size as obtained through TEM analysis. Due to the preparation steps for FESEM analysis slight agglomeration was observed, which increased the average particle diameter of the Fe-NPs. When clove extract was maintained at pH4 and pH 12, lowest average Fe-NPs diameter was obtained about 8.82±3.12 nm, and 10.57±0.1 nm, respectively. It was similarly observed that with increasing pH of clove extract at pH 7 the average diameter of Fe-NPs increases to 21.9±0.25 nm.

The EDX analysis in Figure 5.3 shows that with increasing pH of clove extract from 3 to 7 the carbon (C) content decreases for the synthesized Fe-NPs from 65.8 to 45.8 wt%, which conveys that the aromatic carbon coating was highest at pH 4. On increasing pH of clove extract from 4 to 7 it was observed that Fe and O content of Fe-NPs increases to 29.1, and 13.5 wt% respectively. It suggests that along with Fe content oxide formation of the synthesized Fe NPs also increases, hence the average diameter also increases [203,206]. Moreover, on

increasing the pH of clove extract to 12, the O content was found to decrease at 11.2 wt% with respect to pH 7 and Fe content was found to increase at 34.2 wt% signifying Fe-NPs synthesis with lower oxide formation.

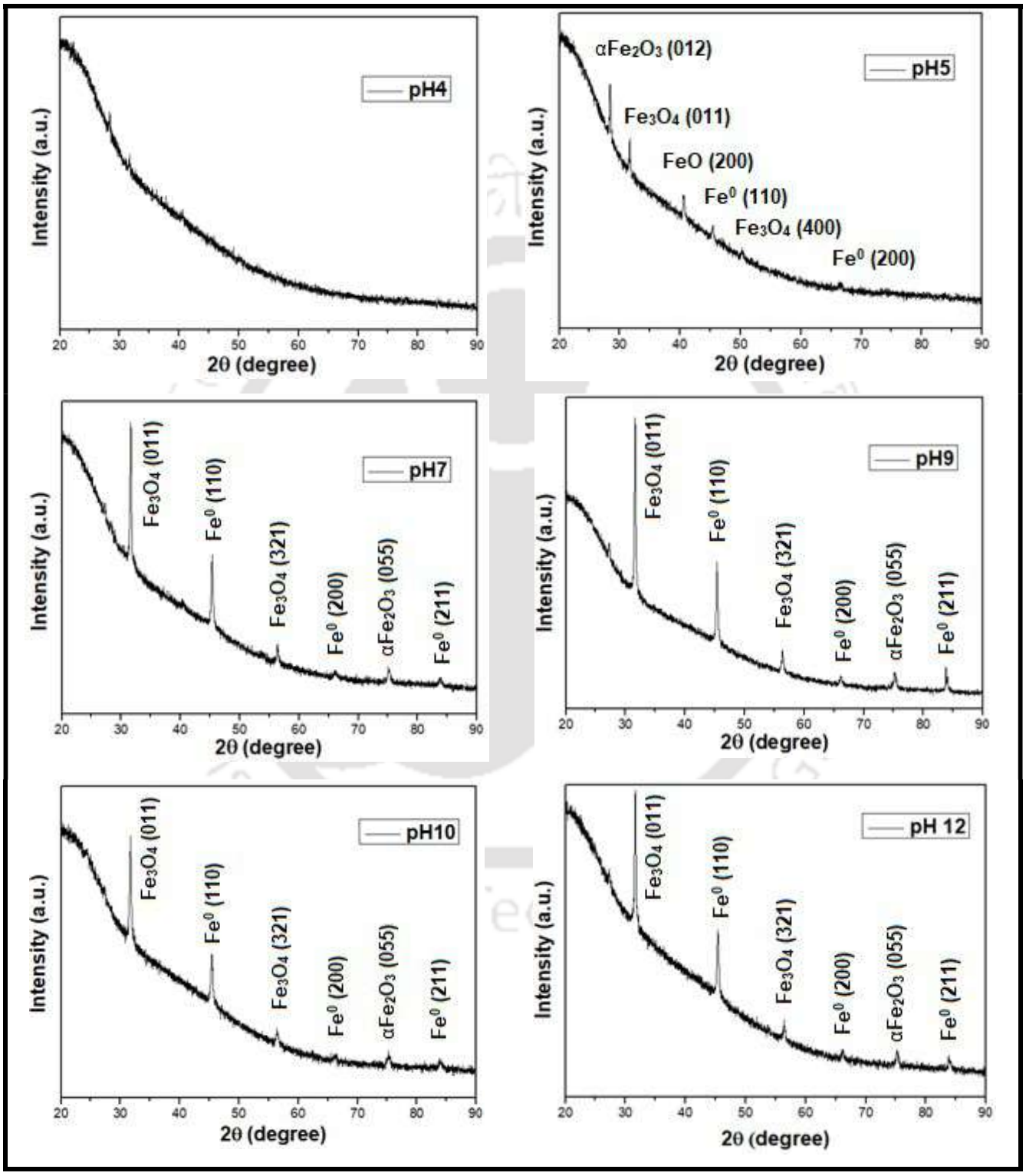

Figure 5.4: XRD analysis of Fe-NPs synthesized from clove extract of different pH

The XRD analysis of the synthesized Fe-NPs from the clove extracts maintained at different pH is shown in Figure 5.4. The various planes obtained for definite pH clove extract mediated Fe-NPs are in accordance with previous literatures [220, JCPDS 65-4899]. The XRD pattern of Fe-NPs prepared from clove extract of pH 4 showed no specific peak, which confirms strong and better coating of aromatic contents of clove extract, which provides no such crystalline plane formation. Similar observation was made through the EDX analysis for pH4 clove extract mediated Fe-NPs which shows highest C content and lower Fe content, and thus the XRD analysis of such prepared Fe-NPs having no specific iron plane is justified. The obtained XRD pattern for other pH maintained clove extract mediated Fe-NPs confirms the presence of zero-valent iron (ZVI), along with oxide forms such as Fe_3O_4, αFe_2O_3, and FeO. Thus the XRD characterization along with EDX analysis confirms the spherical core shell formation of the green synthesized Fe-NPs, where the Fe^0 state ZVI forms the core with the oxide formation covering the shell.

5.2.3. Photoluminescence behavior of prepared Fe-NPs

The prepared Fe-NPs from pH 7 maintained clove extract were first dispersed in millipore deionized water. Then by utilizing the fluorescence spectrophotometer, different excitation wavelength in the range 320-420 nm at a step change of 10 nm were made incident to excite the Fe-NPs in order to obtain better excitation wavelength. From Figure 5.5, the emission spectrum band is obtained in the range of 450-525nm for Fe-NPs. The maximum photoluminescence intensity of the Fe-NPs was obtained at an excitation wavelength of 380 nm with single band emission spectra ~500 nm as shown in Figure 5.5 a(i). Simarly Figure 5.5 a(ii) denotes at excitation wavelength 380 nm the photoluminescence intensity for different Fe-NPs obtained from different pH clove extract. It was obtained that highest PL intensity was obtained for pH 3 followed by pH 12 clove extract mediated Fe-NPs, whereas lowest intensity was obtained for Fe-NPs synthesized from clove extract at pH7.

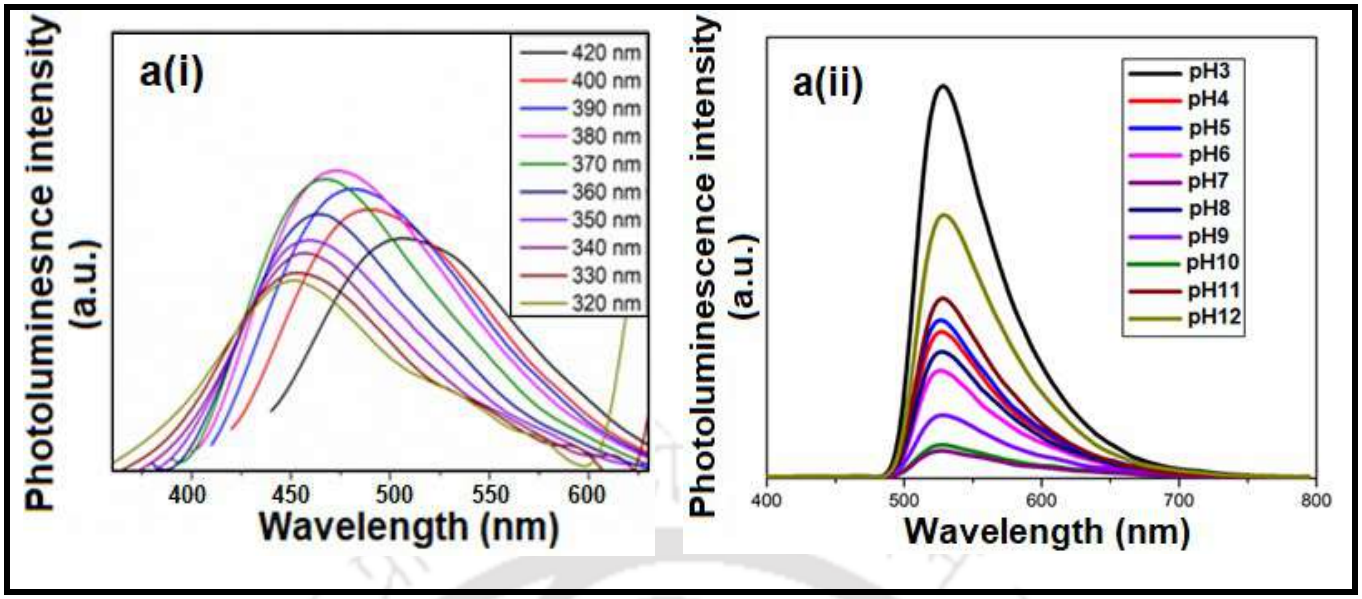

Figure 5.5: a(i) Photoluminescence intensity of of pH 7 clove extract mediated Fe-NPs at different excitation wavelength a(ii) Photoluminescence intensity of different pH clove extract mediated Fe-NPs at excitation wavelength of 380 nm.

5.2.4. Photoluminescence quenching study and selective sensing of Fe^{3+} ion

Figure 5.6 a(i) shows the PL intensity variation of the Fe-NPs prepared from clove extract of pH3 (since it has produced the highest PL intensity) in presence of different heavy metal ions of 20 µM concentration. Figure 5.5 confirms that Fe^{3+} ion quench the PL intensity of the Fe-NPs to the highest, in comparison to other heavy metal ions such as Mn^{2+}, Ca^{2+}, Hg^{2+}, Cd^{2+}, Pb^{2+}, Ca^{2+}, Fe^{2+}, and Cu^{2+}. Figure 5.6 a(ii) shows the normalized PL quenching intensity of different metals, and confirms that Fe^{3+} ion quenches the PL intensity by several times more than other heavy metals. From Figure 5.6 a(i), a shift in emission peak was obtained ~450 nm region in presence of Fe^{3+} ion which indicates the formation of new complex formation between Fe-NPs and Fe^{3+} ion.

Figure 5.6 (b) shows the UV-illuminated image of Fe-NPs in presence of various heavy metals ions. It was clearly visible from the image that Fe^{3+} ion quenched the Fe-NPs solution and turned dark when analyzed through UV-illuminator.

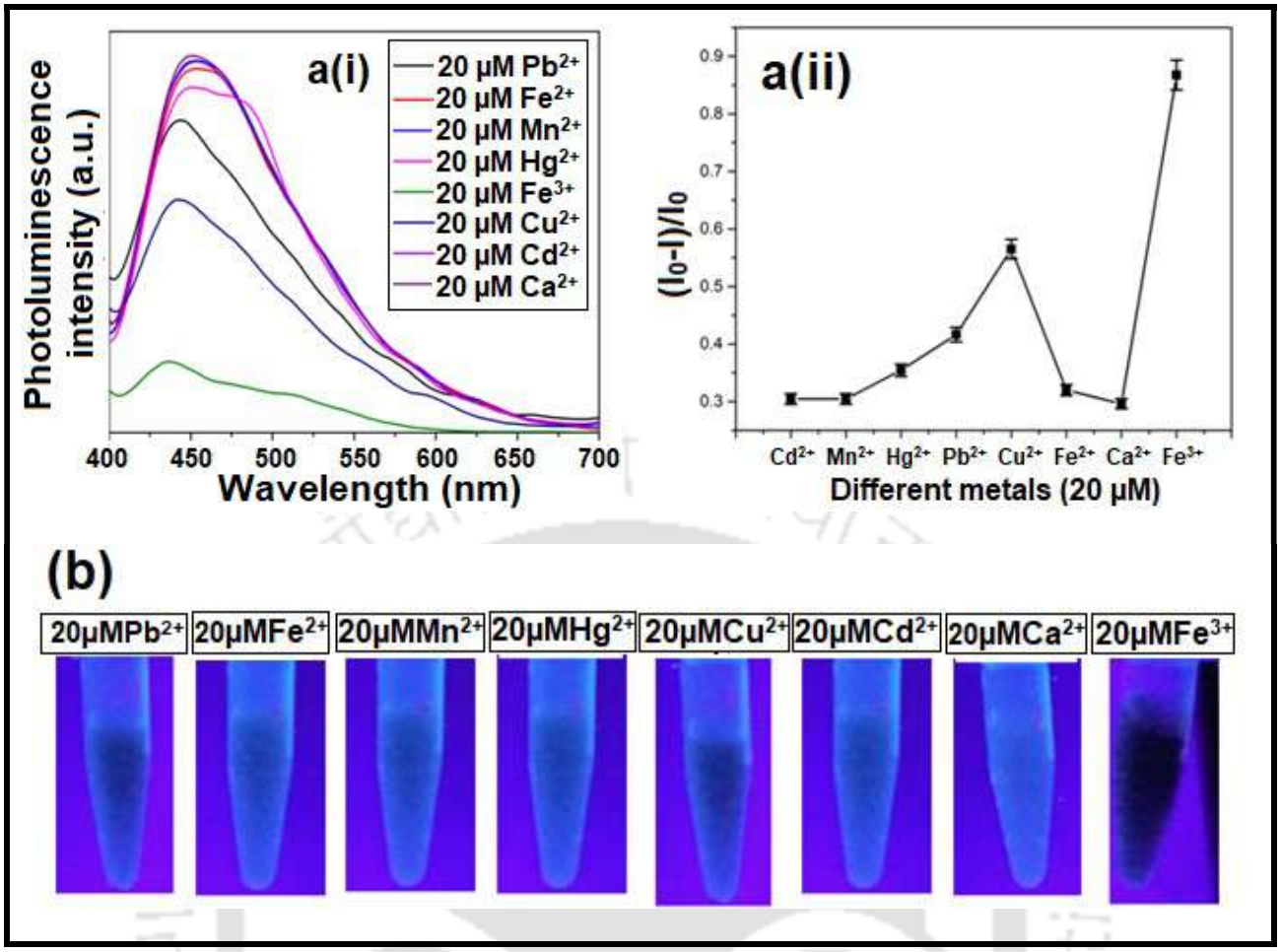

Figure 5.6: a(i) PL intensity quenching effect of Fe-NPs in presence of different heavy metal ion of 20 μM concentration when excited at 380 nm a(ii) normalization of quenching effect on photoluminescent intensity of different metal ions at 20 μM concentration when excited at 380 nm (b) Photoluminescence quenching behaviour of Fe^{3+} ion among other heavy metals through UV-illuminator

Figure 5.7 (a) depicts the linear quenching of PL intensity due to different molar concentration of Fe^{3+} ion. In order to achieve a linear quenching range the molar concentration was varied from 0.039-20.0 μM. It is observed that with increasing Fe^{3+} ion concentration higher quenching of PL intensity occurred. Similarly Figure 5.7 (b) shows that visible quenching image of different molar concentration of Fe^{3+} ion on PL intensity. With respect to the control Fe-NPs solution all the other samples were found to have turned dark due to the quenching effect through UV-illuminator.

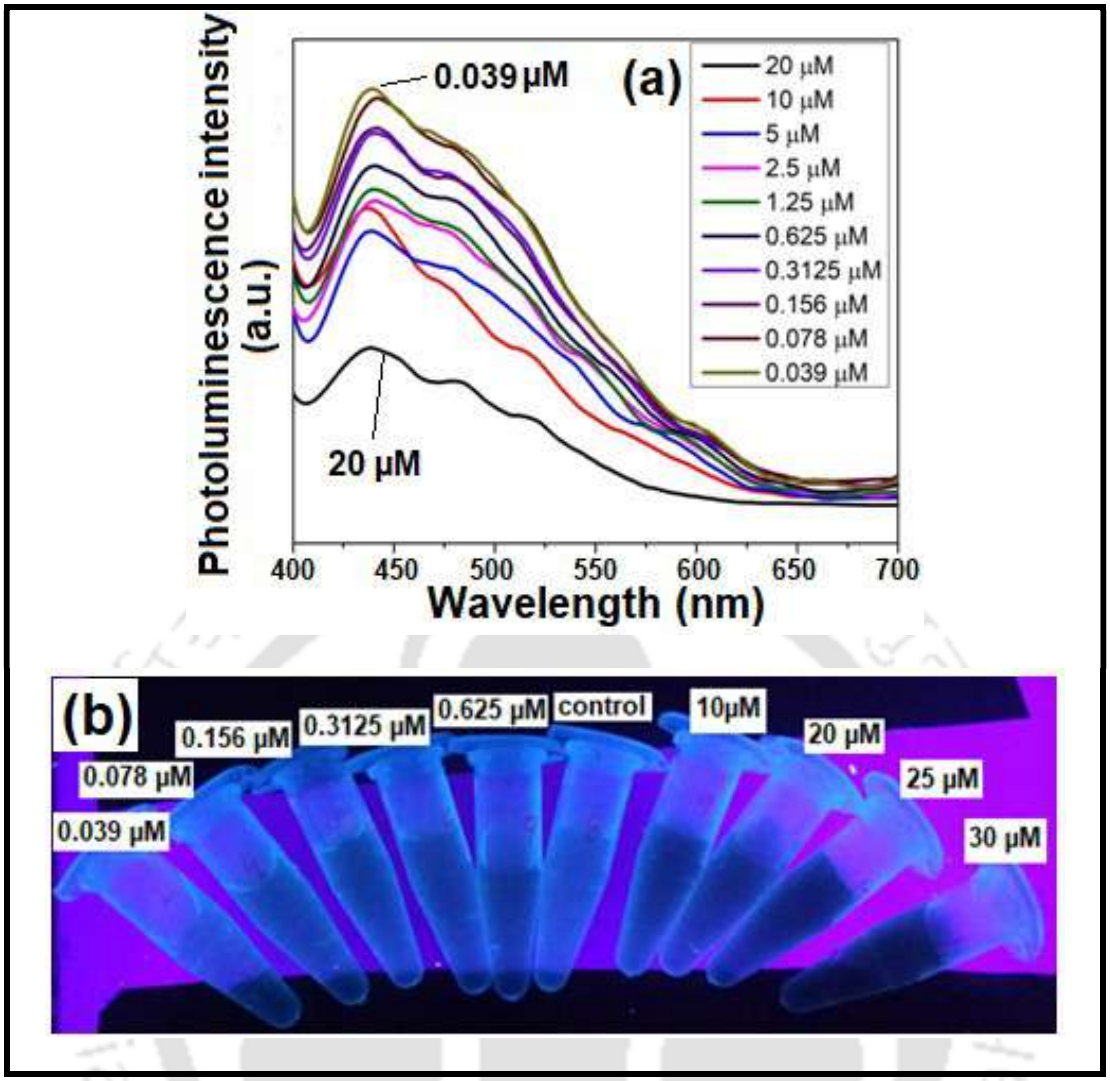

Figure 5.7: (a) Quenching effect on photoluminescence intensity of Fe-NPs due to various concentration of Fe^{3+} ion solution when excited at 380 nm (b) Photoluminescence quenching behaviour of Fe-NPs observed through UV illuminator at different molar concentration of Fe^{3+} ion.

The quenching efficiency of Fe^{3+} ions is quantitatively explained by Stern-Volmer equation and was obtained by varying the Fe^{3+} ion concentration from 0.02-30 µM shown in Figure 5.8 a(i). The relationship between (I_0/I-1) and Fe^{3+} ion concentration is explained by the Stern-Volmer equation $(I_0/I-1)-1 = 1 + K_{sv}[Fe^{3+}]$ [225], where I_0 and I are the Fe-Al NCs PL intensity initially at blank condition, and after adding various concentration Fe^{3+} ion respectively. The K_{sv} denotes quenching constant and from the curve it was observed that quenching of Fe^{3+} is linear in the concentration range of 0.625-10.0 µM as obtained from

Figure 5.8 a(ii). The K_{sv} value was determined to be 4.9×10^3 M^{-1}. The limit of detection (LOD) for Fe^{3+} ion was found to be 0.27µM.

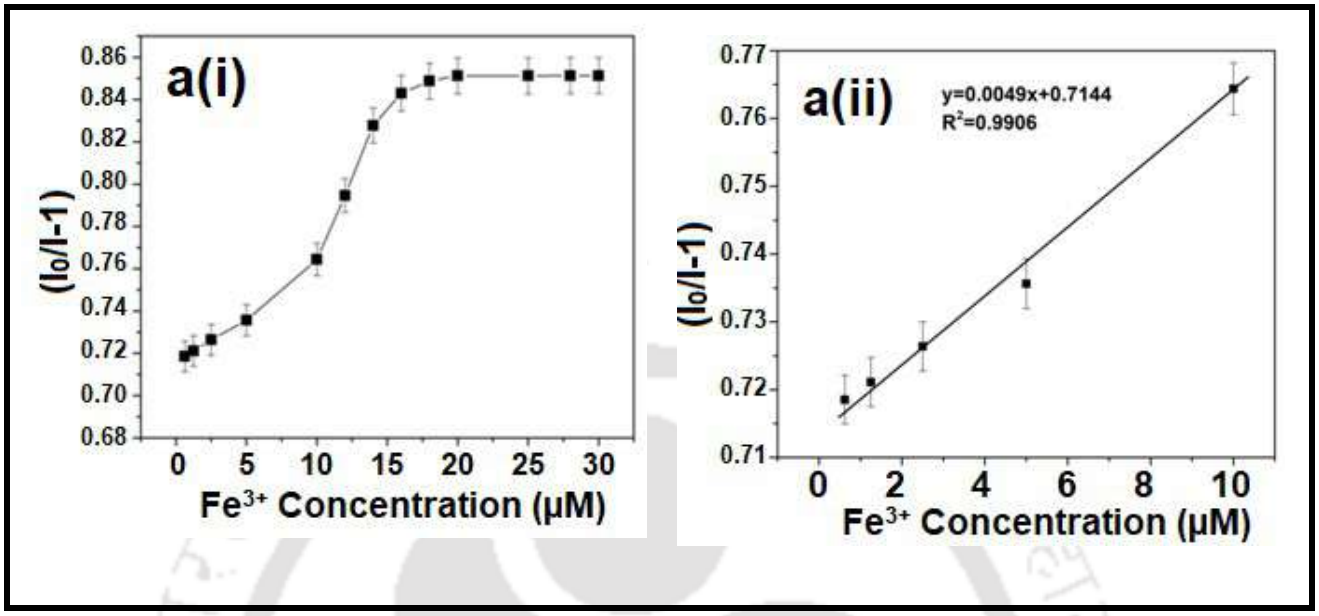

Figure 5.8: a(i) The Stern-Volmer plot of Fe^{3+} ion quenching a(ii) the linear response of PL intensity with varying concentration of Fe^{3+} ion at 440nm.

Figure 5.9 shows the effect of interference due to presence of other heavy metals in the PL quenching effect by Fe^{3+} ions. On addition of equal molar concentration of specific heavy metals to Fe^{3+} ions in the ratio 1:1, it was observed that the PL intensity in presence of other heavy metals remains almost same, whereas on addition of Fe^{3+} ions the PL intensity decreases. Figure 5.9 reflects low quenching effect of heavy metals when present alone, whereas enhanced quenching on addition of Fe^{3+} ions to heavy metals. The results convey least effect of interference by the other heavy metals is associated while detecting Fe^{3+} ions. To understand the quenching mechanism of Fe^{3+} ions, the UV absorption spectra of Fe^{3+} solution and PL emission spectra of synthesized Fe-NPs were studied. It was quite well known that Fe^{3+} produced an UV absorption band in the region 200-600 nm (as obtained in Chapter 3).

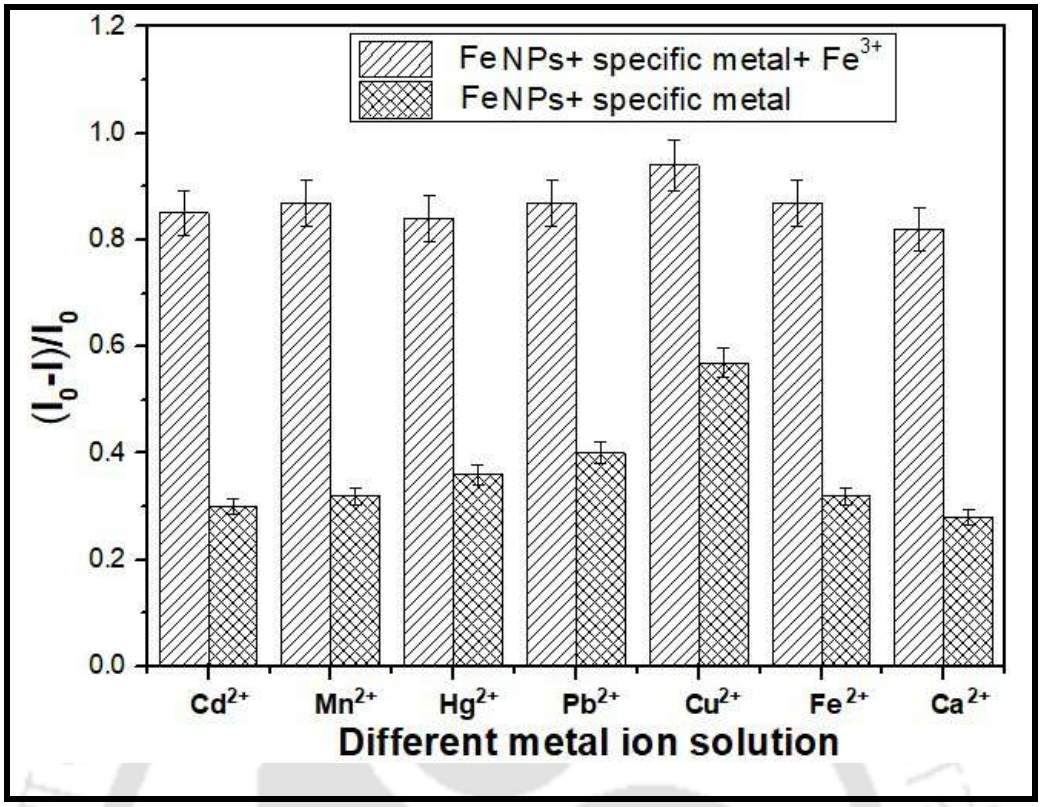

Figure 5.9: Interference studies results affecting photoluminescence quenching in presence of other metal ion in ratio 1:1 to Fe^{3+} ions for Fe-NPs

Hence from the PL emission spectra of Fe-NPs it was observd that an effective overlap occurred between the emission spectra of Fe-NPs and the absorption spectra of Fe^{3+} ions. Such phenomenon indicates that the observed quenching process may be attributed due to the fluorescence resonance energy transfer (FRET) [224]. Because of spectral overlap, which may result in direct transfer of the energy generated by the electronic transition in the Fe-NPs NCs material to to the analytes such quenching can occur. Hence due to hindrance in emitting photoluminescence in the form of radiative transitions, quenching in PL intensity occurs. Moreover due to the presence of vacant d-orbital in Fe^{3+} ions it possess a strong electron withdrawn ability, and thus the PL quenching can also be attributed to the photoinduced electron transfer (PET) process [226,227]. Hence the PL quenching of Fe-NPs by Fe^{3+} ions is attributed, both due to the electron transfer and energy transfer phenomenon.

5.2.5. Applicability of Fe-NPs based Fe^{3+} sensor in real sample water

For real water samples from the campus of IIT Guwahati, India, utilization of Fe-NPs based Fe^{3+} sensor was studied. The tap water from IIT Guwahati, Assam campus was collected and the Fe^{3+} concentration was spiked to about 2.0 µM, 5.0 µM, and 10 µM. The concenrations were confirmed by analyzing through AAS (Atomic Absorption Spectrophotometer, Model No.: Spectra AA 220 FS; Make: M/s Varian, Netherland). For each 200 µL spiked sample (2.0 µM, 5.0 µM, and 10 µM) about 3mL of the Fe-NPs was added and were analyzed through Fluorescence Spectrophometer. Through the quenched intensity obtained and utilizing the linearized equation from Figure 5.8 a(ii), the concentration of the analyzed sample were found to have a error percentage of 5.0±0.1, 4.1±0.3, and 3.2±0.15 for 2.0 µM, 5.0 µM, and 10 µM Fe^{3+} samples respectively. Such results convey that in spite of presence of various unknown organics and chemical species in tap water, still the Fe-NPs based Fe^{3+} sensor can provide effective detection with negligible error %.

Chapter 6

Green synthesized iron nanoparticles supported on pH responsive polymeric membrane for nitrobenzene reduction and fluoride rejection study: Optimization approach

Piyal Mondal & Mihir Kumar Purkait (2018): Green synthesized Iron nanoparticles supported on pH-responsive polymeric membrane for Nitrobenzene reduction and fluoride rejection study: Optimization approach. Journal of Cleaner Production (170) 1111-1123. Published 25/09/2018.

Piyal Mondal & Mihir Kumar Purkait (2017): Effect of Polyethylene glycol methyl ether blend Humic acid on poly (vinylidene fluoride-co-hexafluropropylene) PVDF-HFP membranes: pH responsiveness and antifouling behavior with optimization approach. Polymer Testing (61) 162-176. Published 15/05/2017.

Chapter 6

Green synthesized iron nanoparticles supported on pH responsive polymeric membrane for Nitrobenzene reduction and Fluoride rejection study: Optimization approach

In this part of the thesis green synthesized Fe NPs prepared via clove extract (already discussed in Chapter 3) was immobilized in flat asymmetric pH responsive PVDF-co-HFP membranes by blending method. Polyethylene glycol methyl ether (PEGME) (M_w = 5000 g/mol) and Humic acid (HA) were used as additive for preparation of pH responsive membrane. Fe NPs impregnated pH responsive PVDF-co-HFP membranes imparted reducing property and converted nitrobenzene to aniline, along with enhanced the fluoride rejection phenomenon through dead end filtration experiments. Addition of NPs in different weight percentage (0.01, 0.1, 1 wt%) altered nitrobenzene reduction and aniline formation. Nitrobenzene reduction along with fluoride rejection was dependent on the pH of the solution as well as the pH responsiveness of the polymeric membrane. Field emission scanning electron microscope (FESEM), Transmission electron microscopy (TEM) provided morphological structure whereas EDX gave elemental analysis of NPs. High performance liquid chromatography (HPLC) analyzed formation of aniline and nitrobenzene at different ultra-filtration time. In order to maximize the aniline formation and nitrobenzene reduction, the variables (time, pH and NPs wt%) was optimized using Design expert software 9.0 TRIAL through ANOVA (analysis of variance) using the combination of response surface methodology (RSM) and central composite design

(CCD). Fluoride rejection was studied on optimized wt% of iron NPs from NB reduction experiments with different pH of fluoride solutions.

6.1. Experimental

6.1.1. Materials

PVDF-co-HFP was used as the base polymer for preparing the polymeric membrane. Reagent grade N-methyl pyrrolidone (NMP) was used as solvent. Polyethylene glycol methyl ether (PEGME) (M_w=5000 $gmol^{-1}$) and Humic acid blended together in the ratio 2:1 wt% (optimized) was used as an additive for the membrane. All the other chemicals were of analytical grade and used without further purification. Deionized water (DI) purified by Millipore system (Millipore, France) was used in all processes. The details of the chemicals are provided already in Table 2.1 of chapter 2.

6.1.2. Synthesis of the iron NPs impregnated pH responsive PVDF-co-HFP membrane

Step I: Different weight % of Fe NPs (prepared from pH 7 clove extract discussed in chapter 3) (0.01, 0.1, and 1.0) was mixed with NMP (20 wt %) and thoroughly dispersed in ultra-sonication bath for 15 min.

Step II: NMP (60 wt%), 5 wt% aqueous mixture of PEGME-Humic acid (HA) (mole ratio 2:1 prepared by mixing 20 wt% PEGME, 10 wt% HA and 70 wt% water) and PVDF-co-HFP polymer (15 wt%) was stirred with the help of magnetic hot plate stirrer for 12 h at 60°C.

Both the solutions of Step I and II were mixed and stirred for 12 h followed by degassing for another 6 h at room temperature. The solution was placed on a clean glass plate and casted with the help of a casting knife maintaining a uniform thickness ~ 120 μm. The

glass plate was immediately immersed into the (DI) water bath at room temperature. The fabricated membrane was then immersed in fresh deionized water overnight to remove any residual solvent. Membrane sheets were finally air dried at room temperature thereafter.

6.1.3. pH permeability experiment

Hydraulic permeability of PVDF-co-HFP membranes blended with PEGME-HA in mole ratio of 2:1 and simple PVDF-co-HFP membranes were measured in acidic, basic and neutral conditions, at different trans-membrane pressures. For acidic and basic conditions, pH was maintained at 3 and 12 using 0.1 M HCl and 0.1 M NaOH solution, respectively. For neutral condition DI water was used. The variation in water flux of membranes with pH change was also measured. Each membrane was initially compacted with DI water for 30 min at 240 kPa, after that membrane was soaked in aqueous solution of different pH for 10 min. Then, permeated solution was collected over 10 min after 15 min equilibration at 200 kPa by the feed flow at the given pH.

6.1.4. Batch nitobenzene (NB) reduction experiments

The NB reduction study was carried out in a membrane cell (350 mL capacity) made of stainless steel. It consists of a membrane steel support containing numerous tiny pores as the base on which the membrane was kept. Nitrobenzene (125 ppm) was prepared for each batch study (300 ml), initial pH of the prepared solution was ~6. The pH was maintained at 3, 7 and 12 for reduction study. The prepared solutions were purged with N_2 gas (99.9% purity) and stored in a conical flask mouth sealed with rubber cork. During reduction study the stored NB solutions were poured inside the membrane chamber and once again purged with N_2 gas to prevent presence of any oxygen.

The batch reduction study was carried at 200 kPa using prepared iron NPs impregnated membrane.

6.1.5. Fluoride rejection study

Fluoride rejection study was carried in the same membrane cell specified above. 300 ml fluoride solutions of 5 ppm, 10 ppm and 20 ppm were prepared for batch studies. Solution pH was maintained at 3, 7 and 10 to study the pH effect on rejection of fluoride through iron NPs impregnated membrane. Similar conditions as of nitrobenzene reduction experiments were maintained for this study. After each run the membranes were put in sonication with acidic (0.1N HCl) and basic medium (0.1N NaOH) for 20-30 min. After each batch study the membrane was desorbed and used for 3 consecutive runs and rejection study was analyzed.

6.1.6. Central composite design (CCD) and Response surface methodology (RSM)

Central composite design was selected for the design of nitrobenzene reduction and aniline formation through dead end filtration experiments. Optimization process was only carried on for nitrobenzene reduction study; no effort was made to optimize fluoride rejection study. The optimized iron content with varying pH was used just to show the behaviour of fluoride rejection with the same iron NPs impregnated membrane. CCD was used to investigate the main as well as interaction contribution of three independent factors viz. pH, iron content and time. The number of conducted experiments was calculated as follow:

$$\mathbf{N = 2^k + 2k + n_c} \tag{6.1}$$

Table 6.1: Actual and predicted values for the CCD experiments

Std. Order	Run no.	Coded value			Point type	Response			
						NB reduction (%)		Aniline (ppm)	
		NPs content wt (%) (A)	pH (B)	Time (min) (C)		Actual	Predicted	Actual	Predicted
1	1	-1	-1	-1	Fact	68	67.35	11.45	11.5
2	8	1	-1	-1	Fact	55	54.56	11.28	11.29
3	18	-1	1	-1	Fact	40	39.68	11.35	11.35
4	5	1	1	-1	Fact	21	20.65	11.7	11.74
5	9	-1	-1	1	Fact	78	77.02	12.39	12.4
6	16	1	-1	1	Fact	82.5	81.47	11	11.2
7	14	-1	1	1	Fact	47	46.11	11.6	11.75
8	13	1	1	1	Fact	45	44.33	10.89	10.97
9	4	-1.682	0	0	Axial	55	56.04	13.15	13.28
10	2	1.682	0	0	Axial	43	43.81	12.36	12.56
11	3	0	-1.682	0	Axial	96	97.18	10.6	10.75
12	20	0	1.682	0	Axial	42	42.767	10.3	10.48
13	11	0	0	-1.682	Axial	26	26.4	11.3	11.56
14	7	0	0	1.682	Axial	53	54.45	11.5	11.28
15	10	0	0	0	Center	45	45.64	11.58	11.44
16	17	0	0	0	Center	46	45.64	11.67	11.44
17	15	0	0	0	Center	45.5	45.64	11.49	11.44
18	12	0	0	0	Center	46.7	45.64	11.46	11.44
19	19	0	0	0	Center	45	45.64	11.34	11.44
20	6	0	0	0	Center	46	45.64	11.28	11.44

$$y = \beta_0 + \sum_{i=1}^{2} \beta_i x_i + \sum_{i=1}^{2} \sum_{j=1}^{2} \beta_{ij} x_i x_j + \sum_{i=1}^{2} \beta_{ii} x_i^2 + \varepsilon \quad (6.2)$$

Where, β_0 is a constant coefficient, ε represents the error, x_i and x_j are independent variables. β_i, β_{ii}, and β_{ij} represent coefficients of linear, quadratic, and interaction effects, respectively. The model was verified by statistical tests, e.g., analysis of variance (ANOVA), residuals analysis (RA), scaling residuals (SR) and prediction error sum of squares (PRESS).

Table 6.2: Upper and lower values for design matrix

Factors	Unit	-1 Level	+1 Level	-alpha	+alpha
Iron content (A)	wt%	0.3	1.0	0.061373	1.238627
pH (B)	-	3.5	11	0.943277	13.55672
Time (C)	min	15	50	3.068625	61.93137

Table 6.1 shows the actual and predicted responses of nitrobenzene (NB) reduction and aniline (AN) formation with the coded values for all the 20 runs. All the values are entered in terms of coded variables. Table 6.2 represents the upper and lower values of variables which are taken into account for the necessary response study. Table 6.3 shows the conditions provided for optimization study of the input variables for maximum desirability of the responses to be maximized.

Table 6.3: Main constraints for optimization

Name	Goal	Lower Limit	Upper Limit	Lower Weight	Upper Weight	Importance
Iron content (A)	in range	0.01	1.0	1	1	3
pH (B)	in range	3	12	1	1	3
Time (C)	in range	5	50	1	1	3
NB reduction (%)	maximize	20	94	1	1	3
Aniline (ppm)	maximize	10.3	13.15	1	1	3

6.2. Results and discussion

6.2.1. Characterization of iron NPs and membranes

The FESEM images shown in Figure 6.1 a(i) confirms the spherical shape of iron NPs. The histogram plotting is shown in Figure 6.1 a(ii) shows that the NPs size was around 13.5±0.15 nm. Figure 6.1b shows the TEM image and also confirms the spherical structure of the synthesized iron NPs. The dark portion corroborates the better stabilization of iron NPs whereas the light spots shows carbon related compounds from clove extract. The particle size observed from TEM analysis was also within the range of 10-20 nm. EDX and XRD analysis of the green synthesized Fe-NPs are already discussed in chapter 3. The characterizations confirms that the synthesized Fe-NPs formed core shell structure where zero-valent iron (ZVI) occupied the core and oxides of iron covered the shell.

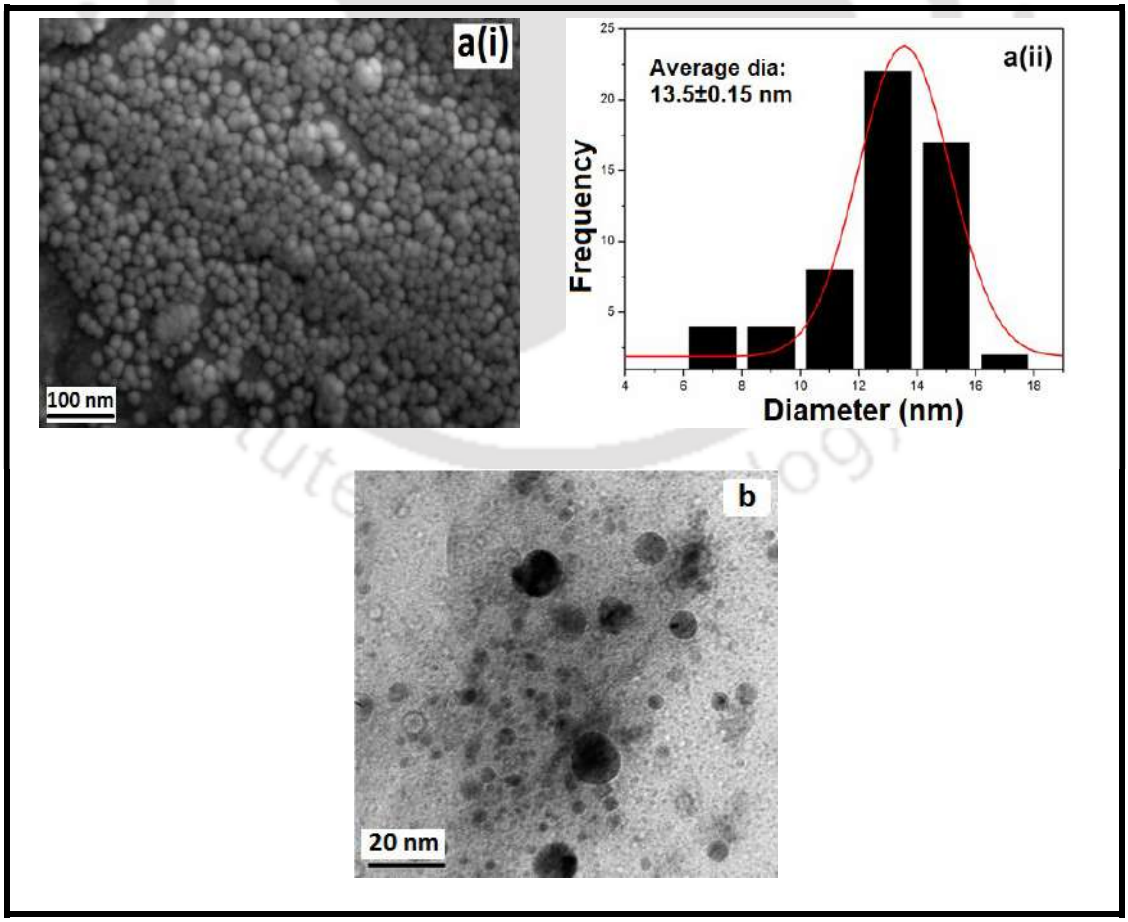

Figure 6.1: (a) FESEM analysis and (b) TEM analysis of prepared iron NPs

Figure 6.2 (a), (b), and (c) depicts the pH responsive cross-section morphology of the pristine PVDF-co-HFP membrane prepared using PEGME blend humic acid as additive at pH 3, 7, and 12 respectively. It was observed that at low pH the pores are well stretched and elongated. Whereas with increase in pH the polymer swelling occurs, and at high pH 12 due to swelling the pores of the pH responsive membrane ultimately gets blocked.

Figure 6.3 (a), (b), and (c) shows the cross-sectional thickness variation of the pH responsive PVDF-co-HFP membrane when submerged in pH solution of 3, 7, and 12 respectively. It was obtained that as described in Figure 6.2 due to polymer swelling the cross-sectional thickness enhances with increasing pH. At pH 3 the thickness was found to be 180 µm, whereas with increase in pH to 7, and 12 the thickness increases to 237 and 309 µm respectively.

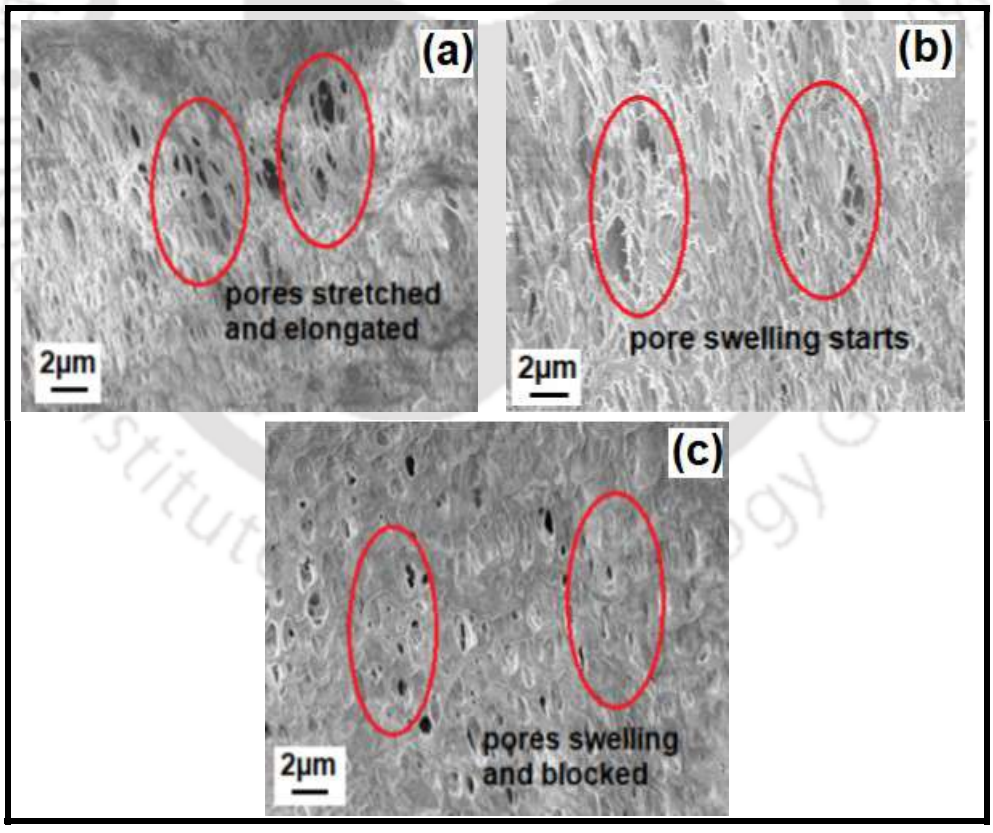

Figure 6.2: Cross-sectional images of pH responsive PVDF-co-HFP polymeric membrane at (a) pH 3 (b) pH 4, and (c) pH 12

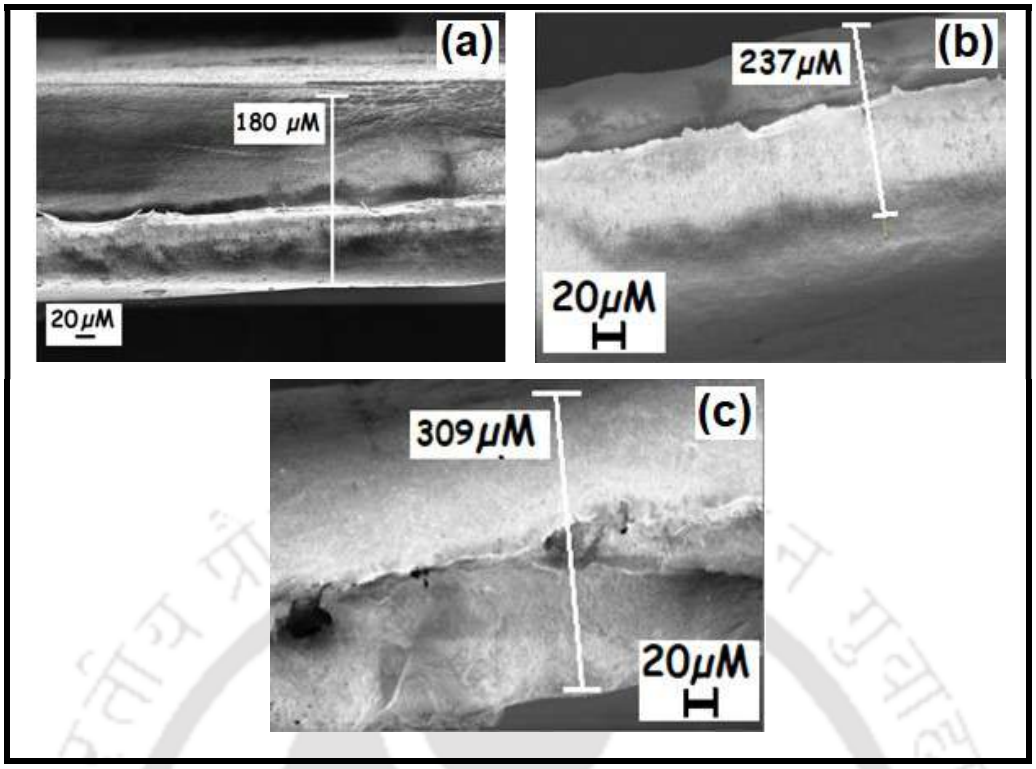

Figure 6.3: Cross-sectional thickness of pH responsive membrane at (a) pH3, (b) pH7 and (c) pH12

The FESEM images in Figure 6.4 depicts the morphological structure of pristine pH responsive membrane and iron NPs impregnated pH responsive membrane. The surface view of the pristine membrane from Figure 6.4 a(i) shows the porosity of the membrane and the minute pore formation over the pristine pH responsive membrane surface.

From the iron NPs impregnated membrane surface view shown in Figure 6.4 a(ii) and a(iii) it is observed that the 1 wt% NPs is distributed over the surface more non-homogeneously than the 0.01 wt% NPs. Large agglomerates are found over 1 wt% NPs dosage membrane, whereas agglomeration decreased for 0.01 wt% NPs dosage. The cross sectional view gives a better insight about the pores formation and iron NPs entrapment inside the pores. From Figure 6.4 b(i) it is observed that the pristine pH responsive membranes have more enlarged porous structure; whereas the iron NPs impregnated

membrane shown in Figure 6.4 b(ii) and b(iii) shows less porous nature and pore blockage.

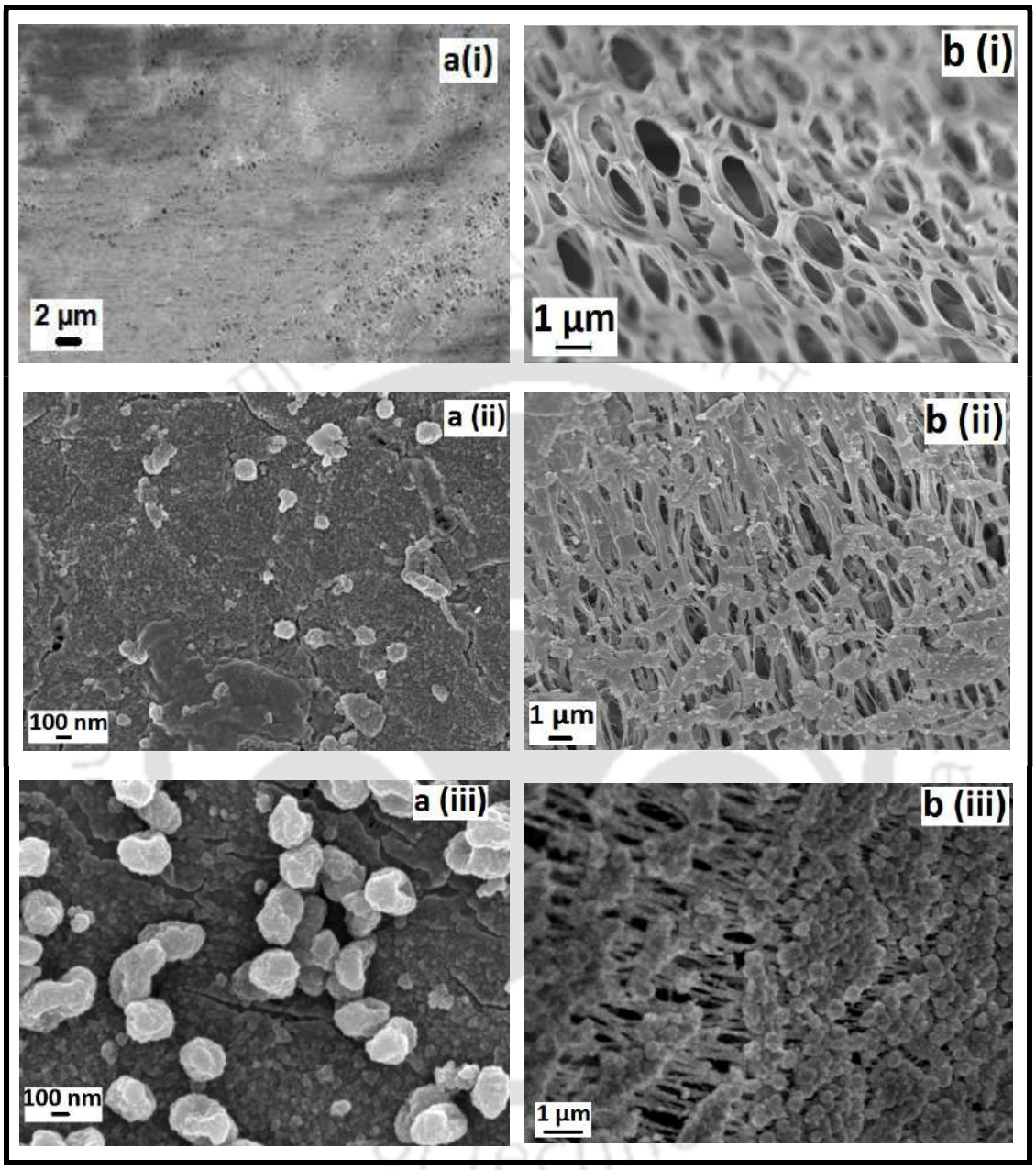

Figure 6.4: FESEM analysis of the (a) surface view and (b) cross sectional view at Mag= 5KX of different membranes (i) pristine PVDF-co-HFP membrane (ii) 0.01 wt% and (iii) 1 wt% NPs impregnated membrane.

Figure 6.4 b(ii) shows less pore blockage by 0.01 wt% NPs dosage, whereas Figure 6.4 b(iii) shows maximum pore blockage by 1 wt% NPs dosage. The cross sectional view confirms that the iron NPs hindered the formation of pores and blocked them.

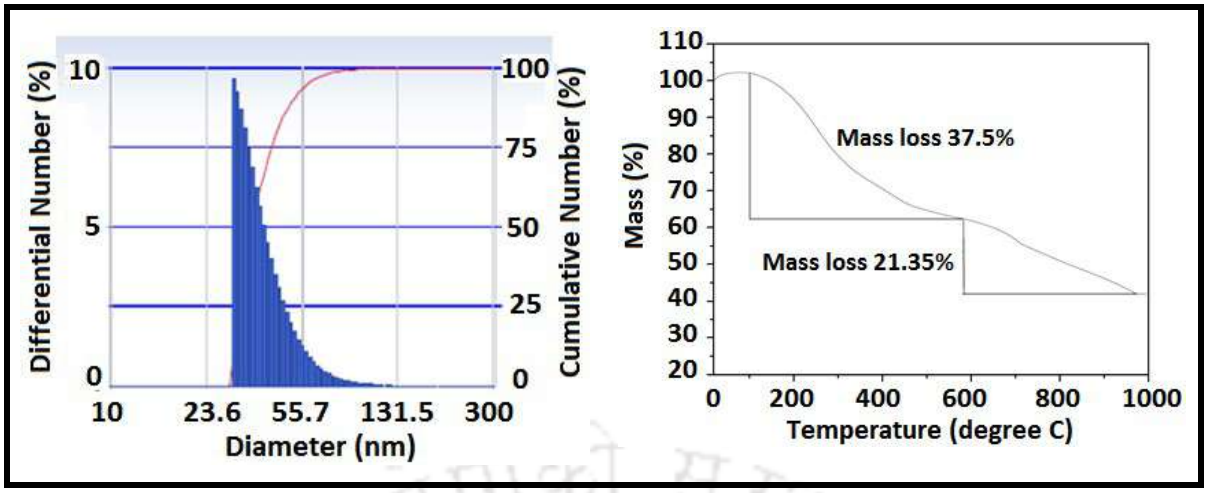

Figure 6.5: (a) Particle size distribution dispersed in ethanol and (b) thermal stability of iron NPs.

Particle size analysis shown in Figure 6.5(a) shows that the highest cumulative % of the iron NPs ranged up to 30 nm. The counts of iron NPs decrease with increase in diameter. TGA analysis of iron NPs from Figure 6.5(b) shows that there are two main weight loss occurred. First one is at around 105 ºC (around 37.5%) which is mainly because of moisture content of the sample, another at around 585 ºC (around 21.3%) which may be denoted as the loss of carbonaceous matter due the biomolecules present in clove extract. A total of around 58.8% of the iron NPs mass is lost due to the biomolecules enabled stabilized coating formed and moisture over the iron NPs. The remaining 41.2% mass is due to the iron NPs.

XRD characterization of iron NPs and iron NPs impregnated PVDF-co-HFP membranes and pristine membrane is shown in Figure 6.6 (a), (b) and (c). From the Figure 6.6 (a) it was observed that no XRD peaks are obtained for the pristine pH responsive PVDF-co-HFP membranes. Iron NPs shows as discussed in earlier chapters shows peaks at different 2θ values for various forms of iron oxide as well as zero valent iron (ZVI) as shown in Figure 6.6(b). The peaks are not so sharp indicating amorphousness of the material.

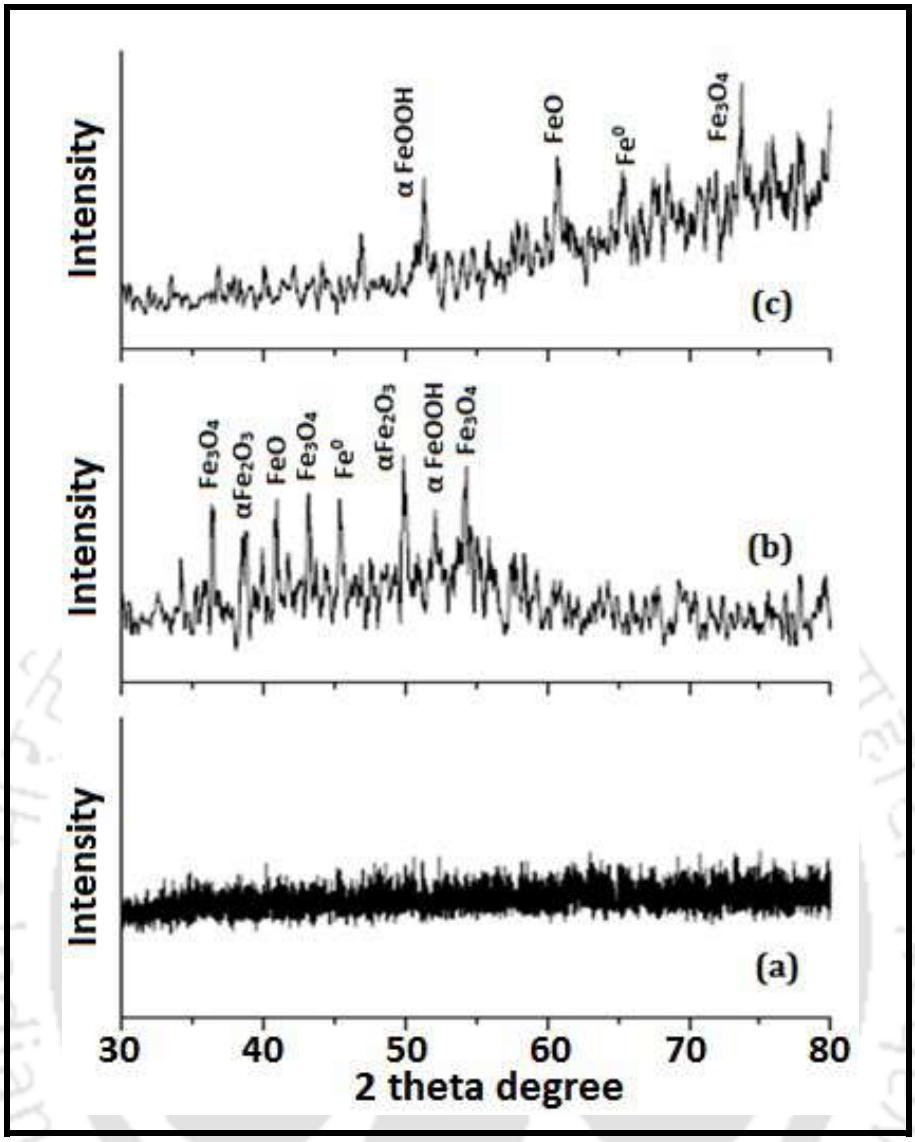

Figure 6.6: XRD graph for (a) pristine membrane (b) iron NPs and (c) iron NPs impregnated membrane.

Peak at 2θ value 45.1º denotes Fe^0 (bcc) (1 1 0) (JCPDS 65-4899). Peak at 51.1º symbolizes α FeOOH at (2 2 1) [220]. Peaks at 36.4º, 43.2º and 54.3º denotes Fe_3O_4 at planes (3 1 1), (4 0 0) and (4 2 2), respectively [33]. Peak at 40.95º stands for FeO at (2 0 0), whereas peaks at 49.9º and 38.9º represents the presence of αFe_2O_3 at (0 2 4) and (1 0 4) [220], respectively. In Figure 6.6(c), Fe-NPs impregnated pH responsive PVDF-co-HFP membrane shows peaks at 52.3º denoting α FeOOH at (2 2 1). Peak at 60.7º indicates FeO at (2 2 0), whereas at 65.45º Fe^0 (bcc) at (2 0 0) present, and at 73.8º Fe_3O_4 at plane (5 3 3)

is present [220]. XRD characterization shows that though zero valent iron NPs are present but along with its oxides forms are also present. Through XRD it can be confirmed that a core shell of iron NPs was formed, with Fe^0 at the core which is shelled by its oxide forms [31]. The impregantion of zero valent iron NPs along with its oxide form within pH responsive PVDF-co-HFP membranes were successfully fabricated.

6.2.2. Kinetics of NB reduction

Degradation of nitrobenzene has been explained in a schematic diagram shown in Figure 6.7. The diagram represents the reduction and oxidation reaction occurring simultaneously between NB and iron NPs respectively. Degradation of nitrobenzene could be explained by pseudo first order kinetic model [228] as:

$$\frac{dC_{NB}}{dt} = -k_{obs}C_{NB} \quad (6.3)$$

Where, C_{NB} is the nitrobenzene concentration and k_{obs} (min^{-1}) is the observed first order rate constant. Integration of the Eq. 6.4 results in the following equation:

$$C_{NB} = C_{NB}^{0}e^{-k_{obs}t} \quad (6.4)$$

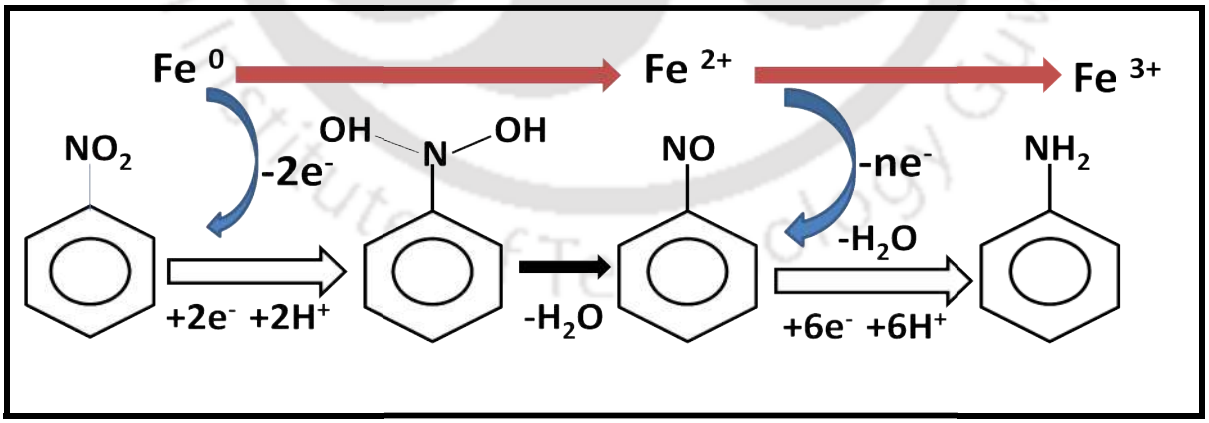

Figure 6.7: Reaction mechanism for red-ox reaction of Nitrobenzene and zero-valent Iron NPs

Where, C_{NB}^{0} is the initial concentration of nitrobenzene and t is the residence time. Therefore, k_{obs} was calculated from the regression of ln C_{NB} versus residence time.

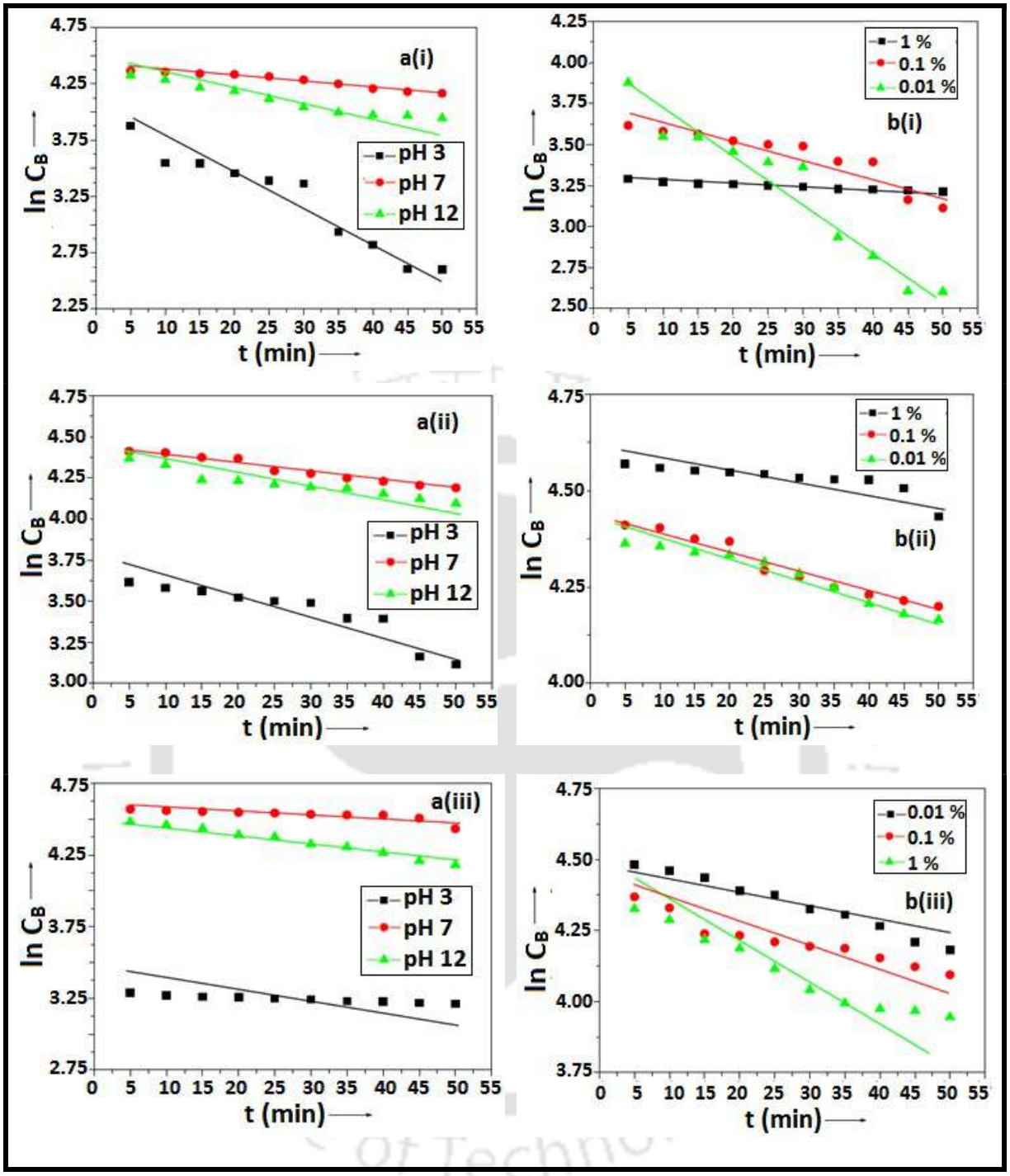

Figure 6.8: (a) Rate constant determination at various pH values for membranes containing (i) 0.01 wt% (ii) 0.1 wt% and (iii) 1 wt% iron NPs and (b) Rate constant determination of various iron NPs wt% membranes at (i) pH 3 (ii) pH 7 and (iii) pH 12.

Previous study shows that the reaction rate decreases as pH increases [228]. In this study which involves NB reduction by iron NPs impregnated in pH responsive PVDF-co-HFP

membranes, the highest NB reduction was obtained at pH 3 and decreases for pH 7 but the rate again increase for pH 12. This sudden increase at pH12 was obtained first in this study which is attributed due to the pH responsiveness of the membrane explained earlier. From Figure 6.8 a(iii), it was observed from the regression line of ln C_{NB} versus residence time that for 1 wt% iron in the pH responsive membrane, the rate of reaction (0.0068 min^{-1}) is highest at pH 3. It decreases for pH 7, (k_{obs} = 0.0016 min^{-1}) but it suddenly increases for pH 12 (k_{obs}= 0.0022 min^{-1}). Similarly, for 0.1 wt% and 0.01 wt% shown in Figure 6.8 a(i) and (ii).

Table 6.4: Observed reaction rate values at different pH and iron wt%

	0.01 wt%			**0.1 wt%**			**1 wt%**	
	k_{obs} (min^{-1})	R^2		k_{obs} (min^{-1})	R^2		k_{obs} (min^{-1})	R^2
pH 3	0.028	0.938	**pH 3**	0.01	0.91	**pH 3**	0.0068	0.978
pH 7	0.005	0.954	**pH 7**	0.005	0.97	**pH 7**	0.0016	0.89
pH 12	0.009	0.958	**pH 12**	0.006	0.942	**pH 12**	0.0022	0.98
	pH 3			**pH 7**			**pH 12**	
	k_{obs} (min^{-1})	R^2		k_{obs} (min^{-1})	R^2		k_{obs} (min^{-1})	R^2
0.01 %	0.028	0.938	**0.01 %**	0.005	0.954	**0.01 %**	0.009	0.958
0.1 %	0.01	0.91	**0.1 %**	0.005	0.97	**0.1 %**	0.006	0.942
1 %	0.0068	0.978	**1 %**	0.0016	0.89	**1 %**	0.002	0.98

Table 6.4 represents the different k_{obs} for different pH at different iron NPs wt% loading. Previous studies [228] confirm that the NB reduction increases the pH which paves the way for zero-valent iron NPs corrosion by forming hydroxide ions. Initially presence of O_2 acts as oxidizing agent and responsible for rapid corrosion. Further it oxidizes Fe^{2+} to Fe^{3+}. So, in the present study, presence of O_2 was avoided by purging N_2 (99.9% purity) over the solution. However, somehow oxidation will prevail, and is executed by the water molecules itself in the solution in absence of O_2. Both the reactions for oxygen and water contributing towards the oxidation and increase in pH are observed as below [228]:

$$Fe^0 + \frac{1}{2}O_2 + H_2O \rightarrow Fe^{2+} + 2\,OH^- \quad (6.5)$$

$$Fe^0 + 2\,H_2O \rightarrow Fe^{2+} + H_2 + 2OH^- \quad (6.6)$$

It can be seen from Figure 6.9 a(i) that 0.01 wt% iron NPs shows highest aniline concentration (19.3 ppm for first 10 min at pH 3). At pH 7 and pH 12 aniline forms around 13.8 ppm and 14.2 ppm, respectively for first 10 min. NB reduction study was carried at different batch reactions, where iron content was varied. It is observed from the Figure 6.8a(i), (ii) and (iii) that at different pH the k_{obs} goes on decreasing as the iron wt% increases. At pH3, k_{obs}=0.0282 min^{-1} for 0.01wt% iron NPs was maximum whereas for 0.1 and 1 wt% the values were 0.0105 min^{-1} and 0.0016 min^{-1} respectively.

The k_{obs} value increased for 0.01 wt% but decreases for 0.1 and 1 wt%, respectively. This trend can be explained due to the agglomeration pattern of the iron NPs on the pH responsive membrane surface. The FESEM image of 1 wt% iron NPs membrane surface from Figure 6.4 a(iii) and b(iii) shows that the iron NPs are somewhat agglomerated over a few regions, and the homogeneity is very less. Agglomeration decreases for 0.1 wt% and maximum homogeneity was achieved for 0.01 wt% shown in Figure 6.4 a(ii). As the homogeneity of the iron NPs increases over the membrane surface, the chance of better and maximum contact between the NB solution and iron NPs occurs. Due to this mass exchange as well as the reaction enhances, which results for better NB concentration reduction as well as aniline formation [34].

6.2.3. Effect of iron NPs content on aniline formation and NB reduction

Figures 6.10 (a), (b) and (c) depict at pH3 the maximum NB reduction was 89.92% for 0.01 wt% iron NPs, whereas for 0.1 wt% and 1 wt% the NB reduction values were 82.75% and 79.45%, respectively.

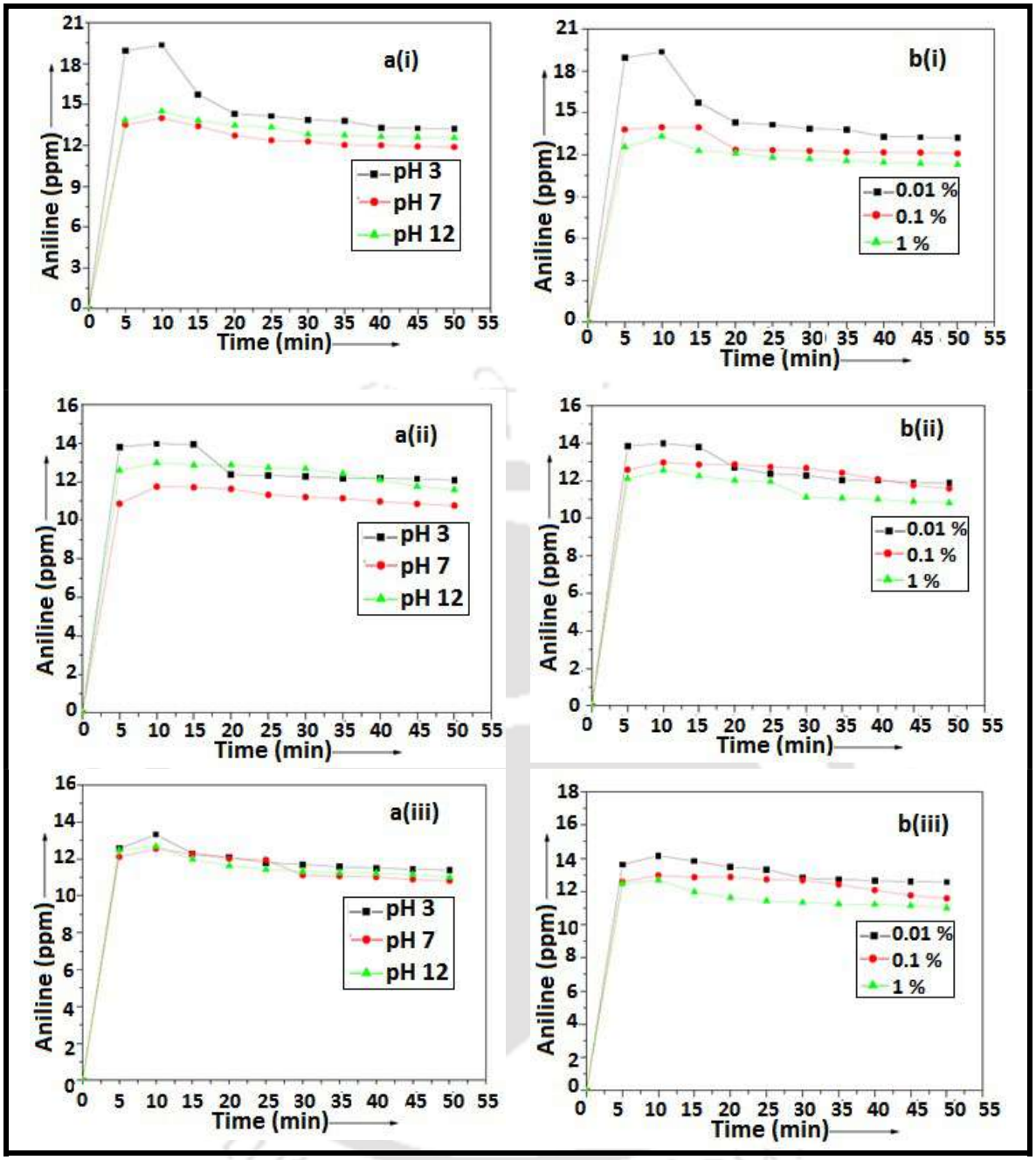

Figure 6.9: (a) Aniline formation vs. time for membranes at different pH containing (i) 0.01 wt% (ii) 0.1 wt% and (iii) 1 wt% iron NPs and (b): Aniline formation vs. time for different iron NPs wt% membrane at (i) 3 pH (ii) 7 pH and (iii) 12 pH.

Similar trend was followed for pH 7 and 12. The overall aniline formation at the end of 50 min is shown in Figure 6.11 where a deviation was observed from usual trend [228]. Maximum aniline formation for 0.1 wt% iron NPs is achieved at pH3 (15 ppm) then for

pH7 it decreases (12.8 ppm) and increases for pH12 (13.9 ppm). For other wt% iron NPs in the pH responsive membrane the same trend is observed.

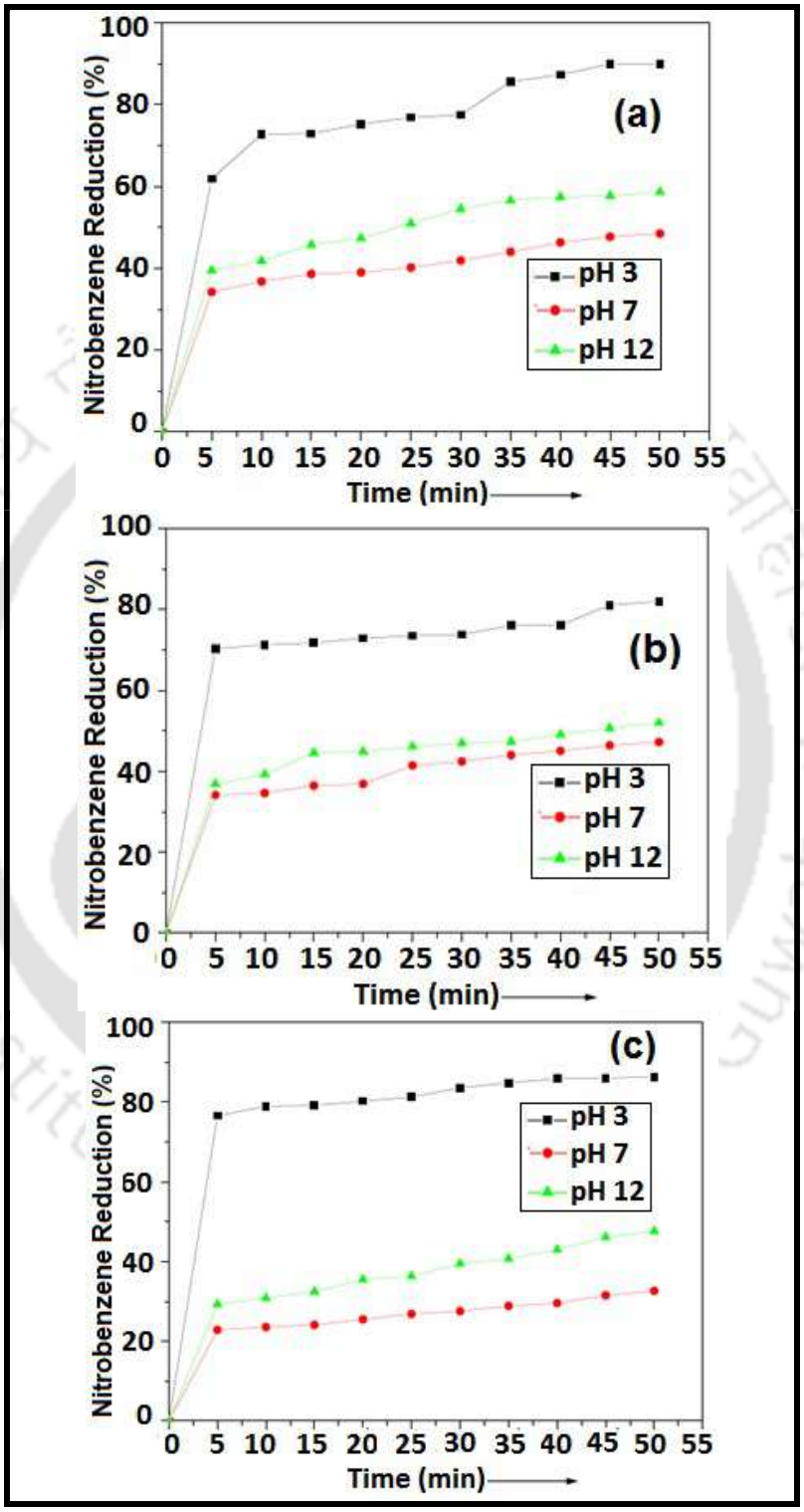

Figure 6.10: Nitrobenzene reduction at various pH for membranes containing (a) 0.01 wt% (b) 0.1 wt% and (c) 1 wt% iron NPs.

6.2.4. Effect of pH on membrane water flux, aniline formation and NB reduction

At low pH, carboxyl groups (-COOH) are protonated and hydrophobic interactions dominate, leading to a volume shrinkage of the polymer that contains the carboxyl groups. Thus, leading to increased average pore size of the membranes [155]. At high pH, carboxyl groups dissociate into carboxylate ions ($-COO^-$) and H^+ ions, whereas phenolic groups into phenolate ions ($-C_6H_5O^-$) and H^+ ions, which results high charge density in the polymer causing it to swell [156]. Thus the pore size of the membranes decreases. The hydraulic permeability of PEGME blend HA membrane revealed that at pH 3 highest flux of 142 L/m^2h was attained, whereas at pH7 it decreases to 117.2 L/m^2h and when pH increased to 12, due to more decrease in pore size flux changed to 58 L/m^2h. PVDF-co-HFP membrane without PEGME and HA as additive, showed steady water flux of 31.2 L/m^2h.

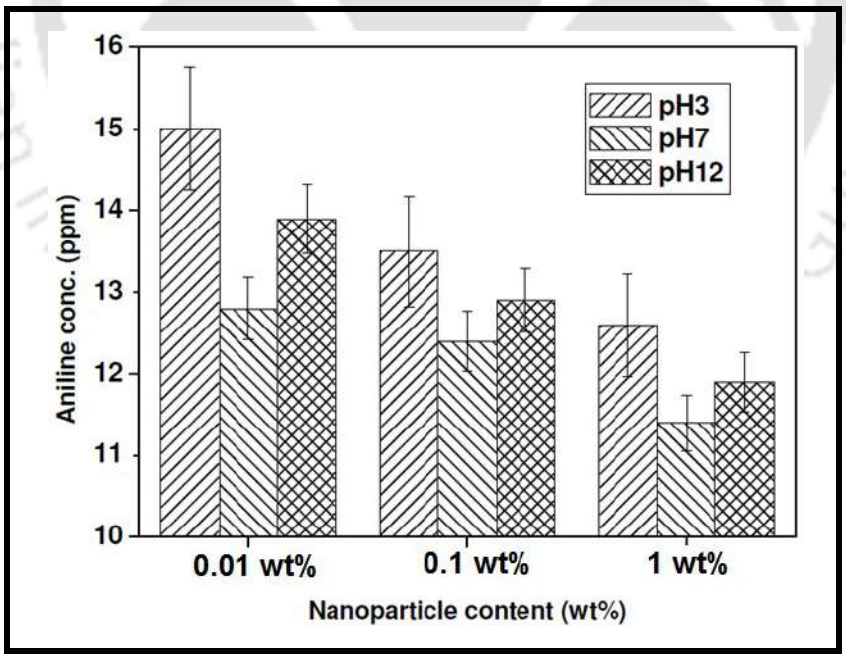

Figure 6.11: Overall aniline production after 50 min of NB reduction

At pH3 much of the degradation of NB and formation of aniline occurs due to high H^+ concentration in solution. With increase in pH from 3 to 7 the reducing property decreases

due to corrosion of zero-valent iron NPs. Even though at pH 4.26 the de-protonation of (–COOH) from membrane layer starts and releases H^+ which helps reducing NB and aniline formation but doesn't exceed the value as that for pH3. However, at pH12, both –COOH and $–C_6H_5OH$ starts deprotonating and high concentration of OH^- helps to form various intermediate products which cause much more NB reduction than that at pH7 [229].

The other feature of the pH responsiveness of the membrane which contributes towards this NB reduction process is that the pore size varies with the pH of the solution. As the pH increases to 4.26 and 7.8 de-protonation of (COOH) and (C_6H_5OH) occurs simultaneously. Due to de-protonation charge density within the membrane increase and as a result the polymer swells. Thus due to the swelling in skin layer of modified membranes at pH7 and pH12, pores of the membranes goes on decreasing [155]. This in fact increases the retention time of the NB solution within the membrane as well as with the iron NPs impregnated. Due to this increase in retention time, there is increase in NB reduction and aniline formation at pH12 rather than at pH7.

6.2.5. Effect of iron content, initial concentration and pH on fluoride rejection

From the above conducted experiments the optimized iron content was found to be 0.01 wt%. Hence the fluoride rejection study was carried out with 0.01 wt% iron NPs impregnated membrane with varying pH solutions of fluoride. From Figure 6.12 it was observed that as the initial concentration of the fluoride solution increases, % rejection also increases. Rejection percentage was found to be dependent on the iron NPs as well as the pore size of the membrane. Fluoride ions get entrapped in between the pores of the membrane. At pH 7 rejection increase from 55.68%to 72% for 5 ppm and 20 ppm

respectively. With increase in fluoride concentration number of participating ions increases which increases the probability of getting trapped within the membrane pores and iron NPs surface.

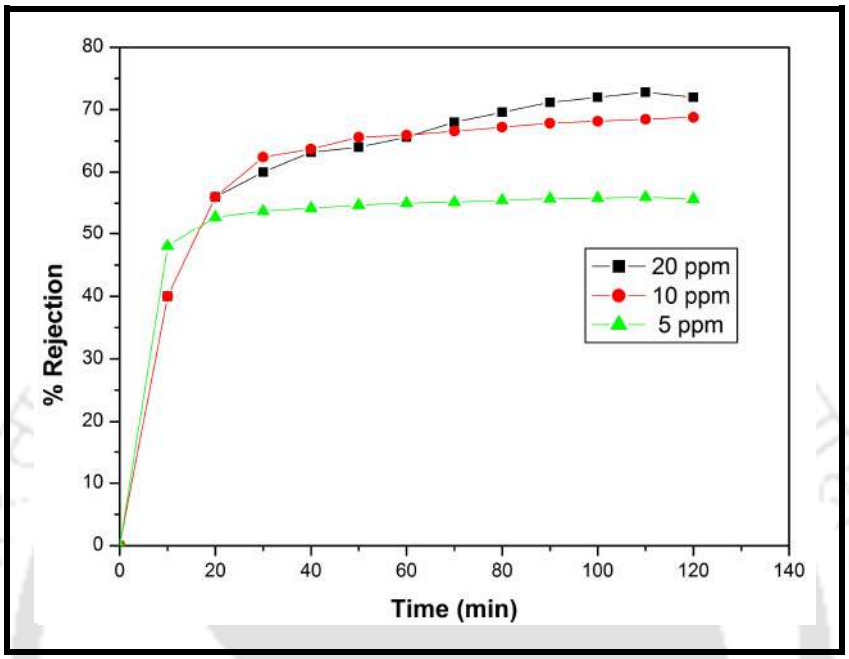

Figure 6.12: Rejection study in accordance to various fluoride concentrations

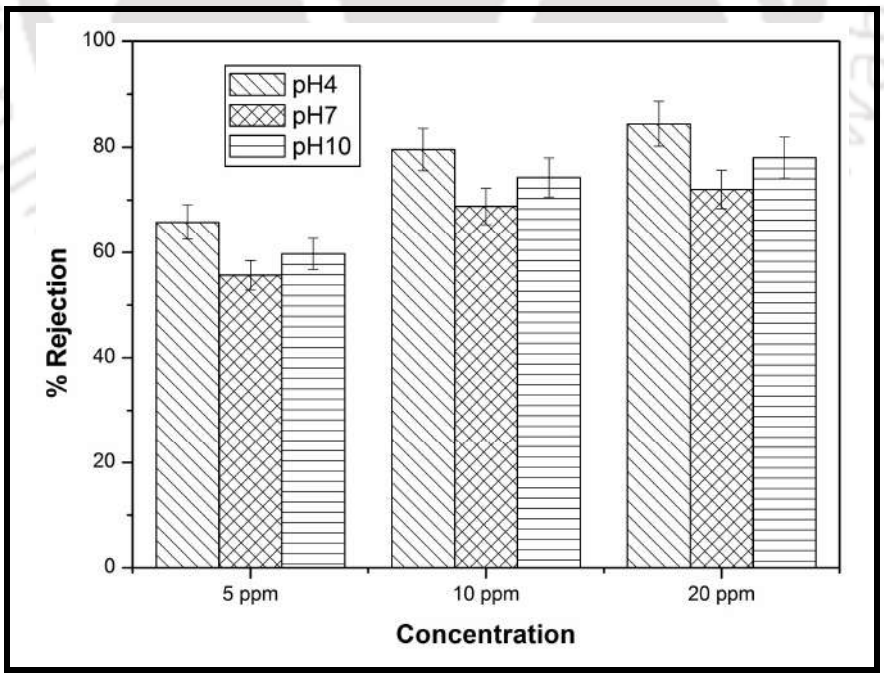

Figure 6.13: Rejection behaviour with respect to pH and different concentration

Figure 6.13 explains the effect of pH on the rejection study of fluoride. The pH responsiveness of the prepared membrane plays an effective role for fluoride rejection. At pH 4 the rejection % was found to be highest for all the prepared fluoride solutions. This can be attributed to the fact that at low pH the electrostatic interaction of the negatively charged fluoride ions increases between iron NPs and the membrane polymer. For 20 ppm, 10 ppm and 5 ppm solutions at pH 4 the rejection was found to be 84.4%, 78.56% and 65.8% respectively. With increase in pH the electrostatic interaction decreases leading to decrease in fluoride rejection. Hence for 20 ppm, 10 ppm and 5 ppm solutions at pH 7 the rejection decreases to 72%, 68.8 % and 55.68% respectively. But interestingly at pH 12 due to the de-protonation behaviour of the prepared membrane (as discussed in previous section) the pore size gets reduced as well as H^+ ions prevail in the membrane polymer. This results for increase in fluoride rejection at pH 12 but not exceeding the value for pH4. For 20 ppm, 10 ppm and 5 ppm solutions at pH 12 the rejection was found to be 78%, 74.25% and 59.7% respectively.

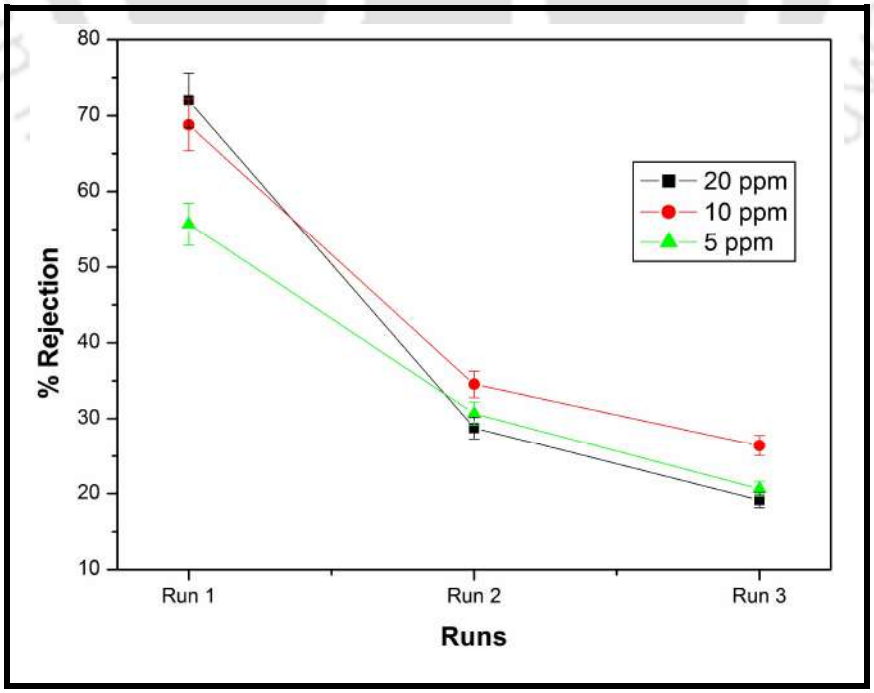

Figure 6.14: % rejection study of fluoride with various run cycle

After each run the membranes were back flushed with acidic (0.1N HCl) and basic (0.1N NaOH) solutions and then sonicated for 20-30 mins in same solution. The basic solution was found to be more effective which reduces the electrostatic bonding nature between fluoride ions with the iron NPs and membrane polymer. Figure 6.14 shows the trend of fluoride rejection for three run cycles. It is observed that at the end of 3rd run fluoride rejection of 20 ppm solution falls to 19.65% whereas for 10 ppm and 5 ppm solutions the rejection is about 25.42% and 22.27% respectively. With decrease in solution concentration increase in desorption rate is observed. Hence for 5 ppm fluoride solution the rejection at the end of 3 run falls by 60%, whereas for 10 ppm and 20 ppm it falls by 63.05% and 72.7% respectively. This result can be attributed to the fact that as concentration increases the amount of fluoride ions which gets trapped inside membrane pore as well as surface of iron NPs also increases [229]. Hence due to concentration polarization the rejection percentage at the end of 3rd cycle decreases with increase in solution concentration.

6.2.6. Central composite designed model for NB reduction and aniline formation

The NB reduction and aniline formation model is given by Eq. 6.7 and 6.8 respectively. The experiments were carried on with the iron content (A) range from (0.3-1) wt%, pH range from (3.5-11) and time (15-50 min). A positive value of a coefficient symbolizes a synergistic effect, whereas a negative value indicates an opposite effect.

$$\textbf{NB reduction} = 48.48 - 4.93\times A - 10.02\times B - 5.76\times C - 9.37A\times B - 1.13\times A\times C + 0.63\times B\times C - 6.73\times A^2 + 10.59\times B^2 + 4.23\times C^2 \quad (6.7)$$

$$\textbf{Aniline} = 11.44 - 0.24\times A - 0.079\times B + 0.007\times C + 0.15\times A\times B - 0.29\times A\times C - 0.15\times B\times C + 0.45\times A^2 - 0.36\times B^2 - 0.06\times C^2 \quad (6.8)$$

Table 6.5: Analysis of variance results for the CCD design

Source	Sum of square	Degree of freedom	Mean square	F- Value	Prob>F
Nitrobenzene reduction (%)					
Model	5688.94	9	632.1	710.85	< 0.0001[s]
A- iron content	323.2	1	323.2	363.46	< 0.0001
B- pH	1325.13	1	1325.13	1490.23	< 0.0001
C- time	464.54	1	464.54	522.42	< 0.0001
AB	752.91	1	752.9	846.72	< 0.0001
AC	5.26	1	5.26	5.92	0.035
BC	4.64	1	4.64	5.21	0.045
A^2	645.6	1	645.6	726.04	< 0.0001
B^2	1628.72	1	1628.72	1831.64	< 0.0001
C^2	354.03	1	354.03	398.14	< 0.0001
Residual	8.89	10	0.89		
Lack of Fit	6.52	5	1.30	2.75	0.146[ns]
Pure Error	2.38	5	0.47		
$R^2 = 0.937$, $R^2_{adj} = 0.92$, $R^2_{pred} = 0.89$, adequate precision = 110.6					
Aniline formation (ppm)					
Model	7.315	9	0.81	137.04	< 0.0001[s]
A- iron content	0.77	1	0.77	130.3	< 0.0001
B- pH	0.086	1	0.086	14.52	0.003
C- time	0.0007	1	0.0007	0.12	0.73
AB	0.18	1	0.18	30.35	0.0003
AC	0.65	1	0.65	109.56	< 0.0001
BC	0.186	1	0.18	31.37	0.0002
A^2	2.97	1	2.97	501.36	< 0.0001
B^2	1.87	1	1.88	316.12	< 0.0001
C^2	0.052	1	0.05	8.79	0.014
Residual	0.06	10	0.006		
Lack of Fit	0.012	5	0.002	0.25	0.92[ns]
Pure Error	0.047	5	0.0094		
$R^2 = 0.943$, $R^2_{adj} = 0.925$, $R^2_{pred} = 0.917$, adequate precision = 52.12					

[s] significant at prob>F value less than 0.05, [ns] not significant at prob>F value greater than 0.1.

The A, B and C are the coded values of variables iron content (wt %), pH and time (min), respectively. The adequacy of the model was ensured and tested by Fischer variation (F-value), probability values (p-value) and the correlation coefficient (R^2). From Table 6.5, the F values for both the quadratic model of NB reduction and aniline formation was quite high and p values <0.0001 for both the models indicates strong significance. It means that there is a probability of 0.01% to not follow the model.

The predicted R^2 value of 0.89 and 0.917 was in reasonable agreement with the adjusted R^2 of 0.92 and 0.925 for NB reduction and aniline formation, respectively. It shows that the model fitted quite nicely. From Table 6.5**,** the linear term of iron content (A), pH (B) and time (C) with F-values 298.9, 1236.5 and 408.5 respectively, indicates the significant role of the factors contributing for NB reduction. Similarly for aniline, iron content (A) and pH (B) showed greater important role than time (C). The interactive term AB, AC and BC were important for both NB reduction and aniline formation, all interactive term played important role. For both the models quadratic terms A^2, B^2 and C^2 were significant. The p value (Prob>F) for all the model terms (A, B, C, AB, AC, BC, A^2, B^2 and C^2) are less than 0.05 which indicates that they all are significant.

6.2.7. Optimization study for NB reduction and aniline formation

An optimization study of all of the independent input variables is performed through a desirability function (D) for two responses (NB reduction and aniline formation). Numerical optimization was carried by setting the variables (iron content, pH and time) within certain range and responses (NB reduction and aniline formation) at maximum value by Design-Expert 7.0 software. The optimization conditions were mentioned in Table 6.3. The optimum value for variables was predicted for maximum NB reduction and aniline formation. The optimum conditions which were predicted then analyzed

experimentally and error percentage was calculated to analyze the adequacy of the quadratic model and optimization feature of the Design-Expert 7.0 software

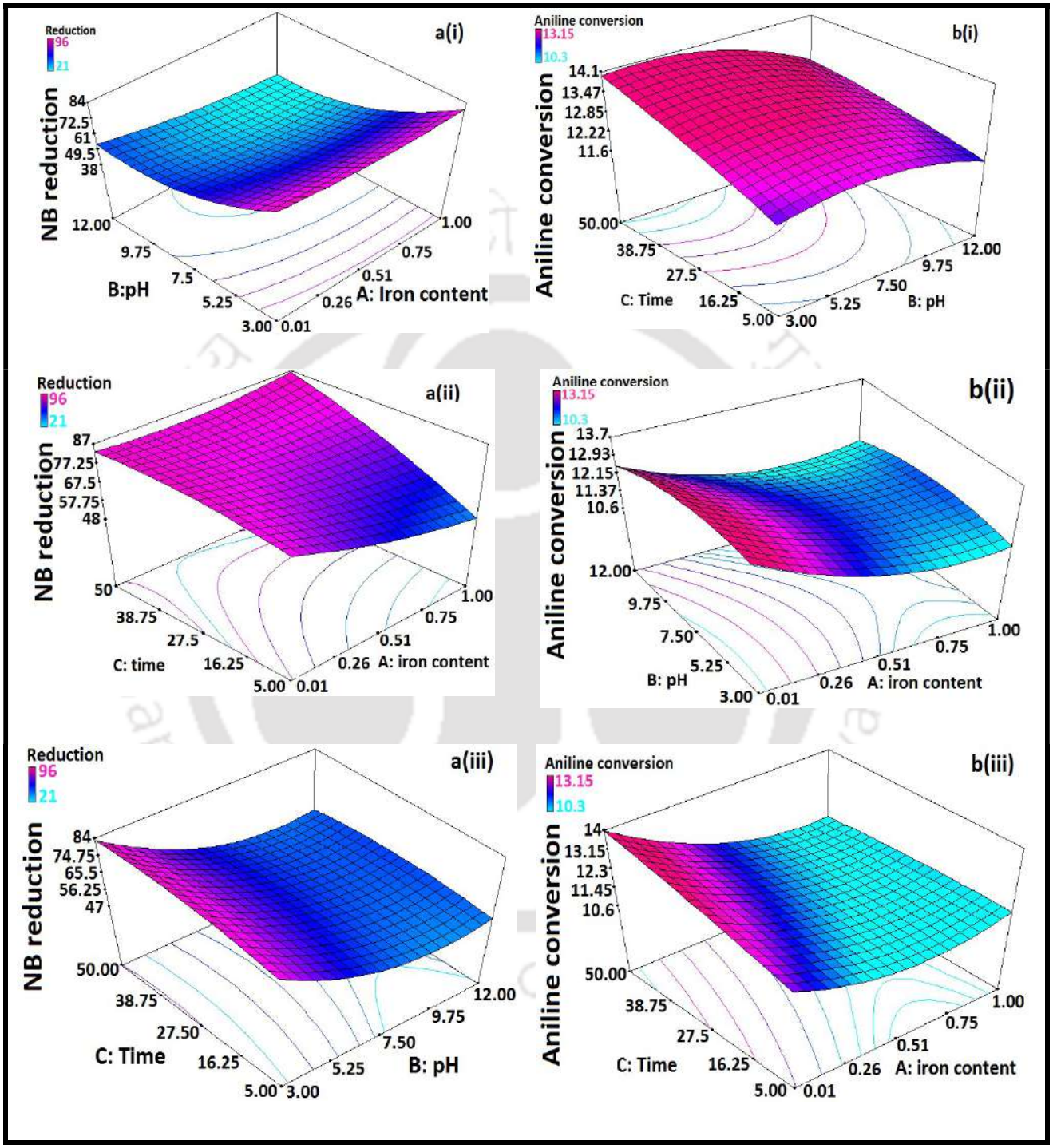

Figure 6.15: (a) NB reduction % varying with (i) iron content and pH (ii) iron content and time (iii) time and pH, and (b) aniline formation varying with (i) pH and time (b) iron content and pH and (c) iron content and time.

. The 3D view of response surface methodology of NB reduction and aniline formation respectively is shown in Figure 6.15, it depicts that how the variables interact with each other. Optimization result of the maximum NB reduction (83.77 %) and aniline formation (13.58) was achieved at iron content 0.01 wt%, pH 3 and time 38.95 min (optimized conditions) with maximum desirability of 0.915. With decrease in iron wt%, NB reduction and aniline formation increases, which was also revealed in our preceding sections.

According to the experimental evaluation, the Design-Expert 7.0 statistical software also converged to the conclusion that at 0.01 wt% iron NPs content, NB reduction and aniline formation was higher than that of 1wt%. The Design Expert 7.0 software at optimized condition provides NB reduction of 83.77 % and aniline formation of 13.25 ppm, whereas experimental results gave NB reduction of 86.7 % (error 3.37%) and aniline formation of 12.7 ppm (error 3.93%) at the same optimized conditions.

Chapter 7

Preparation and characterization of novel green synthesized iron-aluminum nanocomposite and studying its efficiency in fluoride removal

Piyal Mondal & Mihir Kumar Purkait (2019): Preparation and characterization of novel green synthesized iron–aluminum nanocomposite and studying its efficiency in fluoride removal. Chemosphere (235) 391-402. Published 25/06/2019.

Preparation and characterization of novel green synthesized iron-aluminum nanocomposite and studying its efficiency in fluoride removal

This chapter deals with the preparation of a novel green synthesized iron-aluminum nanocomposite. The nanocomposite was characterized by FESEM, FTIR, EDX, XRD, BET, DSC and TGA analysis. The clove extract acting as both reducing and surface coating agent was optimized based on its maximum total flavonoid content (TFC) and total polyphenolic content (TPC). Fluoride adsorption studies was performed at 298K, 303K and 313K within the range of 10-40 mg/L fluoride solution for kinetic and isotherm studies. Maximum adsorption capacity of 42.95 mg/g was obtained for 0.25 g/L adsorbent dosage. Moreover fluoride adsorption obeyed pseudo second order kinetic model whereas the process was multistage diffusion controlled. Langmuir isotherm model best fitted the equilibrium data with monolayer adsorption capacities of 25.09, 26.08 and 28.07 mg/g at 298, 303 and 313K respectively. The findings confirmed that the fluoride adsorption process followed ion-exchange mechanism with the surface hydroxyl groups. The prepared nanocomposite was utilized for treating fluoride contaminated water samples from North- East regions of India which showed efficient removal percentage.

7.1. Experimental

7.1.1. Materials required

Clove was purchased from local market of IIT Guwahati, Assam (India). Folin-Ciocalteu's phenol reagent (FCR), Ferric chloride salt ($FeCl_3$), aluminium chloride

($AlCl_3$), sodium carbonate (Na_2CO_3), sodium nitrite ($NaNO_2$) and sodium hydroxide (NaOH) was procured from Merk, Germany. Sodium sulphate (Na_2SO_4), sodium chloride (NaCl), potassium bicarbonate ($KHCO_3$) and sodium fluoride (NaF) was kindly delivered by Sigma Aldrich Co. USA. The details of the chemicals are provided in Table 2.1.

7.2. Experimental methods

7.2.1. Green synthesis of iron-aluminium nanocomposite

About 40 ml of prepared clove extract was maintained at pH 4 (clove extract preparation already discussed in Chapter 3) was mixed with a solution containing 0.025 (M) $FeCl_3$ (5ml) and 0.025 (M) $AlCl_3$ (5ml) (1:1 volume ratio). The reaction starts as the solution was kept at 70 ºC for 10-15 min and after then without disturbing the content it was again left for 30-40 min. Few minutes later a clear phase separation was observed with colourless solvent at the top and black thick precipitates at the bottom. After filtering, the retentive black portion was freeze dried at -15 ºC. Powdered nanocomposite was formed by using a vacuumed lyophilizer chamber maintained at temperature -50 ºC and pressure 0.04 mbar. Finally the nanocomposite powder was homogenized to pH 7, dried and kept within vacuum desiccators for further use. Figure 7.1 (a) and (b) shows that 1:1 v/v ratio of Fe: Al and 1.25 g/L dosage of the prepared nanocomposite yielded maximum removal (%) for 20 ppm fluoride stock solution.

7.2.2. Experimental techniques and analysis

Equilibrium isotherm and adsorption kinetic experiments were conducted at pH of 6.9 (±0.2) and temperatures 25°C, 30°C and 40°C. About 40 mL of fluoride solution (10, 20 and 40 mg/L) was taken in a 100 mL conical flask and purged with pure N_2 gas to remove excess oxygen if present. After purging, 0.05 g of green synthesized iron-aluminium

nanocomposite (1.25 g/L dosage) were placed in the inert flask, well capped with parafilm tape and kept in a shaker at 200 rpm for 2 h. After collecting samples at certain intervals of time the adsorbents were immediately separated by filtration. The filtrates were analyzed using Multipara meter analyser (CONSORT- C863, Made in Belgium) aided with fluoride electrode for concentration measurement.

For desorption study, the adsorbed fluoride contained nanocomposite was separated from fluoride solution using centrifuge system, maintained at 6000 rpm for 30 min. After that, the clear fluoride solution was discarded and the centrifuge bottles were washed vigorously with 40 mL of NaOH solution of different molar concentration (0.2M, 0.4M, 0.6M, 0.8M, 1.0M, 1.5M, 2.0M, 2.5M) so that the fluoride adsorbed nanocomposite mixes well with the solution. The solution was then agitated at 200 rpm at room temperature for 1h and analyzed further for fluoride concentration measurement.

For studying the effect of various counter ions towards fluoride adsorption process, various concentrations of HCO_3^{-1}, Cl^{-1} and SO_4^{-2} was prepared within 40mL of 40 ppm fluoride stock solution and after agitating at 200 rpm for 120 min the samples were analyzed for fluoride measurement. All the experimental runs were carried out thrice for error analysis and reported values are averaged one.

7.2.3. Real life water sample analysis

In order to implement the nanocomposite for real life water treatment application, fluoride contaminated water samples were collected from Mariani town of Jorhat district, Assam (India) and Kwakta town of Bishnupur district, Manipur (India). The water samples were analyzed in the laboratory for various parameters with the help of Microprocessor water analysis kit (VSI Electronics Pvt. Ltd., India).

7.3. Results and discussion

7.3.1. Influence of Fe-Al content ratio and adsorbent dosage

The (v/v) ratio in which 0.025 (M) Fe: Al was mixed as well as the adsorbent dosage exerted a noticeable variation in the fluoride removal (%) and equilibrium adsorption capacity (mg/g). From Figure 7.1(a) it was observed that 1:1 (v/v) ratio of 0.025 (M) Fe: Al obtained the maximum fluoride removal of 80.4% from 20 ppm fluoride stock solution. From Figure 7.1(b) it was found that for the same 1:1 (v/v) ratio prepared adsorbent, a dosage of 0.25 g/L, 1.25 g/L and 2.5 g/L the adsorption capacity showed a decreasing tendency of 42.95 mg/g, 11.5.82 mg/g and 5.82 mg/g respectively, whereas fluoride removal showed increasing tendency of 70.88%, 82.1% and 72% respectively. These results concluded that the highest adsorption capacity of 42.95 mg/g was achievable for 20PPM fluoride solution. In order to attain maximum fluoride removal percentage all the experiments were conducted with 1.25 g/L adsorbent dosage.

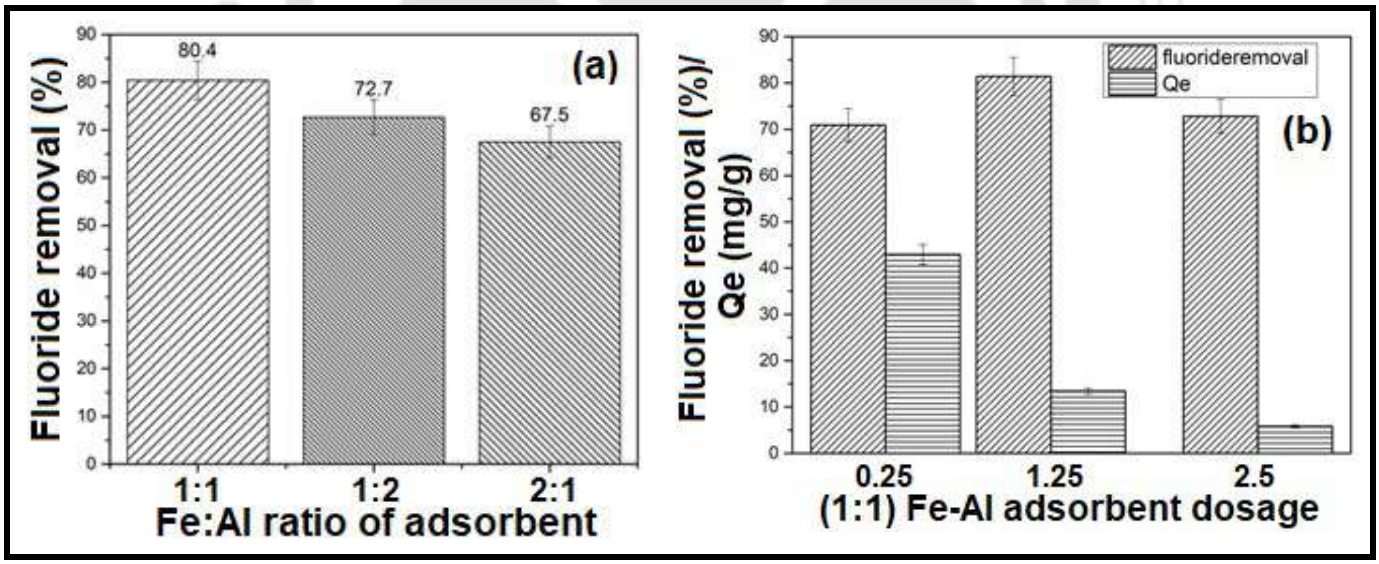

Figure 7.1: (a) Fluoride removal with respect to different Fe: Al (v/v ratio) for 20 ppm fluoride solution (b) Fluoride removal with respect to different dosage amount of (1:1) Fe-Al nanocomposite for 20 ppm fluoride solution.

7.3.2. Characterization analysis

The TEM image of the iron-aluminium composite was shown in Figure 7.2 a(i) and a(ii). Figure 7.2 a(i) shows the spindle like nanostructure of the mixed composite. The inset in Figure 7.2 a(i) SAED pattern shows that the nanocomposite was slightly amorphous in nature with no prominent dotted rings. The inset of Figure 7.2 a(ii) shows the d-spacing of the nanocomposite was ~0.39 nm. This confirms that the nanocomposite was slightly crystalline in nature.

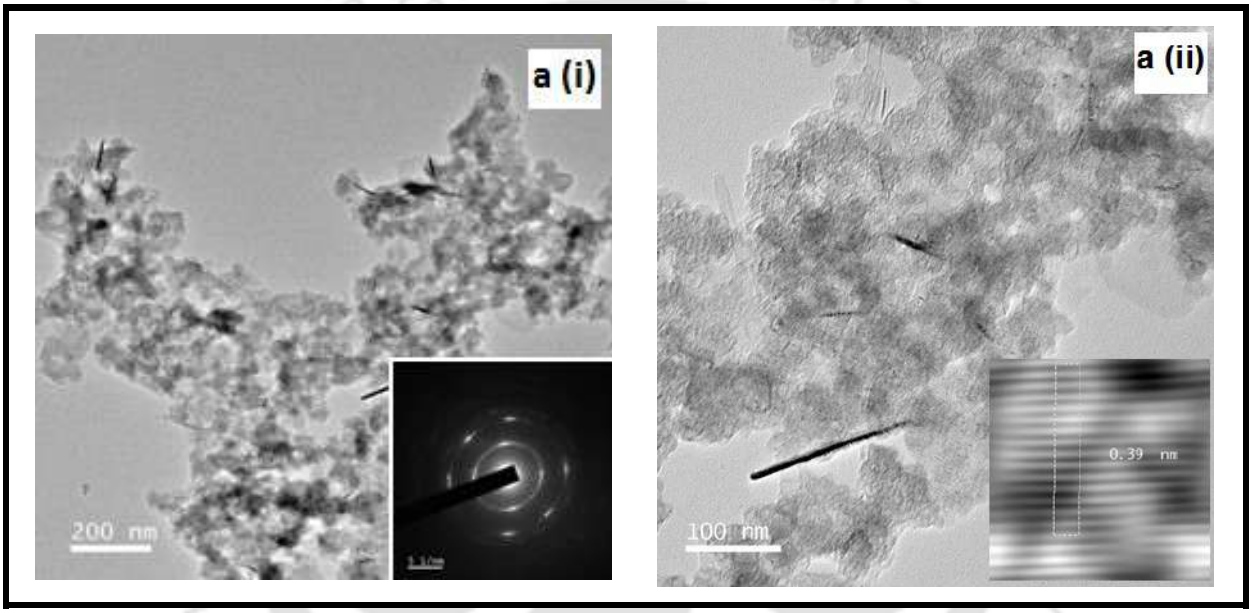

Figure 7.2: a(i) TEM images of green synthesized Fe-Al composite scale 200 nm (SAED pattern inset) a(ii) 100 nm scale with HRTEM image for d-spacing analysis of the Fe-Al composite (inset)

Figure 7.3 a(i) and a(ii) depicts the morphological analysis (FESEM) of the green synthesized iron-aluminium nanocomposite at two different magnifications. The figure describes the irregular crystalline shape of the composite. Mixed composites generally have such irregular pattern which was confirmed from previous literatures [230].

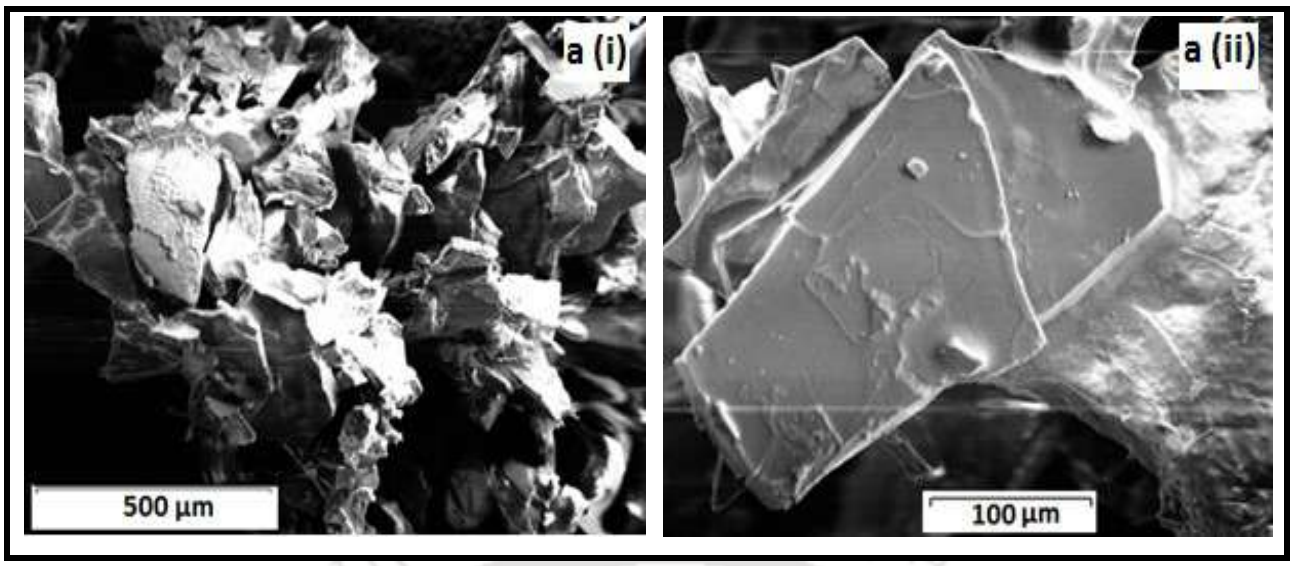

Figure 7.3: FESEM image of green synthesized Fe-Al composite

Figure 7.4 depicts the colour mapping of different element analysis and confirms the presence of carbon, oxygen, iron and aluminium in the green synthesized nanocomposite. The result shows that oxide formation of the mixed metals has taken place after reduction process. Due to the high phenolic and flavonoid content within the clove extract, carbon content within the nanocomposite was found to be quite large. The results confirm the carbonaceous nature of the iron-aluminium nanocomposite prepared through green synthesis.

The after adsorption effect on the green synthesized nanocomposite was evaluated and shown in Figure 7.5. The adsorption of fluoride onto the nanocomposite was quite eminent from the colour mapping of elemental analysis. From the figure it was observed that fluoride adsorption occurred on the green synthesized nanocomposite.

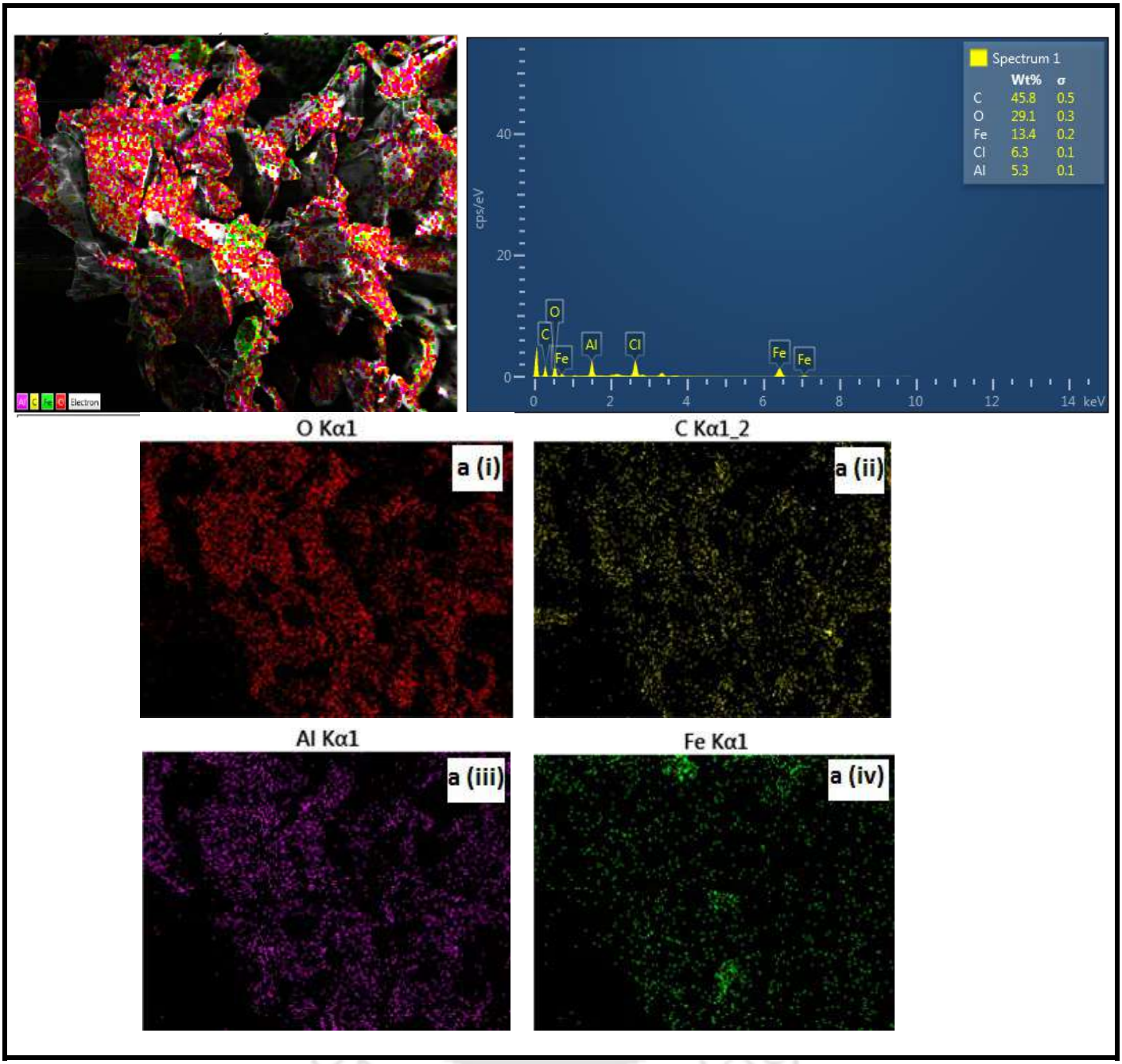

Figure 7.4: Elemental mapping analysis for a(i) Oxygen, a(ii) Carbon, a(iii) Aluminium and a(iv) Iron, of green synthesized Fe-Al composite before fluoride adsorption study.

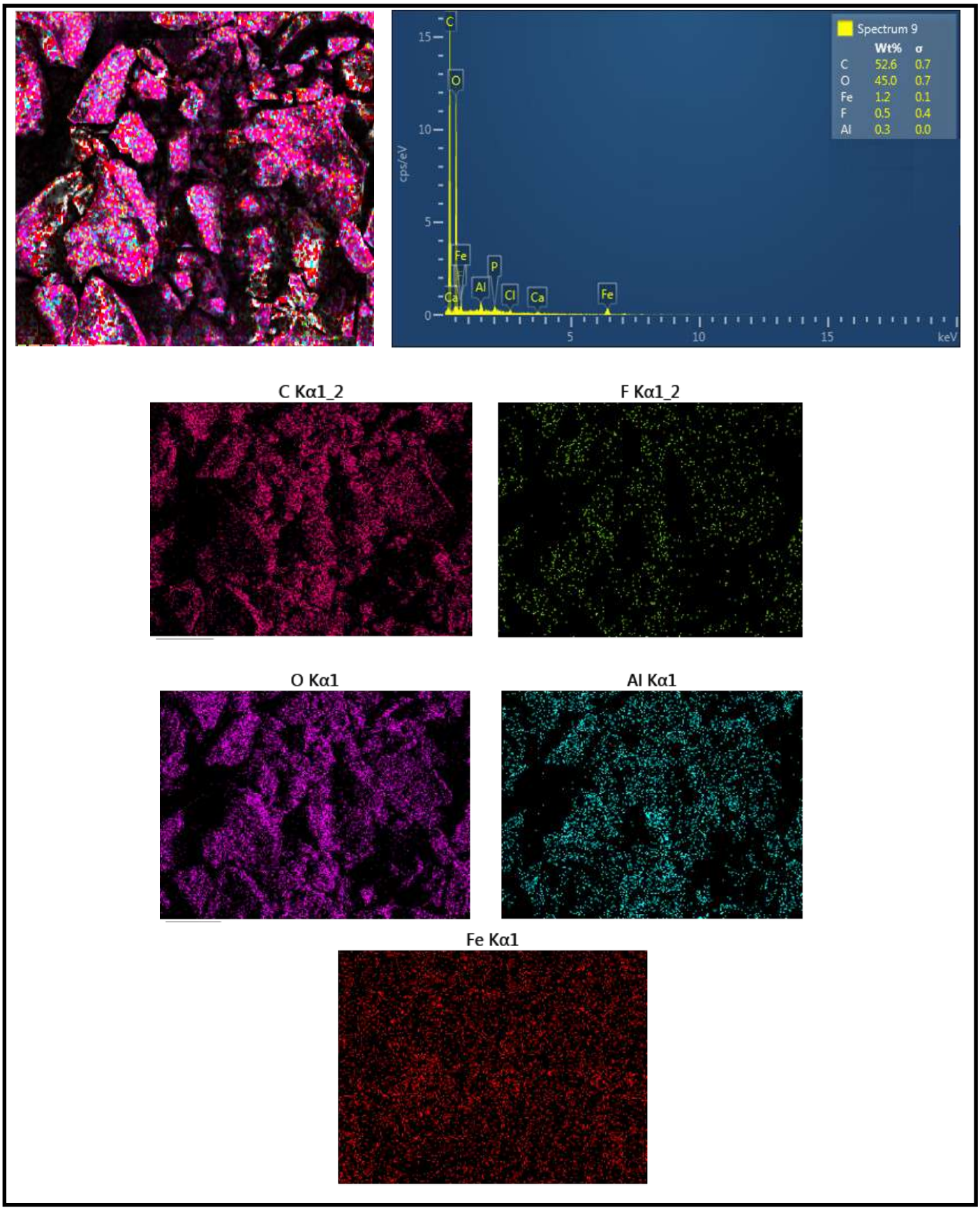

Figure 7.5: Elemental mapping analysis after adsorption showing various weight percentage of carbon, fluoride, oxygen, aluminium and iron.

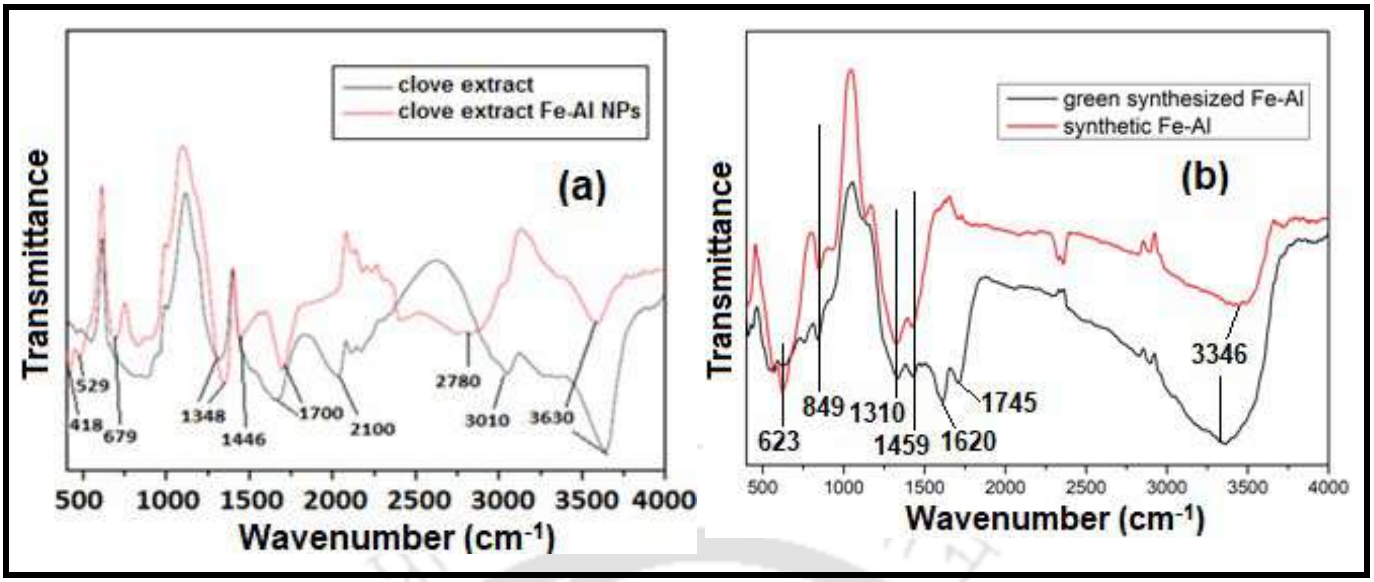

Figure 7.6: Fourier transform infrared spectroscopy (FTIR) study of (a) clove extract and clove mediated Fe-Al nanocomposite (b) green synthesized and synthetic Fe-Al nanocomposite

Figure 7.6(a) shows the FTIR spectra for clove extract and clove extract mediated iron-aluminium nanocomposite. Peaks at 418, 529, 679 and 1446 cm^{-1} were assigned to hydrous metal oxides [34]. Both the graphs showed peaks at 1348 cm^{-1} which were due out to bending vibrations of C-OH alcoholic group. Peak at 1700 cm^{-1} denotes the presence of C=O of the carboxyl groups present for both the graphs. The peak at 2100 cm^{-1} was assigned due to alkyne C-C stretch due to secondary bio-molecules present in clove extract. The peaks at 2780 and 3010 cm^{-1} denotes O-H for carboxyl groups and aromatic C-H stretch respectively. Peak at 3630 cm^{-1} for both the graphs were due to strong stretching vibration frequency of –OH groups.

Figure 7.6(b) represents the functional groups present in synthetic Fe-Al oxide composite and green synthesized Fe-Al nanocomposite. Peaks at 623 cm^{-1} and 849 cm^{-1} in both the FTIR graphs confirms the M-O (metal oxide) bonds were present in both type of synthesis. Similarly peaks at 1310 cm^{-1} and 1459 cm^{-1} confirms the presence of Fe-O-Al and M-OH (metal hydroxide) bonds respectively in both the composites [230]. The distinguishing

peaks at 1620 cm^{-1} and 1745 cm^{-1} shows that green synthesized Fe-Al nanocomposite consists of C=C and C=O respectively which was due to the aromatic constituents of the clove extract [231]. The peak at 3346 cm^{-1} show that both the synthetic and green synthesized Fe-Al nanocomposite consisted of –OH groups at their surface.

Figure 7.7 (a), and (b) shows the spectra of thermo gravimetric and differential thermal analyses of the prepared green synthesized iron-aluminium nanocomposite respectively. The TGA graph shows a rapid loss of mass till 450 ºC (37.5%) and then it reduces after 600 ºC (21.3%). Two endothermic peaks were observed from differential thermal graph at around 220 ºC and 680 ºC. The first endothermic peak was due to the elimination of water from the hydroxyl group of hydrous metal oxides. The second peak was due to the loss of carbonaceous matter present in the clove extract in the form of secondary bio-molecules. The exothermic peak at around 400 ºC was attributed due to the phase transition of the material.

Figure 7.7(c) depicts the hydrodynamic diameter of the prepared nanocomposite when dispersed at different pH solution; it was observed that at higher pH the nanocomposite formed lower average particle diameter. The average diameter of the prepared Fe-Al nanocomposite at pH 3, 7 and 12 were 148.9 nm, 129.8 nm and 81.6 nm respectively. This could be attributed to the fact that as the nanocomposite was synthesized at lower pH (clove extract of pH 4) hence at higher pH, a negative charge developed over the nanocomposite and due to electrostatic repulsion a lower average hydrodynamic diameter was attained.

XRD analysis obtained from Figure 7.7(d) depicts the clear structural nature of the green synthesized Fe-Al nanocomposite. Since there is a carbon coating over the metal composites due to the secondary bio-molecules of clove extract hence no prominent peak for metal and their oxides is found. Both the XRD graphs of before and after fluoride

adsorption confirms that the prepared nanocomposite was well coated with various carbon containing functional groups.

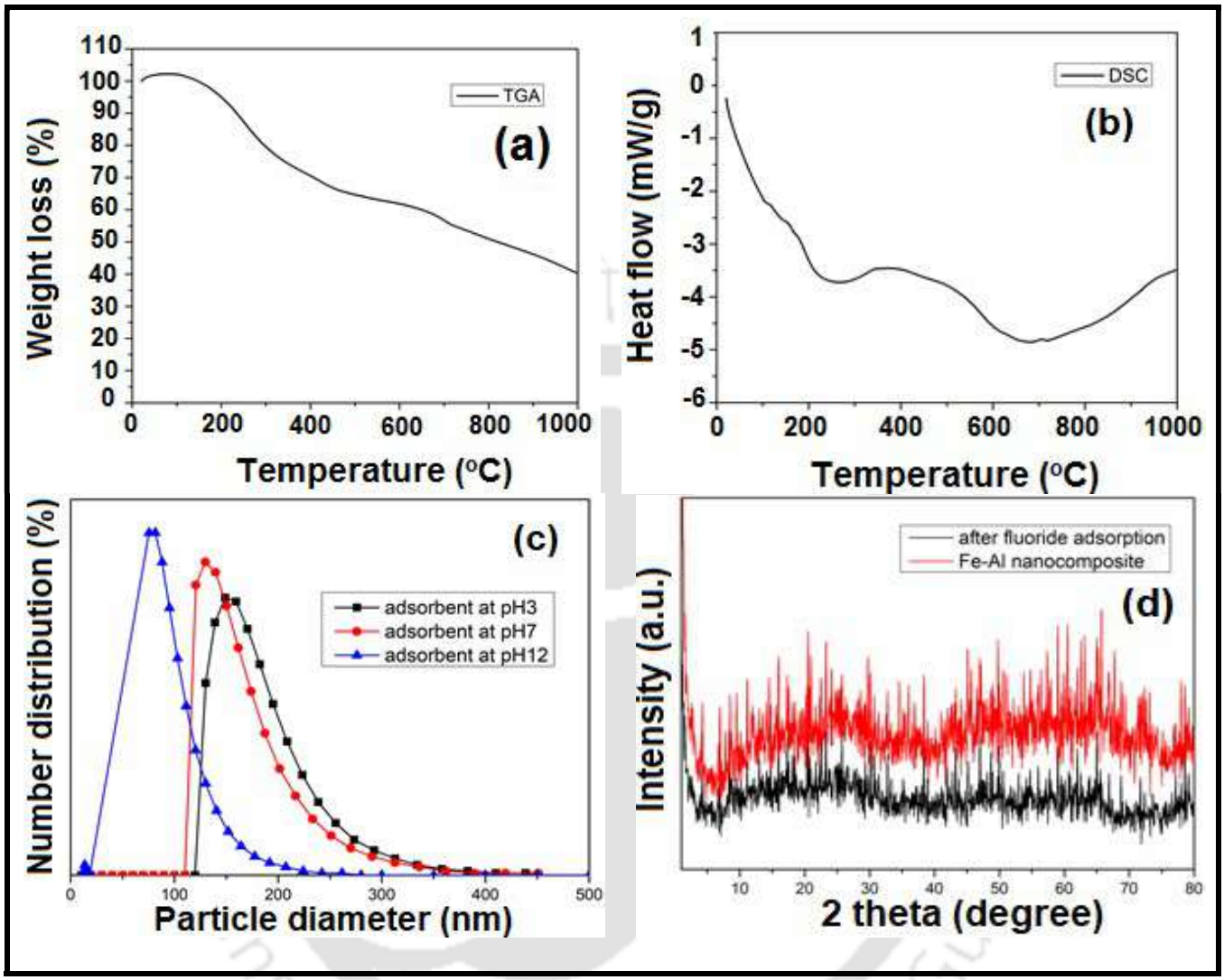

Figure 7.7: (a) TGA graph (b) DSC graph of the green synthesized Fe-Al nanocomposite (c) particle size analysis of nanocomposite at different pH (d) XRD analysis of the prepared Fe-Al nanocomposite before and after fluoride adsorption

7.3.3. Effect of pH on adsorption

The pH_{pzc} is considered to be an important parameter for any adsorption phenomenon. It is the pH value developed over a material during heterogeneous equilibrium when the net charge over the adsorbent surface (MOH_s, where M represents the metal in the green

synthesized nanocomposite) is zero from all source. The following reactions over any metal hydroxide was reported in [34]

$$MOH_{(s)} + H_{aq}^{+} \rightarrow MOH_{2(s)}^{+} \quad [R1]$$

$$MOH_{(s)} + OH_{aq}^{-} \rightarrow MO_{(s)}^{-} + H_2O \quad [R2]$$

During pH lower than pH_{pzc} the adsorbent site becomes protonated and excess positive charge develops over the adsorbent surface [R1]. Similarly at pH higher than pH_{pzc}, excess negative charge develops over the adsorbent surface [R2]. Depending on the relative pK_a values of different sites, mixed oxides can behave in either way. The pH_{zpc} of the green synthesized iron-aluminium nanocomposite was determined according to the method described by Babic et al. [232]. It was observed that pH_{zpc} of the prepared green synthesized iron-aluminium nanocomposite lies ~4.5 [Figure 7.8(a)]. With further investigation it was found that the zero-valent Iron (Fe) and Aluminium (Al) synthesized through same methodology yielded pH_{zpc} ~4.47 and 4.62 respectively. This was attributed because of the clove extract which formed the same organic coating over the NPs as that of the prepared Fe-Al nanocomposite. Reported hydrous iron aluminium mixed oxide and graphene oxide incorporated hydrous iron aluminium mixed oxide was found around 5.5-6 and 6 respectively [230,231]. The relative lower pH_{zpc} of the prepared green synthesized iron-aluminium nanocomposite was probably due to the extract inherited phenolic –OH, –COOH and –C-OH groups.

Fluoride adsorption over green synthesized iron-aluminium nanocomposite was favoured in low pH values as anion adsorption is combined with OH^- ion release. Figure 7.8 (b) shows, fluoride adsorption decreases with increase in pH from 4~4.5, consequently the amount decreases above pH 4.5. Below the pH_{zpc} of prepared nanocomposite (~4.5), due to Columbic force positive charge around adsorbent surface increases the adherence of

negatively charged fluoride ions. The process involves a ligand-exchange phenomenon as reported previously [231].

$$M - OH_2^+ + F^- \rightarrow M - F + H_2O \quad \text{[R3]}$$

On the other hand as the solution pH increases (pH > pH_{zpc}), negative charge develops on the adsorbent surface which incurs a repulsive force on the fluoride ions and consequently the q_e value decreases at pH ≥ 4.5 [Figure 7.8(a)]. The phenomenon can be described similarly as above (R4)

$$M - OH + OH^- \rightarrow M - O^- + H_2O \quad \text{[R4]}$$

Again at pH = pH_{zpc} value, anion exchange mechanism controls the fluoride adsorption over neutral adsorbent surface (R5)

$$M - OH + F^- \rightarrow M - F + OH^- \quad \text{[R5]}$$

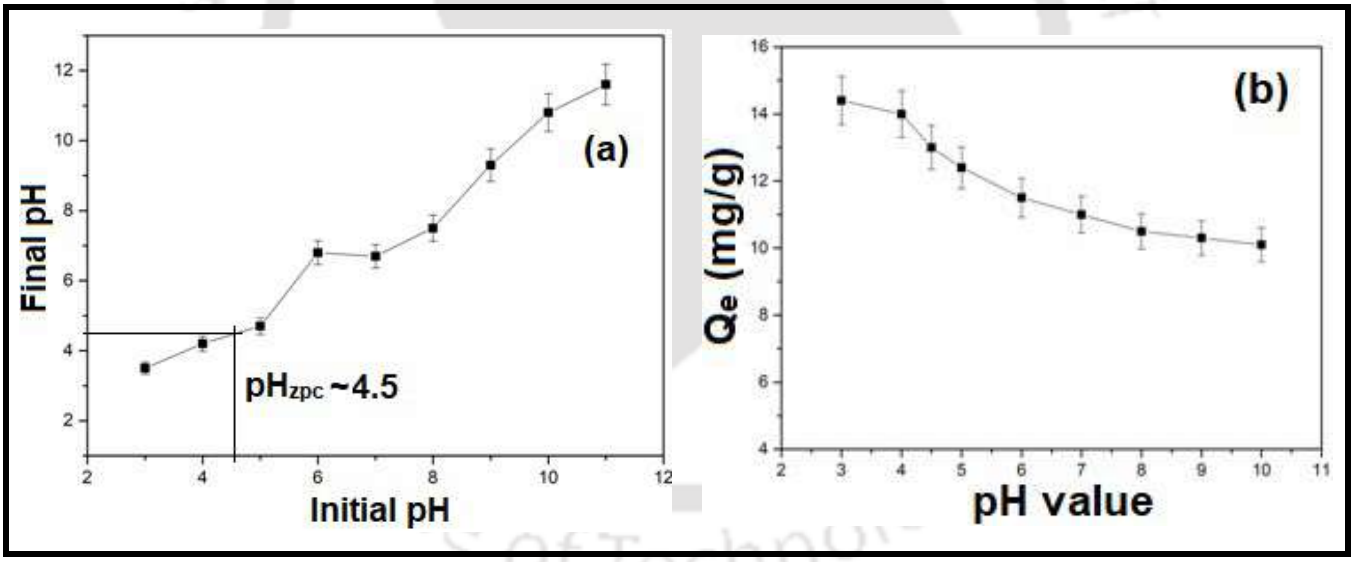

Figure 7.8: (a) pH_{zpc} calculation from initial and final pH values (b) Plots of Q_e (mg/g) against different solution pH.

7.3.4. Adsorption isotherm analysis

Fluoride equilibrium adsorption data at pH 6.7 (±0.2) and at temperatures of 25, 30 and 40°C were shown in Figure 7.9. Results conclude that the green synthesized iron-

aluminium nanocomposite has a high fluoride adsorption affinity. The data (Figure 7.9) were analyzed by non-linear least square fit method using Langmuir, Freundlich and Temkin (Table 7.1) isotherm models.

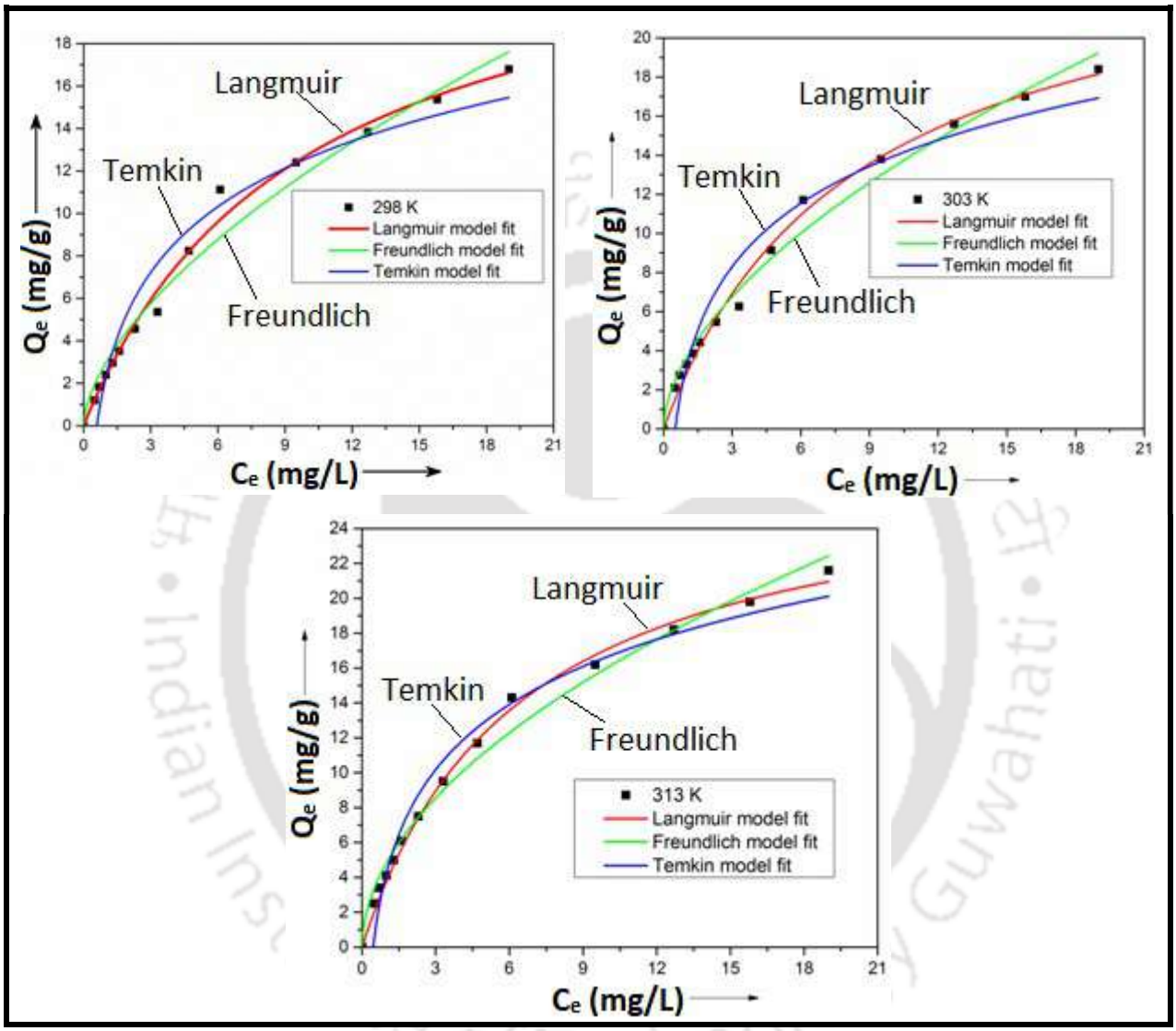

Figure 7.9: Variation of fluoride adsorption capacity (Q_e, mg/g) against the equilibrium solution fluoride concentration C_e (mg/L), and non-linear fits of equilibrium data with the Langmuir, the Freundlich and the Temkin isotherm models at 298 K, 303 K and 313 K.

Table 7.1: Various isotherm parameters for fluoride adsorption onto the green synthesized Fe-Al nanocomposite at different temperature with an initial fluoride concentration of 40 mg/L and pH 6.9 (±0.2)

Parameters	Values		
	298 K	303 K	313 K
	Langmuir isotherm model: $q_e = \frac{q_m K_L C_e}{1 + K_L C_e}$		
q_m (mg/g)	25.09	26.08	28.07
K_L (L/mg)	0.103	0.12	0.156
R^2	0.996	0.992	0.996
Freundlich isotherm model: $q_e = K_F C_e^{1/n}$			
K_F ($mg^{1-(1/n)} L^{1/n} g^{-1}$)	2.97	3.62	4.81
n	1.65	1.76	1.92
R^2	0.976	0.987	0.992
Temkin Isotherm Model: $q_e = a + b \log C_e$			
a	2.32	3.15	4.25
b	10.27	10.77	12.41
R^2	0.955	0.952	0.975
Redlich-Peterson Isotherm Model: $q_e = \frac{AC_e}{1 + BC_e^g}$			
A (mg/L)	2.71	3.89	5.71
B (mg/L)	0.13	0.27	0.35
g	0.83	0.9	0.96
R^2	0.99	0.993	0.997

Similarly Figure 7.10 shows Redlich-Peterson (Table 7.1) isotherm model fitting. The related parameters obtained from above equations are provided in Table 7.1. The results depicts that experimental data are well in accordance with Langmuir and Redlich-Peterson models Figure 7.9 *(r^2>0.99)*.

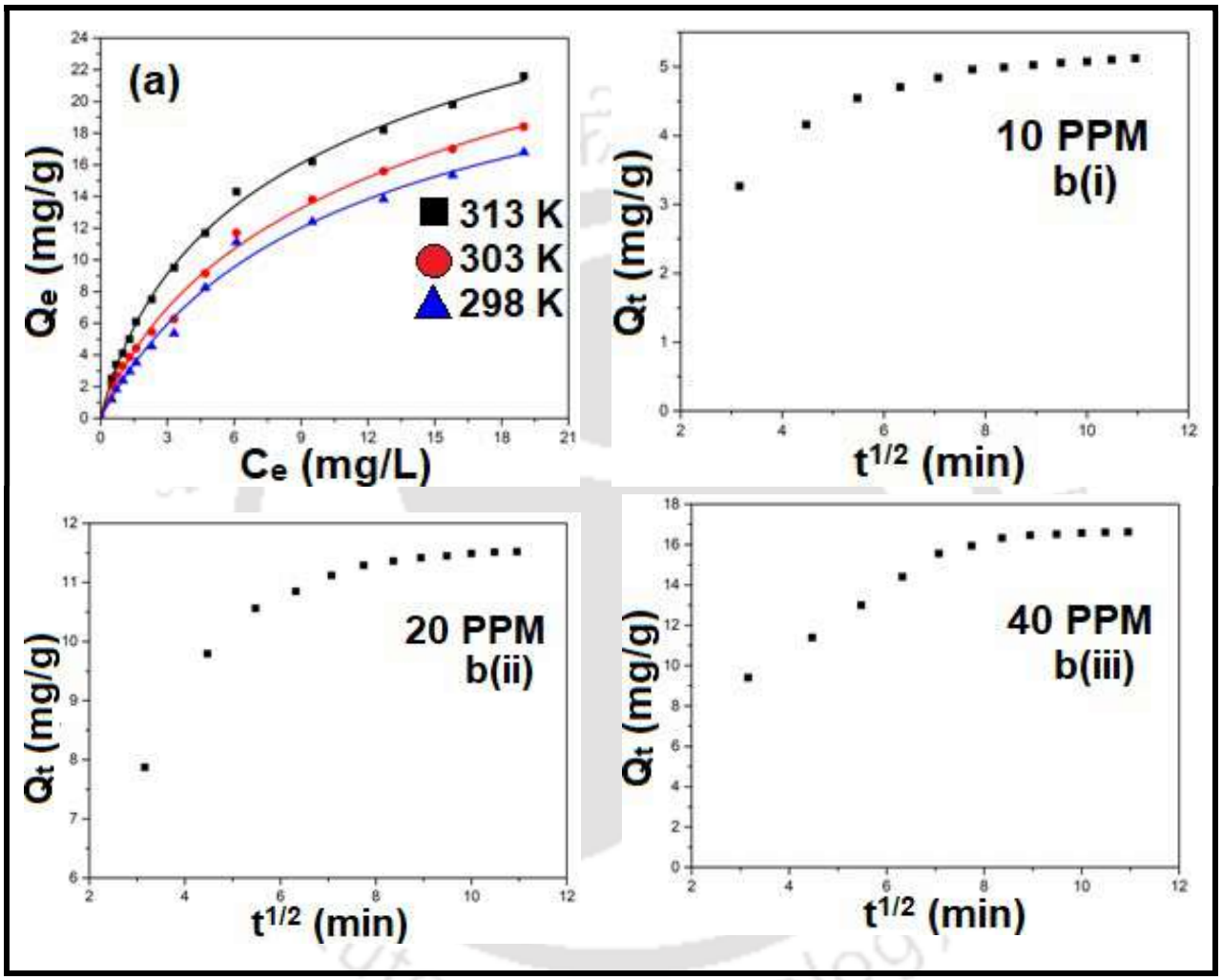

Figure 7.10: (a) Non-linear fits of equilibrium data with the Redlich- Petterson isotherm model at 298 K, 303 K and 313 K (b) Plot of Q_t (mg/g) vs. $t^{0.5}$ for intra-particle diffusion model for (i) 10ppm (ii) 20ppm and (iii) 40ppm fluoride solution.

Langmuir isotherm model where q_e denotes equilibrium adsorption capacity (mg/g) and C_e (mg/L) represents equilibrium adsorbate concentration respectively; q_m denotes monolayer adsorption capacity expressed in (mg/g) whereas K_L (L/mg) is equilibrium

adsorption constant. Similarly, Table 7.1 shows Freundlich isotherm model, where q_e and C_e have usual meanings as discussed above, K_F and n are empirical constants. Temkin isotherm model describes chemisorption phenomenon of an adsorption process.

Redlich-Peterson isotherm model describes both the features of Langmuir as well as Freundlich isotherm. *A, B,* α and β denotes Redlich-Peterson parameters, whereas *'g'* the exponential term close to unity denotes Langmuir adsorption whereas if it deviates from unity then it is assumed to follow Freundlich model. From Table 7.1, the monolayer adsorption capacity (q_m) obtained for the green synthesized iron-aluminium nanocomposite was in the range of 25.09-28.07 mg/g, when compared was found higher than the mixed synthetic iron-aluminium oxide [34] and iron-aluminium oxide-graphene oxide composite material [230]. The BET surface area obtained for the green synthesized Fe-Al nanocomposite was 46.63±0.3m^2/g with molecular cross section of 0.162 nm^2. Such low surface area with high monolayer adsorption capacity gives an idea that the adsorption process was controlled by chemical phenomenon at higher temperatures rather than just adsorption on active sites.

Thus, the present green synthesized iron-aluminium nanocomposite was suggested to be a better adsorbent. Moreover, *'β'* the Redlich-Peterson constant was found in the range of (14.6- 19.75 mg/L) while *'g'* was calculated around (0.83-0.96), which concluded that the green synthesized iron-aluminium nanocomposite has a strong affinity for fluoride [231]. The high g-value (0.83-0.96) confirms that adsorption of fluoride followed Langmuir model. However, the multilayer adsorption of Freundlich isotherm model also described the data fairly well (r^2 varies from 0.976-0.985). The Freundlich adsorption constant (K_F) obtained from the non-linear fit varies from 2.97-4.81. The Freundlich coefficient (n), which should have values ranging from 1 to 10, is found to be in range (1.65-1.92), the results also support the adsorption of fluoride on the green synthesized nanocomposite.

Temkin adsorption isotherm plot (Figure 7.9), which describe the chemisorption process of interaction between fluoride and the prepared nanocomposite, also describes well the present isotherm adsorption data (r^2 varies from 0.95-0.96). The results conclude that fluoride adsorption onto the green synthesized nanocomposite happened mainly due to ion exchange along with the chemisorptions process later at higher temperature. Hereby the order of equilibrium adsorption models which fitted best to the experimental data was: Redlich-Peterson ≥ Langmuir > Freundlich > Temkin. Dimensionless separation factor R_L is considered to be an essential parameter for Langmuir model [33] which can be defined as following:

$$R_L = \frac{1}{1 + K_L C_0} \qquad [7.1]$$

C_0 represents initial fluoride concentration whereas K_L denotes Langmuir constant. R_L Signifies the nature of the isotherm such as (a) unfavorable when R_L greater than 1 (b) linear if R_L equals to 1 (c) favourable in the case when $0 < R_L < 1$ and (d) irreversible when R_L equals to 0. In our present study, R_L was calculated to be in the range of 0-1.0 working range of fluoride concentration which concluded that fluoride adsorption onto the green synthesized nanocomposite was favourable, under the conditions used for the experiments.

7.3.5. Effect of initial fluoride concentration

Figure 7.11 shows time dependent adsorption capacity q_t (mg/g) with respect to different fluoride concentration. The equilibrium adsorption capacity for various fluoride concentrations 10, 20 and 40 mg/L was 5.12, 11.52 and 16.98 mg/g respectively (Figure 7.11a).

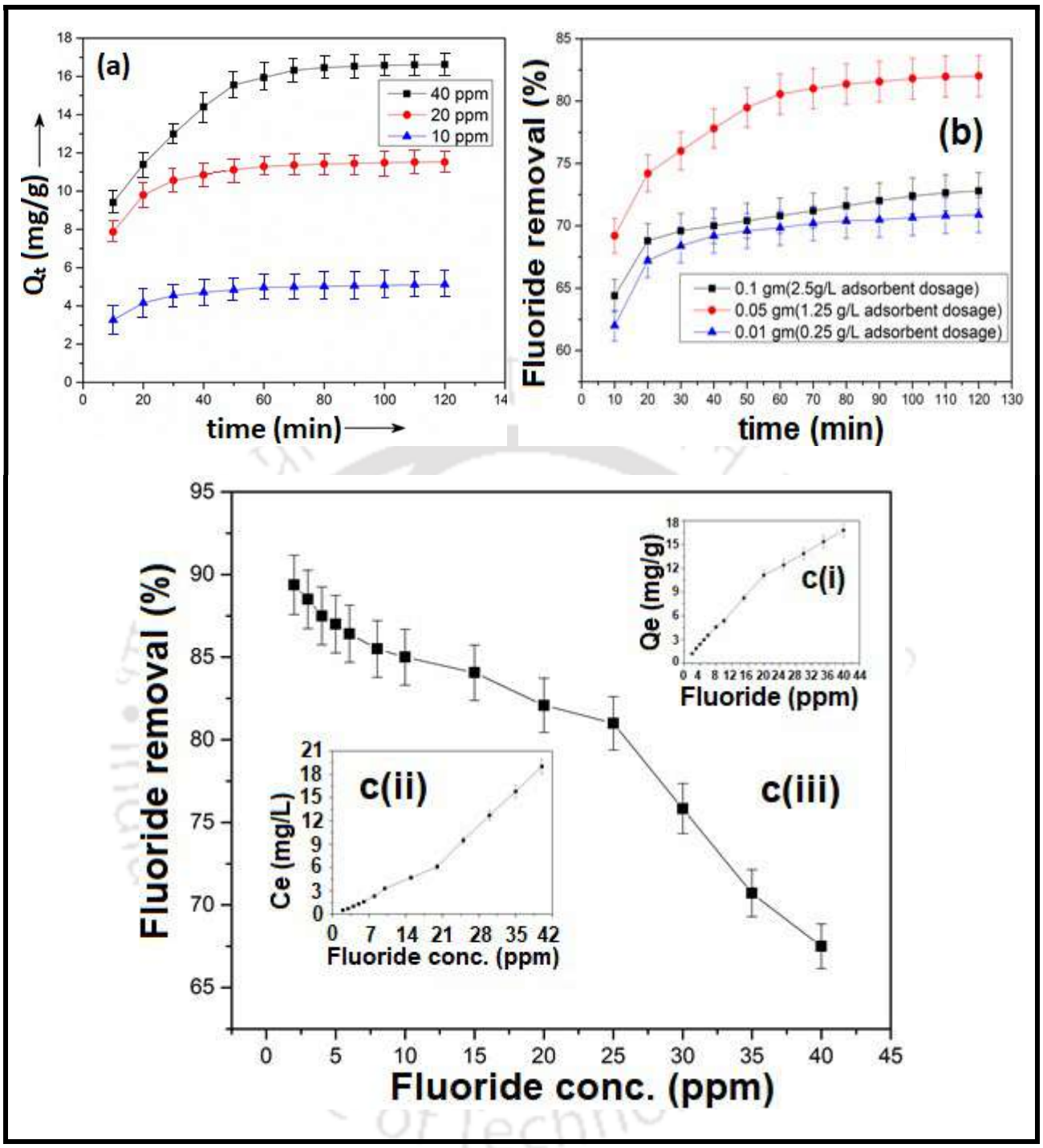

Figure 7.11: (a) Plot of adsorption capacity Q_t (mg/g) with time (minutes) for different initial fluoride concentrations. (b) fluoride removal (%) with time at various adsorbent dosage for 20 ppm fluoride solution. Variation of c(i) Qe (mg/g) and c(ii) Ce (mg/L) with respect to fluoride concentration.

From the adsorption studies it was observed that the equilibrium was achieved at around 80 min for 40 mg/L concentration whereas for 10 and 20 mg/L concentration equilibrium

was attained much earlier around 60 min. The initial rapid adsorption of fluoride on to green synthesized nanocomposite was due to hydroxyl groups present over the surface of prepared adsorbent. However due to rapid uptake of fluoride at the inner surface, slows down the adsorption process in the later stage [233].

Similarly from Figure 7.11(b) it was observed that for 20 ppm fluoride stock solution maximum fluoride removal of 82.1 % was achieved for 1.25 g/L adsorbent dosage. Figure 7.11(c) gives a vivid description of the variation of equilibrium adsorption capacity (mg/g), equilibrium concentration (mg/L) and fluoride removal percentage (%) with various fluoride concentrations (ppm) as observed from Figure 7.11 c(i), c(ii) and c(iii) respectively. It was found that with decreasing fluoride concentration the fluoride removal percentage increases and was highest for 2 ppm fluoride ~89.25%, but reversely the maximum adsorption capacity increased with increasing fluoride concentration.

Table 7.2 shows the various kinetic parameters of pseudo-first order, pseudo-second order, Boyd, Elovich and intraparticle diffusion kinetic models for the fluoride adsorption on to green synthesized iron-aluminium nanocomposite. Where k_1 (min^{-1}), k_2 (g $mg^{-1}min^{-1}$), q_t and q_e represents the pseudo-first-order rate constant, pseudo-second-order rate constant, amount of fluoride adsorbed (mg/g) at any time t (min) and equilibrium respectively (Table 7.2).

The initial adsorption rate h_0 (mg g^{-1} $time^{-1}$) of the fluoride adsorption phenomenon can be obtained from the pseudo second order kinetic equation (Table 7.2) as q_t/t when t approaches zero and is expressed as:

$$h_0 = k_2 q_e^2 \qquad [7.2]$$

Table 7.2: Various Kinetics Parameters for Fluoride Adsorption onto the green synthesized Fe-Al nanocomposite at different initial fluoride concentrations at a temperature of 25 (±1)°C and pH 6.9 (±0.2)

Parameters	Values		
	10 mg/L	**20 mg/L**	**40 mg/L**
	Pseudo-second-order kinetic equation: $q_t = \frac{t}{\frac{1}{k_2 q_e^2} + \frac{t}{q_e}}$		
k_2 (g $mg^{-1}min^{-1}$)	0.032	0.019	0.005
Q_e (mg/g)	5.376	12.05	18.52
R^2	0.999	0.998	0.998
h_0 (mg $g^{-1}min^{-1}$)	0.925	2.75	1.71
Pseudo-first-order kinetic equation: $q_t = q_e[1 - e^{-k_1 t}]$			
k_1 (min^{-1})	0.094	0.124	0.13
Q_e (mg/g)	2.28	6.09	14.46
R^2	0.987	0.965	0.953
Boyd kinetic equation: $\log(1-F) = -\left(\frac{k_R}{2.303}\right)t$			
k_R	0.0225	0.027	0.025
R^2	0.906	0.9376	0.9871
Elovich kinetic equation: $q_t = \frac{1}{\beta}\ln(\alpha\beta) + \frac{1}{\beta}\ln t$			
A_1	2.0143	5.5	2.628
B_1	0.685	1.32	3.08
R^2	0.9118	0.8786	0.9508
Intraparticle diffusion kinetic equation: $q_t = k_{id} t^{1/2} + C$			
k_{id}	0.195	0.373	0.9
R^2	0.789	0.743	0.865

From Table 7.2 intraparticle diffusion kinetic equation, k_{id} is the intraparticle (pore) diffusion rate constant (mg g^{-1} $time^{-0.5}$) and C gives an idea about the thickness of the boundary layer. From Boyd kinetic equation (Table 7.2) where $F = q_e/q_t$, where q_e and q_t have the same meanings as mentioned above and k_R (min^{-1}) is the rate constant. The equation was developed from the pseudo-first-order rate equation for adsorption reaction based on diffusion through boundary liquid film and adsorption kinetics as a chemical phenomenon. In Elovich kinetic model (Table 7.2), α denotes initial adsorption rate whereas β represents Elovich constant. The kinetic equation can be rearranged to the following expression:

$$q_t = A_1 + 2.303B_1 \log t \qquad [7.3]$$

where, A_1 and B_1 are constants and have their usual significance, the values were calculated from the linear plot of q_t versus *log t*. Table 7.2 shows that for pseudo-second order kinetic model, fluoride adsorbed at equilibrium (Q_e) increases (5.37-18.52 mg/g) when initial fluoride concentration increases (10-40 mg/L). This shows that the prepared green synthesized iron-aluminium nanocomposite is an effective fluoride adsorbent. Increase in equilibrium adsorption (Q_e), decrease in second order rate constant (k_2) (varies from 0.032-0.005 g $mg^{-1}min^{-1}$) and initial adsorption rate (h_o) (varies from 0.92-1.71 mg $g^{-1}min^{-1}$) with increasing fluoride concentration was observed from Table 7.2 and similar outcomes were reported earlier [234]. Figure 7.12 shows that kinetic data fits fairly well with pseudo-first order model (r^2 varies from 0.987-0.953), but it fits best with pseudo-second order model (r^2 varies from 0.99-0.998 for fluoride concentration 10-40 mg/L).

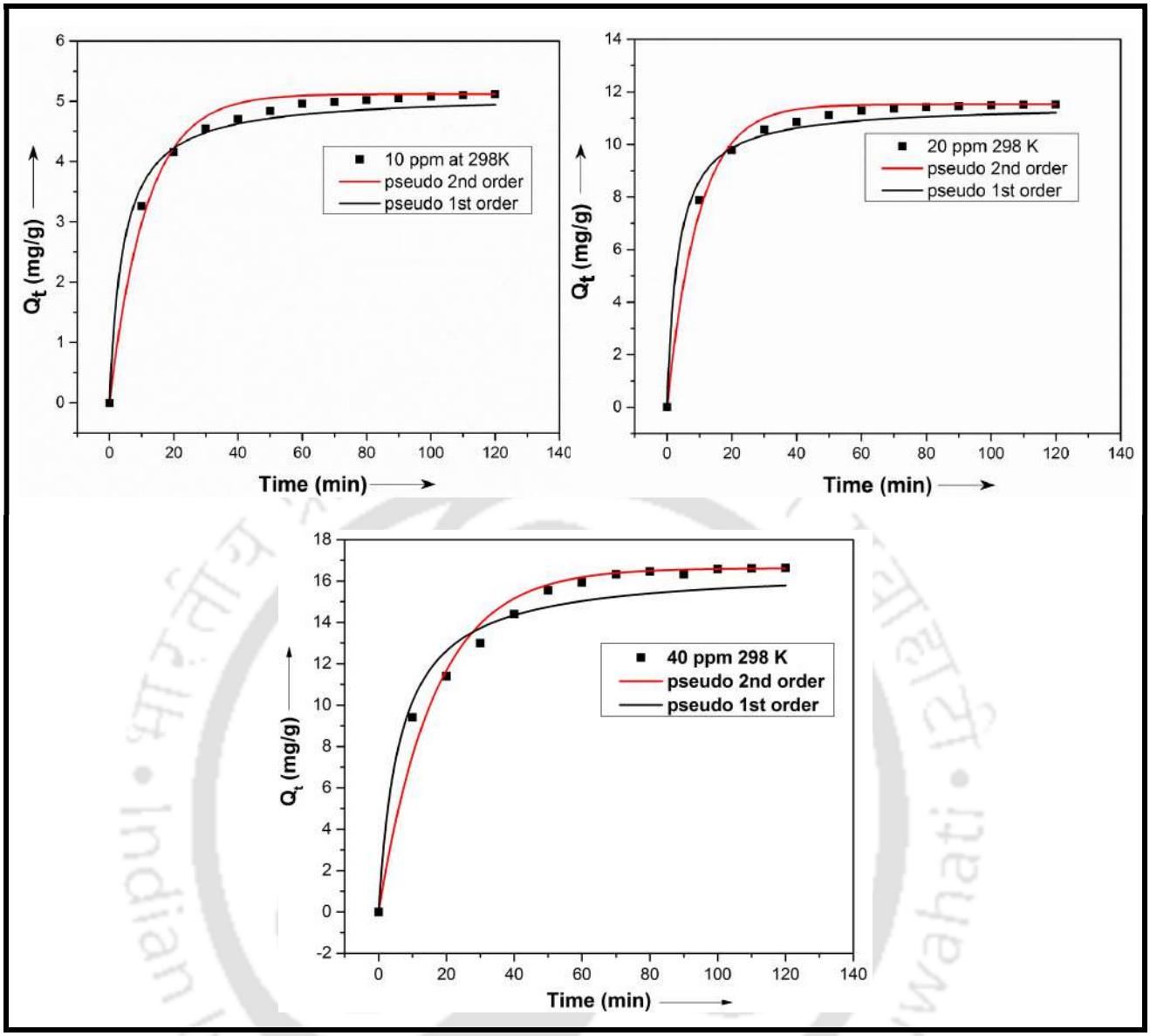

Figure 7.12: Variation of time dependent fluoride adsorption capacity Q_t, (mg/g) against time of contact (min) at different solution concentration with non-linear fits of data with pseudo first order (black) and pseudo-second order (red) kinetic model equations.

The fitting for Elovich and Boyd kinetic model shows that fluoride adsorption was controlled by the chemisorption (r^2 varies from 0.91-0.95) as well as chemical phenomenon process (r^2 varies from 0.9-0.98) since the present data fairly fits both the model. The increasing k_{id} value (0.195-0.9 mg g^{-1} $min^{-0.5}$) for intra-particle pore diffusion kinetic model suggests the higher possibility of fluoride pore sorption on to the green

synthesized nanocomposite. But from Figure 7.10 b(i), (ii) and (iii) it was found that the initial linear data points when extrapolated cuts at positive intercept which suggests for boundary layer thickness. Since the linear extrapolated line doesn't passes through origin hence it can be confirmed that only pore diffusion doesn't control the adsorption process. Moreover since all the data points don't form a linear line passing through origin hence the adsorption process can't be attributed due to boundary layer diffusion effect. Hence the results confirmed that that fluoride adsorption followed a complex step and controlled by multistage diffusion process.

7.3.6. Behaviour of adsorption kinetics due to temperature variation

Adsorption kinetics of fluoride on the prepared green synthesized iron-aluminium nanocomposite was conducted at three different temperatures 25, 30 and 40 ºC respectively. The different parameters obtained from the kinetic model fittings were shown in Table 7.3.

Present fluoride adsorption data dependent on temperature fitted the pseudo-first order kinetic model fairly well (r^2= 0.965-0.969). In contrast the pseudo-second order kinetic model (Figure 7.13) fitted kinetic data best (r^2= 0.99). The equilibrium adsorption capacity q_e was found to increase with temperature rise from 12.03-13.86 mg/g. Similarly an increase in initial adsorption rate (h_0) was noticed from 2.67 to 4.68 mg $g^{-1}min^{-1}$ with increasing temperature. Endothermic nature was confirmed from the above obtained results. Table 7.3 shows that pseudo-second order rate constant (k_2) increased from 1.85×10^{-2} to 2.44×10^{-2} g $mg^{-1}min^{-1}$ with rise in temperature, similar findings were reported by Ho et al. [234]. The chemisorption nature didn't described well the temperature dependent process of fluoride adsorption in this study (r^2= 0.878-0.877). But the Boyd

equation (r^2 = 0.93-0.929) shows that the chemical phenomenon described well the adsorption process.

Table 7.3: Kinetic parameters for fluoride adsorption onto the green synthesized Fe-Al nanocomposite at different temperature with an initial fluoride concentration of 20 mg/L and at pH 6.9 (±0.2)

Parameters	Values		
	298 K	303 K	313 K
	Pseudo-second-order kinetic equation		
k_2 (g $mg^{-1}min^{-1}$)	0.0185	0.0231	0.0244
Q_e (mg/g)	12.03	12.52	13.86
R^2	0.999	0.998	0.999
h_0 (mg $g^{-1}min^{-1}$)	2.67	3.62	4.687
Pseudo-first-order kinetic equation			
k_1 (min^{-1})	0.126	0.157	0.18
Q_e (mg/g)	5.3	6.1	8.69
R^2	0.965	0.983	0.969
Boyd kinetic equation			
k_R (min^{-1})	0.027	0.035	0.036
R^2	0.937	0.985	0.929
Elovich kinetic equation			
A_1	5.59	6.9	8.24
B_1	1.325	1.145	0.954
R^2	0.878	0.876	0.877
Intraparticle diffusion kinetic equation			
k_{id} (mg $g^{-1}min^{-0.5}$)	0.373	0.322	0.268
R^2	0.743	0.74	0.752

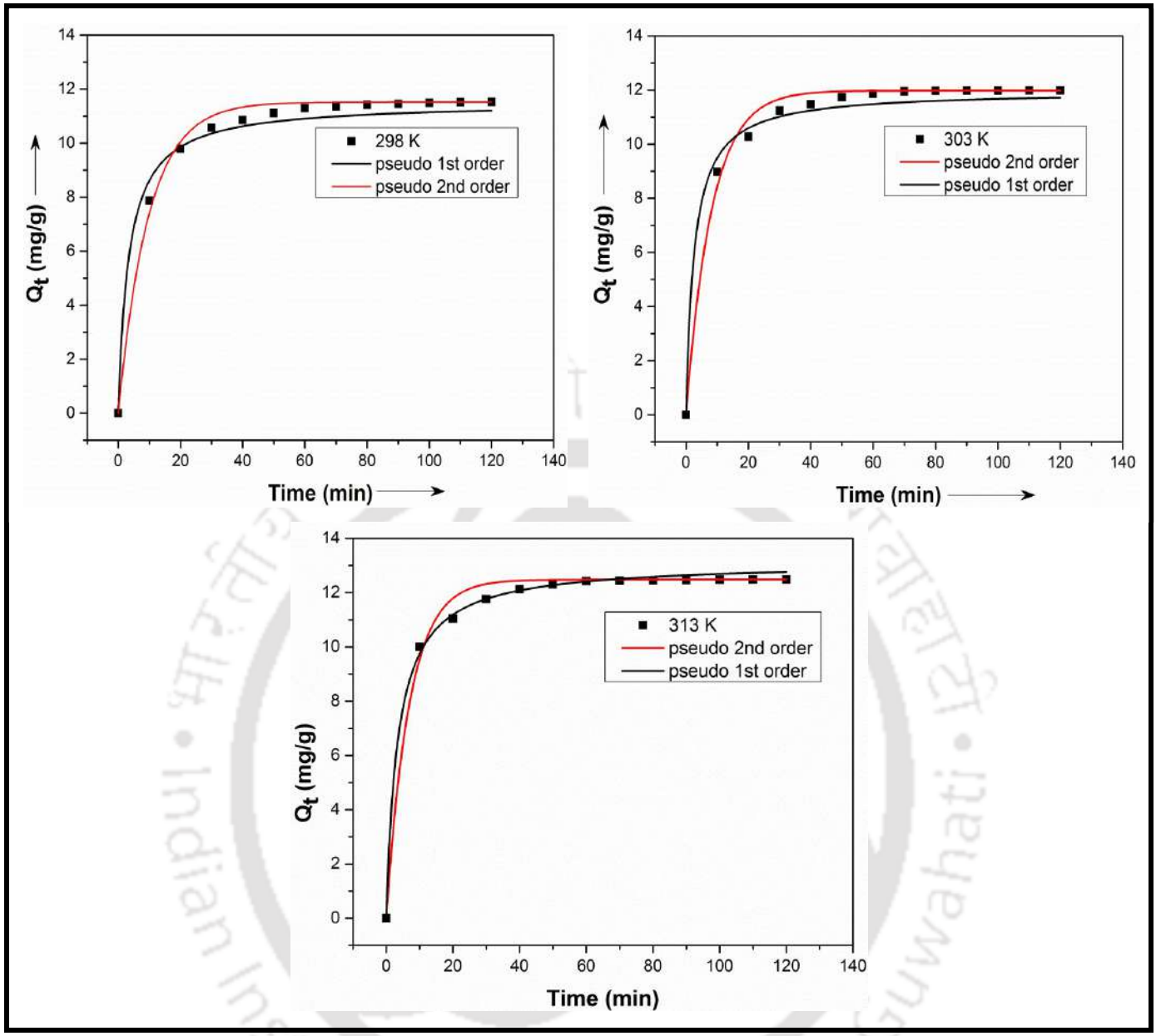

Figure 7.13: Variation of time dependent fluoride adsorption capacity Qt, (mg/g against time of contact (min) at different temperatures with non-linear fits of data with pseudo first order (black) and pseudo-second order (red) kinetic model equations.

Lack of fitness with intra-particle diffusion kinetic model (Table 7.2) (r^2 = 0.74-0.75) as well as with linear plot of q_t versus $t^{1/2}$ confirms that fluoride adsorption was mainly controlled by multistage diffusion on to the green synthesized iron-aluminium nanocomposite. Similar trend and analysis of data as in previous section shows that Boyd

equation (r^2 = 0.93-0.929) and pseudo-first order kinetic equation (r^2= 0.965-0.969) are basically the same model. Table 7.4 provides a comparative assessment of Langmuir monolayer adsorption capacity at 303K for different fluoride adsorption studies carried out by different authors.

Table 7.4: Comparative assessment of Langmuir monolayer adsorption capacity at 303K for different fluoride adsorption studies

Adsorbent	θ (mg/g)	pH; initial conc.	Reference
Algal-biosorbent Spirogyra sp.-IO2	1.27	7.0; 5-25 mg/L	[228]
Manganese-oxide-coated alumina	2.851	7.0±0.2; 2.5-30 mg/L	[229]
Magnetic-chitosan	22.49	7.0; 5-40 mg/L	[230]
Iron–zirconium hybrid oxide	8.21	6.8±0.1; 5-50 mg/L	[231]
Iron–aluminum mixed oxide	17.73	6.9±0.2; 10-50 mg/L	[232]
Iron–tin mixed oxide	10.47	6.4±0.2; 10-50 mg/L	[233]
Quick lime	16.67	6.61; 10-50 mg/L	[235]
La(III) incorporated carboxylated chitosan beads	11.91	7.0; 11-19 mg/L	[237]
Fe(III) loaded carboxylated chitosan beads	15.39	7.0; 11-19 mg/L	[239]
Fe(III)–LECCA	18.55	5.6; 10-200 mg/L	[240]
Hydrated iron-aluminium-chromium mixed oxide	16.34	6.5±0.2; 10-50 mg/L	[227]
Cerium incorporated Fe(III) oxide	22.55	7.0; 10-60 mg/L	[225]
Iron-aluminium oxide-graphene oxide	22.9	7.0; 5-35 mg/L	[234]
Green synthesized Fe-Al composite	**26.08**	**6.9±0.2; 10-40 mg/L**	**This work**

7.3.7. Thermodynamics of adsorption reaction

The thermodynamic parameters for the adsorption process in solution were calculated using the following thermodynamic relations assuming low solute concentration, where activity coefficient is unity (Henry's Law):

$$\Delta G° = \Delta H° - T\Delta S° \quad [7.4]$$

And,

$$\Delta G° = -2.303RT \log K_C \quad [7.5]$$

Combining Eq. 7.4 with Eq. 7.5 the following equation is formed:

$$\log K_C = \frac{\Delta S°}{2.303R} - \left(\frac{\Delta H°}{2.303R}\right)\frac{1}{T} \quad [7.6]$$

Where K_C equilibrium constant, calculated ($K_C = q_e/C_e$) (where q_e/C_e known as adsorption affinity); $\Delta G°$, $\Delta H°$, and $\Delta S°$ are termed as free energy change, enthalpy change and entropy change respectively. Hence Eq. 7.6 can be rearranged and written as:

$$\log\left(\frac{q_e}{C_e}\right) = \frac{\Delta S°}{2.303R} - \left(\frac{\Delta H°}{2.303R}\right)\frac{1}{T} \quad [7.7]$$

The values of $\Delta S°$ and $\Delta H°$ were obtained from Eq. 7.7 through slope and intercept. Again from Eq. 7.4 the value for $\Delta G°$ (free energy change) was calculated at different temperatures. With increasing temperature 25-40 °C, adsorption extent was found to improve. Hence fluoride adsorption on the green synthesized iron-aluminium nanocomposite was determined to be endothermic in nature. The thermodynamic parameters were displayed in Table 7.4 obtained from the plot of $\Delta G°$ versus T (Figure 7.14). The plot was quite linear (r^2=0.986), moreover $\Delta H°$ was calculated to + 37.45 kJ/mol; hence the fluoride adsorption process was confirmed as endothermic in nature. The entropy change ($\Delta S°$) was +139.58 J/mol K for the adsorption process. Positive

values confirmed that fluoride adsorption on the green synthesized nanocomposite increased the entropy of the system.

This indicated that the fluoride adsorption on the green synthesized nanocomposite leads to the increase in the entropy of the system. The $\Delta G°$ values obtained (Table 7.5) indicate that (i) the adsorption of fluoride is spontaneous and (ii) the spontaneity of the process is enhanced with increasing temperature. A similar trend of increasing $\Delta G°$ with increasing temperature was also reported in other research works. [41-43].

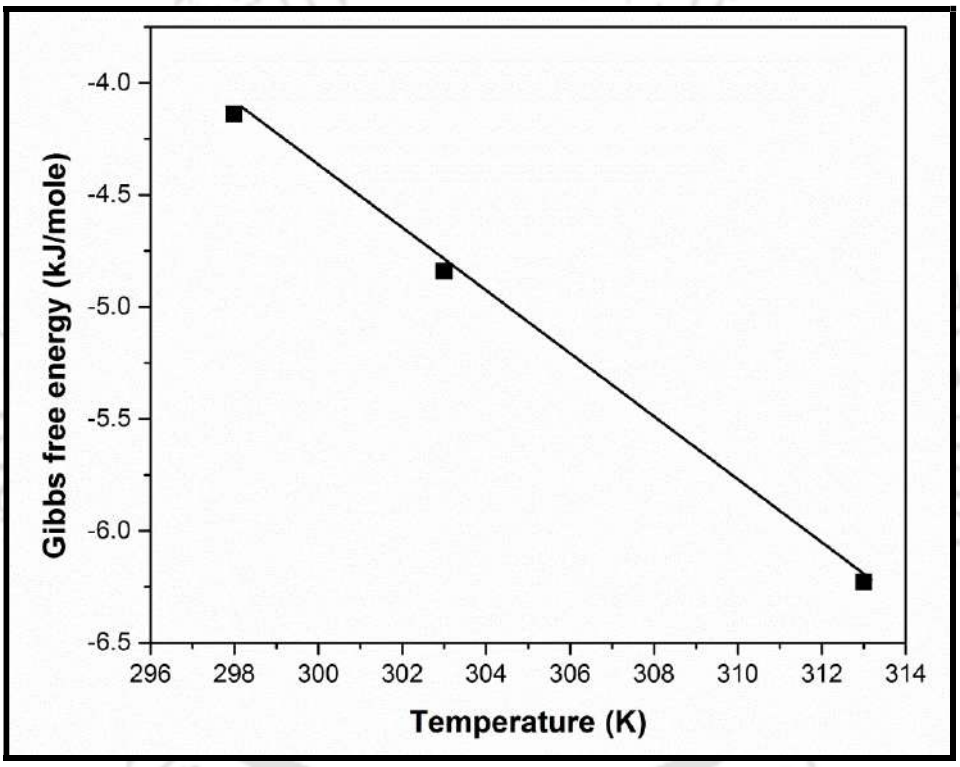

Figure 7.14: The plots of ΔG^0 (kJ mol-1) versus temperature (K) for thermodynamic data on fluoride adsorption by green synthesized Fe-Al nano-composite.

7.3.8. Activation parameters

From the results obtained (Table 7.6), the increasing trend in the second order rate constant with increasing temperature may be described by the Arrhenius equation:

$$k_2 = A\exp\left(\frac{-E_a}{RT}\right) \qquad [7.8]$$

Table 7.5: Thermodynamic parameters for adsorption of fluoride onto green synthesized Fe-Al nanocomposite at pH 6.9 (±0.2)

Temperature (K)	ΔG^o (kJ/ mol)	ΔH^o (kJ/ mol)	ΔS^o (J mol^{-1} K^{-1})
298	-4.14	37.45	139.58
303	-4.83		
313	-6.23		

Where k_2 is the pseudo-second-order rate constant (g mg^{-1} min^{-1}), A temperature-independent factor (g mg^{-1} min^{-1}), E_a the activation energy of adsorption (given in units of kJ/mol), R the gas constant (8.314 J $mol^{-1}K^{-1}$), and T the absolute temperature (Kelvin). Taking the logarithm of Eq. 7.8 gives the following Arrhenius-type linear relationship:

$$\ln k_2 = \ln A + \left(\frac{-E_a}{R}\right)\frac{1}{T} \qquad [7.9]$$

Table 7.6: Activation parameters for fluoride adsorption onto the green synthesized Fe-Al nanocomposite with an initial fluoride concentration of 20 mg/L at pH 6.9 (±0.2)

Temperature (K)	Pseudo-second order rate constant, k_2 (g mg^{-1} s^{-1})	E_a (kJ/ mol)	A (g mg^{-1} s^{-1})
298	3.08×10^{-4}	13.08	6.45×10^{-2}
303	3.85×10^{-4}		
313	4.07×10^{-4}		

7.3.9. Effect of co-occcuring ions on fluoride removal efficiency

For real life experiments related to ground water, presence of different other ions influence the fluoride adsorption very much. It has been found that the adsorption capacity decreases drastically in presence of other ions. For carrying out this experiment 40 mg/L fluoride stock solution was prepared with different salts of various concentrations (10, 30, 50, 70 and 90 mg/L). It was found that with increase in solution salt concentration, the adsorption capacity of fluoride subsequently decreased (Figure 7.15). Adsorption capacity decreased maximum at chloride concentration of 90 mg/L from 16.6 mg/g to 5.28 mg/g (~31.8% of original value). For other competing ions like bicarbonate and sulphate the adsorption capacity decreased to 5.6 mg/g and 6.24 mg/gm respectively. Hence the adverse affecting trend follows the order of $Cl^{-1}>HCO_3^{-1}>SO_4^{-2}$, which was found to be in order with previous studies [235].

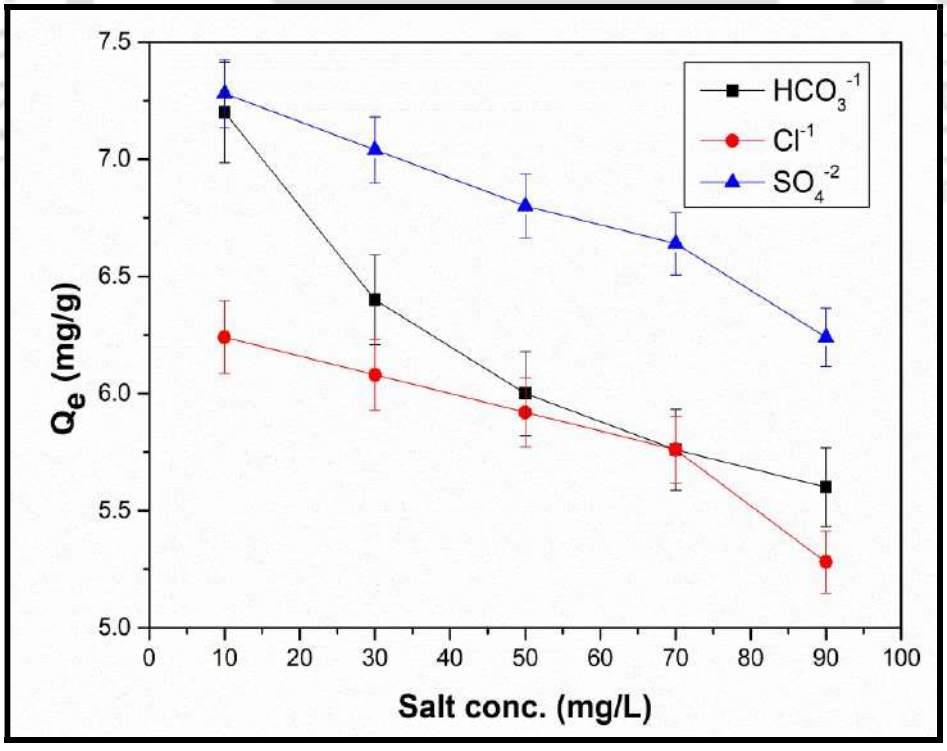

Figure 7.15: Effects of different salt concentrations on fluoride adsorption

7.3.10. Desorption study

From Figure 7.16 it was observed that with increase in base concentration (NaOH) desorption (%) value increases. As the process happened due to ion exchange mechanism followed by chemisorptions at higher temperature, it was found that higher amount of fluoride desorbed at room temperature. A maximum amount of 72.3% desorption was obtained for 2.5 (M) NaOH concentration. Since at higher temperature the adsorption process tends toward chemisorptions phenomenon hence at room temperature the product formation is not such stable and thus much of desorption occurs. The desorption percentage was much moderate and thus the adsorbent after use of 3 recycle process it's adsorption capacity decreased to 3.75 mg/g (~76.5%). After desorption the material was washed with deionised water, dried and again utilized for adsorption study where the same quick response of adsorption happened are previously, which signified the stability of the material.

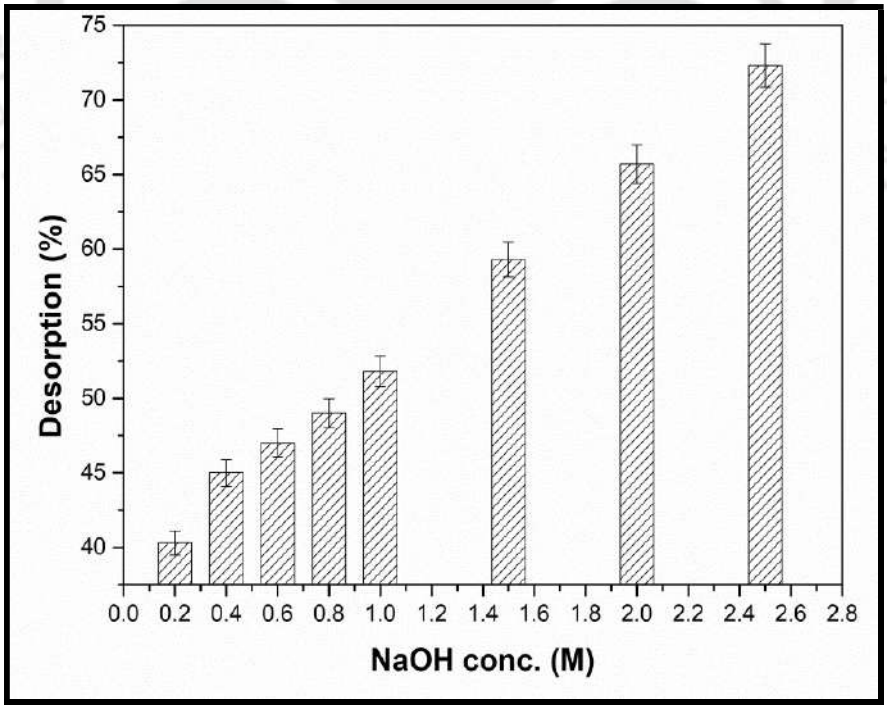

Figure 7.16: Desorption (%) study of fluoride adsorption at different NaOH conc. (M)

7.3.11. Fluoride removal mechanism

From the analysis of pH_{zpc} for the nanocomposite and the effect of pH on fluoride adsorption, it was confirmed that at low pH due to electrostatic attraction between positive adsorbent surface and negative fluoride ions the adsorption process enhanced. Similarly at higher pH the adsorption of fluoride ions decreased. The adsorption isotherm studies revealed that with increase in temperature along with ion exchange phenomenon, chemisorptions process also comes into play. Langmuir isotherm along with pseudo-second order kinetics best suited the fluoride adsorption process which is in accordance with several previous works [236]. Since the process is endothermic in nature thus at higher temperature stable products formed due to chemisorptions process thus at room temperature due to ion exchange fluoride can easily be leached with higher basic solutions from product as confirmed from desorption study. Thermodynamic parameters confirm the spontaneity and increase in adsorption process along with temperature. The experimental results confirm the replacement of hydroxyl ions by the solution fluoride ions. Moreover from Figure 7.17(a) it was observed that the bending mode and stretching modes of vibrations for –OH at 1630 $cm^{-1}$and 3361 cm^{-1}after adsorption diminishes which confirms the ion exchange phenomenon during fluoride adsorption onto green synthesized nanocomposite [236]. Figure 7.17(b) describes the fluoride removal mechanism through a schematic diagram.

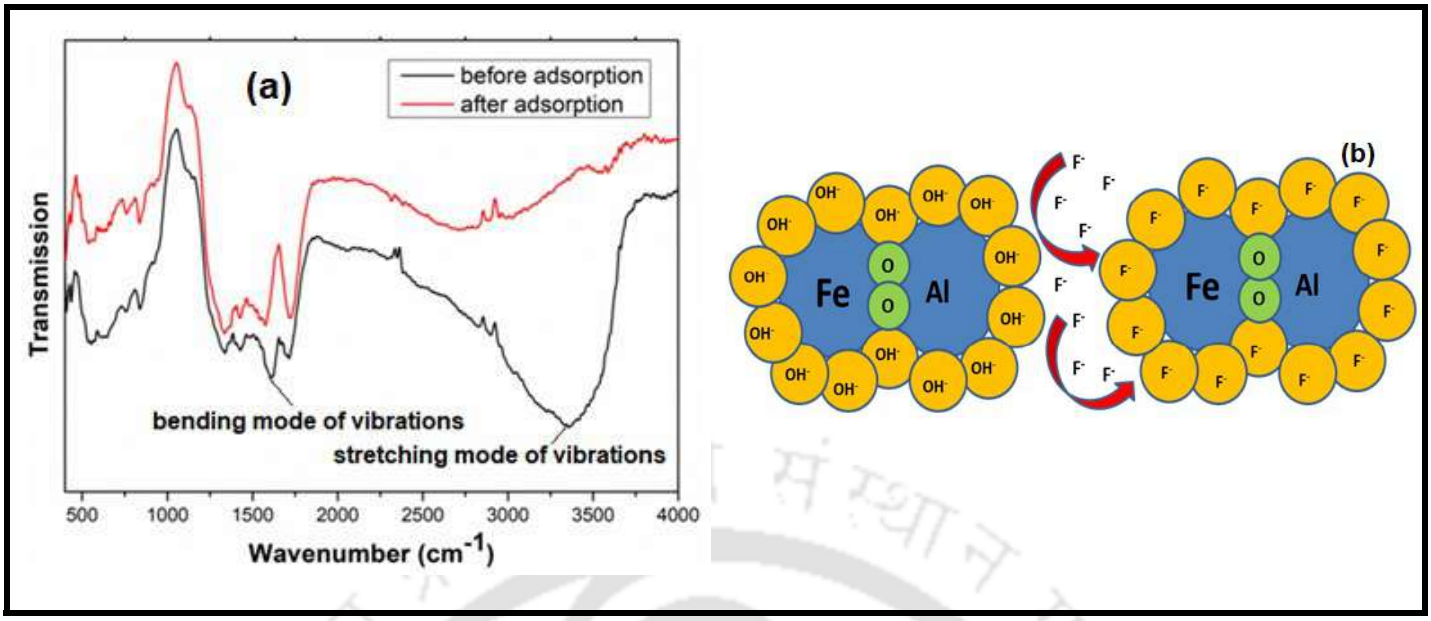

Figure 7.17: (a) FTIR analysis of Fe-Al nanocomposite before and after adsorption. (b) Schematic diagram for fluoride removal mechanism.

7.3.12. Fluoride removal from real life water sample

Water samples were collected from various regions of India like Upper Assam, Jorhat and Kwata, Manipur. From **Table 7.5** it was observed that the fluoride level of collected sample 1 and sample 2 were 4.2 mg/L and 3.3 mg/L respectively. After the adsorption study the fluoride concentrations were well below the specified limit according to WHO (<1.5 mg/L). Moreover the other parameters like TDS, salinity and pH of the samples were found to be well improved for drinking purpose. Oxidation reduction potential counts for the amount of available oxygen within the sample solution. It was also improved for the analyzed sample.

Table 7.7: Fluoride removal study from real life water sample

Sample 1- Water sample collected from Power-Grid corporation of India Ltd. 220 KV, Mariani substation, Jorhat Upper Assam, India		
Parameters	**Before Adsorption**	**After adsorption**
Conductivity (mS/cm)	0.46	0.34 ± 0.02
Total dissolved solid (mg/L)	230	186.7 ± 2.3
Salinity (mg/L)	348	280 ± 4.2
pH	8.23	6.29 ± 0.3
Oxidation reduction potential (mV)	33	81 ± 3
Fluoride (mg/L)	4.2	0.73 ± 0.02
Sample 2- Water sample collected from Site location Kwakta, Manipur, India		
Conductivity (ms/cm)	0.59	0.48 ± 0.01
Total dissolved solid (mg/L)	290	260 ± 3.1
Salinity (mg/L)	450	408 ± 4.5
pH	11.19	6.83 ± 0.1
Oxidation reduction potential (mV)	-33	65 ± 2
Fluoride (mg/L)	3.3	0.56 ± 0.03

Chapter 8

Study of photoluminescence activity and heavy metal ion detection ability of green synthesized iron-aluminum nanocomposite

Piyal Mondal, Mihir Kumar Purkait. Facile one-step green synthesis of Novel Photo-luminescent Fe-Al Nanocomposite and studying its Fe^{3+} ion sensing ability *(submitted to Journal of Cleaner Production)*

Chapter 8

Study of photoluminescence activity and heavy metal ion detection ability of green synthesized iron-aluminum nanocomposite

This chapter focuses on the photoluminescence activity of the already synthesized Fe-Al NCs of single emission similar to carbon dots at ~450nm. The significant effect of pH on the UV absorbance and photoluminescent (PL) behaviour of clove extract on the basis of electronic transition and tautomerism of de-protonated 3-OH flavonols is discussed. The synthesized Fe-Al NCs shows PL behaviour due to the sp^2 hybridized carbon groups (C=C and C=O) and –OH groups with lone pair of electrons present over the nanocomposite coating. In the presence of other various heavy metal ions, ON-OFF PLA intensity was observed for Fe^{3+} ion showing specific ion sensing ability. The nanocomposite was found to linearly quench Fe^{3+} in lower range concentration 0.078-0.125 µM. The LOD was found to be comparably low ~0.78 µM with high quenching constant K_{sv} 9.0×10^5 M^{-1}. Moreover, for real water sample analysis the Fe-Al NCs based Fe^{3+} sensor proved to be efficient with negligible error % of detection. Various water parameters such as pH, TDS, and oxidation potential of the water sample were found to improve.

8.1. Experimental

8.1.1. Materials

The raw materials required along with preparation of clove extract, it's optimization based on maximum phenolic and flavonoid content, and preparation of green synthesized iron-aluminum nanocomposite has been already discussed in Chapter 2, Chapter 3 and Chapter

7, respectively. The already prepared Fe-Al nanocomposite as discussed in Chapter 7 was utilized for carrying out for specific heavy metal ion sensing application in this chapter. The details of the required chemicals are provided in Table 2.1.

8.1.2. Experimental methods

8.1.2.1. UV analysis for polyphenolic content

UV-Vis Spectroscopy was utilized to optimize the pH of the extracted clove solution in order to obtain the better poly-phenolic content clove within clove extract (discussed in **Chapter 3**). Since the total poly-phenolic content increases the antioxidant property of the extract. The pH of the clove extract was adjusted using buffer solutions.

8.1.2.2. Photoluminescence activity of Fe-Al nanocomposite

For studying the PL effect at different pH solutions, the prepared Fe-Al NCs nanocomposite of 0.05 gm was dispersed in 20 mL de-ionized water. The nanocomposite solution was kept in an ultrasonication bath for 30 mins. After sonication, the dispersed nanocomposite solution was added about 1mL each in eight different beakers containing 20 mL of different pH solutions ranging from 3-12. After adding them the final solution was again sonicated for 30 min, and then about 3 mL of each pH controlled nanocomposite solution was transferred to cuvette and analyzed through fluorescence spectrophotometer.

8.1.2.3. Photoluminescence activity of heavy metals in presence of Fe-Al nanocomposite

20µM concentration standards of different metal ion solution was prepared for Mn^{2+}, Hg^{2+}, Cd^{2+}, Pb^{2+}, Cu^{2+}, and Fe^{3+} respectively. For studying the quenching effect of different metal ions on the PL property of Fe-Al NCs at definite pH, about 200µL of each

metal ion solution was added to 3mL of Fe-Al NCs dispersed solution, further sonicated and then transferred in cuvette for analysis in Fluorescence spectrophotometer.

8.1.2.4. Determination of specific heavy metal ion sensing property and analyzing linear range of applicability

Similarly in order to optimize the linear variation of quenching of Fe^{3+} ion, various concentration of Fe^{3+} solution was prepared ranging from 0.039-30µM. After preparing the stocks, 200µL of each prepared sample were added to 3mL of Fe-Al NCs solution in a cuvette and then analyzed in Fluorescence Spectrophotometer.

The effect of PL quenching effect of Fe^{3+} ion due to interference of other heavy metals present in water were investigated so that false signal is not generated during sensing application of Fe^{3+} metal ion. First, 200µL of 20µM of each Mn^{2+}, Hg^{2+}, Cd^{2+}, Pb^{2+}, Cu^{2+} and Ca^{2+} were added to 3mL of prepared Fe-Al NCs solution and their PL quenching were studied. Further to the above prepared solution of different metals, 200µL of 20µM Fe^{3+} ion solution was added to each and again PL intensity quenching was studied. The concentration of Fe^{3+} to other metal ions was fixed at 1:1 ratio. The PL quenching activity due to interference of other heavy metals was analyzed through Fluorescence Spectrophotometer.

8.2. Results and discussion

8.2.1. Morphological, Optical and Characterization outcomes

The morphological and physico-chemical property analysis of the green synthesized Fe-Al NCs utilizing FESEM, TEM, EDX, FTIR, DSC, TGA, XRD, size analysis and zeta potential characterization has already been discussed in previous Chapter 7.

The strong absorption band at 280 nm of clove extract (already discussed in Chapter 4) was denoted due to the n-π* transitions of the chromophore units such as –COOH and –C-O groups [211]. Difference between the energy level in conduction and valance band known as band gap relates directly to the extent of oxygen functionalization of the aromatic carbon present within the clove extract [219]. Hence it was confirmed from chapter 4 that at low pH, the carbon containing groups were present in highest intensity. Similarly from chapter 4 and chapter 5 it was observed that a strong absorption band occurred at both 230 nm and 280 nm which conveys that the formed iron NPs at different pH consists of both π-π* (C=C, and C=O) and n-π* (C=O) electronic transitions of the sp^2 C present in carboxyl and carbonyl groups [211,219]. Due to the variation of amount of oxygen incorporated within the Fe-Al NCs both the peaks position and intensity varied. Hence, from Figure 8.1 (b) it was suggested that at pH 5 higher sp^2 hybridized C atoms are present in the aromatic rings over the surface which results for better n-π* electronic transitions since peak ~ 280 nm is more sharp.

8.2.2. Photoluminescence behaviour of clove extract

It was observed from Figure 8.1 (a) that when the clove extract maintained at different pH, was excited at 320 nm two different bands in photoluminescence emission spectra were observed at ~470nm, and ~540 nm, similar to quercetin and rutin [237]. The variation in quercetin concentration was found to vary with change in pH when analyzed through HPLC chromatography. An initially 4500 mg/L prepared quercetin solution with Millipore water when maintained at pH 3 and pH 12 was found to reduce in quercetin content as compared to pH 7 as shown in Figure 8.4.

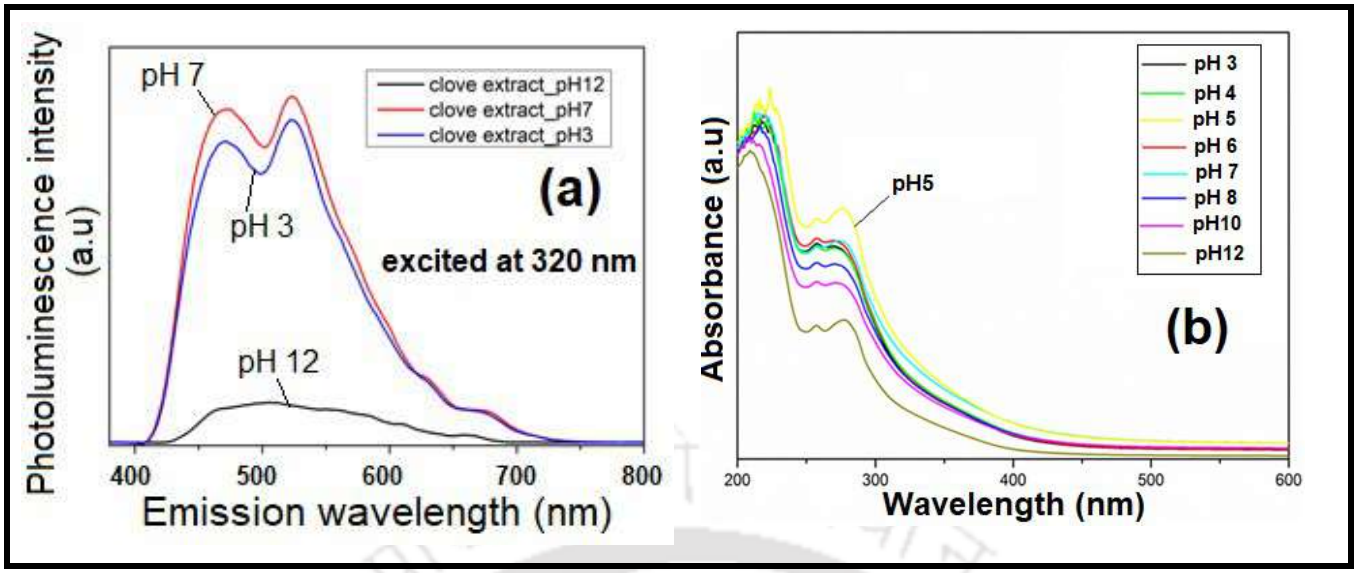

Figure 8.1: (a) Photoluminescence property of clove extract at different pH (b) UV Absorption spectra of green synthesized Fe-Al NCs dispersed at different pH

Photoluminescence behaviour was found to occur due to the excited state intramolecular proton transfer (ESIPT) which forms intramolecular hydrogen bonding between C_3-(OH) and C_4=(O), followed by tautomeric equilibrium exihibited by flavonoid molecules results a two-color photoluminescence spectrum namely blue-violet and yellow-green [237]. Both quercetin and rutin bears chromophore in their 1st ring and are capable of giving rise to such photoluminescence phenomenon since they are present in abundant quantity within clove extract. But it is a well known fact that rutin is more stabilized due to its sugar molecule present, hence its photoluminescence effect is very weak [237]. Thus it is considered that quercetin mostly controlls the photoluminescence phenomenon of clove extract. The enhancement of PL intensity when clove extract was maintained at pH 7 was found to be in accordance with the deprotanation phenomenon shown in Figure 8.2. Quercetin in the clove extract was assumed to attain the structure B or C which enhances the PL intensity due to the intramolecular hydrogen bonding between tautomeric C_3-(OH) and C_4=(O) followed by the tautomeric equilibrium shown in Figure 8.3 (a), (b).

Moreover, at pH 3 it was found that quercetin concentration tends to decrease as shown in Figure 8.4, hence the clove extract was unable to produce better PL intensity.

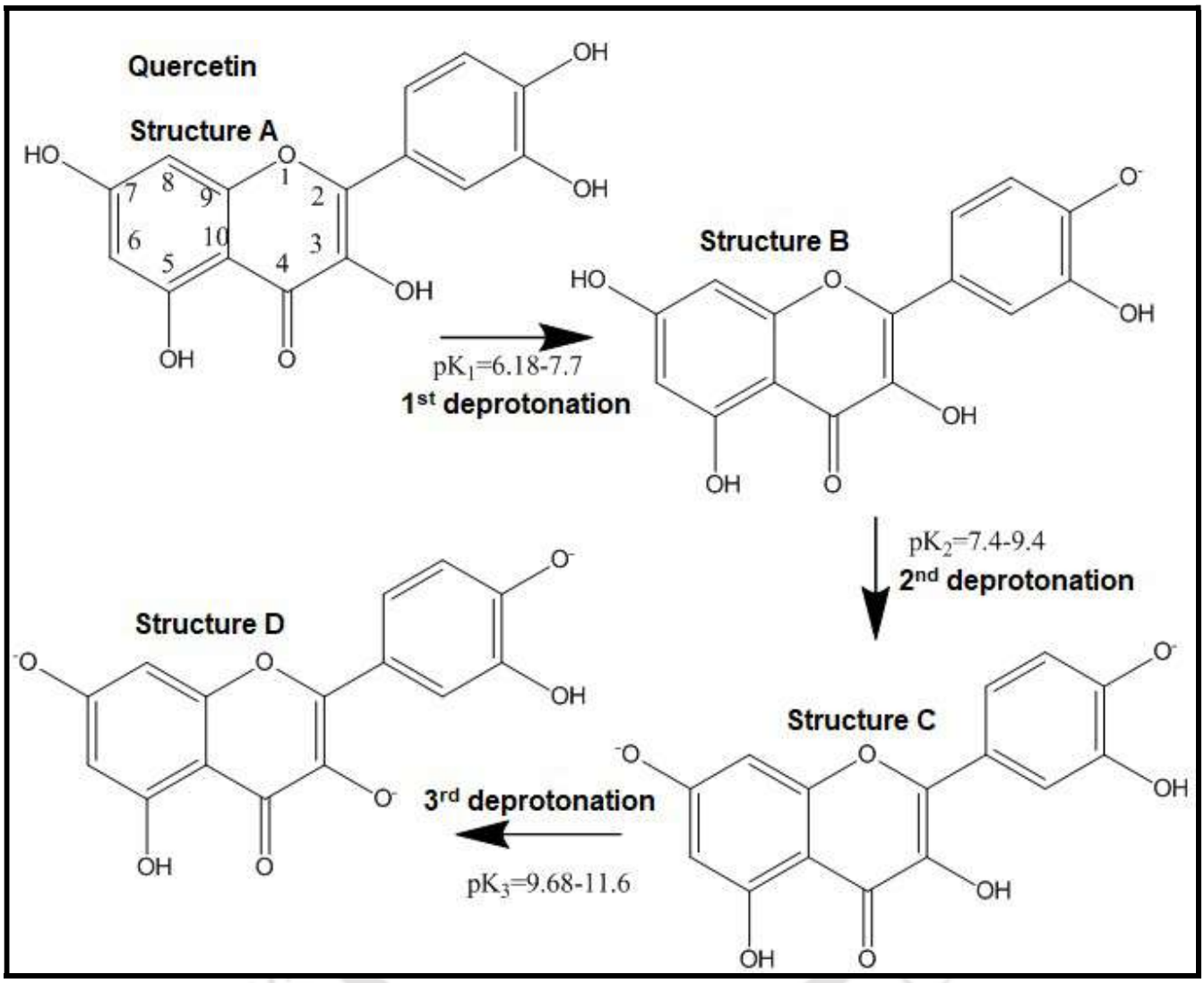

Figure 8.2: Deprotonation mechanism of quercetin at different aqueous pH

Interesting insights were gained at pH 12 where the PL intensity of the clove extract was found to quench drastically as shown in Figure 8.1, though quercetin exists in sufficient amount at pH 12 as shown in Figure 8.4.

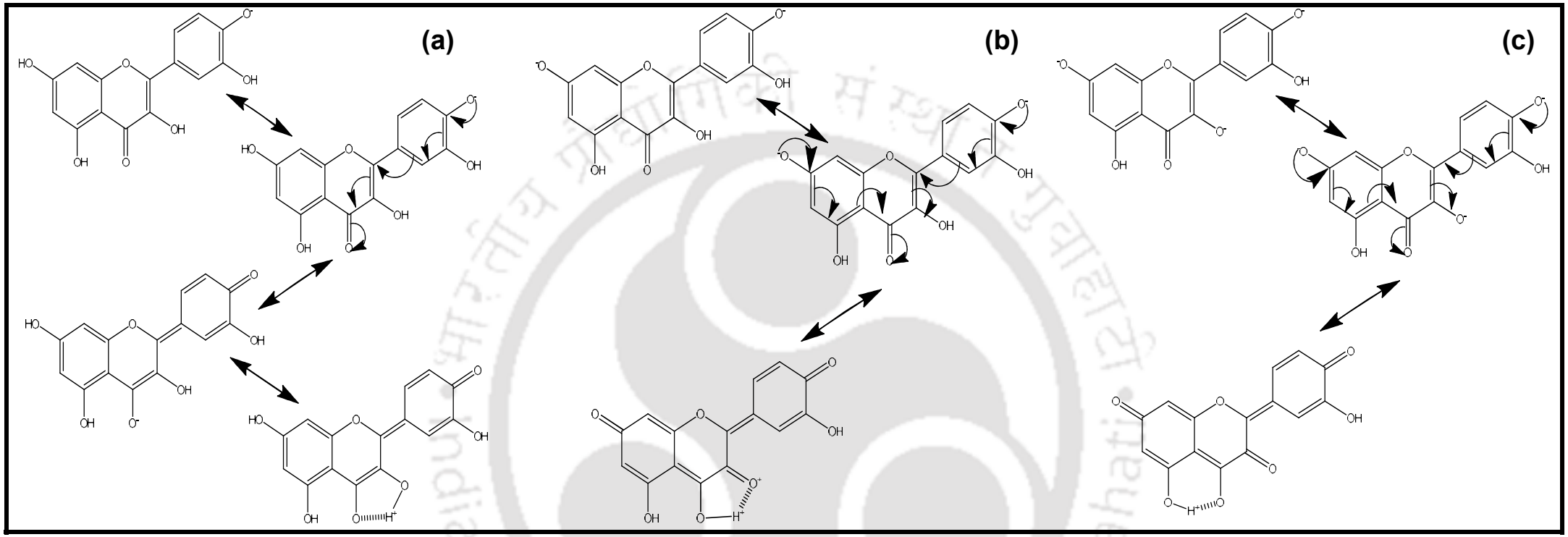

Figure 8.3: (a) Tautomeric form of structure B after 1st deprotonation of quercetin (hydrogen bonding between C(4)=O···HO-C(3) (PL intensity enhances) (b) Tautomeric form of structure C after 2nd deprotonation of quercetin (hydrogen bonding between C(4)=O···HO-C(3) (PL intensity enhances) (c) Tautomeric form of structure D after 3rd deprotonation of quercetin (hydrogen bonding between C(4)=O···HO-C(5) (Interference reducing PL intensity)

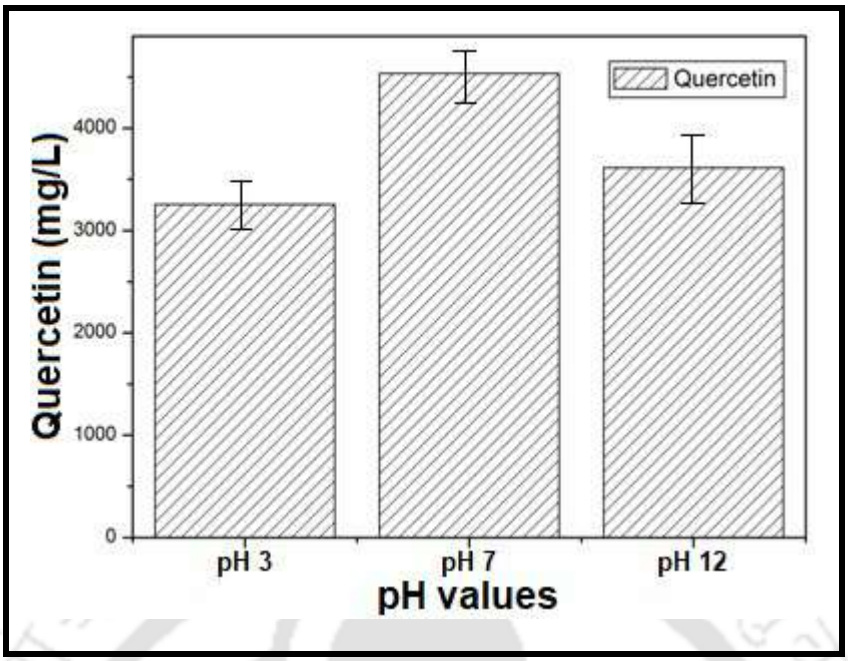

Figure 8.4: Quercetin concentration variation at different pH values

Such findings were denoted due to the deprotonated structure D shown in Figure 8.2) attained at higher pH which initiates tautomeric equilibrium through the hydrogen bond between =O of C(4) and –HO of C(5) as shown in Figure 8.3c, preventing efficient intramolecular proton transfer by interfering with the hydrogen bond of C(4)=O···HO−C(3). Since at lower pH, the tautomeric forms of deprotonated quercetin provides an efficient hydrogen bonding between C(4)=O···HO−C(3) hence PL intensity enhances, which was not found favourable at higher pH.

8.2.3. Photoluminescence behaviour of prepared Fe-Al nanocomposite

The prepared Fe-Al NCs were dispersed at normal pH solution and then utilizing Fluoresence spectrophotometer was excited at different wavelength from 320-420 nm at a step change of 10 nm. The emission spectrum was obtained in the range of 450-460 nm. It was found that maximum photoluminescence intensity was obtained at an excitation wavelength of 320 nm with single band emission spectra near 450 nm shown in Figure

8.5a. Furthermore, optimization of the pH solution in which the Fe-Al NCs imparted highest PL intensity was found out to be ~pH 5 where the emission peak formed at 455nm and shifted towards 460 nm as depicted in Figure 8.5(b). Similar observation was reported by Zhang et al. [238] where sp^2 hybridized carbon dots showed highest PL intensity at pH in the range of 5-6. Hence it was confirmed that new complex were formed at different pH compared to that of clove extract since the emission peak shifted from 470 nm for all the different pH variation. According to the UV absorption results obtained in our study shown in Figure 8.1(b), which also suggests that at pH 5 sp^2 hybridized C atoms in C=C, and C=O of the quercetin and rutin are present in highest quantity.

Similarly the low PL intensity of the synthesized Fe-Al NCs at pH 12 was also confirmed according to the UV absorption trend from Figure 8.1(b) Since the clove extract was found to originate photoluminescence both in blue-violet, and green-yellow emission band, hence it was denoted that electronic transition of sp^2 carbon (non-proton transferred) along with the excited state tautomeric structures (proton transferred) both played an important role. Whereas for the synthesized Fe-Al NCs the transition of sp^2 excited carbon from S_1 ($\pi\pi^*$) $\rightarrow$ S_0 normal (non proton-transferred) emission originated the blue-violet photoluminescence band only.

8.2.4. Photoluminescence study and selective sensing of Fe^{3+} ion

Figure 8.6 shows the PL intensity variation of the nanocomposite when dispersed at pH 5 in presence of different metal ions at 20 µM concentration. Fe^{3+} ion was found to quench the PL intensity highest, with respect to other ions such as Mn^{2+}, Ca^{2+}, Hg^{2+}, Cd^{2+}, Pb^{2+}, Cu^{2+}. The inset of Figure 8.6 shows the PL quenching intensity of different metals which shows Fe^{3+} ion quenches the PL intensity by several times than other heavy metals. A shift in peak was obtained in presence of Fe^{3+} ion which indicated the formation of new

complex. Due to the formation of nanocomposite which hindered the smooth proton transfer to its excited state, hence sharp emission peaks were not obtained.

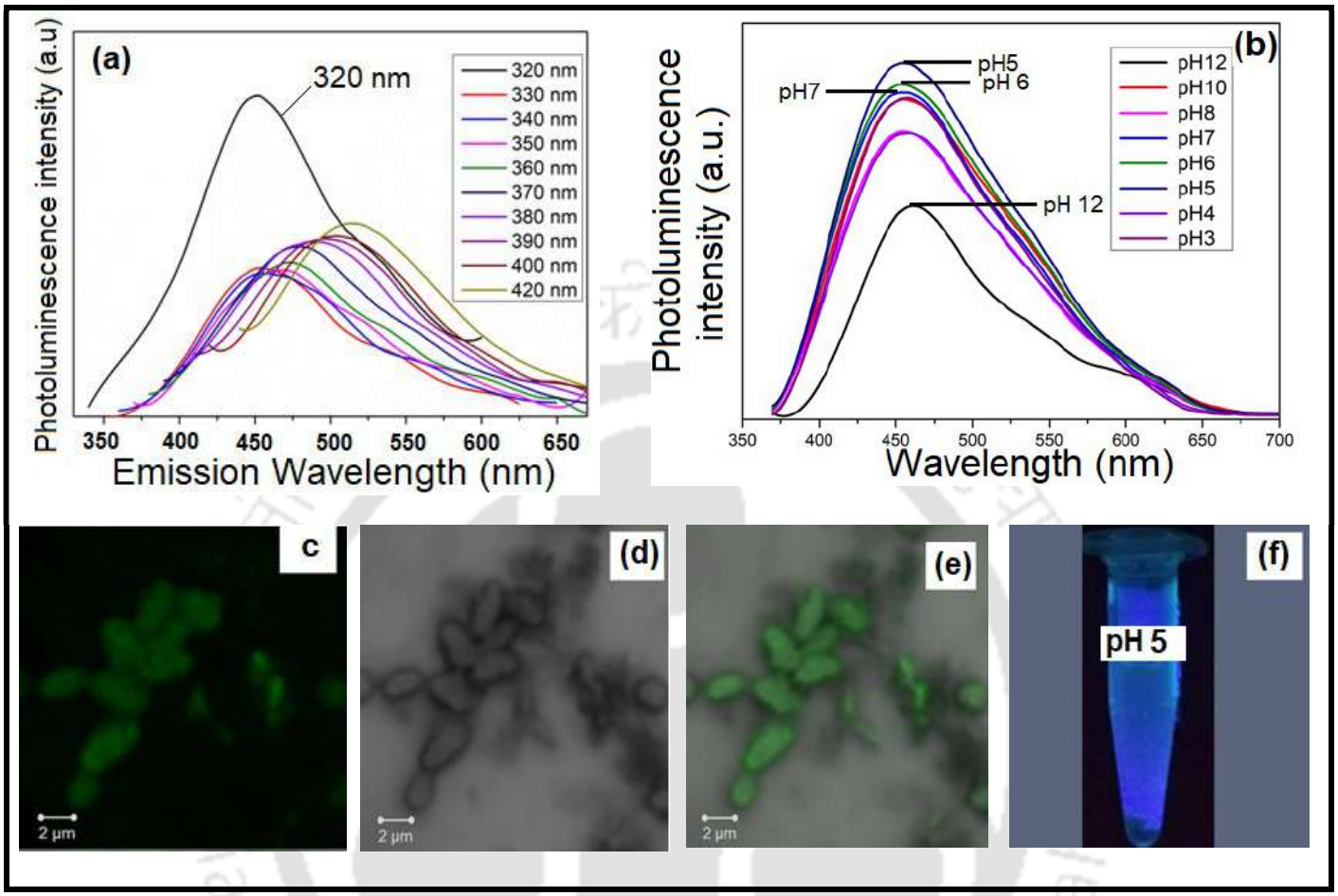

Figure 8.5: (a) Photoluminescence activity at different excitation wavelength for green synthesized Fe-Al nanocomposite kept at normal pH. (b) Photoluminescence effect of different aqueous pH Fe-Al NCs, excited at wavelength 320 nm with maximum emission at wavelength of 470 nm. (c, d, e) shows confocal microscopy image of green synthesized Fe-Al NCs (f) photo-luminescent blue color of the Fe-Al green synthesized nanocomposite at pH 12 through UV illuminator instrument

Figure 8.7 depicts the nature of PL intensity quenching of Fe-Al NCs on variation of Fe^{3+} concentration from 0.039-20.0 µM. It was observed that with increasing Fe^{3+} concentration the quenching property enhanced and after 20µM the equilibrium was attained, where no more further quenching was observed. It was observed that the

emission peak shifted below 450 nm with varying Fe^{3+} concentration and hence formation of metal-organic complex was assumed as observed from Figure 8.7.

Figure 8.8a shows the PL quenching activity of Fe^{3+} among other heavy metal ions, whereas Figure 8.8b depicts the PL quenching phenomenon at lower and higher concentration of Fe^{3+} ion through UV illuminator. A better effect of quenching behaviour was obtained through the images at higher Fe^{3+} ion concentration. The quenching efficiency of Fe^{3+} ions can be quantitatively explained by Stern-Volmer equation shown in Figure 8.9a and was obtained by varying the Fe^{3+} ion concentration from 0.02-30 µM.

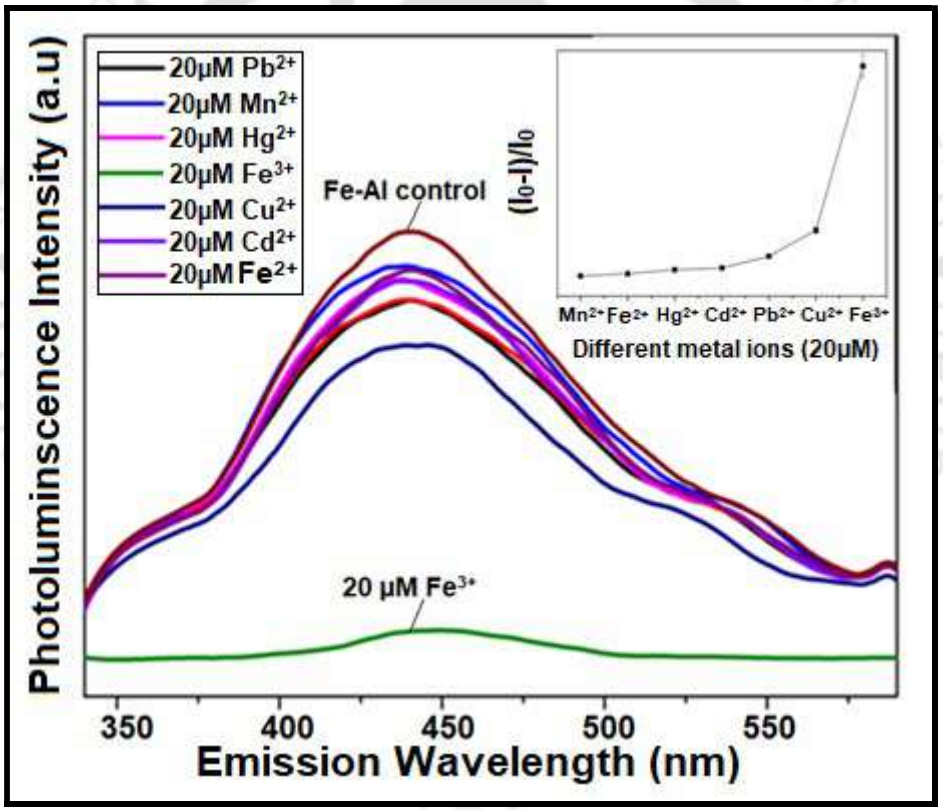

Figure 8.6: Quenching effect on photoluminescene intensity of Fe-Al NCs in presence of different metal ion of 20 µM concentration when excited at 320 nm (inset: normalization of quenching effect on photoluminescent intensity of different metal ions at 20 µM concentration when excited at 320 nm)

The relationship between (I_0/I-1) and Fe^{3+} ion concentration can be explained by the Stern-Volmer equation $(I_0/I-1)-1 = 1 + K_{sv}[Fe^{3+}]$ [225], where I_0 and I are the Fe-Al NCs PL

intensity initially at blank condition, and after adding various concentration Fe^{3+} ion respectively. The K_{sv} denotes quenching constant and from the curve it was observed that quenching of Fe^{3+} was linear in the low concentration range. The K_{sv} value was determined to be 9.05×10^5 M^{-1} as shown in Figure 8.9(b). The limit of detection (LOD) for Fe^{3+} ion was found to be 0.78 µM, which is found to be comparably better than values reported for various other Fe^{3+} ion fluorescence sensors as shown in Table 8.1.

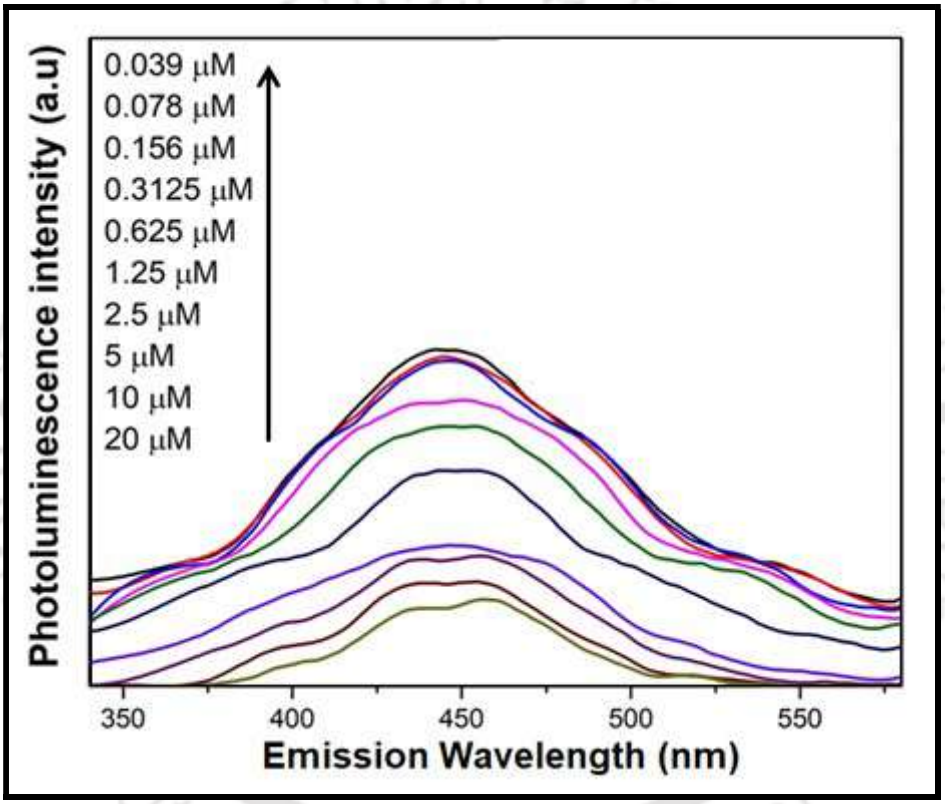

Figure 8.7: Quenching effect on photoluminescence intensity of Fe-Al NCs due to various concentration of Fe^{3+} ion solution when excited at 320 nm (inset: normalization of quenching effect due to various molar concentration of Fe^{3+}, excited at 320 nm)

Figure 8.10 shows the effect of interference due to presence of other heavy metals in the PL quenching effect by Fe^{3+} ions. On addition of equal molar concentration of specific heavy metals to Fe^{3+} ions in the ratio 1:1, it was observed that the PL intensity in presence of other heavy metals remains almost same, whereas on addition of Fe^{3+} ions the PL

intensity decreases. The figure reflects low quenching effect of heavy metals when present alone, whereas enhanced quenching on addition of Fe^{3+} ions to heavy metals.

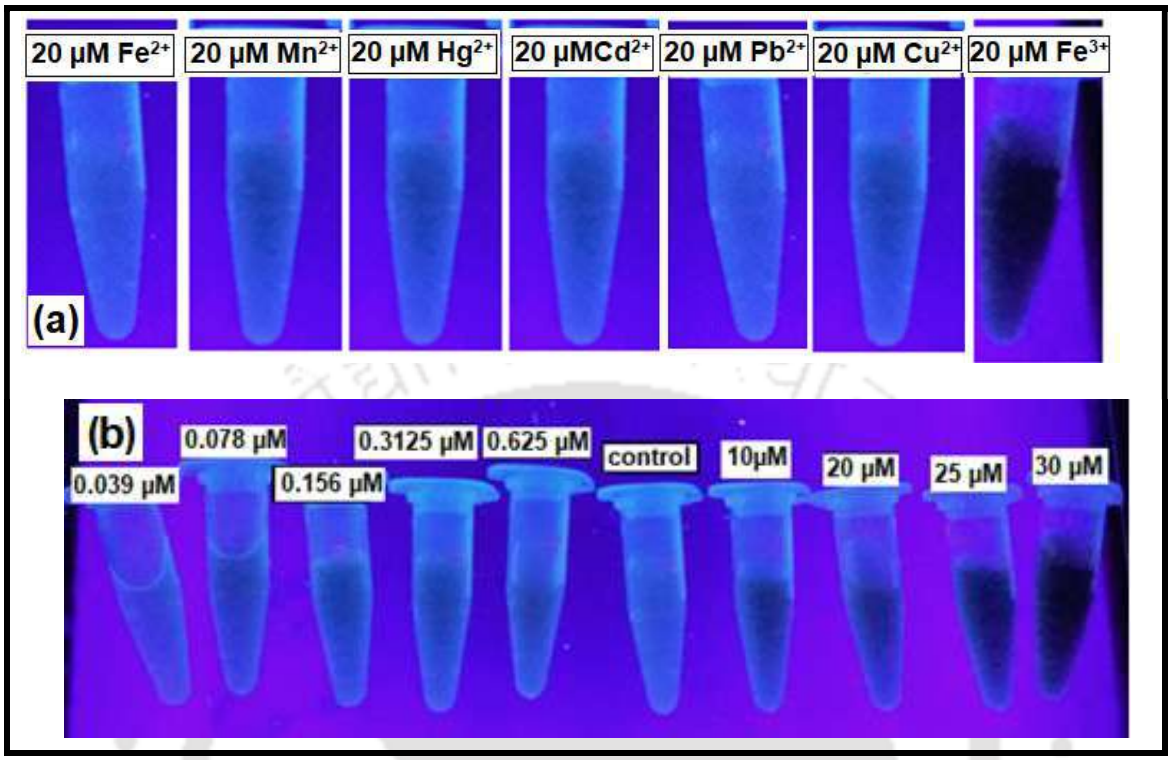

Figure 8.8: (a) Photoluminescence quenching behaviour of Fe^{3+} ion among other heavy metals (b) Photoluminescence quenching behaviour observed through UV illuminator at different molar concentration of Fe^{3+}

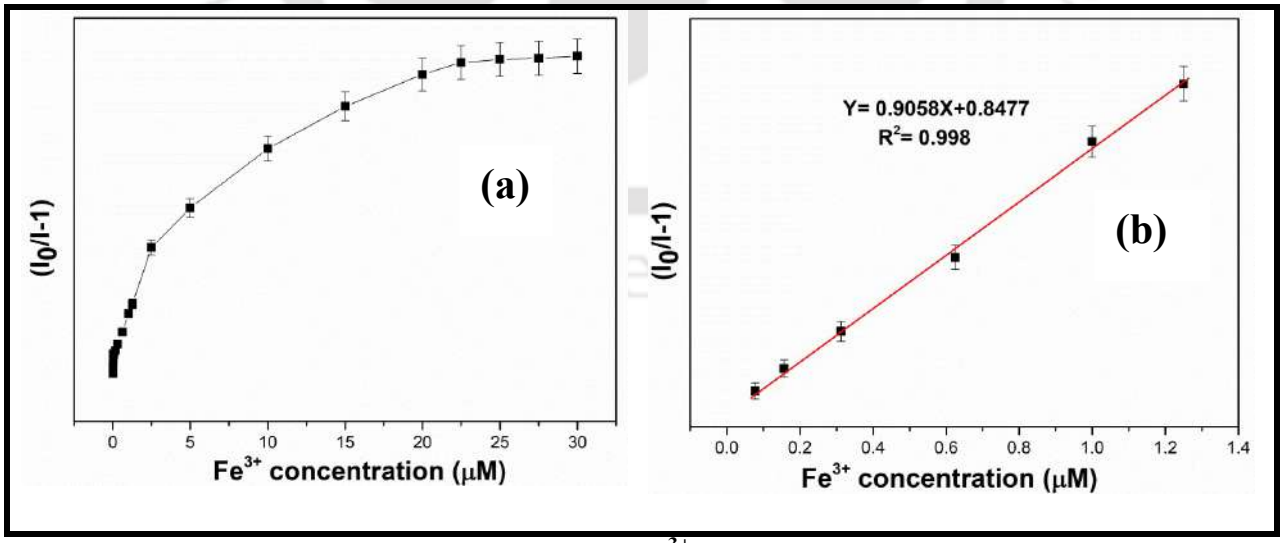

Figure 8.9: (a) The Stern-Volmer plot of Fe^{3+} ion (b) the linear response of PL intensity with varying concentration of Fe^{3+} ion at 450nm.

The results convey least effect of interference by the other heavy metals is associated while detecting Fe^{3+} ions. To understand the quenching mechanism of Fe^{3+} ions, the UV absorption spectra of Fe^{3+} solution and PL emission spectra of synthesized Fe-Al NCs were studied. It was quite well known that Fe^{3+} produced an UV absorption band in the region 200-600 nm [225].

Table 8.1: Comparing the LOD values of various other prepared sensors used for Fe^{3+} ion detection.

Material	LOD value	Reference
Carbon Dots	20 µM	239
Nitrogen-doped Carbon Dots	0.9 µM	240
N, S-co-doped Carbon Dots	1.7 µM	241
Gold Nanoparticle	5.6 µM	242
Polymeric Chemosensor	0.9 µM	243
Julolidine and imidazole based chemosensor	2.11 µM	244
Amidine based chemosensor	14 µM	245
Graphene quantum dots	0.45 µM	246
Fluorescent poly(hydroxyurethane)	4.56 µM	247
534-MOF-Tb	0.13 mM	248
$\{[Zn(ATA)(L)]\cdot H_2O\}_n$	3.76 µM	249
$\{[Cd(L)(SDBA)(H_2O)]\cdot 0.5H_2O\}_n$	7.14 µM	250
$[Tb(HL)(DMF)(H_2O)_2]\cdot 3H_2O$	50 µM	251
Benzothiazole derivative probe	3.05 µM	252
Naphthalimide based sensor	4.5 µM	253
Pyrazoline derivative sensor	1.4 µM	254
Fe-Al NCs	**0.7 µM**	**This work**

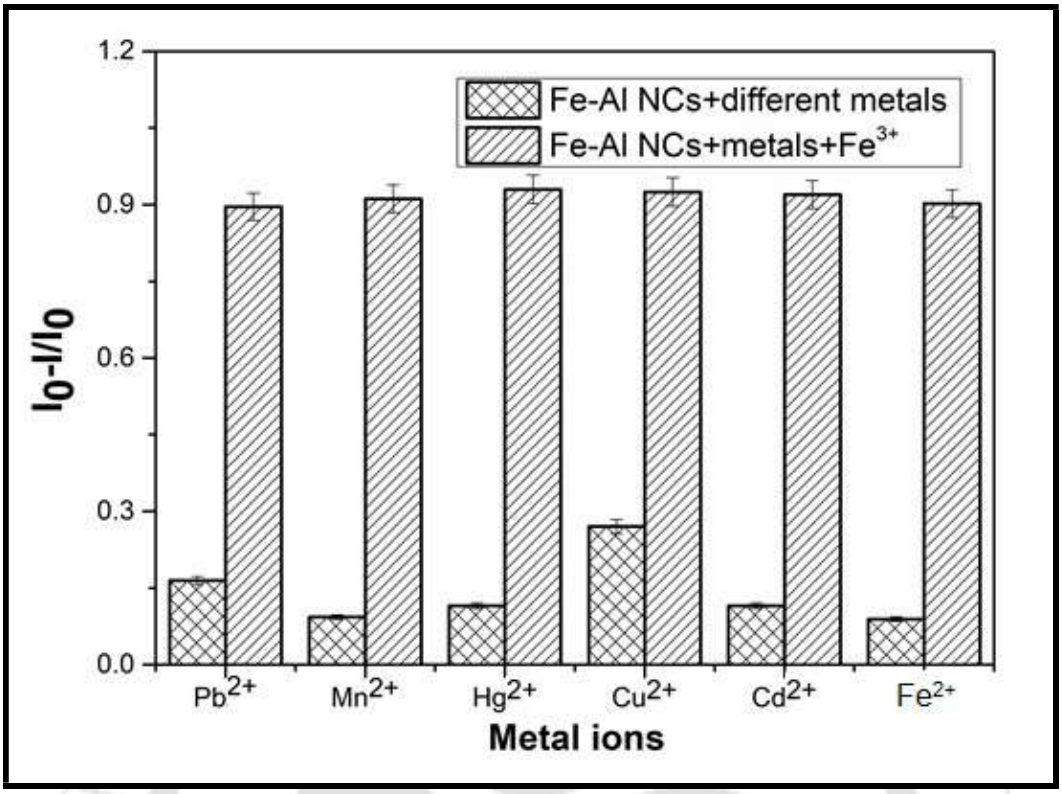

Figure 8.10: Interference studies results affecting photoluminescence quenching in presence of other metal ion in ratio 1:1 to Fe^{3+} ions for Fe-Al NCs

Hence from the PL emission spectra of Fe-Al NCs it was observd that an effective overlap occurred between the emission spectra of Fe-Al NCs and the absorption spectra of Fe^{3+} ions. Such phenomenon indicates that the observed quenching process may arise due to the fluorescence resonance energy transfer (FRET) [224].

Such spectral overlap may result in direct transfer of the energy generated by the electronic transition in the Fe-Al NCs material to to the analytes. Hence due to hindrance in emitting photoluminescence in the form of radiative transitions, quenching in PL intensity occurs. Moreover due to the presence of vacant d-orbital in Fe^{3+} ions it possess a strong electron withdrawn ability, and thus the PL quenching can also be attributed to the photoinduced electron transfer (PET) process [226,227] as shown in Figure 8.11. Hence the PL quenching of Fe-Al NCs by Fe^{3+} ions is believed to occur both due to the electron transfer and energy transfer phenomenon.

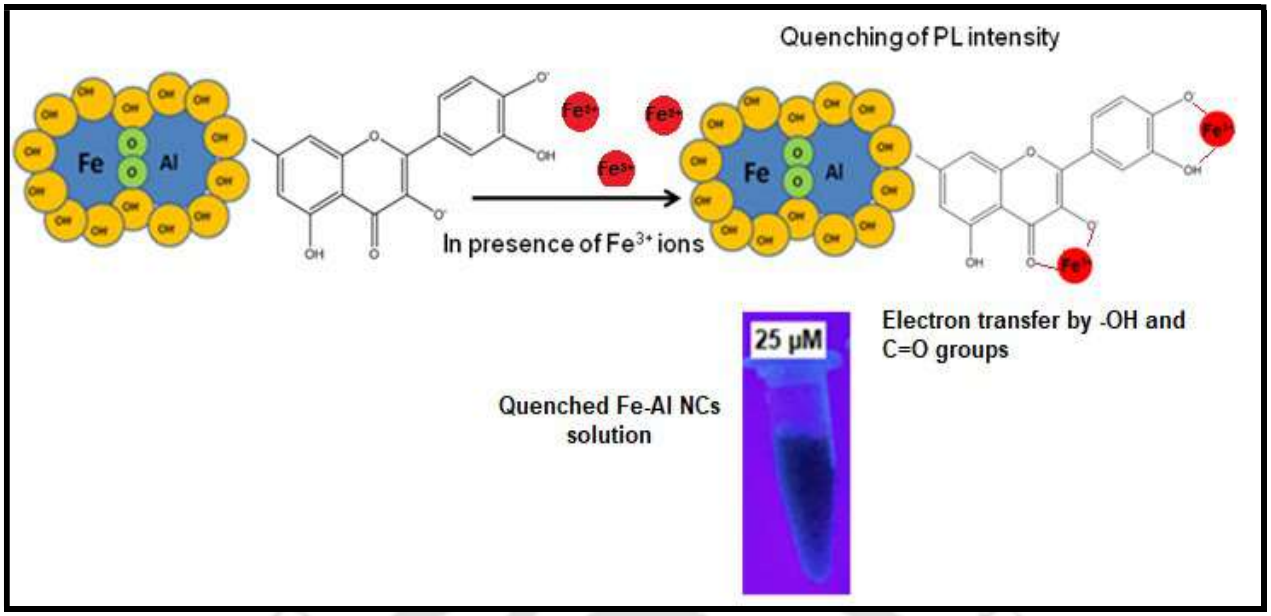

Figure 8.11: Mechanism for quenching of photoluminescence of Fe-Al NCs effect due to Fe^{3+} ion bonding with the electron donor groups of flavonoids

8.2.5. Applicability of Fe-Al NCs based Fe^{3+} sensor in real sample water

The utilization of Fe-Al NCs based Fe^{3+} sensor towards environmental samples was further studied. The tap water from IIT Guwahati, Assam campus was collected and the Fe^{3+} concentration was fixed to about 0.5 µM, 0.7µM, and 1µM and confirmed by analyzing through AAS (Atomic Absorption Spectrophotometer, Model No.: Spectra AA 220 FS; Make: M/s Varian, Netherland). Now the each prepared sample (0.5 µM, 0.7µM, and 1µM) of about 200µL were added to 3mL of the Fe-Al NCs and were analyzed through Fluorescence Spectrophometer. Through the quenched intensity obtained and utilizing the linearized equation from **Figure 9b**, the concentration of the analyzed sample were found to have a error percentage of 4.2±0.2, 3.4±0.3, and 2.8±0.15 respectively for 0.5 µM, 0.7µM, and 1µM Fe^{3+} samples. Such results convey that in spite of presence of various minerals and organics in tap water, but still the Fe-Al NCs based Fe^{3+} sensor can provide effective detection with negligible error %. Moreover, from the previous Chapter 7 it was obtained that the prepared green synthesized Fe-Al nanocomposite when treated

with water samples collected from Mariani substation, Jorhat Upper Assam, India also improved the water quality. Such results conveyed that the prepared green synthesized Fe-Al NCs can play multiple roles in treating a wastewater, by detecting and quantifying Fe^{3+} ions as well as enhancing the water quality.

Chapter 9

Summary, Conclusions and Future Scope of Work

Chapter 9

Summary, Conclusions and Future Scope of Work

This chapter is divided into three parts; the first section elaborates summary which contains a brief gist of all the work presented in this thesis. Second section named as conclusions restrains the winding up of all the chapters and provides the inferences drawn from various work presented in this thesis. Last section is about suggestions towards the future scope of this work.

9.1 Summary

This thesis work comprises of green synthesis of iron and iron-based nanomaterials, its characterization and furthers its application towards environmental remediation purposes. It provides an in-depth knowledge of selecting a better green source, analyzing their phenolic, flavonoid, tannin content, and antioxidant potential capacity. Selecting better solvent and optimizing process parameters for producing a better phenolic and flavonoid content green extract which can efficiently reduce and provide stabilize aromatic coating to the synthesized Fe-NPs was discussed. Moreover insights into morphological variations of synthesized Fe-NPs controlled by the green extract pH were also discussed in this work. Utilization of the green synthesized Fe NPs towards dye degradation activity along with its specific Fe^{3+} ion sensing ability was investigated utilizing photoluminescence property. Moreover green synthesis was utilized for preparing iron-aluminum nanocomposite which was found to have excellent fluoride removal efficiency towards fluoride affected water in North-east regions of India. Further, the synthesized iron-aluminum nanocomposite was investigated for photoluminescent property and was utilized towards ion sensing application, which proved to be specific for Fe^{3+} ions in real water samples. The major conclusions from this study are summarized chapter wise and shown below.

9.2 Conclusion

This section provides the overall gist and important outcomes from specific chapters of the thesis work.

Chapter 3: Preparation of green synthesized iron nanoparticles from extracts of Syzygium aromaticum (clove), Elettaria cardamomum (cardamom), Laurus nobilis (bay leaf) and studying its dye removal effect

1. Aqueous clove extract was found to have highest total polyphenolic content (130.75±4.57 mg rutin/g sample), total flavonoid content (59.56±2.5 mg gallic acid/g sample), and total tannin content (3.46±0.15 g gallic acid/100g sample)
2. Aqueous clove extract was found to have highest antioxidant property with DPPH scavenging value of (83.7±4.8 %), and FRAP assay value of 48.45±2.7µM Fe(II)/ g dry sample
3. Clove extract mediated Fe NPs was found to have lowest average diameter of 8.46±0.6 nm, highest Fe/O elemental weight % ratio 2.1 indicating less oxide formation, and highest cationic dye removal of 91.1% at pH3 at adsorbent dosage of 1.25 g/L

Chapter 4: Selection of extraction solvent and optimizing process parameters for maximizing total phenolic (TPC), and total flavonoid content (TFC) of Syzygium aromaticum (clove) extract

1. Aqueous extract of clove (5g of dry clove powder in 15 mL) was found to have highest common flavonoid content of rutin and quercetin of about 1459.37±65.7 and 63745.15±350.2 mg/L with respect to methanol and ethanol extract

2. On optimization of process parameters utilizing CCD and RSM at time (50 min), temperature (65 °C), and water content (30mL) for 10 g of dry clove, maximum TFC, TPC values obtained were 67.05 mg gallic acid/g sample and 155.15 mg rutin/g sample respectively.
3. At pH4 highest surface plasmon resonance of sp^2 hybridized carbon of polyphenolic groups was obtained.

Chapter 5: Studying the morphological insights of Syzygium aromaticum extract mediated iron nanoparticles with pH variation and its photoluminescence effect towards heavy metal ion detection in real water

1. pH variation of clove extract synthesized Fe NPs showed r, at pH 4 the average diameter of Fe NPs was the least 1.63±0.06 nm, at pH 7 it increased to 9.27±0.23 nm, whereas at pH 12 it again decreased to 4.26±0.23 nm.
2. Elemental analysis showed elemental O (wt%) was highest about 13.5 wt% for Fe NPs formed at pH 7, which confirmed the highest oxide formation.
3. At pH 4, on excitation at 380nm, highest photoluminescence (PL) intensity emission was observed at 530 nm

   Fe^{3+} ion was found to highest quench the PL intensity in presence of other heavy metals, the LOD value was found to be 0.27µM, whereas detection range was 0.625-10.0 µM

Chapter 6: Green synthesized iron nanoparticles supported on pH responsive polymeric membrane for nitrobenzene reduction and fluoride rejection study: Optimization approach

1. Flux variation of 142 L/m^{2}h at pH3 to 58 L/m^{2}h at pH12 confirms pH responsiveness of the membrane along with an IEC value of 0.18.
2. Aniline formation of 15 ppm was found to be highest at pH3 and lowest of 12.8 ppm at pH7 for 0.01 wt% Iron NPs impregnated membrane at end of 50 min, whereas aniline formation increased at pH12 to 13.9 ppm than pH7, which was attributed due to the pH responsiveness of the membrane.
3. NB reduction was highest of 89.92% at pH3 and 0.01wt% Iron NPs content. As Iron NPs content increases at 0.1 and 1 wt% at pH3, NB reduction decreases to 82.75% and 79.45% respectively.
4. For 5 ppm fluoride solution rejection rate at the end of 3rd cycle decreases by 60%, whereas for 10 ppm and 20 ppm 63.05% and 72.7% respectively

Chapter 7: Preparation and characterization of novel green synthesized iron-aluminum nanocomposite and studying its efficiency in fluoride removal

1. Langmuir monolayer adsorption capacity was calculated 28.07 mg/g at 313 K, higher than previously graphene related reported studies.
2. The fluoride adsorption obeys pseudo-second order kinetics whereas rate was controlled by multistage diffusion process.
3. The ion exchange mechanism suitably described the adsorption processes as observed from FTIR and experimental studies
4. Counter ions decreased the fluoride adsorption maximum by 31% for 90 mg/L chloride solution

5. Desorption of maximum 72.3% was obtained when treated with 2.5 (M) NaOH. After 3 successive cycle of adsorption the fluoride removal percentage decreases by 78.3 %
6. A dosage of 1.25 g/L was found to be effective to remove fluoride about 82.6% and 83% from water samples collected from Upper Assam and Manipur, India respectively.

Chapter 8: Study of photoluminescence activity and heavy metal ion detection ability of green synthesized iron-aluminum nanocomposite

1. At an excitation wavelength of 320 nm the highest Pl emission was obtained at 450 nm at pH=5
2. In the presence of other various heavy metal ions, ON-OFF PLA intensity was observed for Fe^{3+} ion showing specific ion sensing ability.
3. The nanocomposite was found to linearly quench Fe^{3+} in lower range concentration 0.078-0.125 µM. The LOD was found to be comparably low ~0.78 µM with high quenching constant K_{sv} 9.0×10^{5} M^{-1}.
4. For real water sample analysis with Fe^{3+} ion concentration 0.5 µM, 0.7µM, and 1µM, negligible error of 4.2±0.2%, 3.4±0.3%, and 2.8±0.15% respectively.

9.3 Future scope of work

Research findings in this work provided a good number of insights with respect to preparation and characterization of green synthesized nanomaterials along with its morphological and physico-chemical properties. Role of green extract and its optimization based on phenolic and flavonoid contents have also been investigated in depth. Few research areas for future work are presented as follows:

Preparation of green synthesized nanomaterials from plant wastes, its mechanism and recovery study

1. Plant wastes could be utilized towards preparing better green source extract, by optimizing extraction solvents and pH to obtain maximum total phenolic and flavonoid content which results in better antioxidant property.
2. Green synthesis of metallic nanoparticle and their mechanism of formation need to investigate in depth. Variation in the formation of oxides and zero-valent NPs with pH variation should be investigated.
3. Studying the multipurpose property of green synthesized nanoparticles, which can be used simultaneously toward wastewater pollutant degradation and heavy metal ion sensing application.
4. To study the magnetic effect of green synthesized iron related nanomaterials, this can be effectively utilized to recover them after wastewater application.

Studying specific sensing abilities of green synthesized nanomaterials

1. Studying the pH responsive color change activity of the NPs doped aqueous solution. The flavonoids present over the NPs coating due to pH variation changes its structure and gives rise to different coloration effect.
2. Doping of green synthesized NPs with effective coating for sensing specific water contaminants like arsenic and fluoride.
3. Utilizing green synthesized NPs towards glucose and other important compounds sensing application in human blood.

Preparation of bi-metallic nanomaterials and studying their photoluminescence activities

1. Preparation of novel green synthesized bi-metallic nanocomposites which could act as better adsorbent than the prevailing chemical reagents.
2. Studying the photoluminescence effect of the green synthesized bi-metallic nanocomposite and investigating the underlying mechanism for such photoluminescence activity.

Preparation of green synthesized nanomaterial embedded pH responsive membranes

1. Preparation of NPs impregnated pH responsive, temperature responsive membranes and studying its catalytic behavior towards water pollutant degradation, and heavy metal ion rejection simultaneously.
2. The dual activity of such stimuli responsive membranes towards rejection and reaction is unique and needs to be investigated further

References

[1] Taghizadeh, F., Ghaedi, M., Kamali, K., Sharifpour, E., Sahraie, R., Purkait, M. K. 2013. Comparison of nickel and/or zinc selenide nanoparticle loaded on activated carbon as efficient adsorbents for kinetic and equilibrium study of removal of Arsenazo (III) dye. Pow. Technol. 245, 217 - 226.

[2] Abdeen, M., Sabry, S., Ghozlan, H., El-Gendy, A.A., Carpenter, E.E., 2016. Microbialphysical synthesis of Fe and Fe_3O_4 magnetic nanoparticles using *Aspergillus niger* YESM1 and supercritical condition of ethanol. J. Nanomater. 2016, 1–7.

[3] Asfaram, A., Ghaedi, M., Purkait, M. K. 2017. Novel synthesis of nanocomposite for the extraction of Sildenafil Citrate (Viagra) from water and urine samples: Process screening and optimization, Ultra. Sono. 38, 463-472.

[4] Raul, P. K., Devi, R. R., Umlong, I. M., Banerjee, S., Singh, L., Purkait, M. K. 2012. Removal of Fluoride from Water Using Iron Oxide-Hydroxide Nanoparticles, J. Nano Sci. and Nano Technol., 12, 3922–3930.

[5] Goswami, A., Purkait, M. K. 2015. Preparation and characterization of nanoporous schwertmannite for defluoridation of water, Res. J Sci. Technol. 2, 65-83.

[6] Jebali, A., Ramezani, F. and Kazemi, B., 2011. Biosynthesis of silver nanoparticles by Geotricum sp. *Journal of Cluster Science*, *22*(2), 225-232.

[7] Hosseini, S. J., Aghaie, H., Ghaedi, M., Dashtian, K., Purkai, M. K. 2016. Lead (II) adsorption from aqueous solutions onto modified Ag nanoparticles: Modeling and optimization, Environ. Prog. & Sustain. En. 3 (35), 743-749.

[8] Ghaedi, M., Hekmati Jah, A., Khodadoust, S., Sahraei, R., Daneshfar, A., Mihandoost, A., Purkait, M. K. 2012. Cadmium telluride nanoparticles loaded on activated carbon as adsorbent for efficient removal of sunset yellow, Spectro. Acta Part A: Mol. Biomol. Spectro. 90, 22-27.

[9] Gonzalez-Moragas, L., Yu, S.-M., Murillo-Cremaes, N., Laromaine, A., Roig, A., 2015. Scale-up synthesis of iron oxide nanoparticles by microwave-assisted thermal decomposition. Chem. Eng. J. 281, 87–95.

[10] Bolade, O.P., Williams, A.B. and Benson, N.U., 2019. Green synthesis of iron-based nanomaterials for environmental remediation: A review. *Environmental Nanotechnology, Monitoring & Management*, 100279.

[11] Dey, A., Singh, R., Purkait, M. K. 2014. Cobalt Ferrite nanoparticles aggregated Schwertmannite: A novel adsorbent for the efficient removal of arsenic, J. Water Proc. Eng. 3, 1-9.

[12] Ghaedi, M., Yousefinejad, M., Safarpoor, M., Zare Khafri, H. Purkait, M. K. 2015. Rosmarinus officinalis leaf extract mediated green synthesis of silver nanoparticles, and antimicrobial properties, J. Ind. and Eng. Chem. 31, 167–172.

[13] Mohanpuria, P., Rana, N.K. and Yadav, S.K., 2008. Biosynthesis of nanoparticles: technological concepts and future applications. J. Nano. Res. 10(3), 507-517.

[14] Arabi, M., Ostovan, A., Ghaedi, M., Purkait, M. K. 2016. Novel strategy for synthesis of magnetic dummy molecularly imprinted nanoparticles based on functionalized silica as an efficient sorbent for the determination of acrylamide in potato chips: optimization by experimental design methodology, Talanta, 154 (2016) 526-532.

[15] Clemons, T.D., Kerr, R.H. and Joos, A., 2019. Multifunctional magnetic nanoparticles: Design, synthesis, and biomedical applications. In *Comprehensive Nanoscience and Nanotechnology: Volume 3: Biological Nanoscience* (pp. 193-210). Elsevier BV.

[16] Frenkel, J. and Doefman, J., 1930. Spontaneous and induced magnetisation in ferro-magnetic bodies. *Nature*, *126* (3173), 274-275.

[17] Anastas, P.T., Werner, J.C., 1998. Green Chemistry: Theory and Practice. *Oxford University Press*, New York.

[18] Yew, Y.P., Shameli, K., Miyake, M., Khairudin, N.B.B.A., Mohamad, S.E.B., Naiki, T. and Lee, K.X., 2020. Green biosynthesis of superparamagnetic magnetite Fe_3O_4 nanoparticles and biomedical applications in targeted anticancer drug delivery system: A review. Arab. J. Chem. 13(1), 2287-2308.

[19] He, F., Zhao, D. 2005. Preparation and characterization of a new class of starch-stabilized bimetallic nanoparticles for degradation of chlorinated hydrocarbons in water. Environ. Sci. Technol. 39, 3314–3320.

[20] Gao, S., Shi, Y., Zhang, S., Jiang, K., Yang, S., Li, Z., Takayama-Muromachi, E. 2008. Biopolymer-assisted green synthesis of iron oxide nanoparticles and their magnetic properties. J. Phys. Chem. C. 112, 10398–10401.

[21] Jegan, A., Ramasubbu, A., Saravanan, S., Vasanthkumar, S. 2011. One-pot synthesis and characterization of biopolymer—Iron oxide nanocomposite. Int. J. Nano Dimens. 2, 105–110.

[22] Nadagouda, M.N. and Varma, R.S., 2007. A greener synthesis of core (Fe, Cu)-shell (Au, Pt, Pd, and Ag) nanocrystals using aqueous vitamin C. Cryst. Growth Des. 7(12), 2582-2587.

[23] Savasari, M., Emadi, M., Bahmanyar, M.A., Biparva, P. 2015. Optimization of Cd(II) removal from aqueous solution by ascorbic acid-stabilized zero valent iron nanoparticles using response surface methodology. J. Ind. Eng. Chem. 21, 1403–1409.

[24] Krishna, R., Titus, E., Krishna, R., Bardhan, N., Bahadur, D., Gracio, J. 2012. Wet-chemical green synthesis of L-lysine amino acid stabilized biocompatible iron-oxide magnetic nanoparticles. J. Nanosci. Nanotechnol. 12, 6645–6651.

[25] Siskova, K.M., Straska, J., Krizek, M., Tucek, J., Machala, L. and Zboril, R., 2013. Formation of zero-valent iron nanoparticles mediated by amino acids. Proc. Environ. Sci. 18, 809-817.

[26] Sayyad, A.S., Balakrishnan, K., Ci, L., Kabbani, A.T., Vajtai, R., Ajayan, P.M. 2012. Synthesis of iron nanoparticles from hemoglobin and myoglobin. Nanotechnology. 23, 055602.

[27] Lu, W., Shen, Y., Xie, A., Zhang, W., 2010. Green synthesis and characterization of superparamagnetic Fe_3O_4 nanoparticles. J. Magn. Magn. Mater. 322, 1828–1833.

[28] Sun, X., Zheng, C., Zhang, F., Yang, Y., Wu, G., Yu, A., Guan, N. 2009. Size-controlled synthesis of magnetite (Fe_3O_4) nanoparticles coated with glucose and gluconic acid from a single Fe(III) precursor by a sucrose bifunctional hydrothermal method. J. Phys. Chem. C. 113, 16002–16008.

[29] Yan, Q., Street, J., Yu, F. 2015. Synthesis of carbon-encapsulated iron nanoparticles from wood derived sugars by hydrothermal carbonization (HTC) and their application to convert bio-syngas into liquid hydrocarbons. Bio. Bioenergy. 83, 85–95.

[30] Demir, A., Baykal, A., So¨ zeri, H., 2014. Green synthesis of Fe_3O_4 nanoparticles by one-pot saccharide-assisted hydrothermal method. Turk. J. Chem. 38, 825–836.

[31] Herrera-Becerra, R., Rius, J.L., Zorrilla, C. 2010. Tannin biosynthesis of iron oxide nanoparticles. Appl. Phys. A. 100, 453–459.

[32] Dorniani, D., Hussein, M.Z., Kura, A.U., Fakurazi, S., Shaari, A.H., Ahmad, Z. 2012. Preparation of Fe_3O_4 magnetic nanoparticles coated with gallic acid for drug delivery. Int. J. Nanomed. 7, 5745–5756.

[33] Chang, P.R., Yu, J., Ma, X. and Anderson, D.P., 2011. Polysaccharides as stabilizers for the synthesis of magnetic nanoparticles. *Carbohydrate polymers*, *83*(2), 640-644.

[34] Klemm, D., Heublein, B., Fink, H.P. and Bohn, A., 2005. Cellulose: fascinating biopolymer and sustainable raw material. Angewandte chemie international edition, 44(22), 3358-3393.

[35] López-Téllez, G., Balderas-Hernández, P., Barrera-Díaz, C.E., Vilchis-Nestor, A.R., Roa-Morales, G. and Bilyeu, B., 2013. Green method to form iron oxide nanorods in orange peels for chromium (VI) reduction. J. Nanosci. Nanotech. 13(3), 2354-2361.

[36] Park, T.J., Lee, K.G. and Lee, S.Y., 2016. Advances in microbial biosynthesis of metal nanoparticles. App. Micro. Biotechnol. 100(2), 521-534.

[37] Singh, P., Kim, Y.J., Zhang, D. and Yang, D.C., 2016. Biological synthesis of nanoparticles from plants and microorganisms. Trends in biotechnol. 34(7), 588-599.

[38] Bharde, A., Rautaray, D., Bansal, V., Ahmad, A., Sarkar, I., Yusuf, S.M. Sanyal, M.; Sastry, M. 2006. Extracellular biosynthesis of magnetite using fungi. Small. 2, 135–141.

[39] Bharde, A., Wani, A.; Shouche, Y., Joy, P.A., Prasad, B.L.V., Sastry, M. 2005. Bacterial aerobic synthesis of nanocrystalline magnetite. J. Am. Chem. Soc. 127, 9326–9327.

[40] Moon, J.W., Rawn, C.J., Rondinone, A.J., Love, L.J., Roh, Y., Everett, S.M., Lauf, R.J. and Phelps, T.J., 2010. Large-scale production of magnetic nanoparticles using bacterial fermentation. J. Ind. Micro. & Biotech. 37(10), 1023-1031.

[41] Sundaram, P.A., Augustine, R., Kannan, M. 2012. Extracellular biosynthesis of iron oxide nanoparticles by *Bacillus subtilis* strains isolated from rhizosphere soil. Biotechnol. Bioprocess Eng. 17, 835–840.

[42] Elcey, C., Kuruvilla, A.T., Thomas, D. 2014. Synthesis of magnetite nanoparticles from optimized iron reducing bacteria isolated from iron ore mining sites. Int. J. Curr. Microbiol. Appl. Sci. 3, 408–417.

[43] Mukherjee, P., 2017. Stenotrophomonas and Microbacterium: Mediated Biogenesis of Copper, Silver and Iron Nanoparticles—Proteomic Insights and Antibacterial Properties versus Biofilm Formation. J. Cluster Sci. *28*(1), 331-358.

[44] Das, K.R., Kowshik, M., Kumar, M.P., Kerkar, S., Shyama, S.K. and Mishra, S., 2018. Native hypersaline sulphate reducing bacteria contributes to iron nanoparticle formation in saltpan sediment: A concern for aquaculture. *Journal of environmental management*, *206*, 556-564.

[45] Bharde, A., Rautaray, D., Bansal, V., Ahmad, A., Sarkar, I., Yusuf, S.M. Sanyal, M.; Sastry, M. 2006. Extracellular biosynthesis of magnetite using fungi. Small. 2, 135–141.

[46] Kaul, R.K., Kumar, P., Burman, U., Joshi, P., Agrawal, A., Raliya, R., Tarafdar, J.C. 2012. Magnesium and iron nanoparticles production using microorganisms and various salts. Mater. Sci. Poland. 30, 254–258.

[47] Mohamed, Y.M., Azzam, A.M., Amin, B.H., Safwat, N.A. 2015. Mycosynthesis of iron nanoparticles by Alternaria alternata and its antibacterial activity. Afr. J. Biotechnol. 14, 1234–1241.

[48] Sarkar, J., Mollick, M.M.R., Chattopadhyay, D., Acharya, K., 2017. An eco-friendly route of γ-Fe_2O_3 nanoparticles formation and investigation of the mechanical properties of the HPMC-γ-Fe_2O_3 nanocomposites. Bioprocess Biosyst. Eng. 40 (3), 351–359.

[49] Mazumdar, H., Haloi, N., 2011. A study on biosynthesis of iron nanoparticles by Pleurotus sp. J. Microbiol. Biotech. Res. 1 (3), 39–49.

[50] Tarafdar, J.C. and Raliya, R., 2013. Rapid, low-cost, and ecofriendly approach for Iron nanoparticle synthesis using Aspergillus oryzae TFR9. *Journal of Nanoparticles*.

[51] Mahdavi, M., Namvar, F., Ahmad, M.B. and Mohamad, R., 2013. Green biosynthesis and characterization of magnetic iron oxide (Fe_3O_4) nanoparticles using seaweed (*Sargassum muticum*) aqueous extract. Molecules, *18*(5), 5954-5964.

[52] Subramaniyam, V., Subashchandrabose, S.R., Thavamani, P., Megharaj, M., Chen, Z., Naidu, R. 2015. Chlorococcum sp. MM11—A novel phyco-nanofactory for the synthesis of iron nanoparticles. J. Appl. Phycol. 27, 1861–1869.

[53] Kalaiarasi, R., Jayallakshmi, N. and Venkatachalam, P., 2010. Phytosynthesis of nanoparticles and its applications. *Plant Cell Biotechnology and Molecular Biology*, *11*(1/4), 1-16.

[54] Huang, L., Luo, F., Chen, Z., Megharaj, M., Naidu, R. 2015. Green synthesized conditions impacting on the reactivity of Fe NPs for the degradation of malachite green. Spectrochim. Acta A. 137, 154-159.

[55] Wang, T., Jin, X., Chen, Z., Megharaj, M., Naidu, R., 2014. Green synthesis of Fe nanoparticles using eucalyptus leaf extracts for treatment of eutrophic wastewater. Sci. Total Environ. 466–467, 210-213.

[56] Machado, S., Pinto, S.L., Grosso, J.P., Nouws, H.P.A., Albergaria, J.T. and Delerue-Matos, C., 2013. Green production of zero-valent iron nanoparticles using tree leaf extracts. Sci. Tot. Environ. 445, 1-8.

[57] Fazlzadeh, M., Rahmani, K., Zarei, A., Abdoallahzadeh, H., Nasiri, F., Khosravi, R., 2017. A novel green synthesis of zero valent iron nanoparticles (NZVI) using three plant extracts and their efficient application for removal of Cr(VI) from aqueous solutions. Adv. Powder Technol. 28 (1), 122–130.

[58] Borja, J.Q., Ngo, M.A.S., Saranglao, C.C., Tiongco, R.P.M., Roque, E.C., Dugos, N.P., 2015. Synthesis of green zero-valent iron using polyphenols from dried green tea extract. J. Eng. Sci. Technol. 10 (Spec.issue7), 22–31.

[59] Singh, K.K., Senapati, K.K., Sarma, K.C., 2017. Synthesis of superparamagnetic Fe_3O_4 nanoparticles coated with green tea polyphenols and their use for removal of dye pollutant from aqueous solution. J. Environ. Chem. Eng. 5 (3), 2214–2221.

[60] Mohan Kumar, K., Mandal, B.K., Siva Kumar, K., Sreedhara Reddy, P., Sreedhar, B., 2013. Biobased green method to synthesise palladium and iron nanoparticles using Terminalia chebula aqueous extract. Spectro. Acta A. 102, 128–133.

[61] Saikia, I., Hazarika, M., Hussian, N., Das, M.R., Tamuly, C., 2017. Biogenic synthesis of Fe_2O_3@SiO_2 nanoparticles for ipso-hydroxylation of boronic acid in water. Tetrahedron Lett. 58 (45), 4255–4259.

[62] Manquian-Cerda, K., Cruces, E., Angelica Rubio, M., Reyes, C., Arancibia-Miranda, N., 2017. Preparation of nanoscale iron (oxide, oxyhydroxides and zero-valent) particles derived from blueberries: reactivity, characterization and removal mechanism of arsenate. Ecotoxicol. Environ. Saf. 145, 69–77.

[63] Venkateswarlu, S., Kumar, B.N., Prasad, C., Venkateswarlu, P., Jyothi, N., 2014. Bio-inspired green synthesis of Fe_3O_4 spherical magnetic nanoparticles using *Syzygium cumini* seed extract. Physica. B. Condens. Mat. 449, 67–71.

[64] Sajadi, S.M., Nasrollahzadeh, M., Maham, M., 2016. Aqueous extract from seeds of Silybum marianum L. as a green material for preparation of the Cu/Fe_3O_4 nanoparticles: a magnetically recoverable and reusable catalyst for the reduction of nitroarenes. J. Colloid Interface Sci. 469, 93–98

[65] Buazar, F., Baghlani-Nejazd, M.H., Badri, M., Kashisaz, M., Khaledi-Nasab, A., Kroushawi, F., 2016. Facile one-pot phytosynthesis of magnetic nanoparticles using potato extract and their catalytic activity. Starch-Starke 68, 796–804.

[66] Niraimathee, V., Subha, V., Ravindran, R.E., Renganathan, S., 2016. Green synthesis of iron oxide nanoparticles from Mimosa pudica root extract. Int. J. Environ. Sustain. Dev. 15, 227-240.

[67] Wei, Y., Fang, Z., Zheng, L., Tan, L., Tsang, E.P., 2016. Green synthesis of Fe nanoparticles using *Citrus maxima* peels aqueous extracts. Mater. Lett. 185, 384–386.

[68] Ehrampoush, M.H., Miria, M., Salmani, M.H., Mahvi, A.H., 2015. Cadmium removal from aqueous solution by green synthesis iron oxide nanoparticles with tangerine peel extract. J. Environ. Health Sci. Eng. 13 (1), 84-90.

[69] Njagi, E.C., Huang, H., Stafford, L., Genuino, H., Galindo, H.M., Collins, J.B., Hoag, G.E., Suib, S.L. 2011. Biosynthesis of iron and silver nanoparticles at room temperature using aqueous Sorghum bran extracts. Langmuir. 27, 264–271.

[70] Lunge, S., Singh, S., Sinha, A. 2014. Magnetic iron oxide (Fe_3O_4) nanoparticles from tea waste for arsenic removal. J. Magn. Magn. Mater. 356, 21–31.

[71] Khataee, A., Kayan, B., Kalderis, D., Karimi, A., Akay, S., Konsolakis, M. 2017. Ultrasound-assisted removal of Acid Red 17 using nanosized Fe_3O_4-loaded coffee waste hydrochar. Ultrason. Sonochem. 35, 72–80.

[72] Senthil, M., & Ramesh, C. 2012. Biogenic synthesis of Fe_3O_4 nanoparticles using Tridax procumbens leaf extract and its antibacterial activity on Pseudomonas aeruginosa. Dig. J. Nanomat. Biostruc. 7, 1655–1660.

[73] Kiruba Daniel, S. C. G., Vinothini, G., Subramanian, N., Nehru, K., & Sivakumar,M. M. 2013. Biosynthesis of Cu, ZVI, and Ag nanoparticles using Dodonaea viscosa extract for antibacterial activity against human pathogens. J. Nano. Res. 15, 1–10.

[74] Mondal, P., Purkait, M. K. 2019. Preparation and characterization of novel green synthesized iron–aluminum nanocomposite and studying its efficiency in fluoride removal. Chemosphere, 235, 391 – 402.

[75] Weng, X., Guo, M., Luo, F., Chen, Z., 2017. One-step green synthesis of bimetallic Fe/Ni nanoparticles by eucalyptus leaf extract: biomolecules identification, characterization and catalytic activity. Chem. Eng. J. 308, 904–911.

[76] Hoag, G.E., Collins, J.B., Holcomb, J.L., Hoag, J.R., Nadagouda, M.N., Varma, R.S. 2009 Degradation of bromothymol blue by ‘greener’ nano-scale zero-valent iron synthesized using tea polyphenols. J. Mater. Chem. 19, 8671–8677

[77] Huang, L.,Weng, X., Chen, Z., Megharaj, M., Naidu, R. 2013 Synthesis of iron-based nanoparticles using Oolong tea extract for the degradation of malachite green. Spectrochim. Acta A 117, 801–804.

[78] Kuang, Y., Wang, Q., Chen, Z., Megharaj, M., Naidu, R. 2013. Heterogeneous fenton-like oxidation of monochlorobenzene using green synthesis of iron nanoparticles. J. Colloid Interface Sci. 410, 67-73.

[79] Wang, Z. 2013 Iron complex nanoparticles synthesized by eucalyptus leaves. ACS Sustain. Chem. Eng. 1, 1551–1554.

[80] Wang, T., Lin, J., Chen, Z., Megharaj, M., Naidu, R. 2014. Green synthesized iron nanoparticles by green tea andeucalyptus leaves extracts used for removal of nitrate in aqueous solution. J. Clean. Prod. 83, 413-419.

[81] Luo, F., Chen, Z., Megharaj, M., Naidu, R. 2014 Biomolecules in grape leaf extract involved in one-step synthesis of iron-based nanoparticles. RSC Adv. 4, 53467–53474.

[82] Prasad, C., Karlapudi, S., Venkateswarlu, P., Bahadur, I., Kumar, S., 2017. Green arbitrated synthesis of Fe_3O_4 magnetic nanoparticles with nanorod structure from pomegranate leaves and Congo red dye degradation studies for water treatment. J. Mol. Liq. 240, 322-328.

[83] Ahmed, F., Arshi, N., Anwar, M.S., Danish, R., Koo, B.H., 2014. Quantum-confinement induced enhancement in photocatalytic properties of iron oxide nanoparticles prepared by ionic liquid. Ceram. Int. 40 (10), 15743–15751.

[84] Barhoumi, L., Dewez, D. 2013. Toxicity of superparamagnetic iron oxide nanoparticles on green alga Chlorella vulgaris. BioMed. Res. Int. 2013, 1-11.

[85] Rao, A., Bankar, A., Kumar, A.R., Gosavi, S., Zinjarde, S. 2013. Removal of hexavalent chromium ions by Yarrowia lipolytica cells modified with phyto-inspired Fe^0/Fe_3O_4 nanoparticles. J. Contam. Hydrol. 146, 63-73.

[86] Savasari, M., Emadi, M., Bahmanyar, M.A., Biparva, P. 2015. Optimization of Cd(II) removal from aqueous solution by ascorbic acid-stabilized zero valent iron nanoparticles using response surface methodology. J. Ind. Eng. Chem. 21, 1403–1409.

[87] Sebastian, A., Nangia, A., Prasad, M.N.V., 2018. A green synthetic route to phenolics fabricated magnetite nanoparticles from coconut husk extract: implications to treat metal contaminated water and heavy metal stress in Oryza sativa L. J. Clean. Prod. 174, 355–366.

[88] Nithya, K., Sathish, A., Senthil Kumar, P., Ramachandran, T., 2017. Fast kinetics and high adsorption capacity of green extract capped superparamagnetic iron oxide nanoparticles for the adsorption of Ni(II) ions. J. Ind. Eng. Chem. 59, 230-241.

[89] Groiss, S., Selvaraj, R., Varadavenkatesan, T., Vinayagam, R., 2017. Structural characterization, antibacterial and catalytic effect of iron oxide nanoparticles synthesised using the leaf extract of Cynometra ramiflora. J. Mol. Struct. 1128, 572–578.

[90] Shanker, U., Jassal, V., Rani, M., 2017. Green synthesis of iron hexacyanoferrate nanoparticles: potential candidate for the degradation of toxic PAHs. J. Environ. Chem. Eng. 5 (4), 4108–4120

[91] Al-Ruqeishi, M.S., Mohiuddin, T., Al-Saadi, L.K., 2016. Green synthesis of iron oxide nanorods from deciduous Omani mango tree leaves for heavy oil viscosity treatment. Arab. J. Chem. 12(8), 4084-4090.

[92] Smuleac, V., Varma, R., Sikdar, S., Bhattacharyya, D. 2011. Green synthesis of Fe and Fe/Pd bimetallic nanoparticles in membranes for reductive degradation of chlorinated organics. J. Membr. Sci. 379, 131–137.

[93] Smuleac, V., Varma, R., Sikdar, S., Bhattacharyya, D. 2011. Green synthesis of Fe and Fe/Pd bimetallic nanoparticles in membranes for reductive degradation of chlorinated organics. J. Membr. Sci. 379, 131–137.

[94] Chang, P.R., Yu, J., Ma, X. and Anderson, D.P., 2011. Polysaccharides as stabilizers for the synthesis of magnetic nanoparticles. *Carbohydrate polymers*, *83*(2), 640-644.

[95] Mondal, P., Purkait, M. K. 2017. Green synthesized iron nanoparticle-embedded pH-responsive PVDF-co-HFP membranes: Optimization study for NPs preparation and nitrobenzene reduction. Sep. Sci. Technol. 52(14), 2338-2355.

[96] Mondal, P., Purkait, M. K. 2018. Green synthesized iron nanoparticles supported on pH responsive polymeric membrane for nitrobenzene reduction and fluoride rejection study: Optimization approach. J. Clean. Prod. 170, 1111-1123.

[97] Martins, N., Roriz, C.L., Morales, P., Barros, L., Ferreira, I.C.F.R. 2013 Food colorants: challenges, opportunities and current desires of agro-industries to ensure consumer IOSR J. Appl. Phys. 5, 01–06.

[98] Aljaff, P., Banaz, O.R., Trifa, A.O. 2013. A comparison between natural and synthetic food flavoring extracts using infrared spectra and optical activity, IOSR J. Appl. Phys. 5 , 01–06.

[99] Kumar Vikrant, R.S.S.P., Giri,B.S., Raza,N., Roy, K., Rai, B.K. 2016. Recent advancements in it bioremediation of dye: current status and challenges, Solid. Electron. 112-134.

[100] Ahmad, A., Mohd- Setapar, S.H., Chuong, C.S., Khatoon, A., Wani, W.A., Kumar, R., Rafatullah, M. 2015. Recent advances in new generation dye removal technologies: novel search for approaches to reprocess wastewater, RSC Adv. 5, 30801–30818

[101] Zwane, S., Masheane, M.L., Kuvarega, A.T., Vilakati, G.D., Mamba, B.B., Nyoni, H., Mhlanga, S.D., Dlamini, D.S. 2017. Polyethersulfone/chromolaena odorata (PES/CO) adsorptive membranes for removal of Congo red from water, J. Water Process Eng. 233-245.

[102] Morshedi, D., Moohammadi, Z., Akbar, B., Masoud, M., Aliakbari, F. 2013. Using protein nanofibrils to remove azo dyes from aqueous solution by the coagulation process, Colloids Surf. B Biointerfaces 112, 245–254.

[103] Pan, Y., Wang, Y., Zhou, A., Wang, A., Wu, Z., Lv, L., Li, X., Zhang, K., Zhu, T. 2017. Removal of azo dye in an up-flow membrane-less bioelectrochemical system integrated with bio-contact oxidation reactor, Chem. Eng. J. 326, 454–461.

[104] Guaratini, C.C.I., Valnice, M., Zanoni, B., Corantes têxteis, Quim. Nova 23 (2000) 71–78.

[105] Oliveira, A.P.M. , Aparecido, N.B., Maria, E.H., Camila, L.T., Daniela, E.G.O.B., Isabella, G. 2018. Use of grape pomace as a biosorbent for the removal of the Brown KROM KGT dye, Bioresour. Technol. Rep. 2, 92–99.

[106] Surthar, R.G., Gao, B. 2017. Nanotechnology for drinking water purification, Water Purif. Elsevier, pp. 75–118.

[107] Lin, J., Su, B., Sun, M., Chen, B. 2018. Biosynthesized iron oxide nanoparticles used for optimized removal of cadmium with response surface methodology, Sci. Total Environ. 627 , 314–321.

[108] Devatha, C.P., Thalla, A.K., Katte, S.Y. 2016. Green synthesis of iron nanoparticles using different leaf extracts for treatment of domestic waste water, J. Clean. Prod. 139 , 1425–1435.

[109] Agarwal, H., Kumar, S.V., Rajeshkumar, S. 2017. A review on green synthesis of zinc oxide nanoparticles – an eco-friendly approach, Resour. Technol. 3 , 406–413.

[110] Iravani, S. 2011. Green Chemistry Green Synthesis of Metal Nanoparticles Using Plants, pp. 2638–2650.

[111] Fazlzadeh, M., Rahmani, K., Zarei, A., Abdoallahzadeh, H., Nasiri, F., Khosravi, R. 2017. A novel green synthesis of zero valent iron nanoparticles (NZVI) using three plant extracts and their efficient application for removal of Cr(VI) from aqueous solutions, Adv. Powder Technol. 28 , 122–130.

[112] Dubey, S.P., Lahtinen, M., Sillanpää, M. 2010. Green synthesis and characterizations of silver and gold nanoparticles using leaf extract of Rosa rugosa, Colloids Surf. A Physicochem. Eng. Asp. 364 , 34–41.

[113] Vidhu, V.K., Aromal, S.A., Philip, S.A. 2011. Green synthesis of silver nanoparticles using Macrotyloma uniflorum, Spectrochim. Acta Part A Mol. Biomol. Spectrosc. 83 392–397.

[114] Melo, C.M.T., Faria, J.V. 2014. Composition, phenolic compounds and antioxidant activity in conventional not edible parts of six vegetables, Biosci. J. 30 , 93–100.

[115] Ali, I., Al-Othman, Z.A., Alwarthan, A. 2016. Synthesis of composite iron nano adsorbent and removal of ibuprofen drug residue from water, J. Mol. Liq. 219 , 858–864.

[116] Cao, G., Booth, S. L., Sadowski, J. A., Prior, R. L. Increases in human plasma antioxidant capacity after consumption of controlled diets high in fruit and vegetables. Am. J. Clin. Nutr. 68, 1081-1087.

[117] Carbonneau, M.-A., Le´ger, C. L.; Descomps, B.; Michel, F.; Monnier, L. Improvement in the antioxidant status of plasma and low-density lipoprotein in subjects receiving a red wine phenolics mixture. J. Am. Oil Chem. Soc. 1998, 75, 235-240.

[118] Chen, J. H.; Ho, C. T. Antioxidant activities of caffeic acid and its related hydroxycinnamic acid compounds. J. Agric. Food Chem. 1997, 45, 2374-2378.

[119] Chipault, J. R.; Mizuno, G. R.; Hawkins, J. M.; Lundberg, W. O. The antioxidant properties of natural spices. Food Res. 1952, 17, 46-55.

[120] Constantino, L.; Albasino, A.; Rastelli, G.; Benvenuti, S. Activity of polyphenolic crude extracts as scavengers of superoxide radicals and inhibitors of xanthine oxidase. Planta Med. 1992, 58, 342-344.

[121] Dimberg, L. H., Theander, O.; Lignert, H. Avenanthramides-a group of phenolic antioxidants in oats. Cereal Chem. 1993, 70, 637-641.

[122] Ducrey, B.; Wolfender, J. L.; Marston, A.; Hostettmann, K. Analysis of flavonol glycosides of thirteen Epilobium species (Onagraceae) by LC-UV and thermospray LC-MS. Phytochemistry 1995, 38, 129-137.

[123] Duve, K. J.; White, P. J. Extraction and identification of antioxidants in oats. J. Am. Oil Chem. Soc. 1991, 68, 365- 370.

[124] Fischwick, M. J.; Swoboda, P. A. T. Measurement of oxidation of polyunsaturated fatty acids by spectrophotometric assay of conjugated derivates. J. Sci. Food Agric. 1997, 28, 387-393.

[125] Fitzpatrick, D. F.; Bing, B.; Rohdewald, P. Endotheliumdependent vascular effects of Pycnogenol. J. Cardiovasc. Pharmacol. 1998, 32, 509-515.

[126] Fluorescence decoration of defects in carbon nanotubes, J. Phys. Chem. C 114 (2010) 20941-20946.

[127] Liu,M.L., Chen,B.B., Li,C.M., Huang,C.Z., Carbon dots: synthesis, formation mechanism, fluorescence origin and sensing applications, Green Chem. 21 (2019) 449-471.

[128] Fan,L., Wang,Y., Li,L., Zhou,J., Carbon quantum dots activated metal organic frameworks for selective detection of Cu(Ⅱ) and Fe(III), Colloids Surf. A. 588 (2020) 124378.

[129] Pu,Z.-F., Wen,Q.-L., Yang,Y.-J., Cui,X.-M., Ling, J., Liu, P., Cao,Q.-E., Fluorescent carbon quantum dots synthesized using phenylalanine and citric acid for selective detection of Fe^{3+} ions, Spectrochim. Acta Part A 229 (2020) 117944.

[130] Cong,S., Liu,K., Qiao,F., Song,Y., Tan,M.,Biocompatible fluorescent carbon dots derived from roast duck for in vitro cellular and in vivo C. elegans bio-imaging, Methods 168 (2019) 76-83.

[131] Shariati-Rad,M., Ghorbani,Z., Carbon dot-based colorimetric sensor array for the discrimination of different water samples, Anal. Methods-Uk 11 (2019) 5584-5590.

[132] Liang,J.Y., Han,L., Liu,S.G., Ju,Y.J., Li,N.B., Luo,H.Q., Carbon dots-based fluorescent turn off/on sensor for highly selective and sensitive detection of Hg^{2+} and biothiols, Spectrochim. Acta Part A 222 (2019) 117260.

[133] Wang,C., Shi, H., Yang, M., Yan,Y., Liu, E., Ji, Z., Fan, J., Facile synthesis of novel carbon quantum dots from biomass waste for highly sensitive detection of iron ions, Mater. Res. Bull. 124 (2020) 110730.

[134] Das,P., Ganguly,S., Agarwal,T., Maity,P., Ghosh,S., Choudhary,S., Gangopadhyay,S., Maiti,T.K., Dhara,S., Banerjee,S., Das,N.C., Heteroatom doped blue luminescent carbon dots as a nano-probe for targeted cell labeling and anticancer drug delivery vehicle, Mater. Chem. Phys. 237 (2019) 121860.

[135] Yuan,T., Meng,T., He,P., Shi,Y.X., Li,Y.C., Li, X.H., Fan, L.Z., Yang,S.H., Carbon quantum dots: an emerging material for optoelectronic applications, J. Mater. Chem. C 7 (2019) 6820-6835.

[136] Mistry,B., Machhi,H.K., Vithalani,R.S., Patel,D.S., Modi,C.K., Prajapati,M., Surati,K.R., Soni,S.S., Jha,P.K., Kane,S.R., Harnessing the N-dopant ratio in carbon quantum dots for enhancing the power conversion efficiency of solar cells, Sustain. Energy Fuels 3 (2019) 3182-3190.

[137] Chu,K.W., Lee,S.L., Chang,C.J., Liu, L., Recent progress of carbon dot precursors and photocatalysis applications, Polymers 11 (2019).

[138] Das,R., Bandyopadhyay,R., Pramanik, P., Carbon quantum dots from natural resource: a review, Mater. Today Chem. 8 (2018) 96-109.

[139] Gao,Y., Qi,H., Shang,M.X., Zhang,J.L., Yan, J.Y., Song,W.B., Carbon dots-sensitized amorphous MoSx photoanode: Sequential electrodeposition preparation and dual amplified photoelectrochemical aptasensing of adenosine, Biosens. Bioelectron. 146 (2019).

[140] Yang,X.F., Zhang,M.T., Zhang,Y.L., Wang, N., Bian,W., Choi, M.M.F., Nitrogen and phosphorus co-doped carbon dots as a “turn-off-on” fluorescence probe for the detection of Hg^{2+} and GSH and cell imaging, Anal. Methods-Uk 11 (2019) 5803-5809.

[141] Aslandaş,A.M., Balcı,N., Arık,M., Şakiroğlu,H., Onganer,Y., Meral,K., Liquid nitrogen- assisted synthesis of fluorescent carbon dots from Blueberry and their performance in Fe^{3+} detection, Appl. Surf. Sci. 356 (2015) 747-752.

[142] Lai,C.W., Hsiao,Y.H., Peng,Y.K., Chou,P.T., Facile synthesis of highly emissive carbon dots from pyrolysis of glycerol; gram scale production of carbon dots/mSiO (2) for cell imaging and drug release, J. Mater. Chem. 22 (2012) 14403-14409.

[143] Zulfajri,M., Gedda,G., Chang,C.J., Chang,Y.P., Huang,G.G., Cranberry beans derived carbon dots as a potential fluorescence sensor for selective detection of Fe^{3+} ions in aqueous solution, ACS Omega 4 (2019) 15382-15392.

[144] Jana,J., Lee, H.J., Chung,J.S., Kim,M.H., Hur,S.H., Blue emitting nitrogen-doped carbon dots as a fluorescent probe for nitrite ion sensing and cell-imaging, Anal. Chim. Acta 1079 (2019) 212-219.

[145] Zhao,X., Liao,S., Wang,L., Liu,Q., Chen,X., Facile green and one-pot synthesis of purple perilla derived carbon quantum dot as a fluorescent sensor for silver ion, Talanta 201 (2019) 1-8.

[146] Farahmandfar,R., Tirgarian,B., Dehghan,B., Nemati,A., Comparison of different drying methods on bitter orange (Citrus aurantium L.) peel waste: changes in physical (density and color) and essential oil (yield, composition, antioxidant and antibacterial) properties of powders, J. Food Meas. Charact. (2019).

[147] Peixoto,J.S., Comar,J.F., Moreira,C.T., Soares,A.A., de Oliveira,A.L., Bracht,A., Peralta,R.M., Effects of Citrus aurantium (bitter orange) fruit extracts and p-synephrine on metabolic fluxes in the rat liver, Molecules 17 (2012) 5854−5869.

[148] Suntar,I., Khan,H., Patel,S., Celano,R., Rastrelli,L., An overview on Citrus aurantium L.: its functions as food ingredient and therapeutic agent, Oxid. Med. Cell Longev. (2018).

[149] Arbo,M.D. Larentis,E.R. Linck,V.M., Aboy,A.L. , Pimentel,A.L. , Henriques,E. Dallegrave,A.T. , Garcia,S.C., Leal,M.B., R.P.,Limberger, Concentrations of p-synephrine in fruits and leaves of Citrus species (Rutaceae) and the acute toxicity testing of Citrus aurantium extract and p-synephrine, Food Chem. Toxicol. 46 (2008) 2770−2775.

[150] Khan,Z.M.S.H., Rahman,R.S., Shumaila,S., Islam,M.Z., Hydrothermal treatment of red lentils for the synthesis of fluorescent carbon quantum dots and its application for sensing Fe^{3+}, Opt. Mater. 91 (2019) 386−395.

[151] Tammina,S.K., Yang,D., Li,X., Koppala,S., Yang,Y., High photoluminescent nitrogen and zinc doped carbon dots for sensing Fe(3+) ions and temperature, Spectrochim. Acta Part A 222 (2019) 117141.

[152] Xu,X., Ren,D., Chai,Y., Cheng,X., Mei,J., Bao,J., Wei,F., Xu,G., Hu,Q., Cen,Y., Dual emission carbon dots-based fluorescent probe for ratiometric sensing of Fe(III) and pyrophosphate in biological samples, Sens. Actuators B 298 (2019) 126829.

[153] Zulfajri,M., Gedda,G., Chang,C.J., Chang,Y.P., Huang,G.G., Cranberry beans derived carbon dots as a potential fluorescence sensor for selective detection of $Fe^{(3+)}$ ions in aqueous solution, ACS Omega 4 (2019) 15382−15392.

[154] Sinha,M.K., Purkait,M.K., Preparation of fouling resistant PSF flat sheet UF membrane using amphiphilic polyurethane macromolecules, Desalination, 355 (2015) 155-168.

[155] M. K. Sinha, M. K. Purkait, Preparation and characterization of stimuli-responsive hydrophilic polysulfone membrane modified with poly (N- vinylcaprolactum-co-acrylic acid), Desalination, 348 (2014), 16-25.

[156] Sharma,N., Purkait,M.K., Preparation of hydrophilic polysulfone membrane using polyacrylic acid with polyvinyl pyrrolidone, J. Appl. Polymer Sci., 132 (2015).

[157] Wongchitphimon,S., Wang,R., Jiraratananon,R., Shi,L., Loh,C.H., Effect of polyethylene glycol (PEG) as an additive on the fabrication of polyvinylidene fluoride-*co*-hexafluropropylene (PVDF-HFP) asymmetric microporous hollow fiber membranes, J. Membr. Sci., 369 (2011) 329-338.

[158] Shi,L., Wang,R., Cao,Y., Liang, D.T., Tay,J. H., Effect of additives on the fabrication of poly (vinylidene fluoride-co-hexafluropropylene) (PVDF-HFP) asymmetric microporous hollow fiber membranes, J. Membr. Sci., 315 (2008) 195–204.

[159] Shi,L., Wang,R., Cao,Y., Feng,C., Liang,D.T., Tay,J.H., Fabrication of poly (vinylidene fluoride-co-hexafluropropylene) (PVDF-HFP) asymmetric microporous hollow fiber membranes, J. Membr. Sci., 305 (2007) 215–225.

[160] Sinha,M.K., Purkait,M.K., Enhancement of hydrophilicity of poly (vinylidene fluoride-co-hexafluoropropylene) (PVDF-HFP) membrane using various alcohols as nonsolvent additives, J. Membr. Sci., 338 (2014) 106-114.

[161] Feng,C., Wang,R., Shi,B., Li,G., Wu,Y., Factors affecting pore structure and performance of poly(vinylidene fluoride-co-hexafluoro propylene) asymmetric porous membrane, J. Membr. Sci., 277 (2006) 55–64.

[162] Fontananova,E., Jansen,J.C., Cristiano,A., Curcio,E., Drioli,E., Effect of additives in the casting solution on the formation of PVDF membranes, Desalination, 192 (2006) 190–197.

[163] Shi,L., Wang,R., Cao,Y., Effect of the rheology of poly(vinylidene fluoride-co-hexafluropropylene) (PVDF-HFP) dope solutions on the formation of microporous hollow fibers used as membrane contactors, J. Membr. Sci., 344 (2009) 112–122.

[164] Feng,C.S., Wang,R., Shi,B.L., Li,G.M., Wu,Y.L., Factors affecting pore structure andperformance of poly(vinylidene fluoride-co-hexafluoro propylene) asymmetric porous membrane, J. Membr. Sci., 277 (2006) 55-64.

[165] Tian,X.Z., Zhu,B.K., Xu,Y.Y., PVDF-co-HFP membrane for recovery of aroma compounds from aqueous solutions by pervaporation: I. Ethyl acetate/water system, J. Membr. Sci., 248 (2005) 109-117.

[166] Atchariyawut,S., Feng,C.S., Wang,R., Jiraratanano,R., Liang,D.T., Effect of membrane structure on mass-transfer in the membrane gas-liquid contacting process using microporous PVDF hollow fibres, J. Membr. Sci., 285 (2006) 272-281.

[167] Lee,K.W., Seo,B.K., Nam,S.T., Han,M.J., Trade-off between thermodynamic enhancement and kinetic hindrance during phase inversion in the preparation of polysulfone membranes, Desalination, 159 (2003) 289-296.

[168] Sinha,M.K., Purkait,M.K., Increase in hydrophilicity of polysulfone membrane using polyethylene glycol methyl ether, J. Membr. Sci., 437 (2013) 7–16.

[169] Curcio,E., Fontananova,E., Profio,G.Di, Drioli,E., Infuence of the structural properties of poly (vinylidene fluoride) membranes on the heterogenous nucleation rate of protein crystals, J. Phys. Chem. B., 110 (2006) 12438-45.

[170] Agrawal,A., Tratnyek,G.P., 1996. Reduction of nitro aromatic compounds by zero-valent iron metal, En. Sci. Technol., 30, 153–160.

[171] Harrison,P.T.C., 2005. Fluoride in water: a UK perspective, J. Fluor. Chem., 126, 1448-1456.

[172] Xu, J., Dozier, A., Bhattacharyya, D., 2005. Synthesis of nanoscale bimetallic particles in polyelectrolyte membrane matrix for reductive transformation of halogenated organic compounds, J. Nan. Res., 7, 449–467.

[173] Xu, J., Bhattacharyya, D., 2008. Modeling of Fe/Pd nanoparticle-based functionalized membrane reactor for PCB dechlorination at room temperature, J. Phys. Chem. C, 112, 9133–9144.

[174] Zhang, Y., Lin, X., Zhou, Q., Luo, X., 2016. Fluoride adsorption from aqueous solution by magnetic core shell Fe3O4@alginate-La particles fabricated via electro-coextrusion, App. Surf. Sc., 389, 34–45.

[175] Wang, C.B., Zhang, W.X., 1997. Synthesizing nanoscale iron particles for rapid and complete dechlorination of TCE and PCBs, En. Sc. Tech., 31, 2154–2156.

[176] Liu, Z., Ling, X.Y., Su, X., Lee, J.Y., 2004. Carbon-supported Pt and Pt Ru nanoparticles as catalysts for a direct methanol fuel cell, J. Phys. Chem. B., 108, 8234–8240.

[177] Mallick, K., Scurrell, S.M., 2003. CO oxidation over gold nanoparticles supported on TiO_2 and TiO_2–ZnO: catalytic activity effects due to surface modification of TiO_2 with ZnO, App. Cat. A: Gen., 253, 527–536.

[178] Sun, C., Peltre, M.J., Briend, M., Blanchard, J., Fajerwerg, K., Krafft, J.M., Breysse, M., Cattenot, M., Lacroix, M., 2003. Catalysts for aromatics hydrogenation in presence of sulfur: reactivities of nanoparticles of ruthenium metal and sulphide dispersed in acidic Y zeolites, App. Cat. A: Gen., 245, 245–255.

[179] Xu, J., Bhattacharyya, D., 2007. Fe/Pd nanoparticle immobilization in microfiltration membrane pores: synthesis, characterization, and application in the dechlorination of polychlorinated biphenyls, Ind. Eng. Chem. Res., 46, 2348–2359.

[180] Ohya, H., Shibata, M., Negishi, Y., Guo, H.Q., Choi, H.S., 1994. The effect of molecular weight cut-off of PAN ultrafiltration support layer on separation of water–ethanol

mixtures through pervaporation with PAA-PAN composite membrane, J. Membr. Sci., 90, 91–100.

[181] Choi, H.S., Hino, T., Shibata, M., Negishi, Y., Ohya, H., The characteristics of a PAA-PSf composite membrane for separation of water–ethanol mixtures through pervaporation, J. Membr. Sci., 72, 259–266.

[182] Parshetti, G.K., Doong, R.A., 2009. Dechlorination of trichloroethylene by Ni/Fe nanoparticles immobilized in PEG/PVDF and PEG/nylon 66 membranes, Water Res., 43, 3086–3094.

[183] Reddad, Z., Gerente, C., Andres, Y., 2002 Adsorption of several metal ions onto a low-cost biosorbent: kinetic and equilibrium studies, Environ. Sci. Technol. 36, 2067–2073.

[184] Gotoh, T., Matsushima, K., Kikuchi, K. I. 2004 Adsorption of Cu and Mn on covalently cross-linked alginate gel beads, Chemosphere 55, 57–64.

[185] Biswas, K., Debnath, S., Ghosh, U. C. 2010 Physicochemical aspects on fluoride adsorption for removal from water by synthetic hydrous iron (III)-chromium (III) mixed oxide, Sep. Sci. Technol. 45, 472–485.

[186] Shortt, W. E. 1937. Endemic fluorosis in Nellore District, South India, Indian Medical Gazette, 72–396.

[187] Mariappan, R., Vairamuthu, R., Ganapathy, A. 2015 Use of chemically activated cotton nut shell carbon for the removal of fluoride contaminated drinking water: kinetics evaluation, Chin. J. Chem. Eng. 23, 710–721.

[188] Xu, X., Li, Q., Cui, H. 2011 Adsorption of fluoride from aqueous solution on magnesia-loaded fly ash cenospheres, Desalination 272, 233–239.

[189] Rajkumar, S., Murugesh, S., Sivasankar, V., Darchen, A., Msagati, T.A.M., Chaabane, T. Low-cost fluoride adsorbents prepared from a renewable biowaste: Synthesis,

characterization and modelling studies, Arab. J. Chem. https://doi.org/10.1016/ j.arabjc.2015.06.028.

[190] Ghosh, A., Chakrabarti, S., Biswas, K., Ghosh, U. C. 2015 Column performances on fluoride removal by agglomerated Ce(IV)-Zr(IV) mixed oxide nanoparticles packed fixed-beds, J. Environ. Chem. Eng. 3, 653–661.

[191] Biswas, K., Gupta, K., Ghosh, U. C. 2009. Adsorption of fluoride by hydrous iron(III)-tin (IV) bimetal mixed oxide from the aqueous solutions, Chem. Eng. J. 149, 196–206.

[192] Biswas, K., Gupta, K., Goswami, A., Ghosh, U. C. 2010 Fluoride removal efficiency from aqueous solution by synthetic iron(III)-aluminum(III)-chromium(III) ternary mixed oxide, Desalination. 255, 44–51.

[193] Nigussie, W., Zewge, F., Chandravanshi, B.S. 2007 Removal of excess fluoride from water using waste residue from alum manufacturing process, J. Hazard. Mat., 147, 954-963.

[194] Shimelis, B., Zewge, F., Chandravanshi, B. S. 2006 Removal of excess fluoride from water by aluminium hydroxide, Bull. Chem. Soc. Ethiop., 20, 17-34.

[195] Alemu, S., Mulugeta, E., Zewge, F., Candravanshi, B. S. 2014 Water defluoridation by aluminium oxide–manganese oxide composite material, Environ. Technol. 35, 1893-1903.

[196] Gómez-Hortigüela, L. , Pérez-Pariente, J., García, R. 2013 Natural zeolites from Ethiopia for elimination of fluoride from drinking water, Sep. Purif. Technol., 120 (2013) 224-229.

[197] Hernández-Montoya, V., Elizalde-González, M. P. , Trejo-Vázquez, R. 2007 Screening of commercial sorbents for removal of fluoride in synthetic and groundwater, Environ. Technol., 28, 595-607.

[198] Airado-Rodríguez, D., Galeano-Díaz, T., & Durán-Merás, I. (2009). Usefulness of fluorescence excitation–emission matrices in combination with PARAFAC, as fingerprint of red wines. Journal of Agricultural and Food Chemistry, 57, 1711–1720.

[199] Álvarez-Diduk, R., Ramírez-Silva, M. T., Galano, A., & Merkoci, A. (2013). Deprotonation mechanism and acidity constants in aqueous solution of flavonol: A combined experimental and theoretical study. Journal of Physical Chemistry B, 117, 12347–12359.

[200] Andersen, C. M., & Bro, R. (2003). Practical aspects of PARAFAC modelling of excitation–emission data. Journal of Chemometrics, 17, 200–215.

[201] Bae, H., Jayaprakasha, G. K., Jifon, J., & Bhimanagouda, S. P. (2012). Extraction efficiency and validation of an HPLC method for flavonoid analysis in peppers. Food Chemistry, 130, 751–758.

[202] Cao, W., Hu, S. S., Li, X.-Y., Pang, X.-Q., Cao, J., Ye, L.-H., ... Chu, C. (2014). Highly sensitive analysis of flavonoids by zwitterionic microemulsion electrokinetic chromatography coupled with light-emitting diode-induced fluorescence detection. Journal of Chromatography A, 1358, 277–284.

[203] Careri, M., Bianchi, F., & Corradini, C. (2002). Recent advances in the application of mass spectrometry in food-related analysis. Journal of Chromatography A, 970, 3–64.

[204] Delgado, C., Tomás-Barberán, F. A., Talou, T., & Gaset, A. (1994). Capillary electrophoresis as an alternative to HPLC for determination of honey flavonoids. Chromatographia, 38(1/2), 72–78.

[205] Di Anibal, C. V., Rodríguez, M. S., & Albertengo, L. (2015). Synchronous fluorescence and multivariate classification analysis as a screening tool for determining Sudan I dye in culinary spices. Food Control, 56, 18–23.

[206] Ehala, S., Vaher, M., & Kaljurand, M. (2005). Characterization of phenolic profiles of Northern European Berries by capillary electrophoresis and determination of their antioxidant activity. Journal of Agricultural and Food Chemistry, 53, 6484–6490.

[207] Escandar, G. M., Goicoechea, H. C., Muñoz de la Peña, A., & Olivieri, A. C. (2014). Second- and higher-order data generation and calibration: A tutorial. Analytical Chimica Acta, 806, 8–26.

[208] Espinosa Mansilla, A., Muñoz de la Peña, A., & González Gómez, D. (2005). Using univariate linear regression calibration software in the MATLAB environment. Application to chemistry laboratory practices. Chemical Education, 10, 337–345.

[209] Haaland, D. M., & Thomas, E. V. (1988a). Partial least-squares methods for spectral analyses. 1. Relation to other quantitative calibration methods and the extraction of qualitative information. Analytical Chemistry, 60, 1193–1202.

[210] Haaland, D. M., & Thomas, E. V. (1988b). Partial least-squares methods for spectral analyses. 2. Application to simulated and glass spectral data. Analytical Chemistry, 60, 1202–1208.

[211] Jeffery, D. W., Parker, M., & Smith, P. A. (2008). Flavonol composition of Australian red and white wines determined by high-performance liquid chromatography. Australian Journal of Grape and Wine Research, 14, 153–161.

[212] Jiménez Girón, A., Durán-Meras, I., Muñoz de la Peña, A., Espinosa Mansilla, A., Cañada Cañada, F., & Olivieri, A. C. (2008). Photoinduced fluorimetric determination of folic acid and 5-methyltetrahydrofolic acid in serum using the kinetic evolution of the emission spectra accomplished with multivariate second-order methods. Analytical Bioanalytical Chemistry, 391, 827–835.

[213] Singleton V, Rossi J. Colorimetry of total phenolics with phosphomolibdic-phosphotungstic acid reagents. Am J Enol Vitic .1965; 16:144–158.

[214] Zhishen J., Mengcheng T., Jianming W. The determination of flavonoid contents in mulberry and their scavenging effects on superoxide radicals. Food Chem, 1999; 64: 555-559.

[215] Broadhurst RB, jones WT. Analysis of condensed tannins using acidified vanillin. Journal of the Science of Food and Agriculture. 1978; 48(3): 788–794.

[216] Brand-Williams W, Cuvelier ME, Berset C. Use of a free radical method to evaluate antioxidant activity. LWT – Food Sci Technol. 1995; 28: 25-30.

[217] Benzie IFF, Strain JJ. Ferric reducing ability of plasma (FRAP) a measure of antioxidant power: The FRAP assay. Anal. Biochem. 1996; 239: 70-76.

[218] Rehman, M.A., Yusoff, I., Ahmmad, R., Alias, Y., 2015. Arsenic Adsorption Using Palm Oil Waste Clinker Sand Biotechnology: an Experimental and Optimization Approach, Water Air Soil Pol., 226, 1-13.

[219] Kaniyoor, A., Baby, T.T., Arockiadoss, T., Rajalakshmi, N. 2011 Wrinkled graphenes: a study on the effects of synthesis parameters on exfoliation-reduction of graphite oxide, J. Phys. Chem. C. 115 (36), 17660-17669.

[220] Sun, Y., Ding, C., Cheng, W., Wang, X., 2014. Simultaneous adsorption of and reduction of U (VI) on reduced grapheme oxide-supported nanoscale zerovalent iron, J. Hazard. Mat., 280, 399-408.

[221] Zhou, G., Chen, Z., Fang, F., He, Y., Sun, H., Shi, H., 2015. Fenton-like degradation of Methylene Blue using paper mill sludge-derived magnetically separable heterogeneous catalyst: characterization and mechanism. J. Environ. Sci. (China) 35, 20–26.

[222] Lin, J., Weng, X., Dharmarajan, R., Chen, Z., 2017. Characterization and reactivity of iron based nanoparticles synthesized by tea extracts under various atmospheres. Chemosphere 169, 413–417

[223] Huang, L., Weng, X., Chen, Z., Megharaj, M., Naidu, R., 2014a. Synthesis of iron-based nanoparticles using oolong tea extract for the degradation of malachite green. Spectrochim. Acta Part A Mol. Biomol. Spectrosc. 117, 801–804.

[224] Xu, H., Gao, J., Qian, X., Wang, J. 2016 Metal–organic framework nanosheets for fast-response and highly sensitive luminescent sensing of Fe^{3+}, J. Mater. Chem. A. 4, 10900–10905.

[225] Zhong, F., Li, C., Xie, Y. 2019 Titanium metal-organic framework nanorods for highly sensitive nitroaromatic explosives detection and nanomolar sensing of Fe^{3+}, J. Sol. State Chem. 278, 120892.

[226] Feng, P.L., Leong, K., Allendorf, M.D. 2012 Charge-transfer guest interactions in luminescent MOFs: implications for solid-state temperature and environmental sensing, DTr 41, 8869–8877

[227] Gutierrez, M., Cohen, B., Sánchez, F., Douhal, A. 2016 Photochemistry of Zr-based MOFs: ligand-to-cluster charge transfer, energy transfer and excimer formation, what else is there? Phys. Chem. Chem. Phys. 18, 27761–27774.

[228] Dong, J., Zhao, Y., Zhao, R., Zhou, R., 2010. Effects of pH and particle size on kinetics of nitrobenzene reduction by zero-valent iron, J. En. Sci., 22, 1741-1747.

[229] Mondal, P., Purkait, M.K., 2016. Green synthesized iron nanoparticle embedded pH responsive PVDF-co-HFP membranes: Optimization study for NPs preparation and nitrobenzene reduction, Sep. Sci. and Technol., doi: 10.1080/01496395.2016.1274759.

[230] Kanrar, S., Debnath, S., De, P., Parashar, K., Pillay, K., Sasikumar, P., Ghosh, U. C. 2016 Preparation, characterization and evaluation of fluoride adsorption efficiency from water of iron-aluminium oxide-graphene oxide composite material, Ch. Eng. J. 306, 269-279.

[231] Biswas, K., Saha, S. K., Ghosh, U. C. 2007 Adsorption of Fluoride from Aqueous Solution by a Synthetic Iron(III)-Aluminum (III) Mixed Oxide, Ind. Eng. Chem. Res. 46, 5346-5356.

[232] Babic, B. M., Milonjic, S. K., Polovina, M. J., Kaludierovic, B. V. 1999 Point of zero charge and intrinsic equilibrium constants of activated carbon cloth, Carbon 37, 477–481.

[233] Low, K. S., Lee, C. K. 1990 The Removal of Cationic Dyes Using Coconut Husk as an adsorbent, Pertanika 13, 221-228.

[234] Ho, Y. S., Chiang, T. H., Hsueh, Y. M. 2005 Removal of Basic Dye from Aqueous Solution Using Tree Fern as a Biosorbent. Process Biochem. 40, 119-124.

[235] Mukhopadhyay, K., Ghosh, A., Das, S.K., Show, B. 2017 Synthesis and characterization of cerium (IV) incorporated hydrous iron (III) oxide as an adsorbent for fluoride removal from water, RSC Adv. 7, 26037-26051.

[236] Kheirandish, S., Ghaedi, M., Dashtian, K., Heidari, F. 2017 Chitosan extraction from lobster shells and its grafted with functionalized MWCNT for simultaneous removal of Pb^{2+} ions and eriochrome cyanine R dye after their complexation, Int. J. Biol. Macro. 102, 181-191.

[237] Sengupta, B. , Reilly, S. M., Davis, D. E. 2015 Excited State Proton Transfer of Natural Flavonoids and Their Chromophores in Duplex and Tetraplex DNAs, J. Phys. Chem. B 119(6), 2546-2556.

[238] Zhang, C., Hu, Q., Wu, S., Chen, F. 2020 Selective determination of DNA based on the fluorescence recovery of carbon dots quenched by $Ru(bpy)_2(dppz)^{2+}$, Talanta 217, 121103.

[239] Chandra, S., Laha, D., Pramanik, A., Ray, C. A., Karmakar, P., Sahu, S. K. 2016 Synthesis of highly fluorescent nitrogen and phosphorus doped carbon dots for the detection of Fe^{3+} ions in cancer cells. Luminescence. 31(1), 81–87.

[240] Atchudan, R., Aseer, K. R., Perumal, S., Karthik, N., Yong, R. L. 2017 Highly fluorescent nitrogendoped carbon dots derived from Phyllanthus acidus utilized as a fluorescent probe for label-free selective detection of Fe^{3+} ions, live cell imaging and fluorescent ink. Biosens. Bioelectron. 99, 303–311.

[241] Zhu, X., Wang, J., Zhu, Y., Jiang, H., Tan, D., Xu, Z. 2018 Green emitting N,S-co-doped carbon dots for sensitive fluorometric determination of Fe(III) and Ag(I) ions, and as a solvatochromic probe. Microchimi. Acta. 185(11), 510-520.

[242] Wu, S.-P., Chen, Y.-P., Sung, Y.-M. 2011. Colorimetric detection of Fe^{3+} ions using pyrophosphate functionalized gold nanoparticles, Analyst, 136 (9), 1887–1891.

[243] Jin, L. et al. 2016 Fluorescence turn-on detection of Fe^{3+} in pure water based on a cationic poly (perylene diimide) derivative, RSC Adv. 6 (63) , 58394–58400.

[244] Kim, S.Y. 2018. Colorimetric detection of $Fe^{3+/2+}$ and fluorescent detection of Al^{3+} in aqueous media: applications and DFT calculations, J. Coord. Chem. 1–21.

[245] Nandre, J. 2014 The amidine based colorimetric sensor for Fe^{3+}, Fe^{2+}, and Cu^{2+} in aqueous medium, J. Fluoresc. 24 (6), 1563–1570.

[246] Zhu, X. 2017 Understanding the selective detection of Fe^{3+} based on graphene quantum dots as fluorescent probes: the K_{sp} of a metal hydroxide-assisted mechanism, Anal. Chem. 89 (22), 12054–12058.

[247] Xu, W. 2018 Fluorescent poly (hydroxyurethane): biocompatibility evaluation and selective detection of Fe (III), J. Appl. Polym. Sci. 135 (40), 46723.

[248] Chen, M., Xu, W.-M., Tian, J.-Y., Cui, H., Zhang, J.-X., Liu, C.-S., Du, M. 2017. A terbium(III) lanthanide–organic framework as a platform for a recyclable multi-responsive luminescent sensor, J. Mater. Chem. C. 5, 2015-2021.

[249] Parmar, B., Rachuri, Y., Bisht, K. K., Suresh, E. 2017. Mixed-Ligand LMOF Fluorosensors for Detection of Cr(VI) Oxyanions and Fe^{3+}/Pd^{2+} Cations in Aqueous Media. Inorg. Chem. 56, 10939-10949.

[250] Chen, S., Shi, Z., Qin, L., Jia, H. 2017 Two New Luminescent Cd(II)-Metal Organic Frameworks as Bifunctional Chemosensors for Detection of Cations Fe^{3+}, Anions CrO_4^{2-}, and $Cr_2O_7^{2-}$ in Aqueous Solution. Cryst. Growth Des. 17, 67-72.

[251] Zhang, S.-T., Yang, J., Wu, H., Liu, Y.-Y., Ma, J.-F. 2015 Systematic Investigation of High Sensitivity Luminescent Sensing for Polyoxometalates and Iron(III) by MOFs Assembled with a New Resorcin[4]arene-Functionalized Tetracarboxylate, Chem. Eur. J. 21, 15806-15819.

[252] Jiang, K., Wu, Y.-C., Wu, H.-Q., Li, S.-L., Luo, S.-H., Wang, Z.-Y 2018. A highly selective, pH tolerable and fast-response fluorescent probe for Fe^{3+} based on star-shape benzothiazole derivative, J. Photochem. Photobiol. A: Chem., 350 52-58.

[253] Xu, J.-H., Hou, Y.-M., Ma, Q.-J., Wu, X.-F., Wei, X.-J. 2013. A highly selective fluorescent sensor for Fe^{3+} based on covalently immobilized derivative of naphthalimide Spectrochim. Acta A Mol. Biomol. Spectrosc., 112 116-124.

[254] Hu, S., Zhang, S., Gao, C., Xu, C., Gao, Q 2013. A new selective fluorescent sensor for Fe^{3+} based on a pyrazoline derivative Spectrochim. Acta A. Mol. Biomol. Spectrosc., 113 325-331.

Appendix A: Calibration Curve for the determination of dye concentration

The determination of crystal violet dye concentration in the samples after adsorption study is determined by first preparing a calibration curve. Standard crystal violet concentration in the range of 100-500 ppm was prepared using Millipore water and specific amounts of crystal violet dye powder. The prepared standards thus prepared were mixed well utilizing magnetic stirrer maintained at 100 rpm for 30 min. The obtained dye samples with varied concentrations were analyzed for their absorbance using UV-Visible spectrophotometer at a wavelength of 617 nm. Subsequently, the obtained absorbance values were plotted with respect to variations in dye solution concentration. Figure A1 presents the obtained calibration curve. It can be observed that the absorbance varied linearly with variation in dye concentration. Thus, using the obtained calibration curve, the concentration of the samples after degradation utilizing Fe-NPs were evaluated by measuring its absorbance.

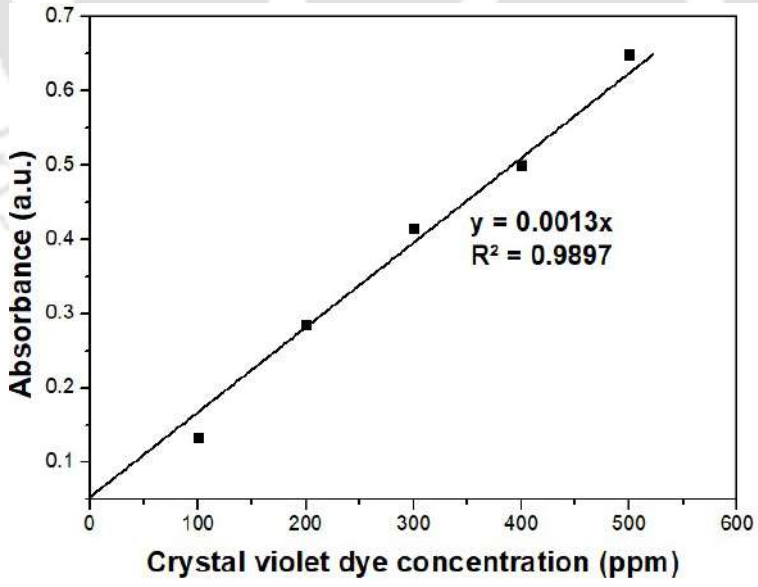

Figure A1: Calibration curve for the evaluation of crystal violet dye concentration in samples after degradation utilizing clove extract mediated Fe-NPs.

Appendix B: Calibration curve for determination of rutin, quercetin, and catechin in plant extracts

The determination of flavonoids (rutin, quercetin, and catechin) in green extracts was performed using HPLC technique. The pure rutin was obtained from Sigma Aldrich, U.S.A. Standard samples of rutin ranging from 250-1000 mg/L were prepared and calibration curve was obtained utilizing the area under the peak value varying with different concentration of rutin obtained from HPLC analysis at a specific retention time (for rutin the retention time was 2.59 min). Figure B1 represents the obtained calibration curve. The green extracts were then analyzed through HPLC analysis and at 2.59 min area under the peak was noted. From the standard calibration curve obtained equation, the area under peak of the green extract at retention time 2.59 min was analyzed and the concentration of rutin present in the green extract sample was obtained. Similar calculations were performed for obtaining the values of quercetin and catechin present in green extracts through HPLC analysis.

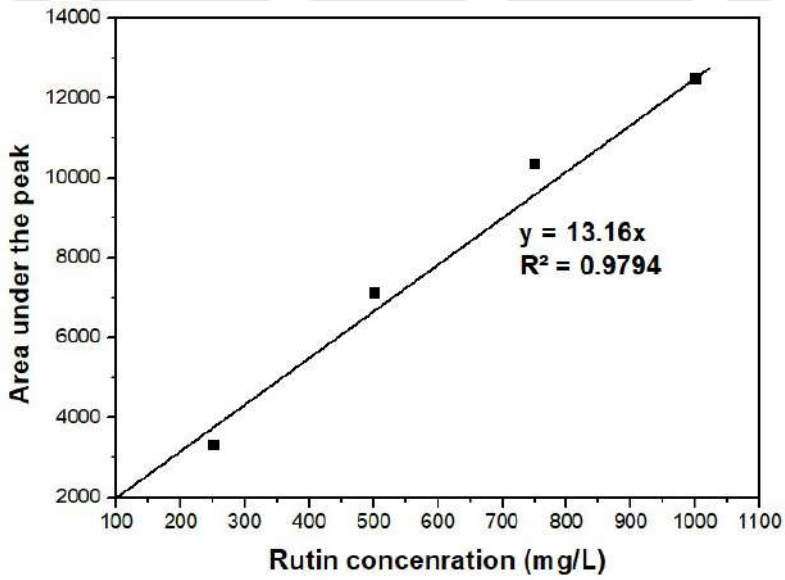

Figure B1: Calibration curve for the evaluation of rutin concentration in green extracts obtained from clove, cardamom, and bay-leaf.

Appendix C: Limit of detection calculation for Fe-Al NCs for Fe^{3+} ion sensing application

The below calculation was done in order to calculate the limit of detection of Fe-Al nanocomposite for analysing Fe^{3+} ion. A calibration curve was obtained between photoluminescence intensity and different Fe^{3+} ion concentration. Utilizing the curve and average intensities LOD value was calculated as shown below. Similar method was followed for Fe-NPs LOD calculation.

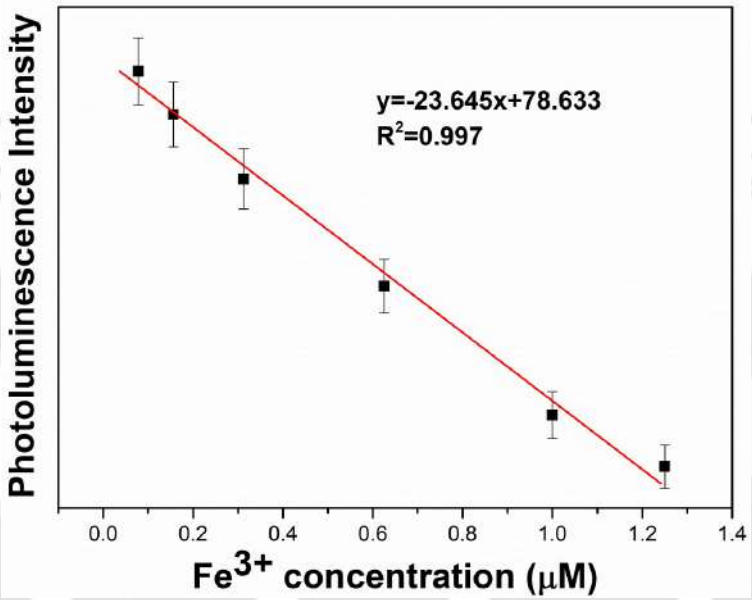

Figure C1: Corresponding Stern-Volmer plot for PL quenching of Fe-Al NCs when Fe^{3+} ions are added

Linear Equation: Y = - 23.645X + 78.63

$S = 2.36 \times 10^{7}\ M^{-1}$

$I_a = \frac{150.6+157.8+160.5+16\ .2+153.8+165.8}{6} = 158.95$

$S_b = \sqrt{\frac{\sum(I_0-I_a)^2}{N-1}} = 6.09 \quad (N = 6)$

$LOD = \frac{3\times S_b}{S} = \frac{3\times 6.09}{2.36\times 10^{7}} = 0.775 \times 10^{-6} M$

S is the slope of the calibration curve, $\mathbf{S_b}$ is the standard deviation of the blank group, $\mathbf{I_0}$ is the fluorescence intensity of the Fe-Al NCs aqueous solution, and $\mathbf{I_a}$ is the average of $\mathbf{I_0}$.

Appendix D: Error Analysis

Error analysis is necessary as it infers to the accuracy of calculations and reliability of reported data. Although experiments are carried out with utmost care, yet due to measurement errors, the data obtained or calculated may not be accurate. There are different types of errors viz. absolute error, relative error, systematic error and random error. Absolute error refers to the difference between the measured or inferred value of a quantity and its actual value. Relative error is the ratio of the error to the best value of the quantity. Systematic errors are the results of faulty assumptions and measuring techniques, whereas random errors result from variation in the precision of measuring parameters and the slight variations that occur in successive measurements under nearly identical conditions.

Error measurement in dye degradation and nitrobenzene (NB) reduction experiments

The measurement maximum error for the estimation of crystal violet concentration reduction by ZVI NPs, and NB reduction through Fe-NPs impregnated polymeric membrane is about ± 2-3%. These errors were taken under consideration considering the variations in the experimental measurements during the determination of permeate flux during MF experiments.

Error measurements for kinetic and equilibrium models

Error calculations were performed for the HPLC analysis of flavonoid content in different green extracts. Flavonoids such as quercetin, rutin, and catechin were measured and error of ±3-4% was observed for all the calculations throughout the study.

Error measurements for kinetic and equilibrium models

Error calculations were also done for the kinetic and equilibrium models for the green synthesized iron-aluminum nanocomposite utilized for fluoride adsorption experiments. An error of ± 2 % was observed for each of the models calculated.

Error measurements for measuring pure water flux through membranes

For studying the pH dependent water permeability through pH responsive membranes and Fe-NPs impregnated membranes, an error within the range of ± 3% was observed for all the cases.

Appendix E: Yield of Nanoparticles

For preparing 0.025 (M) $FeCl_3$ solution about 4.05g of $FeCl_3$ powder was taken in 1000 mL deionized water. By calculating it was obtained that in 4.05 g $FeCl_3$ powder, Fe ion present was 1.37g in 1000 mL.

For preparing green synthesized Fe NPs, about 10 mL of the prepared 0.025 (M) $FeCl_3$ solution was taken, thus the **amount of Fe ion utilized was (A)**= [(1.37/1000)×10] g = 0.0137 g.

After the green synthesis reaction utilizing 40 mL pH 7 clove extract and 10 mL 0.025 (M) $FeCl_3$ solution, about 0.033g of Iron NPs coated with plant biomolecules were obtained.

When about 0.01g of the prepared green synthesized Iron NPs was utilized for elemental analysis (EDX), Fe ion content was found to be about 29.1 wt%.

Hence, **Fe ion content of the total green synthesized Iron NPs was (B)** = [(29.1/100) × 0.033]g = 0.0096g

Therefore **Yield %= Amount of Fe ion in synthesized Fe NPs (B)/ Amount of Fe ion utilized (A) for the synthesis of Fe NPs**

Yield%= 70.07%